Development of Beam Instrumentation for Exotic Particle Beams

Thesis submitted in accordance with the requirements of the

University of Liverpool

for the degree of Doctor in Philosophy by

Alejandro Garcia Sosa

June 2015

Abstract

Modern nuclear physics makes extensive use of exotic particle beams created using accelerators, such as unstable ion isotopes and antiprotons. These give access to a wide range of fundamental studies that are at the cutting edge of science. The commissioning and operation of these accelerators require powerful beam diagnostic devices that are specially adapted to these unusual, and often very faint, beams.

The work leading to this thesis, focuses on the development of the beam diagnostic system of the future superconducting linear accelerator at the High Intensity and Energy Isotope Separator On-Line Device (HIE-ISOLDE), which shall deliver stable and unstable isotope beams ranging from Helium to Radium at beam energies between 0.3 and 10 MeV/u and intensities from few particles per second up to 1 nA. The main elements of the diagnostics system are a Faraday cup for the measurement of the absolute beam current, a scanning blade with a V-shaped slit, which together with the Faraday cup allows one to measure the transverse beam profiles and the beam position, a silicon detector for energy spectroscopy and time of flight measurements, plus a set of collimators and attenuating or stripping foils. The performance of the beam instrumentation will impact directly on the operation of the facility, therefore a lot of care has been put to identify the performance requirements and ensure that the design fulfills the needs. The techniques used by the systems studied during this work are widely used, but had to be adapted to the special design of the superconducting HIE-ISOLDE Radioactive EXperiment (REX) linac. In particular the compactness of the accelerator, and as a consequence of the diagnostic devices, required pushing the understanding of the physics behind the techniques in order to overcome limitations in the design parameters usually considered unbreakable. For this realistic models of all devices had to be developed that allowed detailed numerical studies. This new set of diagnostics for the HIE-ISOLDE REX linac is the most compact in the facility, and has been tested extensively in a wide range of ion beams.

In addition to the HIE-ISOLDE work, a Secondary Emission Monitor (SEM) was tested at the Antiproton Decelerator (AD) facility using a 300 keV antiproton beam, together with other detector groups in the AEgIS collaboration such as nuclear emulsions,

the MIMOTERA and the 3D pixel detector. In the frame of this thesis, a performance comparison among these detector technologies is done with the aim to identify an ideal set of diagnostics for the AD and for other similar antiproton facilities.

This thesis first presents the models developed as well as the results of the numerical simulations, then the design of the prototypes and the experimental results obtained with beams in antiproton and ion accelerator facilities. All devices and techniques part of this R&D are characterized in detail, their performance and limitations described and options for further improvements indicated.

Contents

Abstract **i**

Table of contents **v**

Acronyms **v**

1 Introduction **1**

1.1 Heavy Ion Facilities 1

1.1.1 ISOLDE 1

1.1.2 REX-ISOLDE 3

1.1.3 HIE-ISOLDE 5

1.1.4 TRIUMF 7

1.2 Antiproton Facilities 10

1.2.1 Antiproton Decelerator 10

1.2.2 The AE$\bar{g}$IS Experiment 13

2 REX-ISOLDE Beam Diagnostics **16**

2.1 Introduction 16

2.2 Collimators 17

2.3 Beam Intensity 18

2.4 Secondary Emission Beam Profile Measurement 20

2.5 Transverse Emittance 21

2.6 Silicon Detectors 23

2.7 Silicon PIN Photodiode 26

2.8 Chapter Summary 28

3 HIE-REX Beam Diagnostics **29**

3.1 Instrumentation Requirements 29

3.2 The Diagnostics Box and the Intercryomodule Challenge 30

3.2.1 Effect of Slit Width on Beam Profiles 33

3.2.2 Slit Scanner Actuator Tests 35

3.2.3 Conclusions 42

3.3 PIPS Detector . . . 43
3.4 Collimators & Stripping Foils . . . 44
3.5 Emittance Meter . . . 45
3.6 Chapter Summary . . . 45

4 Faraday Cup **47**
4.1 Motivation . . . 47
4.2 Design Aspects . . . 51
4.3 Prototype 1 . . . 52
4.3.1 Experimental Setup and Results . . . 53
4.4 Prototype 2 . . . 56
4.4.1 Experimental Setup and Results . . . 57
4.4.2 Beam Profile Measurements with Prototype 2 . . . 58
4.5 Prototype 3 . . . 62
4.5.1 Experimental Setup and Results . . . 62
4.6 Particle Tracking Simulations . . . 66
4.6.1 Prototype 1 . . . 67
4.6.2 Prototype 2 . . . 69
4.6.3 Prototype 3 . . . 69
4.7 Chapter Summary . . . 74

5 PIPS Detector **75**
5.1 Motivation . . . 75
5.2 Principle of Operation . . . 77
5.3 Technical Considerations . . . 78
5.4 Data Acquisition Electronics . . . 80
5.5 Range of Projectiles in the Detector . . . 82
5.6 Radiation Damage . . . 83
5.7 Experiments with Ions . . . 84
5.7.1 Experimental Setup and Results . . . 84
5.8 Cavity Phase-up . . . 95
5.9 Chapter Summary . . . 98

6 Beam Instrumentation for Low-energy Antiprotons **100**
6.1 Secondary Emission Monitor . . . 101
6.1.1 Working Principle . . . 101
6.1.2 Experimental Setup . . . 103
6.1.3 Results . . . 106
6.2 Nuclear Emulsions . . . 113
6.3 Silicon Detectors . . . 116

6.3.1 MIMOTERA 117
6.3.2 3D Pixel Sensor (CNM 55) 120
6.4 Optimizing Instrumentation for Low-energy Antiproton Beams 123
6.5 Chapter Summary 125

7 Conclusions **127**

Appendices **132**

A Energy loss of ions at the entrance window of the Si detectors **133**

B Table of ion beams delivered at REX-ISOLDE **135**

Bibliography **152**

List of Figures **158**

List of Tables **159**

Chapter 1

Introduction

In this chapter an overview of the facilities where the research activities of this work took place is presented, showing their evolution through history and their future prospects.

1.1 Heavy Ion Facilities

1.1.1 ISOLDE

The Isotope On-Line DEvice (ISOLDE) facility at the European Organization for Nuclear Research (CERN) produces a wide range of exotic nuclides ranging from light isotopes like ^{6}He up to heavy ions such as ^{229}Rn [1]. These isotopes are used for different experiments in the fields of nuclear, atomic and solid-state physics, materials sciences and life sciences, such as ISOLTRAP [2] or MISTRAL [3]. The ISOLDE facility is connected to the 1.4 GeV Proton-Synchrotron Booster (PSB) at CERN, and is operated by the ISOLDE Collaboration, whose members are Belgium, CERN, Denmark, Finland, France, Germany, Greece, India, Ireland, Italy, Norway, Romania, Spain, Sweden and the UK.

Originally, ISOLDE was developed around the 600 MeV Proton Synchro-Cyclotron back in 1964. 1967 marked the start of the first experiments in the facility. ISOLDE experienced several upgrades until it was finally moved to the PSB in 1992. As in other existing Radioactive Ion Beam (RIB) facilities, ISOLDE offers a wide variety of radioactive isotopes, but the installation of the post-accelerator Radioactive EXperiment at ISOLDE (REX-ISOLDE) in 2002 has opened new fields of research with RIBs of higher energies [4]. In this sense, ISOLDE is complementary to other European RIB accelerators such as the Système de Production d'Ions Radioactifs Accélérés en Ligne - System for Producing Online Accelerated Radioactive Ions (SPIRAL) at the Grand Accélérateur National d'Ions Lourds - Large Heavy Ion National Accelerator (GANIL) in France, and the GSI Helmholtz Centre for Heavy Ion Research (GSI) in Darmstadt, Germany. It provides a wider range of intense ion beams compared to the Holifield

Radioactive Ion Beam Facility (HRIBF) at Oak Ridge, USA and the Isotope Separator and ACcelerator (ISAC) in TRIUMF, Canada [4].

At ISOLDE radioactive isotopes are produced via nuclear reactions such as spallation, fission or fragmentation in one of the two target stations available. Targets are prepared on site with suitable porous materials. Because of the issues with handling Uranium (highly flammable, even at room temperature), other target materials including UC_X, Ti, etc are used instead. The target is bombarded with the high intensity, 1.4 GeV proton beam from the PS-Booster at CERN, with average proton currents of up to 2 μA [5]. Multistage laser ionization of selected chemical elements allows for precise selection and in some cases can provide a beam prepared in a particular isomeric state [6]. This production device is coupled to two powerful mass separators; the General Purpose Separator (GPS) and the High Resolution Separator (HRS), from which high intensity radioactive ion beams are extracted with high isotopic and often isobaric purity [4].

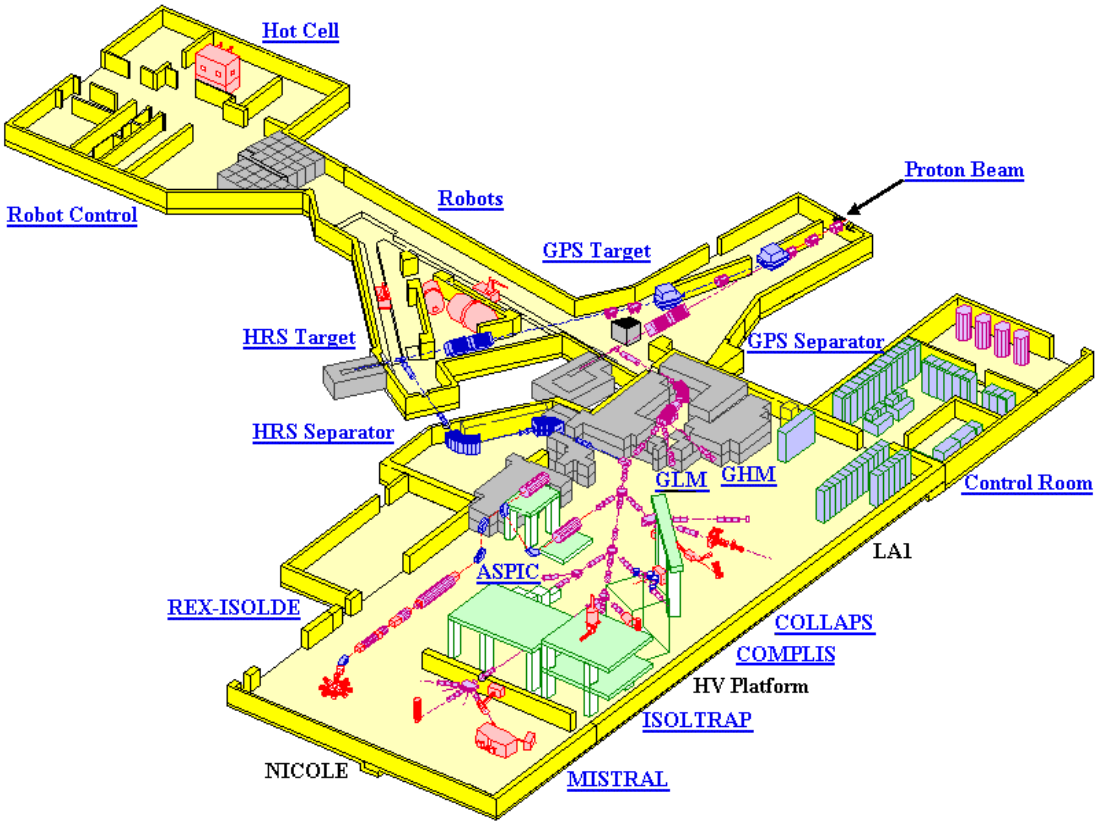

Figure 1.1: Layout of the ISOLDE facility. Image taken from [4].

A layout of the ISOLDE facility is presented in Fig. 1.1. ISOLDE has two online isotope separators with independent target-ion extraction systems that deliver 60

keV mass-selected RIBs. The GPS comprises one bending magnet and an electrostatic switch-yard allowing the simultaneous extraction of three mass-separated RIBs, although simultaneous extraction has not yet been implemented. The HRS comprises two bending magnets with an advanced beam-optical system for higher order corrections resulting in a mass resolving power ($\frac{m}{\Delta m}$) of 5000 [7]. In addition, an off-line mass separator, i.e. not connected to the PSB beam line, is available for tests and calibrations. Both on-line separators are connected to a common beam-line system which feeds the experimental stations for nuclear spectroscopy and nuclear orientation, laser spectroscopy, mass measurements, solid state and surface studies.

The large variety of species available at ISOLDE makes possible a wide range of experiments regarding atomic and nuclear properties of nuclei far from beta-stability. Research also takes place in related fields like astrophysics and weak-interaction physics. Solid-state physics and biomedical studies are an important part of the scientific programme as well. More than 600 isotopes with half-lives down to milliseconds of almost 70 elements ($2 \leq Z \leq 88$) have been produced at intensities ranging from 10^{-1} to 10^{11} atoms per second [8, 9].

At ISOLDE, selected beams coming from any of the two separators mentioned above can be steered to the low-energy experimental area, or to high-energy experiments through REX-ISOLDE, a post-accelerator of up to 3 MeV/u.

1.1.2 REX-ISOLDE

At present, research on nuclear structure far from stability is at the forefront in the field of nuclear physics since such nuclei allow for the amplification and isolation of particular aspects of nuclear interactions [10]. The installation of the REX-ISOLDE post-accelerator has widened the fields of research with radioactive ion beams of higher energies, specifically light-medium mass nuclei for reaction studies with energies up to 3 MeV/u. Ions up to mass A=140 can be accelerated in REX with a total efficiency between 1-10% [11]. The operation of the REX post-accelerator started in 2002, and today REX provides RIBs of up to 34 elements and 108 isotopes, see Appendix B, with beam energies ranging from 0.3 to 3 MeV/u for ions with a mass-to-charge ratio of $A/q \leq 4.5$ [12, 13].

REX is used to accelerate the low-energy ISOLDE ion beams. The radioactive singly-charged ions from the separators are first accumulated, bunched and cooled in a Penning trap, REXTRAP. This trap stores the ions for up to 20 ms and then 10 μs bunches are transferred to an Electron Beam Ion Source (EBIS), where the ions are

charge bred to a mass-to-charge ratio below 4.5. Finally, the ions are injected into the LINear particle ACcelerator (LINAC) via an achromatic separator, which separates the ions according to their mass-to-charge ratio, or A/q. More information about the EBIS can be found in [14].

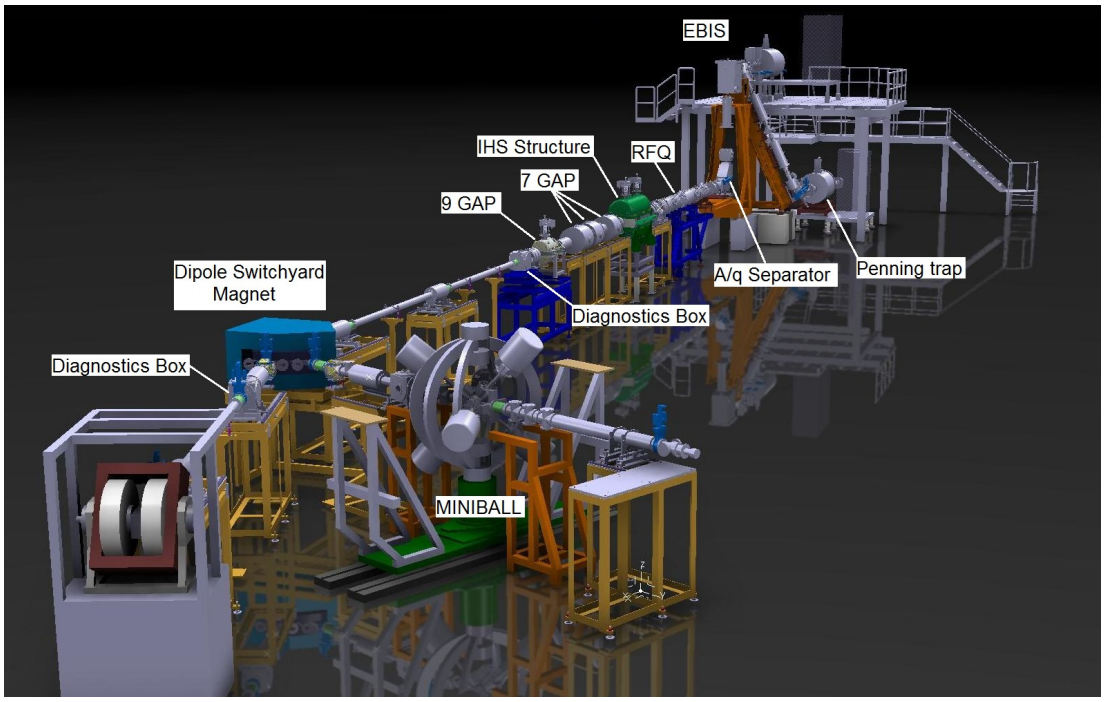

Figure 1.2: Layout of the REX-ISOLDE LINAC. Image taken from [4].

The REX LINAC, shown in Fig. 1.2, consists of a Radio Frequency Quadrupole (RFQ), which accelerates ions from 5 to 300 keV/u, a rebuncher [15], an Interdigital H-type Structure (IHS) that boosts the energy to 1.2 MeV/u, three 7-gap resonators (2.21 MeV/u) and a 9-gap resonator[1] that allows the beam energy to reach up to 3 MeV/u [11, 12]. The Interdigital H-type structure is an efficient drift-tube structure with special beam dynamics. After an initial accelerating section with a 0°-synchronous particle structure the ions drift through a magnetic quadrupole triplet lens for transverse focusing. Then the particles are rebunched using a negative synchronous phase ($\phi_s \approx 30°$) in the first three gaps behind the quadrupole triplet, followed by a second accelerating section with $\phi_s \approx 0°$ [16].

The original REX-ISOLDE post-accelerator, which was developed by the ISOLDE collaboration, had two main objectives. The first was to demonstrate a new concept for bunching, charge-breeding and post-accelerating single-charged, low-energy ions in

[1]The 9-gap resonator operates at twice the Radio Frequency (RF) of the other cavities, that is 202.56 MHz

an efficient way. Second, to study the structure of neutron-rich Na, Mg, K and Ca isotopes in the vicinity of the closed neutron shells N = 20 and N = 28 by Coulomb excitation and neutron transfer reactions with a highly efficient γ and particle-detector array MINIBALL [17]. The design is supported by well established techniques, but represents a new way of combining these structures [16]. Since 2003, the machine is fully operational and is now fully integrated in the ISOLDE facility, providing a wider range of RIBs than initially considered in the original design. REX is regularly used for accelerating isotopes with masses up to A>200 for experiments in nuclear physics, astrophysics and solid-state physics. Reviews of the machine performance can be found in [11].

1.1.3 HIE-ISOLDE

The High Intensity and Energy ISOLDE (HIE-ISOLDE) upgrade is based upon three major fronts: higher energies, improvements in beam quality and flexibility, and higher beam intensities [18]. This requires developments in target-ion sources, radioisotope selection and improvements in charge-breeding, as well as the increase of the proton beam current by replacing the injector for the PS Booster, LINAC4 [19].

In order to fully benefit from the increase in beam energy by a factor 3 and the increase in intensity of the proton beam by a factor 2, a design study of an improved and redesigned target module and front-end has been created. This enhancement, combined with upgrades in the Resonant Ionization Laser Ion Source (RILIS) [6], cooler and buncher (ISCOOL) [20] and the RFQ will lead to increased RIB intensities of up to an order of magnitude [21].

The most significant element of the energy upgrade will come from replacing most of the existing REX post-accelerator by a superconducting LINAC whose parameters are summarized in Table 1.1.

This 16-metre long superconducting LINAC, presented in Fig. 1.3, comprises two cryomodules with 6 low-β cavities (geometric β_0=6.3%) and four cryomodules with 5 high-β cavities (geometric β_0=10.3%), for a total of 32 superconducting Nb-sputtered quarter-wave resonators. The low-β cavities are 0.9 m tall and 0.195 m diameter, whereas the high-β cavities are 0.9 m tall and 0.3 m diameter. These cavities provide a 6 MV/m accelerating gradient which will allow all ISOLDE beams to be accelerated over a wide range of energies from well below the Coulomb barrier to significantly above it, facilitating a broad programme of nuclear structure and nuclear astrophysics studies using different types of nuclear reactions [12, 21].

Table 1.1: Parameters of the HIE-ISOLDE LINAC.

Parameter	Value
Mass to Charge Ratio A/q	2.5 to 4.5
Input Kinetic Energy	1.2 MeV/u
Output Kinetic Energy (A/q=4.5)	0.3-10 MeV/u
RF Frequency	101.28 MHz
RF Period	9.87 ns
Beam Pulse Length	50-500 μs
Energy Spread FWHM at Injection	0.9 %
Bunch Length at Injection	0.2 ns
Beam Transmission	95 %
Pilot Beam Intensity	1 pA - 1 nA
Radioactive Beam Intensity	pps - pA

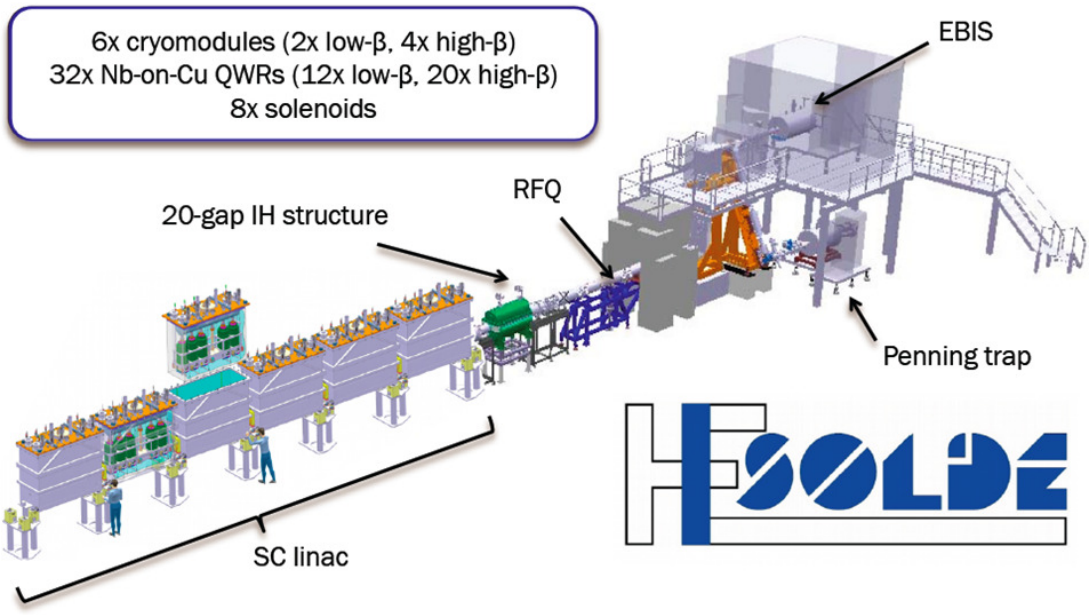

Figure 1.3: Layout of the HIE-ISOLDE Linac. Image taken from [4].

In the first stage of the HIE-ISOLDE upgrade, REX will be extended with the addition of two low-β cryomodules during 2015 and will provide a maximum energy of 5.5 MeV/u, reaching the Coulomb barrier threshold for a wide range of nuclei. At the end of the HIE upgrade, REX will be equipped with 6 cryomodules providing beam energies up to 10 MeV/u.

HIE-REX will deliver ion beams to 2 high-energy experimental stations using two 90° beamlines. The MINIBALL gamma array will be installed in the first station, while temporary experiments will be installed in the second beamline. There is space foreseen for possible extensions such as a third beam line or an ion storage ring.

1.1.4 TRIUMF

The TRI-University Meson Facility (TRIUMF) was founded in 1968 by a consortium of Canadian universities (Simon Fraser University, the University of British Columbia (UBC), and the University of Victoria) in order to satisfy research needs very difficult to provide by a single university [22]. The University of Alberta joined the TRIUMF consortium shortly after. There are currently over 15 different member and associate member universities from across Canada in the consortium that governs TRIUMF, and has allowed it to evolve into a national laboratory while still maintaining strong ties to the research programs of the Canadian universities. The science program has expanded from nuclear physics to include particle physics, molecular and materials science, and nuclear medicine. At present, TRIUMF provides infrastructure and tools for research that are too large and complex for a single university to build, operate, or maintain [23].

The facility's proton driver machine is the H^- Cyclotron. In operation since 1974, this six-sector variable energy cyclotron is able to deliver simultaneously up to 4 proton beams with energies between 70-520 MeV, and currents up to 300 μA [24], a factor 3 above the original goal of 100 μA at 500 MeV [25, 26]. The cyclotron is 18 m in diameter, and today maintains a 90% availability for about 6000 hours annually.

Beam line 1A (BL1A) can deliver 180 to 500 MeV protons to two target stations. The beam power ranges from 50 to 75 kW. The first target, T1, services three experimental channels, one of which is used for detector tests for the Tokai to Kamioka (T2K) experiment [27]. The second target, T2, services two muon experimental channels [28]. Downstream of T2 is a 500 MeV facility used to produce strontium isotopes for medical-imaging generators as well as the Thermal Neutron Facility (TNF)[29]. Beam line 1B (BL1B) separates off Beam line 1 (BL1) (see Fig. 1.4) at the edge of the cyclotron vault

and provides international users with the Proton Irradiation Facility (PIF) [30] that is used for radiation testing of electronic circuits. Beam Line 2A (BL2A) is capable of providing 475 to 500 MeV proton beams at up to 50 kW to the ISAC target facility that produces rare-isotope ion beams for Canadian and international experiments. Beam Line 2C (BL2C) is used for the Proton Therapy (PT) programme to treat eye melanomas [31]. This beam line also has the flexibility to provide protons of lower energy for PIF users. The energy range in BL2C is 70 to 120 MeV. Beam line 4 (BL4) in its present configuration can deliver protons of energy from 180 to 500 MeV, albeit at only 5 kW and was last used as a production facility in 2000 for the parity violation experiment [32].

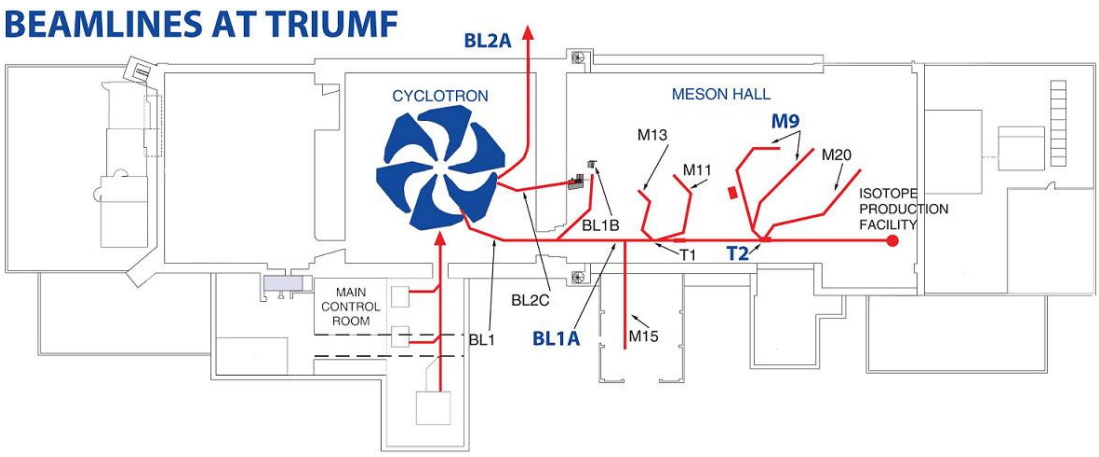

Figure 1.4: Layout of the beam lines coming out of the cyclotron at TRIUMF. Image taken from [22].

ISAC

The ISAC facility at TRIUMF receives up to 100 μA of beam current from the proton cyclotron to produce radioactive ion beams using the Isotope Separation On-Line (ISOL) method. The ISAC-I facility comprises two target stations, a mass separator [33], an Off-Line Ion Source (OLIS) [34, 35] and the beam delivery lines to the low energy experimental area and to a normal conducting LINAC composed of a 4-rod RFQ and an IHS Drift Tube LINAC operating in Continuous Waveform (CW) mode. ISAC-I can provide ion beams of $A \leq 30$ with an energy range from 0.153 to 1.53 MeV/u [26]. The ISAC-I LINAC delivers ion beams to the Detector of Recoils And Gamma-rays Of Nuclear reactions (DRAGON) [36] and the TRIUMF UK Detector Array(TUDA) [37] experiments.

The ISAC-II facility comprises a 40 MV superconducting LINAC inside a concrete accelerator vault, an RF room, a cryogenic plant and the high-energy experimental

hall which hosts the ElectroMagnetic Mass Analyser (EMMA) [38], TRIUMF-ISAC Gamma-Ray Escape Suppressed Spectrometer (TIGRESS) [39] and the HEavy-ion Reaction Array for the Characterization of Light Excited Systems (HERACLES) [40] experiments. The ISAC-II superconducting LINAC, in operation since 2006, extends the capability of the room temperature LINAC in ISAC-I and is composed of 40 bulk-niobium quarter-wave resonators in a total of eight cryomodules. The ISAC-II LINAC was installed in two phases. The Phase-I Linac, completed in 2009, consists of 8 low-β cavities (β=5.7%) and 12 medium-β cavities (β=7.1%) housed in five cryomodules (SCB1-5), with four cavities resonating at 106.1 MHz in each cryomodule. Phase-II, completed in 2011, adds twenty more cavities with a high-β of 11%, resonating at 141.44 MHz and housed in three cryomodules. There are six cavities in SCC1 and SCC2 and eight cavities in SCC3 [41]. All LINACs in ISAC operate in CW mode to make full usage of the beam intensity available. A layout of the LINAC facility is shown in Fig. 1.5.

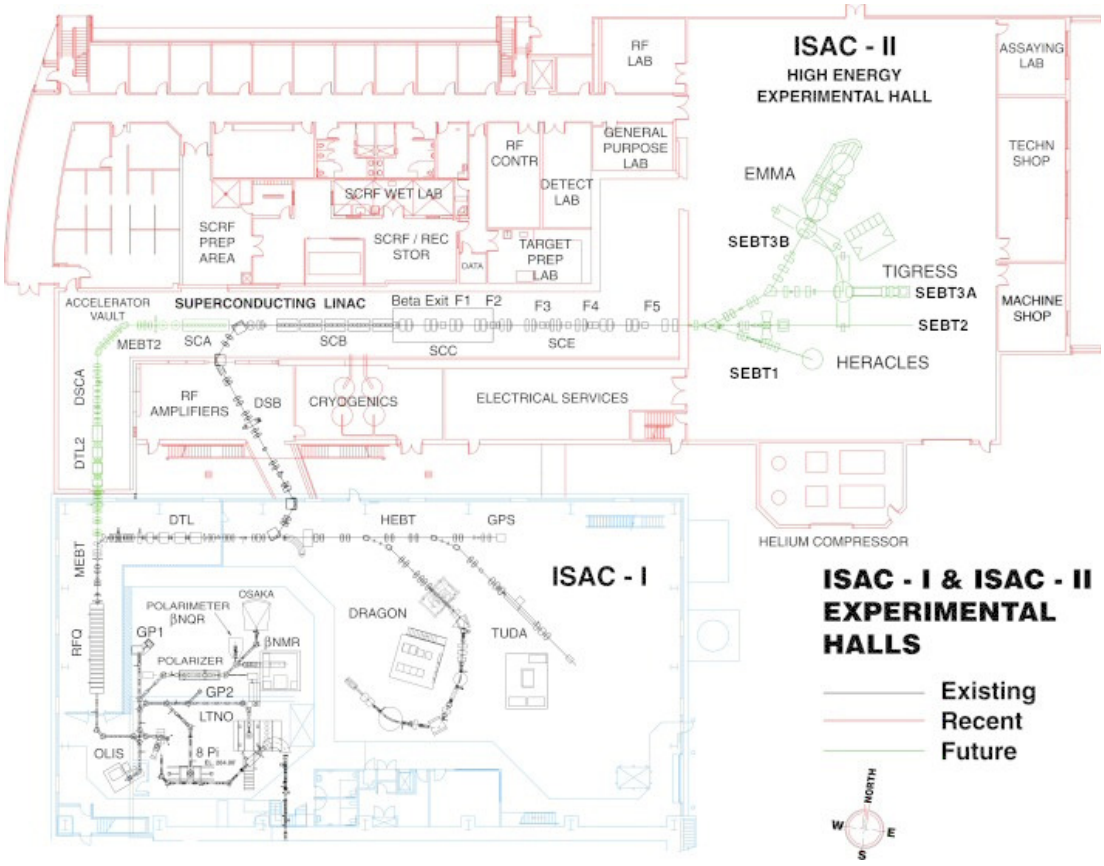

Figure 1.5: Layout of the ISAC I and II halls. Image taken from [42].

1.2 Antiproton Facilities

1.2.1 Antiproton Decelerator

In 1997, a project to convert the Antiproton Collector (AC) into an Antiproton Decelerator (AD) was approved. The AD at CERN is a facility dedicated to experiments with low energy antiprotons. In operation since 2000 [43, 44], the AD target is bombarded with the high-energy proton beam (26 GeV/c) from the PS as a source to produce antiprotons from a water-cooled iridium target. In a typical deceleration cycle, as shown in Fig. 1.6, antiprotons are injected at 3.5 GeV/c into the AD, filling its large acceptance (200 π μm in both planes and 3% in Δp/p). After injection bunches are very short and have a large momentum spread. By means of bunch rotation cavities, the momentum spread is reduced and the bunches become longer. This 90° rotation in longitudinal phase space is done in order to fit the beam momentum spread to the longitudinal acceptance of the stochastic cooling system. Stochastic and electron cooling follows in two steps each in order to compensate the adiabatic beam blow-up due to deceleration. The $\bar{p}$ beam is cooled for 20 s within 1 π mm mrad, decelerated down to 2 GeV/c, cooled again for 15 s, and decelerated down to 0.3 MeV/c. In the last stage of the cycle the beam is electron cooled for 6 s, decelerated down to 0.1 GeV/c and cooled again for 1 s. Then the beam is bunched and extracted with an emittance suitable for AD experiments (typical requirements are $\varepsilon < 1\pi$ mm mrad and bunch length <170 ns) [45]. The whole cycle takes around 100 seconds.

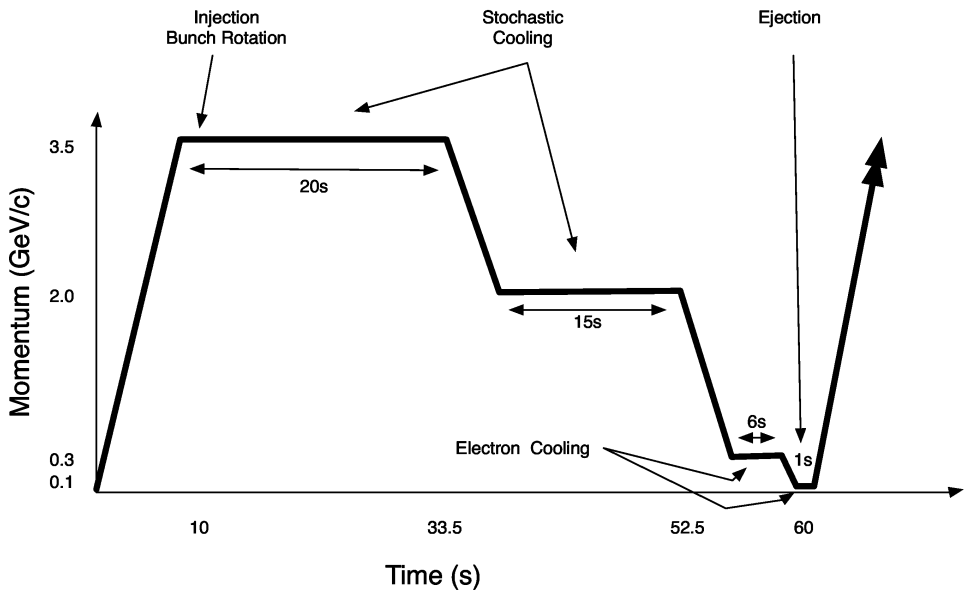

Figure 1.6: AD deceleration cycle. Image taken from [46].

One of the main experiments in the AD is the production of antihydrogen with

the aim to produce antimatter atoms with an energy low enough such that they can be trapped in a magnetic field. The ALPHA [47] and Antihydrogen TRAP (ATRAP) [48] experiments use a set of thin metal degraders to slow the AD beam to a few keV whereas Atomic Spectroscopy And Collisions Using Slow Antiprotons (ASACUSA) [49] achieves ultra-slow antiprotons (10 eV - 10 keV) with a combination of RFQ deceleration plus an electromagnetic trap. Still, collecting large numbers and high densities of antiprotons with the present AD remains a challenging issue.

Both the effectiveness and the availability for additional experiments at this unique facility would drastically increase, if the antiproton beam of 5 MeV kinetic energy would be reduced by an additional decelerator to something in the realm of 100 keV [50]. The Extra Low ENergy Antiproton (ELENA) ring, first discussed in 1982 for the Low-Energy Antiproton Ring (LEAR), is now being constructed inside the AD ring. This allows the use of the existing experimental areas and makes the beam lines from the AD to ELENA and from ELENA to the experiments reasonably short. The main beam parameters at ELENA are presented in Table 1.2.

Table 1.2: Main beam parameters at the ELENA ring.

Momentum range (MeV/c)	100 - 13.7
Energy range (MeV)	5.3 - 0.1
Circumference (m)	30.4
Intensity of injected beam ($\bar{p}$pp)	3×10^{7}
Intensity of ejected beam ($\bar{p}$pp)	1.8×10^{7}
Number of extracted bunches	3 or 4
Emittances (H/V) at 100 keV (π·mm·mrad) [95%]	6/4
Δp/p before extraction (bunched beam cooling), [95%]	$2\cdot10^{-3}$
Bunch length at 100 keV, (m/ns)	1.3/300
Vacuum level (Torr)	3×10^{-12}

ELENA will slow antiprotons down to under 1/50 of the current AD energy, improving the antiproton trapping efficiency by a factor of 10-100. ELENA will allow to serve up to four experiments in parallel. At the AD, antiprotons have to be slowed down by passing them through a series of foils, a process that results in the loss of some 99.9% of the antiprotons extracted from the AD before they reach the experiments. Commissioning of ELENA is scheduled for 2015 with the installation and setting-up of the electrostatic beam lines a year later [51]. The layout of the AD, the future ELENA ring and the experimental areas can be seen in Fig. 1.7.

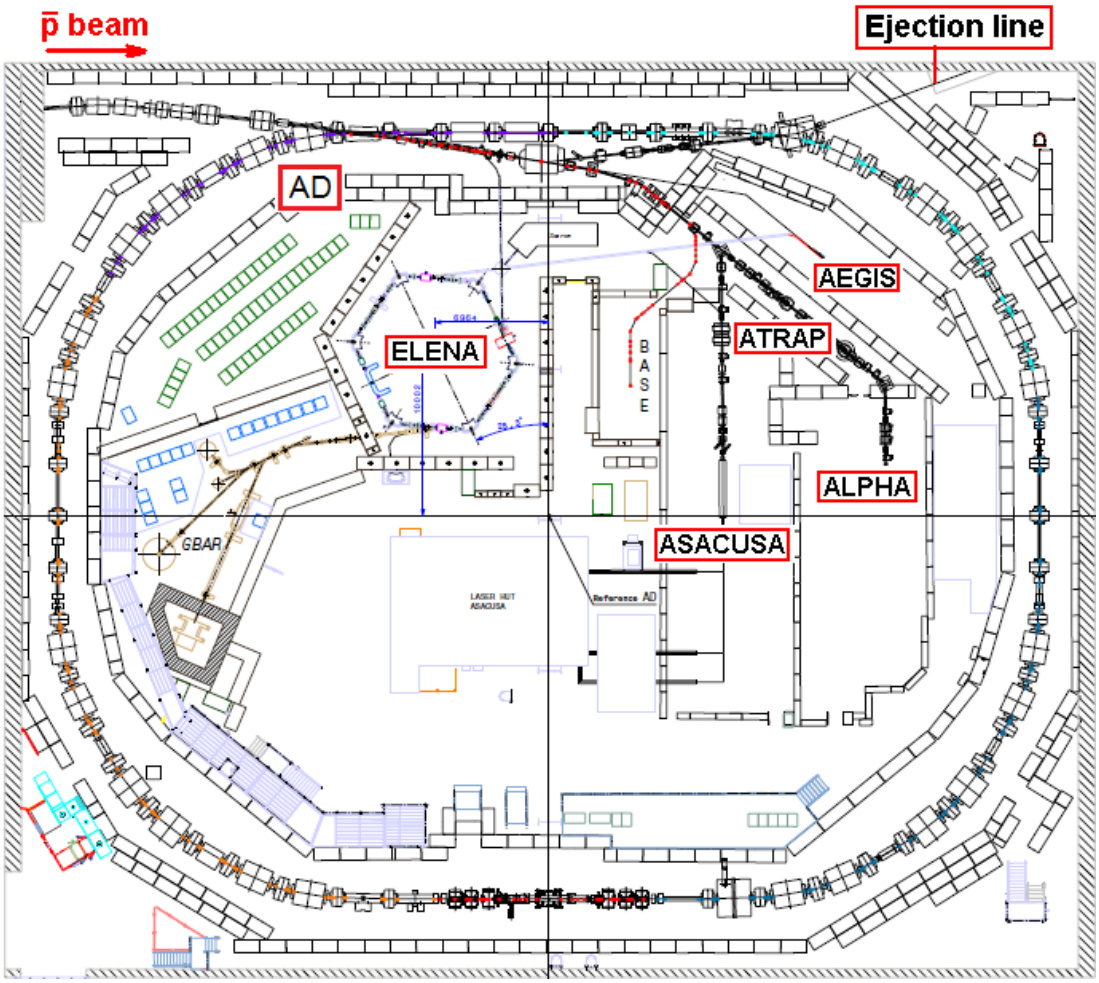

Figure 1.7: Layout of AD, ELENA and experimental areas. Image taken from [52].

1.2.2 The AE$\bar{g}$IS Experiment

The main goal of the Antimatter Experiment: Gravity, Interferometry, Spectroscopy (AE$\bar{g}$IS) experiment is a first direct measurement of the Earth's gravitational acceleration on the simplest form of electrically neutral antimatter, i.e., antihydrogen [53, 54]. It is estimated that the detection of 10^3 antihydrogen atoms is required to determine the gravitational acceleration with a precision of 1% [55]. A schematic drawing of the set-up is shown in Fig. 1.8.

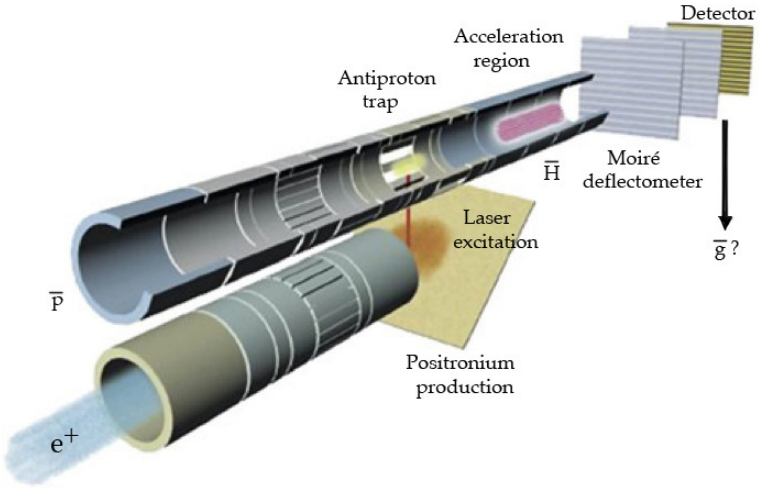

Figure 1.8: 3D Schematic of the AE$\bar{g}$IS experiment shows antihydrogen formation and post-acceleration regions towards the Moiré deflectometer and detector. Image taken from [56].

In order to create antihydrogen, about 10^7 $\bar{p}$ are delivered to the experiment by the AD every 100 seconds. A set of degrader foils placed along the $\bar{p}$ path reduce their kinetic energy from 5.3 MeV to 300 keV. Antiprotons are then captured in a Malmberg-Penning trap mounted in a horizontal cryostat inside the bore of a 5 T superconducting magnet (see Fig. 1.9) and cooled by electron cooling down to a few eV in a cryostat at about 4 K. The $\bar{p}$ cloud is radially compressed by sideband cooling [57, 58] and transferred into the antihydrogen formation trap, mounted in a colder region inside a 1 T magnet, where antiprotons are cooled down to 100 mK by a dilution refrigerator. By accumulating several AD shots an average of about 10^5 cold antiprotons ready for recombination are expected once the construction of AE$\bar{g}$IS is complete [54]. A layout of AE$\bar{g}$IS is shown in Fig. 1.9.

In parallel, approximately 10^8 positrons coming from a Na (Surko-type) source are accumulated and transferred from the accumulator to a dedicated trap mounted inside the same magnetic field as the antiproton catching trap. Here, the bunch is compressed

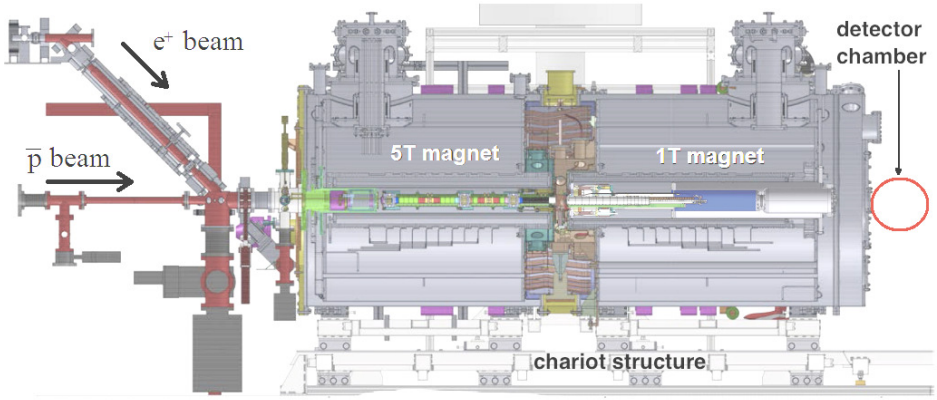

Figure 1.9: Layout of the AE$\bar{g}$IS experiment. Image taken from [59].

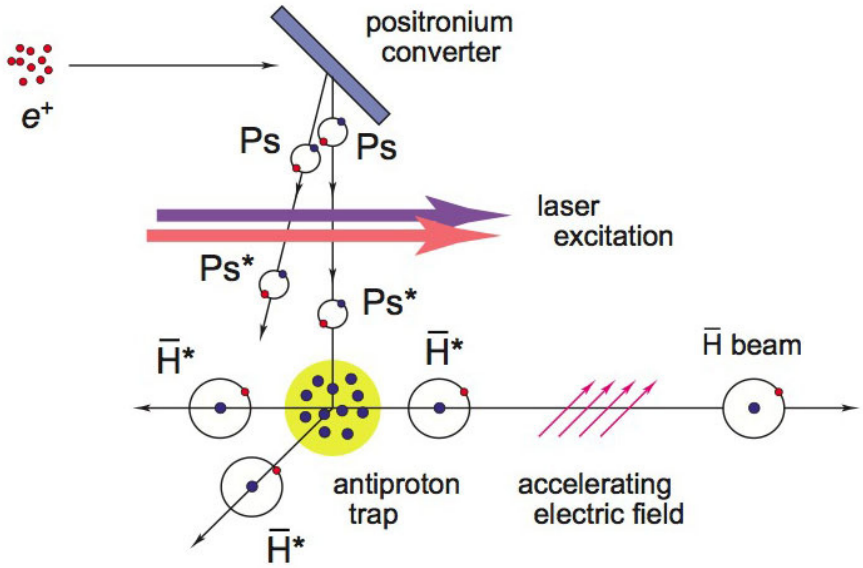

Figure 1.10: Principle of antihydrogen production at AE$\bar{g}$IS. Image taken from [56].

and accelerated towards a nanoporous target material where ground state positronium (Ps) is produced. The positronium cloud coming from the target is excited by two laser pulses into a selected Rydberg state, and in this way 10^6 excited positronium atoms can be obtained. Cold (100 mK) antihydrogen atoms will be produced in a charge-exchange reaction during the time in which the Rydberg Ps atoms traverse the antiproton cloud. The expected number of Rydberg antihydrogen atoms is in the range of 100-1000 per cycle [54]. The resulting antihydrogen atoms are finally accelerated (Fig. 1.10) by means of inhomogeneous electric fields towards a deflectometer and detector. The acceleration of neutral antihydrogen is possible due to the electric force experienced by the antihydrogen atoms which, although neutral, have an electric dipole moment which is affected when exposed to an electric-field gradient. If the excited atoms are moving in a region where the amplitude of the electric field is changing, their internal energy changes and thus, to conserve the total energy, they are accelerated or decelerated. This effect is called Stark acceleration [60, 61].

The gravitational acceleration of antihydrogen will be measured using the Moiré deflectometer, a set of two identical transmission gratings and a spatially resolving emulsion detector behind. The Moiré deflectometer allows to measure the vertical deflection of the antihydrogen beam flying horizontally with a velocity of a few 100 m/s for a path length of about 1 metre. The small deflection of a few tens of μm can be measured with this technique [62].

Chapter 2

REX-ISOLDE Beam Diagnostics

In this chapter the status of the beam diagnostics system of REX-ISOLDE up to its upgrade is detailed along with its performance limits. The main diagnostics devices commonly used in REX operation include Faraday Cups (FCs), beam profile monitors and an emittance meter.

In addition, two types of devices were tested at REX as part of a R&D effort on beam diagnostics. The first one is a Passivated Implanted Planar Silicon (PIPS) silicon detector for energy spectroscopy and time of flight measurements. The second is a PIN photodiode which was also investigated to test its ability as a beam diagnostics device for monitoring the time structure of the beam.

2.1 Introduction

In the REX-ISOLDE post-accelerator, it is necessary to monitor the beam parameters after every accelerating structure. The beam diagnostics system of the REX-ISOLDE LINAC was originally developed by the University of Leuven [63], and later modified by CERN. This system is designed to operate in the energy (0.3 - 2.85 MeV/u) and intensity (pps - nA) ranges of REX-ISOLDE. All the beam diagnostic devices of REX are located in dedicated diagnostic boxes throughout the machine. This facilitates maintenance in a LINAC with modular design, comprised of different accelerating structures in sections, while allowing the beam parameters to be measured at different locations along the machine, as presented in Fig. 2.1.

Each of the seven diagnostic boxes contains:

- Collimator wheel
- Faraday cup
- Beam profiler (Aluminium foil + Micro-Channel Plate (MCP))

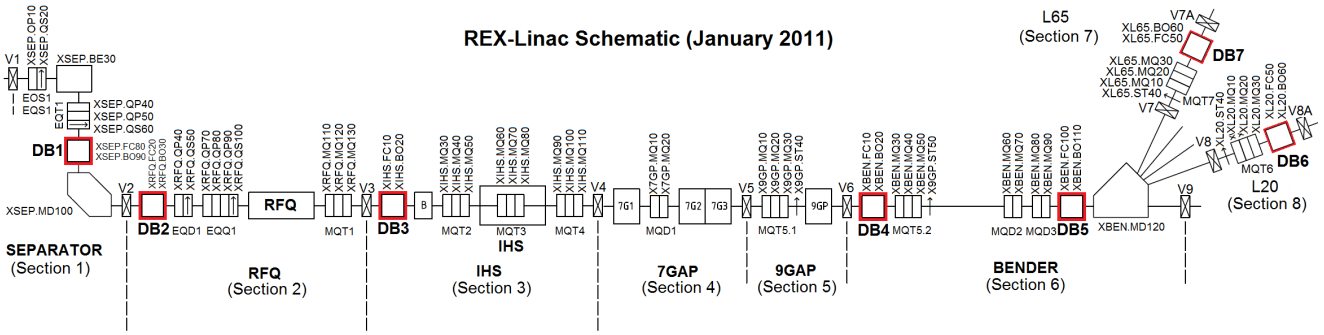

Figure 2.1: Schematic of the REX-ISOLDE post-accelerator showing the location of the different Diagnostic Boxes (DBs). Dotted lines mark the different sections in the machine indicated by sector valves.

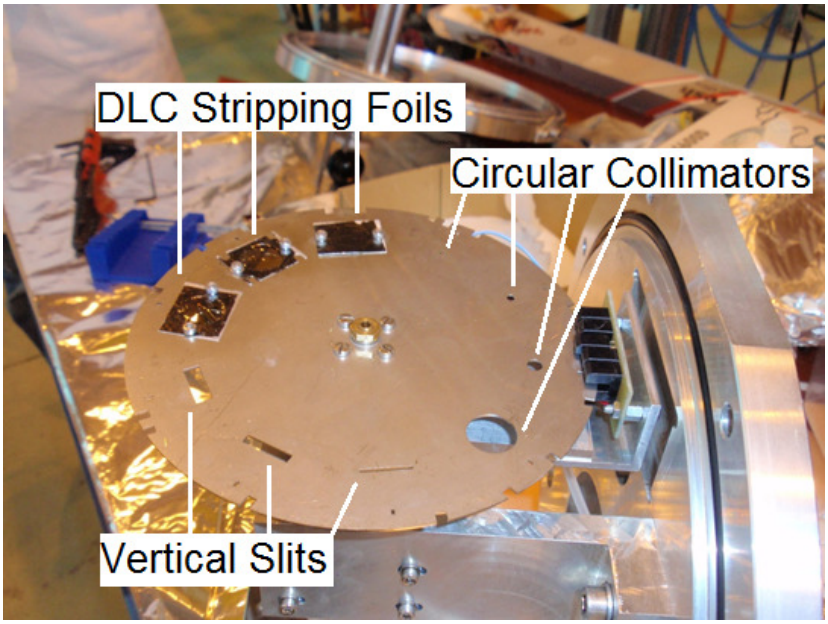

Figure 2.2: Carbon stripping foils installed in a wheel of a REX-ISOLDE diagnostic box.

2.2 Collimators

Attached to a stepper motor inside vacuum, these collimator wheels have 10 preset positions and contain circular collimators of 1, 3, 5 and 15 mm hole diameters, 1, 3 and 5 mm wide vertical slits, as well as three positions occupied by either stripping foils or copper attenuator foils, depending on the location in the machine, see Figs. 2.2 and 2.3.

Evaporated carbon stripping foils of two different thicknesses (25 and 50 μg/cm^2) from ACF-Metals [64] and a Diamond-Like Carbon (DLC) foil with a thickness of 4 μg/cm^2 from the Technical University of Munich (TUM) were installed upstream of

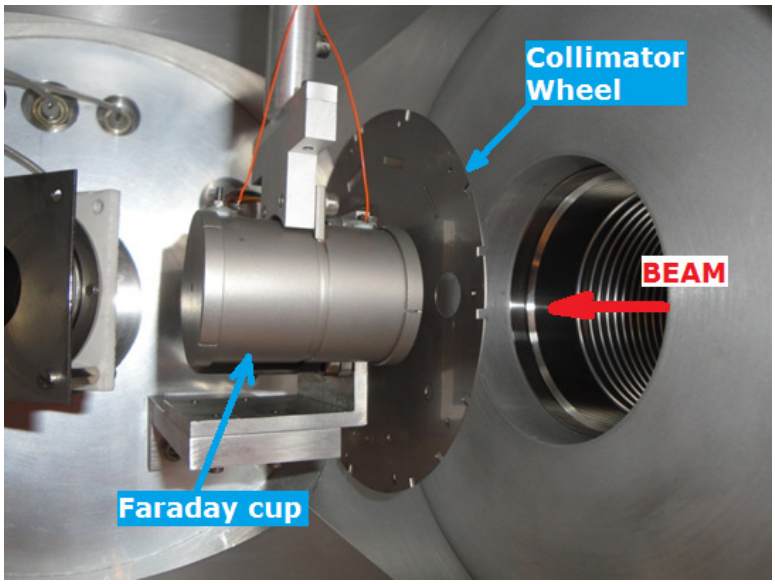

Figure 2.3: Picture of a collimator wheel and Faraday cup inside DB5.

the bending dipole magnet in DB5, see Fig. 2.1 [65].

Fig. 2.2 shows the foils mounted on the collimator wheel, which in turn is installed upstream of the Faraday cup inside the diagnostic box, as shown in Fig. 2.3. The desired foil is exposed to the beam by turning the collimator wheel to its pre-set position.

Two kinds of perforated copper foils were used in REX-ISOLDE for beam intensity attenuation. Their main characteristics are:

1. Foil thickness: 15 μm.
2. Hole diameter: 50 μm and 35 μm.
3. Hole spacing: 0.2 - 5 mm.
4. Transmission factor per foil: 0.1 and 0.01%.

These foils, presented in Figs. 2.4 and 2.5 were located upstream and downstream of the RFQ. By setting a combination of attenuator foils before and after the RFQ, the operator can attenuate the beam down to 10^{-5} of the intensity of the incident beam.

2.3 Beam Intensity

Since the intensities available in REX-ISOLDE are too low ($\leq$1 nA) for standard electromagnetic detectors like beam current transformers, the most appropriate method to

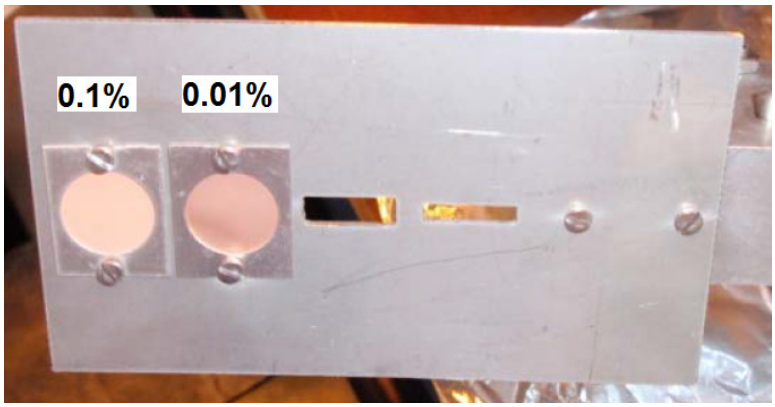

Figure 2.4: From left to right: Perforated copper foils of different transmission factors (0.1 and 0.01%) and two horizontal slits (3 and 1 mm), manually operated in DB2, upstream of the RFQ.

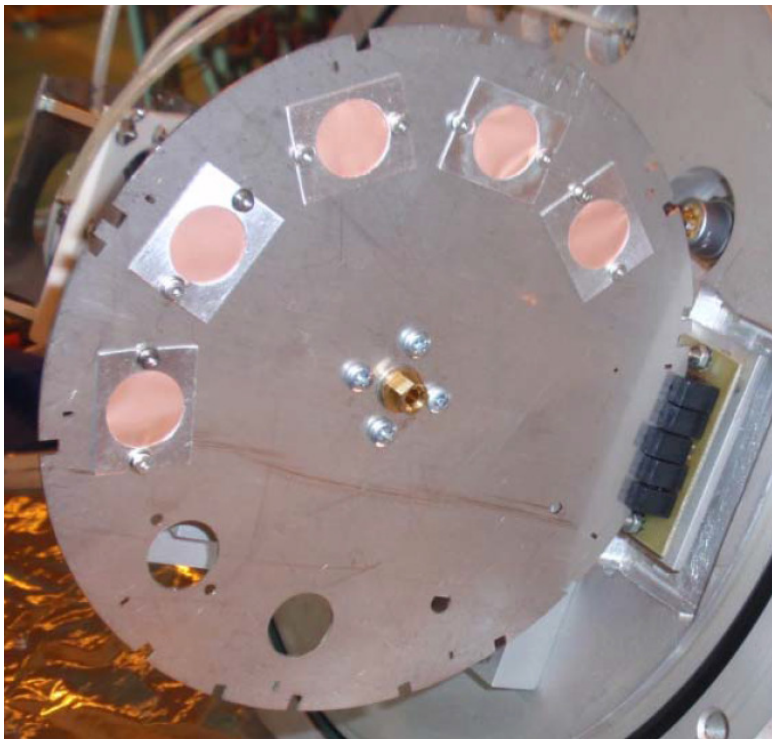

Figure 2.5: Up to 6 perforated copper foils can be installed in this wheel, along with circular collimators of 1, 3, 5 and 15 mm diameter, being remotely operated in DB3, downstream of the RFQ.

measure beam intensity is by using a Faraday cup, which is a beam diagnostics device that measures the electric charge of a particle beam. More details of the working principle of a Faraday Cup (FC) are presented in Chapter 4.

The REX-ISOLDE Faraday cup, as shown in Fig. 2.6, is 58 mm long and has an aperture of 26 mm. It is made of stainless steel and has cylindrical parts made out of VESPEL [66] as electric insulators. The 32 mm long bias ring is biased to -60 V during standard operation. Pneumatic actuators are used for moving the cup in and out of the beam path. Its position is monitored by two micro-switches on IN/OUT mode.

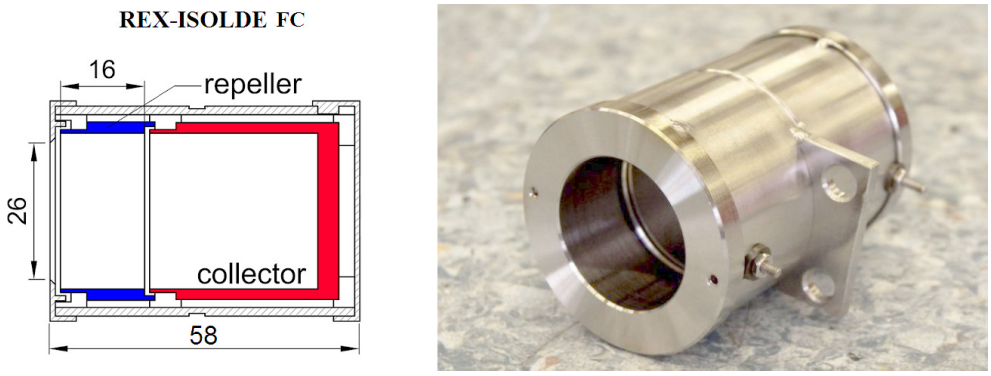

Figure 2.6: Left: Cross section of the REX-ISOLDE Faraday cup. Right: Picture of the REX-ISOLDE Faraday cup.

The readout of the beam intensity signal is generally acquired by a picoammeter and an Analog to Digital Converter (ADC) as front end electronics (bandwidth $\leq$1 Hz and integration times of 0.2-1 s), and then transmitted via PROFIBUS to a Programmable Logic Controller (PLC) which is regularly monitored from a PC in the control room. The range of the picoammeter can be set to auto or chosen manually from a range of values (200 pA, 200 μA, 500 μA, 1 mA, 2 mA, 5 mA or 10 mA). The integration time can be set to 0.2, 0.5 or 1 second.

2.4 Secondary Emission Beam Profile Measurement

This system is designed to obtain transverse profiles of the ion beam and to monitor the beam position with a spatial resolution of $\leq$1 mm.

Shown in Fig. 2.7, the profile monitor is based on Secondary Electron Emission (SEE) produced by the beam impinging on an aluminium plate at a 45° angle. The secondary electrons produced on the plate's surface are accelerated by the electric field set between the plate and the grid towards an MCP, where the electrons are multiplied

and impinge on a phosphor screen to produce photons with wavelengths λ in the range of $350< \lambda <700$ nm [67] which are then recorded by a Charge-Coupled Device (CCD) camera. The intensity of light is proportional to the number of electrons hitting the screen, which is proportional (with gain 10^5) to the number of ions hitting on a particular spot in the plate. In this way, a 2D image of the beam profile can be recorded by the CCD camera.

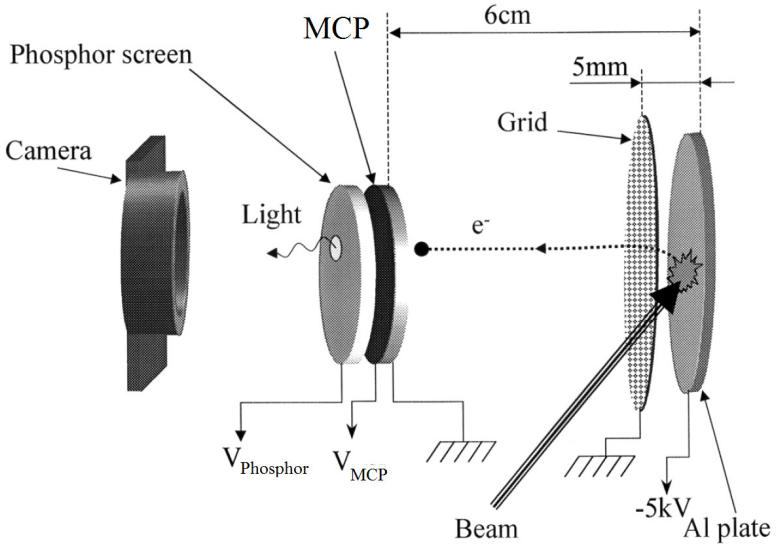

Figure 2.7: Working principle of the SEE beam profiler at REX. Image taken from [68].

The image readout is monitored from the control room, where parameters like the MCP, foil and acceleration grid bias voltages can be set. An image of the beam profiler application is shown in Fig. 2.8. Beam size can be monitored with this system with a spatial resolution better than 1 mm [63], while the typical REX beam size is 5 mm ($1\ \sigma$).

2.5 Transverse Emittance

In order to measure transverse beam emittance, the Neue Technologien Gelnhausen (NTG) Emittance meter [69] is used both at REX and other ISOLDE locations. This device uses a "slit-grid" scanning method, illustrated in Fig. 2.9, where a moving blade with two slits (horizontal and vertical) scans through the beam while a wire-grid system reads the transverse profiles of the beamlets downstream. It is deployed around the facility to measure emittance where needed. The device is shown in Fig. 2.10. It includes highly sensitive current measurement electronics, consisting of 32 low-noise integrating amplifiers with Field-Effect Transistor (FET) operational amplifiers, switchable integrating capacitors and low leakage FET [70]. On each emittance plane, only 30 amplifier channels are used, leaving the remaining two as spare. Due to the very low

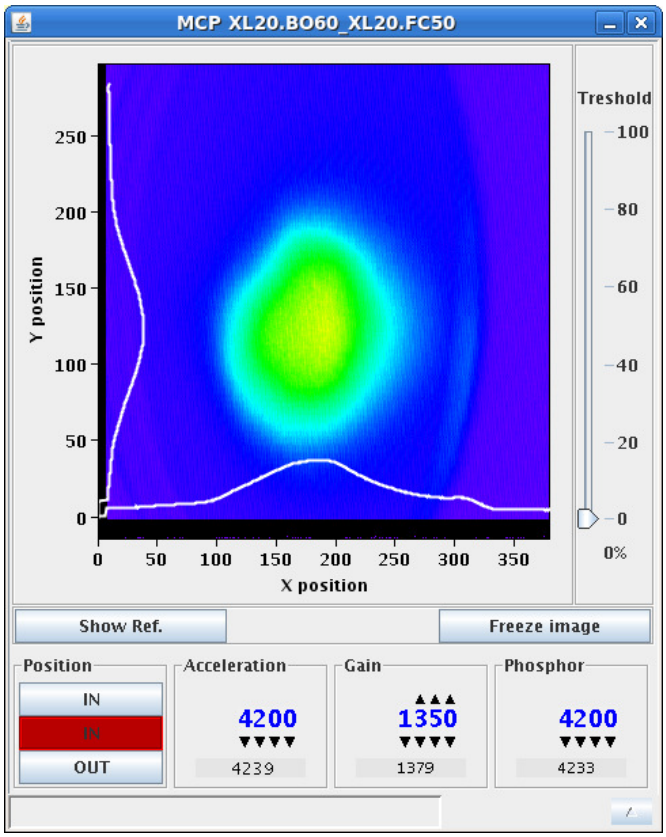

Figure 2.8: Screenshot of the application monitoring the beam profiler at REX.

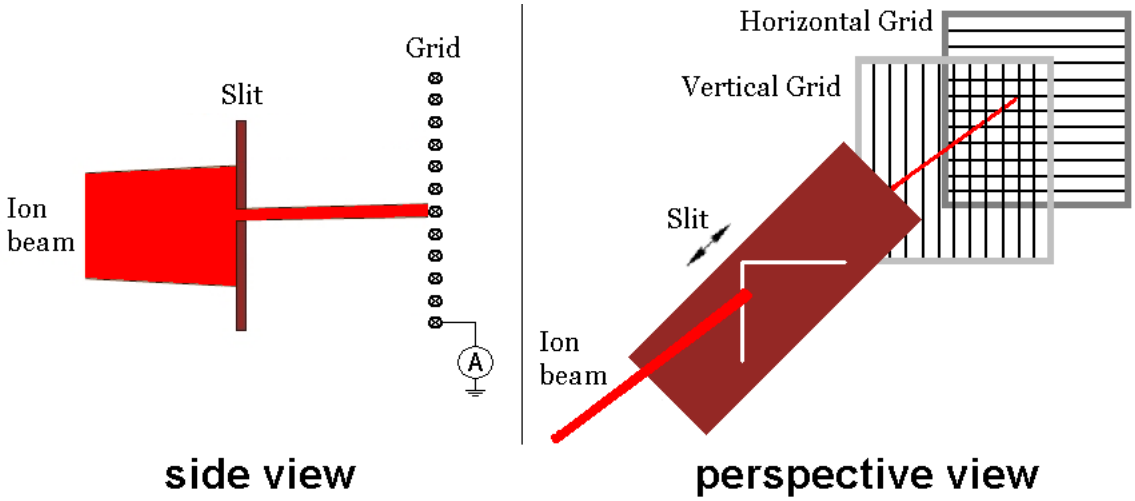

Figure 2.9: Working principle of a slit-grid emittance meter.

Figure 2.10: REX-ISOLDE NTG Emittance meter.

noise and low input leakage current, measurements in the pA range are possible. The scanning blade is made from tantalum, with two slits of 0.2 mm width. The wire-grid system consists of a square frame holding 30 tungsten wires on each plane. The wire diameter is 0.2 mm and the wire spacing is 2 mm. This spacing allows measurements of beam sizes up to 60 mm. Both the slits and the grid can be moved in steps of 25 μm by stepping motors. A measurement example of transverse beam emittance in ISOLDE is shown in Fig. 2.11. The main limitations of this device are its small data memory, the lack of open source access for data analysis and a poor user interface. It would be very useful to integrate it in the main control system, after a complete refurbishment of its hardware and software.

2.6 Silicon Detectors

Passivated implanted planar silicon detectors provided by Canberra were previously tested at REX-ISOLDE for energy spectroscopy and Time of Flight (ToF) measurements as part of an R&D effort for HIE-ISOLDE [71] with the aim to study their ability to achieve fast cavity phase tuning in the HIE-ISOLDE LINAC and to obtain beam energy measurements in order to compare with the spectrometer magnet method.

Two kind of Silicon detectors were tested in REX, the first with 300 μm thickness, 50 mm^2 active area and 29 pF capacitance [71]. The second was 500 μm, 25 mm^2 active area and 11 pF capacitance. The detectors were installed in DB5 in REX-ISOLDE (Fig. 2.12), before the switch-yard dipole magnet [4]. The detector was tested with

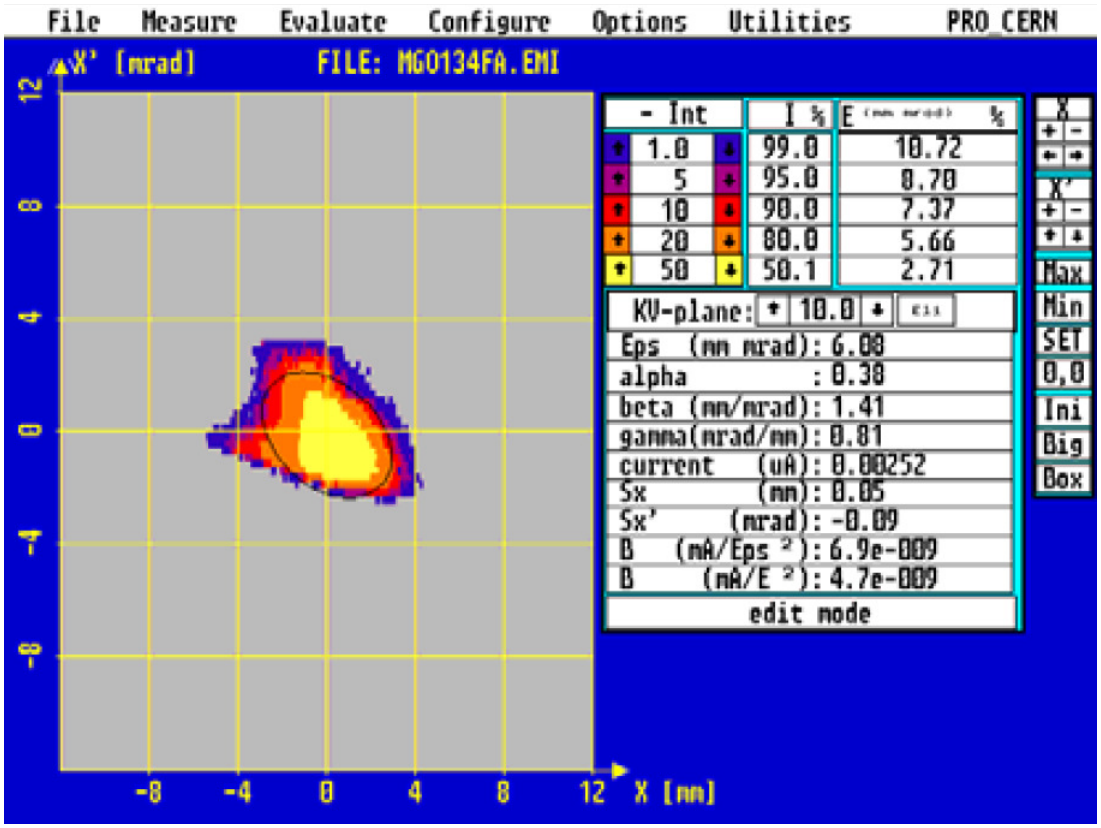

Figure 2.11: Emittance measurement with a 2.8 nA beam of Ar^{+2} at ISOLDE. The $\varepsilon^{95\%}$=2.77 π·mm·mrad, while the ε_{RMS}=1.93 π·mm·mrad. The integration time is one second. Image taken from [69].

stable ion beam at energies in the range of 0.3 - 2.82 MeV/u. The achieved energy resolution was 1.4% - 0.5% rms in the measured energy range. This is adequate for an accurate cavity phase-up. The achieved timing resolution is better than 200 ps rms, which is also adequate for a ToF phase-up procedure if a beam chopper is incorporated in the LINAC and the bunch spacing is increased accordingly [72, 71]. PIPS detectors have ion-implanted contacts to form thin junction that allow good alpha resolution, and leakage currents are typically much less than that of Silicon Surface Barrier detectors and Diffused Junction detectors. More details will be explained in chapter 5.

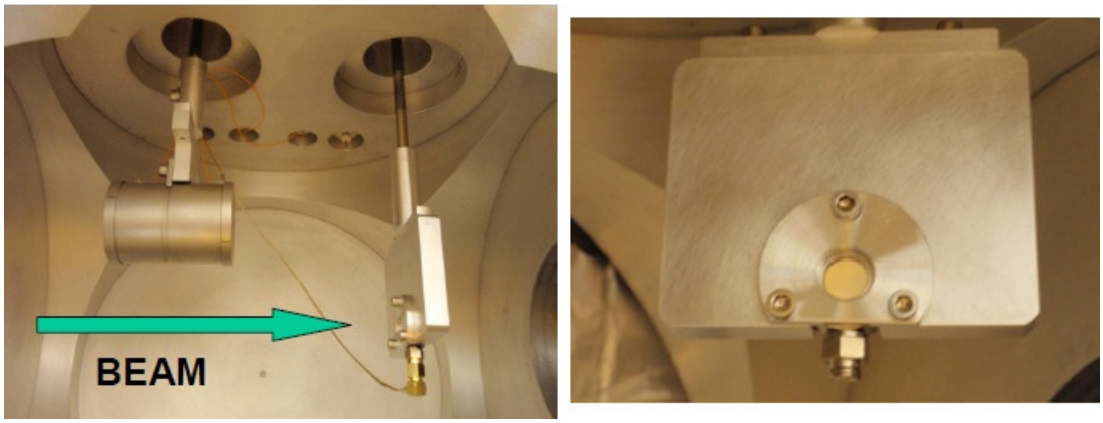

Figure 2.12: PIPS detector installed in REX DB5. Image taken from [71].

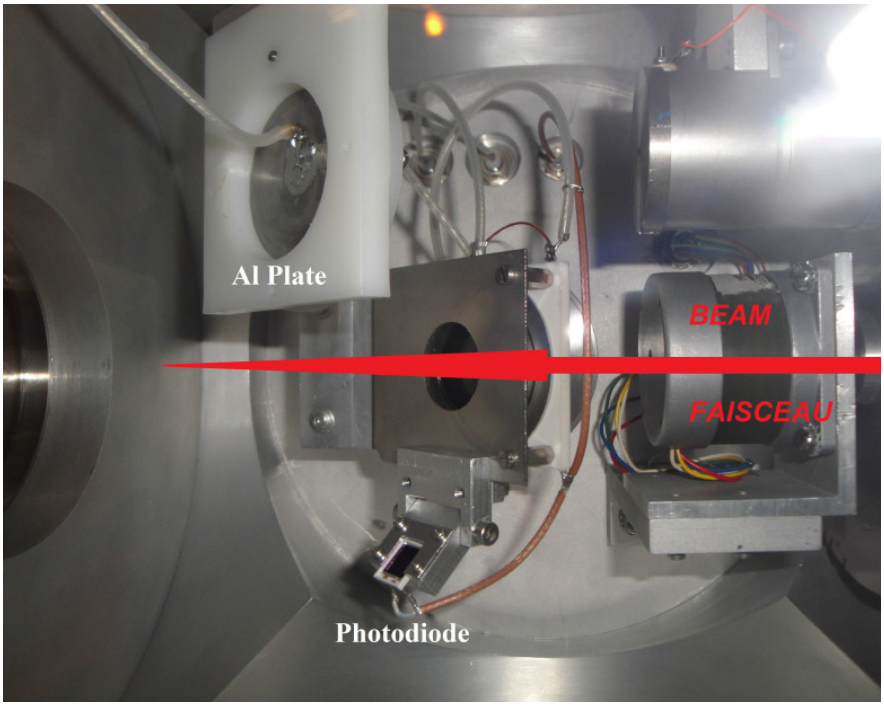

Figure 2.13: PIN photodiode installed in REX DB7.

2.7 Silicon PIN Photodiode

A silicon PIN photodiode S3590-08 from Hamamatsu [73] was tested in the REX-ISOLDE LINAC in order to test its capacity as a future beam diagnostics tool to measure beam energy and intensity at REX-ISOLDE. As shown in Fig. 2.13, it was installed in the diagnostic box DB7 of REX-ISOLDE, see Fig. 2.1. Connected to a A1422 1 channel CAEN preamplifier [74], and installed facing the aluminium plate of the beam profiler. In this way, the scintillating light coming from the beam hitting the aluminium plate is collected by the photodiode.

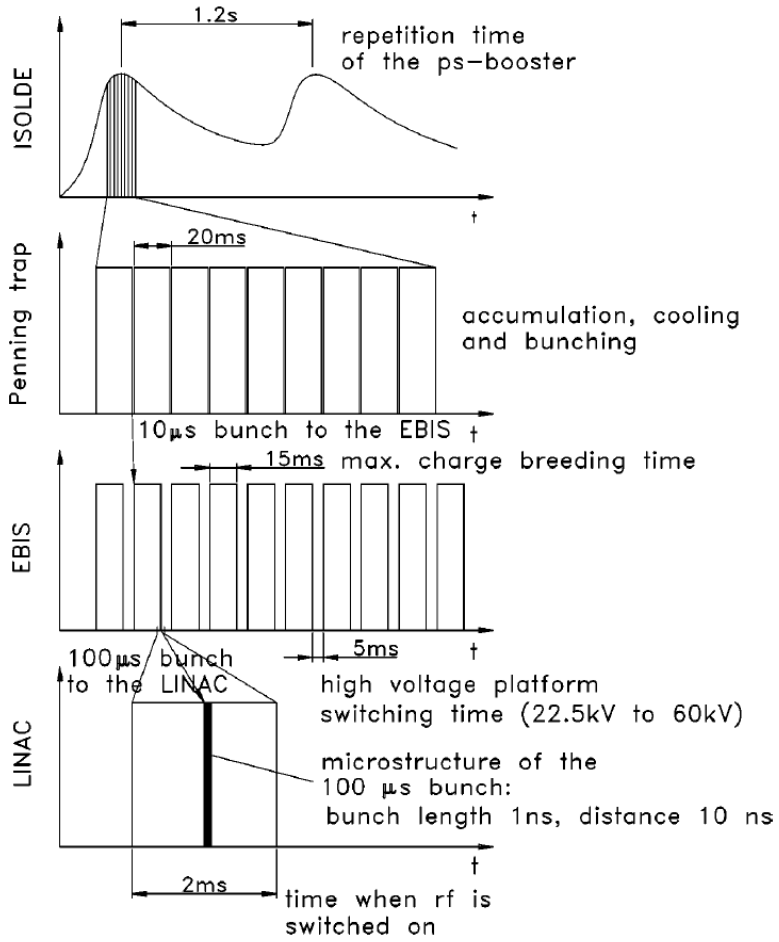

Figure 2.14: Time structure of the pulses from ISOLDE, the Penning trap, EBIS and REX. Image taken from [13].

The photodiode was tested using a pilot beam from the EBIS, i.e., a mixture of ^{20}Ne, ^{16}O, ^{12}C and ^{40}Ar with a beam energy of 1.2 MeV/u and a beam intensity of 7.3 pA, while the mass-to-charge ratio was A/q=4. The pulse of the photodiode signal was observed using a scope to change width while changing the EBIS ramping time. The EBIS trigger pulse is a 3.2 V TTL signal that can be varied in time from 10 to 910 μs.

The pulses on the photodiode ranged in the scope from 625 to 1500 μs, as they result from the sum of the ramping time plus the extraction time of the EBIS, also known as the charge breeding time, as shown in Fig. 2.14.

The photodiode signal (V_{max}) also changes with beam current (I_{FC}). A constant EBIS pulse width of 110 μs was set and then the beam current was changed gradually obtaining the results shown in Fig. 2.15.

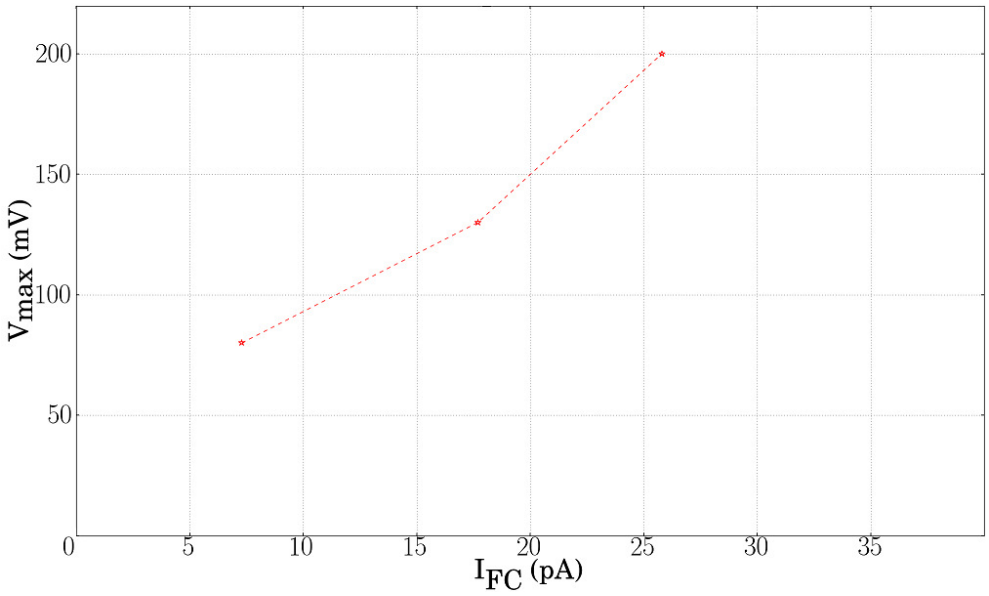

Figure 2.15: Photodiode signal as a function of beam current.

The photodiode signal changes with beam energy too. Fixing the beam current to 7.3 pA and switching the IHS cavity on/off two data points could be measured as shown in Fig. 2.16.

These measurements are preliminary and incomplete due to beam downtime. However, these tests indicate that the PIN photodiode is responsive to the time structure of the EBIS pulse under the given conditions in the machine. The signal-to-noise ratio appeared sufficient to identify the changes in beam pulse distribution even for relatively low-intensity beams. Further tests are needed to characterize the performance of the photodiode accurately, but these preliminary tests indicate that the PIN photodiode could be used as a possible operators' tool for slow extraction optimization.

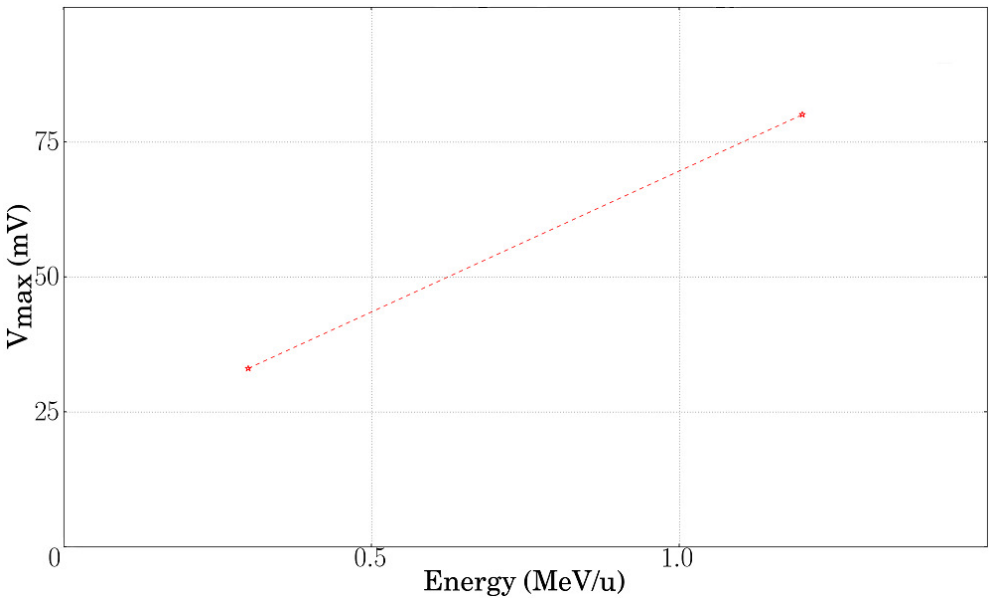

Figure 2.16: Photodiode signal as a function of beam energy.

2.8 Chapter Summary

The beam diagnostics system of REX-ISOLDE provides a comprehensive set of tools for operators in order to measure beam intensity and monitor transverse beam profile and emittance. All of these diagnostic tools need to be redesigned or replaced in the context of the HIE-ISOLDE linac, as explained in the following chapter. The previous work by [72] on the PIPS detector for beam energy and ToF paved the way for the R&D effort on beam diagnostics to be continued as part of this PhD thesis.

Chapter 3

HIE-REX Beam Diagnostics

In this chapter the design requirements and performance limits of the beam diagnostics system of HIE-REX are detailed, as well as a summary of the different devices foreseen, showing the research and development involved in the process. Taking the instrumentation requirements as a starting point, the work focused mainly on the Faraday cup and the slit scanner as priority tools for beam diagnostics, then on the development of the PIPS detector system.

3.1 Instrumentation Requirements

In the HIE-REX superconducting LINAC beam parameters such as beam current, transverse beam profile, beam position and transverse emittance need to be measured by the beam diagnostics system, each with a specific accuracy, as required from beam dynamics studies [75].

Beam current measurements are essential in order to measure and optimize transmission and set up the beam. For stable pilot beams, beam currents in HIE-REX range from 1-1,000 pA. Beam currents need to be measured with an absolute accuracy of 1%. Faraday cups were selected for this purpose, as these allow measuring absolute beam intensities in this range. The diameter of the Faraday cup will be 30 mm to cover the full beam aperture, as the maximum beam size in the LINAC is 5 mm (1σ).

For transverse beam profile measurements, an accuracy of 10% on the beam size measurement is required for the minimum beam size (1σ= 1 mm). The profiles will be acquired by sampling the beam current that goes through a slit into the Faraday cup downstream, therefore registering the beamlet current as a function of the position of the slit. From the mean of the beam profile distribution, the position of the beam will be extracted. The typical beam sizes in HIE-REX will be 1 - 5 mm (1σ). The main challenges that were raised with the HIE-ISOLDE upgrade lie in the confined

longitudinal space available for beam diagnostics of just 58 mm, as explained in the next section, and the addition of new devices to the diagnostics box such as the silicon detector and the slit scanner combined with the demanding performance requirements [75].

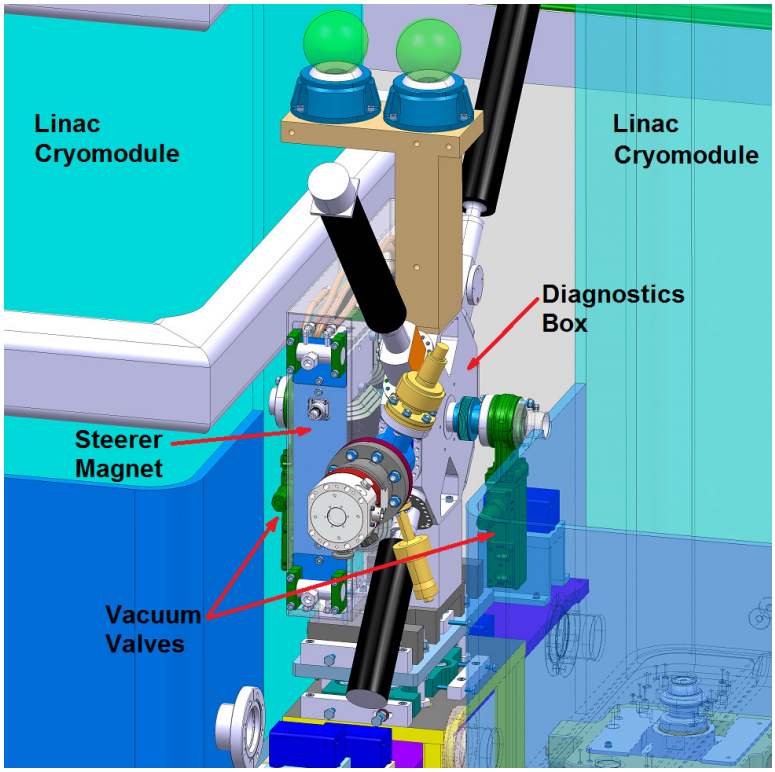

Figure 3.1: Layout of the intercryomodule region in HIE-ISOLDE. Image by E. Urrutia (personal communication, May 22, 2014.

3.2 The Diagnostics Box and the Intercryomodule Challenge

In all of the intercryomodule regions there will be a diagnostics box, two vacuum valves and a steerer magnet as shown in Fig. 3.1. These intercryomodule regions have been designed 320 mm long each to optimize beam acceleration and minimize the debunching of the beam between acceleration stages. In order to properly set up the beam, current, profile and position measurements are necessary to ensure a correct transport of the beam, hence the need for diagnostic devices in every intercryomodule region. The diagnostic boxes share space with the other elements such that only 58 mm in longitudinal space are available for the diagnostic devices. The longitudinal space available for diagnostics in the HIE-REX LINAC has been reduced by almost a factor 5 compared to the REX LINAC. The space constraint poses a serious challenge for the design of

the Faraday cup and its integration with all other devices.

The purpose-built diagnostics box for the HIE-REX LINAC is machined from a bulk piece of stainless steel (AISI 316L) [76] in an octagonal shape. It has a modular design as shown in Fig. 3.2, with one vacuum port and five ports to house various detectors, collimators and stripping foils [77]. The octagonal box has metal surfaces with drilled holes to install laser alignment equipment on top and a mechanical support on the bottom. The main beam diagnostics system for which the box was developed lies in the Faraday cup and the slit scanner system, which are detailed in the following sections. There are two working planes to insert different devices on the beam path. The slit scanner, slits and collimators move along the first plane, which is upstream of the second plane of movement, reserved for the Faraday cup and the PIPS Si detector.

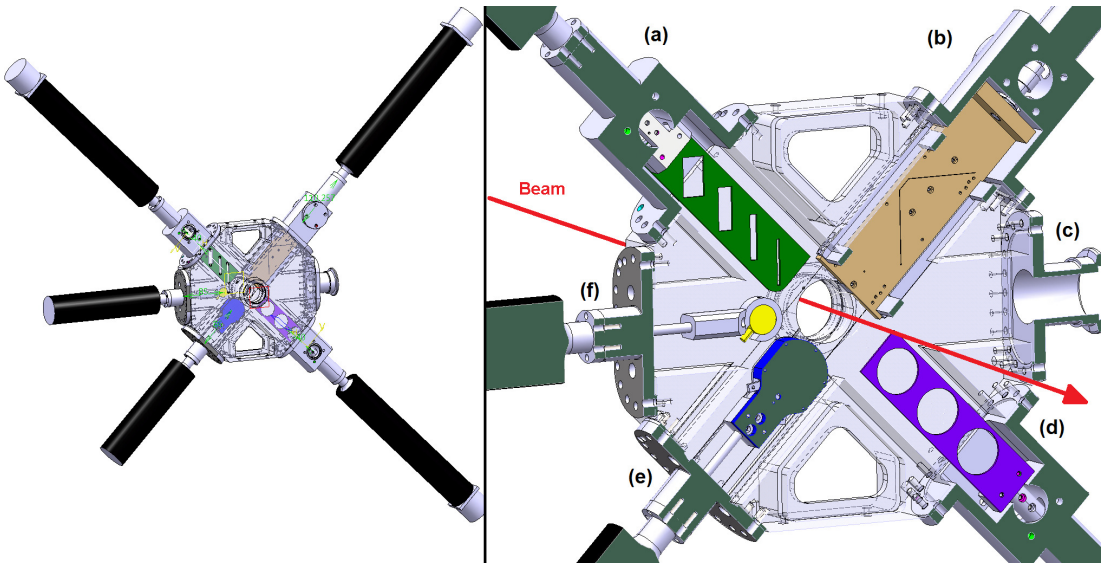

Figure 3.2: Left: layout of the HIE-ISOLDE diagnostic box showing the linear-motion actuators. Right: Detail of the DB as seen from the back. (a) Vertical collimator slits; (b) slit scanner; (c) Vacuum port; (d) Blade of stripping foils; (e) Faraday cup; (f) PIPS Si detector. Image by W. Andreazza (personal communication, June 2, 2013).

For stable beams a Faraday cup is the baseline solution to measure beam intensity. An unusual design of short Faraday cup is required because of the limited longitudinal space available between cryomodules. In this short Faraday cup design, particular care has to be taken in biasing the repeller ring to prevent the escape of the secondary electrons and to be able to reliably measure all the beam charge. The Faraday cup has to be mounted on a movable support in order to allow its insertion and extraction from the beam path. The Faraday cup necessarily needs to be "in beam" at the same time as either the slit scanner or the collimator blades, in order to measure beam profiles in the slit scanner and centre the beam with the different collimators. An initial mechanical

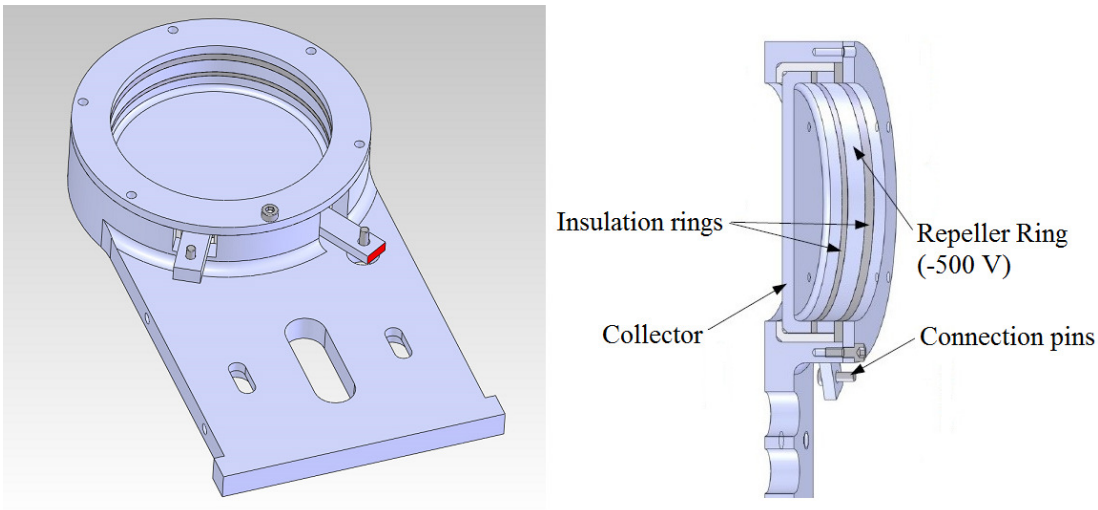

Figure 3.3: Original 3D design of the HIE-ISOLDE Faraday cup. Image by P. Noguera (personal communication, Feb 24, 2012).

design of this Faraday cup, as shown in Fig. 3.3, was built at Added Value Solutions (AVS) [78] with input from the Beam Instrumentation group (BI) at CERN prior to the start of this PhD study.

The slit scanner together with the Faraday cup forms the beam profile monitor. The slit scanner consists of a stainless steel blade with horizontal and vertical slits mounted on a shaft and moved using a linear motion actuator (MDC BLM-133-6-03 MP 660012-200) which is coupled to a stepper motor (P21NRXD-LNF-NS-00) [79]. The slit scanner is located 5 mm upstream of the Faraday cup, moving in a plane in front of the cup and scanning through the beam, as shown in Fig. 3.4. Using an inside vacuum guiding design, the slit scanner was supported by metallic skids with a DICRONITE coating [80], which glided tightly along grooves inside the box. The stroke of the slit scanner was 152 mm.

The scanning blade must be installed at 45° with respect to the floor plane in order for the V-shaped slits to measure the horizontal and vertical beam profile with a single blade scan. The location of the Faraday cup in the diagnostics box is irrelevant for measurements, but in the initial design (see Fig. 3.2) it was foreseen to be installed in the port opposite to the slit scanner, because of the guiding skids of the scanning blade. With this system, the transverse beam profile can be extracted by sampling the beam current using the Faraday cup behind the slit scanner, so the value of the measured current is recorded as a function of the slit position. From the mean of that profile distribution the beam position is easily measured with a resolution given by the slit width and the step size.

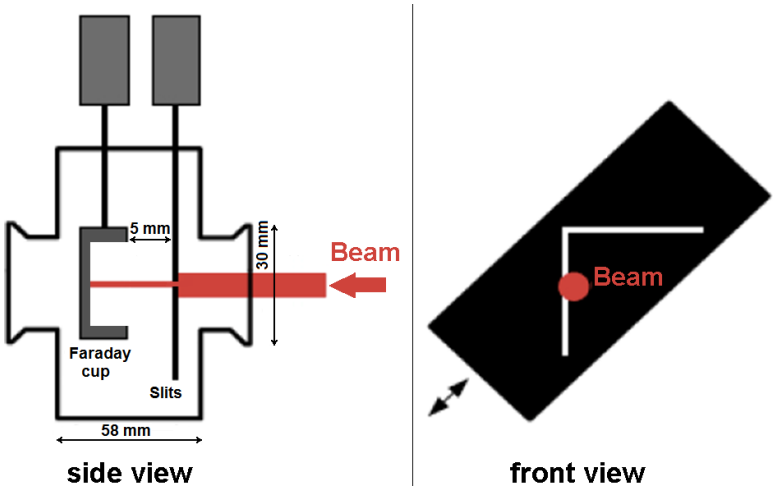

Figure 3.4: Illustration of the Beam Profile Monitor principle. Modified image taken from [75].

As a requirement, an accuracy of 10% is needed on the beam size measurement for all (1-5 mm 1σ) possible beam sizes and normal setup beam currents. This means that the expected slit width must be around 0.5-1 mm, but this parameter needed to be studied and optimized. From the point of view of the range of particles in matter, the blade thickness is not a constraint as the ion beam is stopped in much less than 1 mm of steel or aluminium, however, for mechanical reasons it was manufactured 1 mm thick. The resolution in the position of the slits is required to be better than 100 μm in order to have sufficient resolution on a transverse beam profile of a minimum size beam.

3.2.1 Effect of Slit Width on Beam Profiles

Calculations were done using MATLAB in order to study the influence of the slit width on the profile measurements. A gaussian beam with an intensity of 50 pA and a beam size of σ= 1 mm was scanned with a slit width ranging from 0.5 to 1.5 mm. The normalized beam current of the resulting beamlets as a function of the slit position is presented in Fig. 3.5. The difference between the Full Width at Half Maximum (FWHM) of the original beam and the FWHM of the profile reconstructed from the beamlets is defined as ΔFWHM. As shown in Fig. 3.5, there is little or no distortion on the profiles measured with a slit width $\leq \sigma$ (ΔFWHM<10%), while the profile is significantly distorted with a slit width larger than σ. This is in the most critical case (minimum beam size), and the effect in the case of a beam size of σ=5 mm is negligible for the slit width range mentioned above.

The slit width also has an effect on how much beam current is transmitted down-

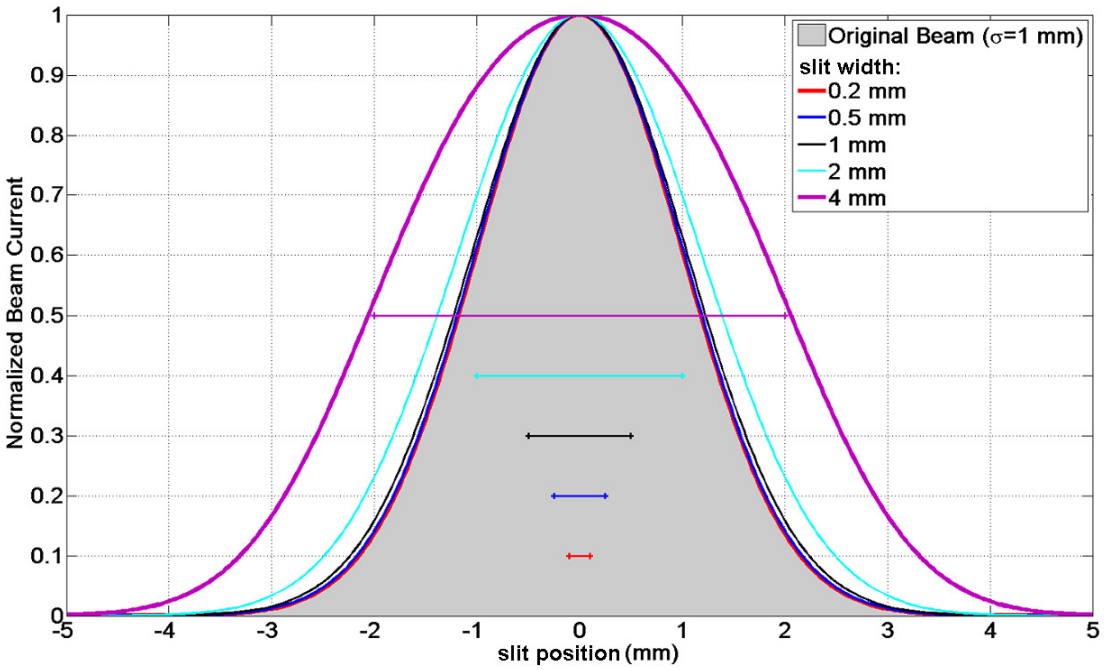

Figure 3.5: Normalized intensity of a σ=1 mm beam as a function of slit position with different values of slit width as parameters. The coloured lines represent the different slit widths.

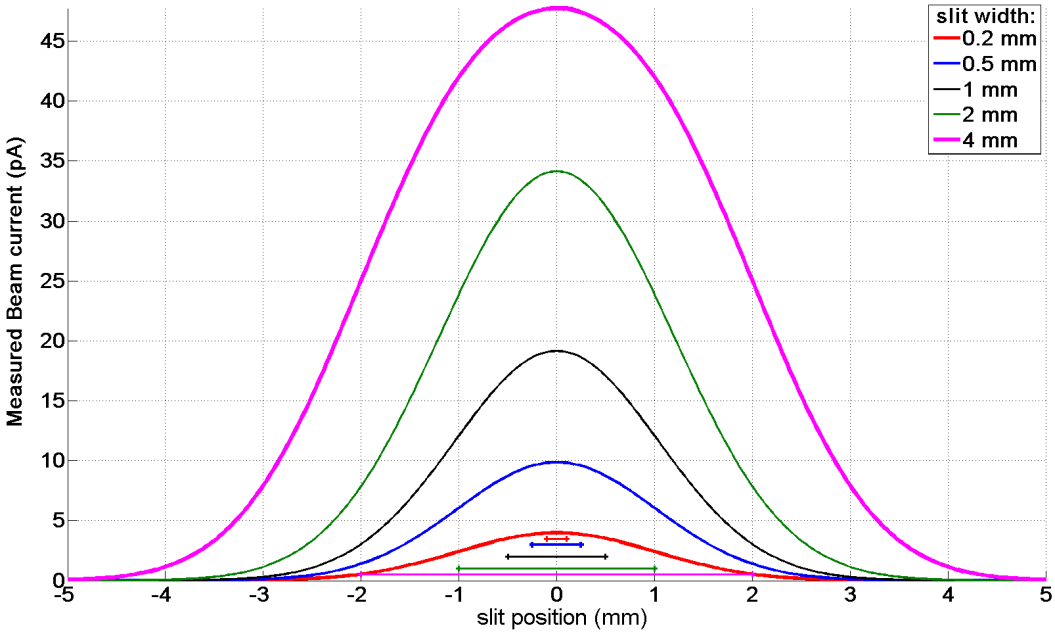

Figure 3.6: Effect of the slit width on the beamlet intensity measured from a 50 pA σ=1 mm gaussian beam. The coloured lines at the bottom represent the different slit widths.

stream. Using the same gaussian beam as above, the result of a calculation showing the profiles reconstructed from the beamlets measured with different slit widths is presented in Fig. 3.6. In principle, to measure the beam profile with a 10% error on the beam size some sensitivity is needed on the beam tails (S/N ratio in the beam centre must be at least 100). As the typical noise of the picoammeters used in these FCs has an amplitude of 0.2 pA, the beam intensity in the centre must be at least 20 pA.

A summary of the effects of different slit widths on beam transmission and on ΔFWHM is shown in Table 3.1. For these two reasons the optimum slit width in this particular machine would be 1 mm. This value is a compromise between measuring a beam profile with little distortion with respect to the original beam but also allowing enough beam intensity to be transmitted to the FC in order to have a good S/N ratio.

Table 3.1: Effect of the slit width of the slit scanner on the measured beam transmission and beam size.

Parameter/Slitwidth (mm)		0.2	0.5	1	2	4
σ=1 mm	ΔFWHM (%)	0.33	1.39	4.57	17.31	74.64
	Beam Transmission at centre (%)	7.9	19.74	38.28	68.27	95.45
σ=5 mm	ΔFWHM (%)	0	0	0	0.86	2.56
	Beam Transmission at centre (%)	1.60	3.99	7.97	15.85	31.09

3.2.2 Slit Scanner Actuator Tests

A stress test of the slit scanner system was performed on the prototype of short diagnostic box at CERN with the aim to assess the robustness of the guiding system and also to identify possible metallic dust production issues because of the moving blade that could contaminate the cavities in the LINAC. The test was performed at a vacuum pressure of 5.5×10^{-5} mbar. In this test setup, the scanning blade was left moving automatically at full stroke in and out continuously, with a thermocouple monitoring the temperature of the stepper motor. During the first cycles IN/OUT, the temperature readout from the thermocouple was between 40 and 60 °C. The maximum operational temperature quoted for that stepper motor is 90 °C. During the IN/OUT movement cycles, the speed of the slit scanner was set to 7 mm/s, a convenient value that will be used in machine operations in order to measure beam profiles in less than a minute.

After 24 hours of test, or 1,340 cycles, the slit scanner jammed inside the box and the test had to be aborted. After a thorough inspection of every component it was found that the mechanical tolerances between the slit scanner and the grooves in the box were too tight, and the DICRONITE coating may have worn out, jamming the slit

scanner inside the box.

It was decided to change the guiding system completely and aim for an out-of-vacuum guiding system with the scanning blade moving freely inside vacuum, without any rails or support skids. Given the relatively large lever arm between the actuator flange and the slit position, tests needed to be carried out to fulfil the 100 μm requirement with the new guiding system.

The proposed solution for this problem was a linear actuator based on two parallel guiding metal rods and an endless screw with a ball-bearing feedthrough connected to a stepper motor, as shown in Fig. 3.7. The screw pitch is 1 mm and the full stroke of the mechanism is 138.7 mm. The start/stop positions are software controlled, with a limit switch used as safety interlock.

An acceptance test for this guiding system was done at AVS. The linear actuator with the slit scanner was installed in the short diagnostic box prototype. The control unit for the stepper motor including the limit switches was provided by AVS for this test. A thermocouple was connected to the outside of the stepper motor to monitor its temperature with a multimeter. Two glass view ports were mounted on the beam ports of the diagnostics box. A high intensity illuminator (Edmund MI-150) and a CCD camera (IDS UI-2210SE) were installed on each side of the box on independent supports and mechanically detached from the support of the box. A 2 mm thin Polytetrafluoroethylene (PTFE) teflon screen was placed in front of the illuminator in order to illuminate the viewport homogeneously. A high-vacuum pumping group (roughing+turbo pumps) was connected to a port on one side. A picture of the experimental setup is shown in Fig. 3.8 [81].

A special scanning blade was built for this test. A picture of the scanning blade used is presented in Fig. 3.9. The blade has two slits 0.2 mm wide at 45° from the movement axis, with six holes of 0.1 mm in diameter spaced 20 mm apart. The purpose of the holes is to track their transverse position as the blade moves IN/OUT.

The experimental procedure consisted of tracking the transverse position of the drilled holes labelled 1 to 6 (being 1 the first and 6 the last holes to be scanned when moving the blade IN) while moving the scanning blade. When the scanning blade crossed the beam aperture the light passing through the drilled holes (or the slits) was recorded by the CCD camera, whose axis was also tilted 45° in order to easily track the motion perpendicular to the blade movement. By analysing the size and position of the light spots frame by frame, the displacements of the blade due to mechanical

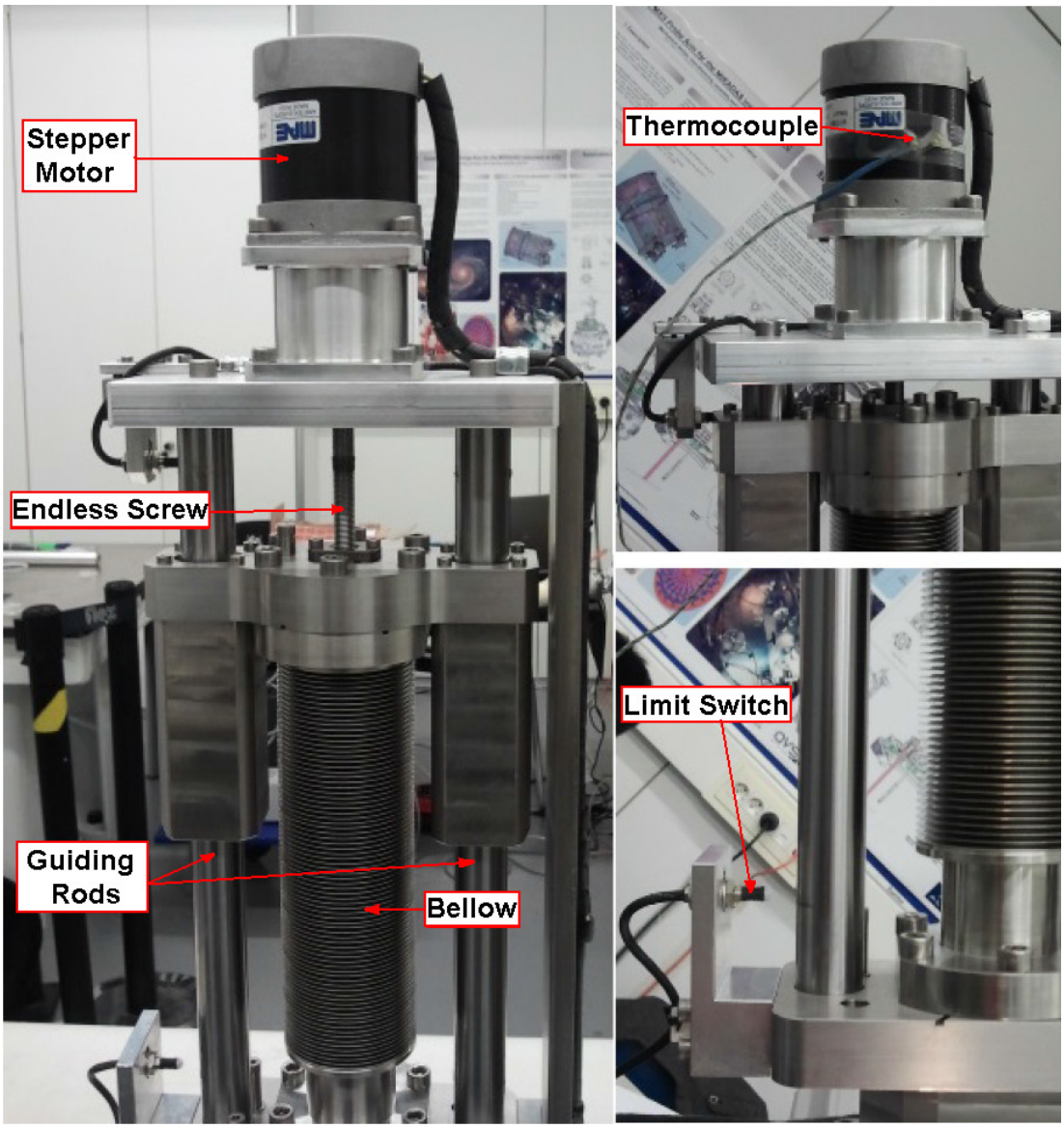

Figure 3.7: Left: AVS out of vacuum guiding system for the slit scanner. Top right: Thermocouple attached to stepper motor for temperature monitoring. Bottom right: Limit switches. Image taken from [81].

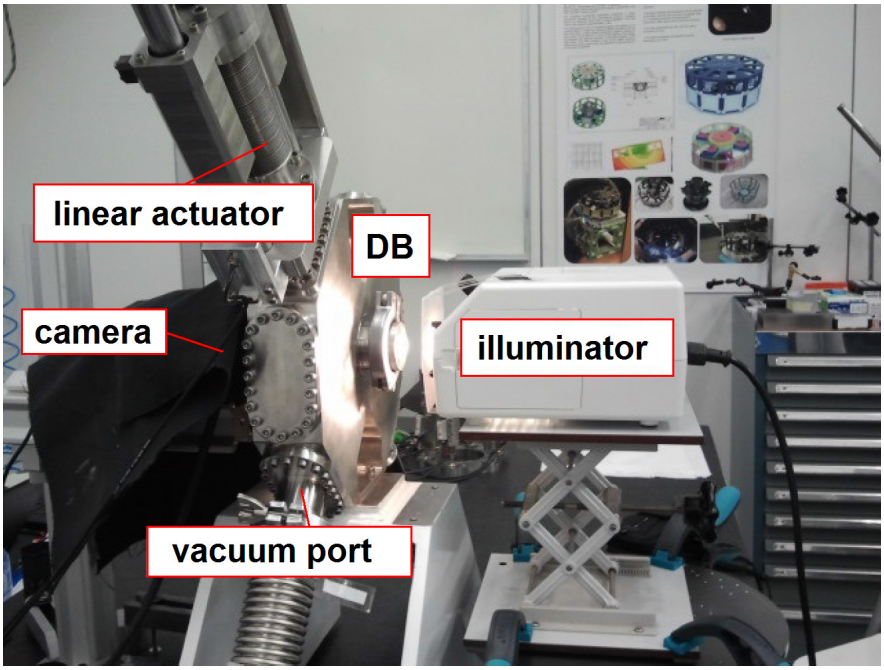

Figure 3.8: Experimental setup at AVS for the acceptance test of the slit scanner system. Image taken from [81].

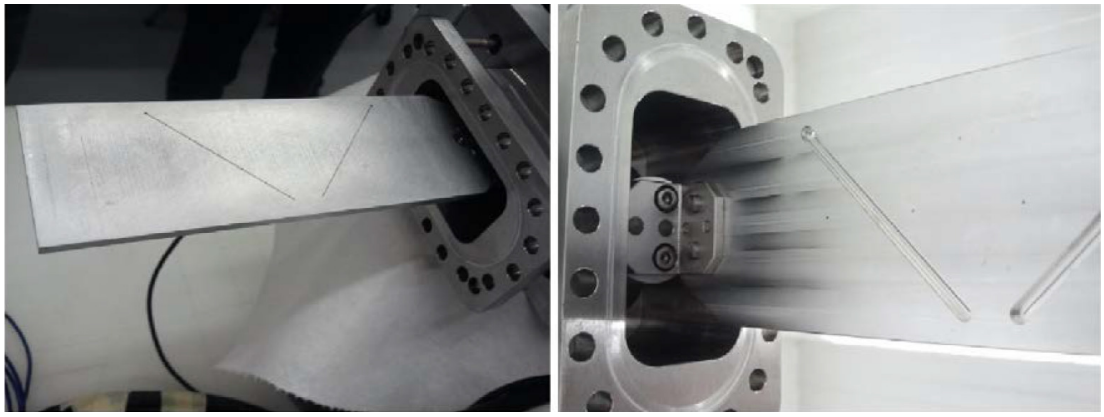

Figure 3.9: Picture of the scanning blade. Notice the almost imperceptible holes on the blade. Image taken from [81].

vibrations and due to the lever arm were determined. The shortest exposure time of the camera was 100 μs, and the frame rate was 37.6 Frames Per Second (FPS). The size of the frames is 640x480 pixels with 8 bits grey scale. The test was carried out under high vacuum conditions, at a vacuum level of 2×10^{-6} mbar. One of the frames taken is shown in Fig. 3.10, where the shape of one slit and a hole are visible. On the right side of the figure, a small area around the hole identified on the left is isolated and magnified. The profiles of the light intensity in the horizontal and vertical directions are fitted, and from these the position and size of the spot are determined.

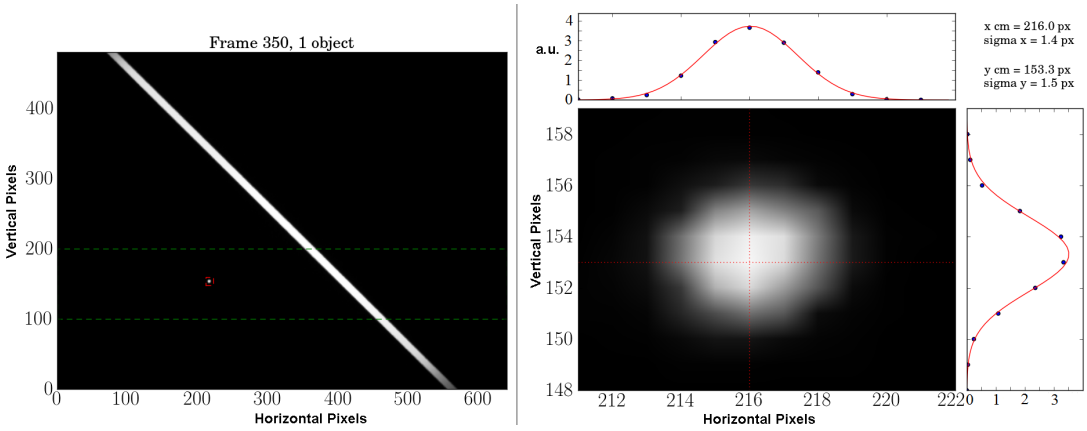

Figure 3.10: Left: Camera frame showing the light passing through a slit and a hole. Right: Horizontal and vertical profiles of the light passing through the hole. Image taken from [81].

The calibration of the camera pixel scale was done by measuring the steps needed to centre the different holes in the camera. The obtained value is δ_{scale}=43.42 pixels/mm. This δ_{scale} compared to the pixel size (9.9 μm) results in a 0.43 conversion factor. δ_{scale} is the value used for all the data presented below. After the scale calibration a series of tests, which are detailed below, were carried out.

Continuous full movement of the blade in both directions (OUT→IN and IN→OUT), tracking the position of the six holes at 5 and 10 mm/s. With this test the maximum excursion (peak to peak) of the movement of a hole in the direction perpendicular to the blade movement can be determined. The results are presented in Fig. 3.11. The maximum excursion for each hole in the direction perpendicular to the blade movement is less than 20 μm. The same test was performed at 5 mm/s, and the results are shown in Fig. 3.12. The maximum excursion for each hole is of the order of 20 μm, and it appears to be independent of the blade speed [81]. The presence of small offsets in the graphs are systematic and probably due to the finite accuracy in the drilling of the holes on the blade. The offsets do not influence the results on the overall amplitudes in the position of the slit in the vertical axis, and therefore were not considered as relevant

in the analysis.

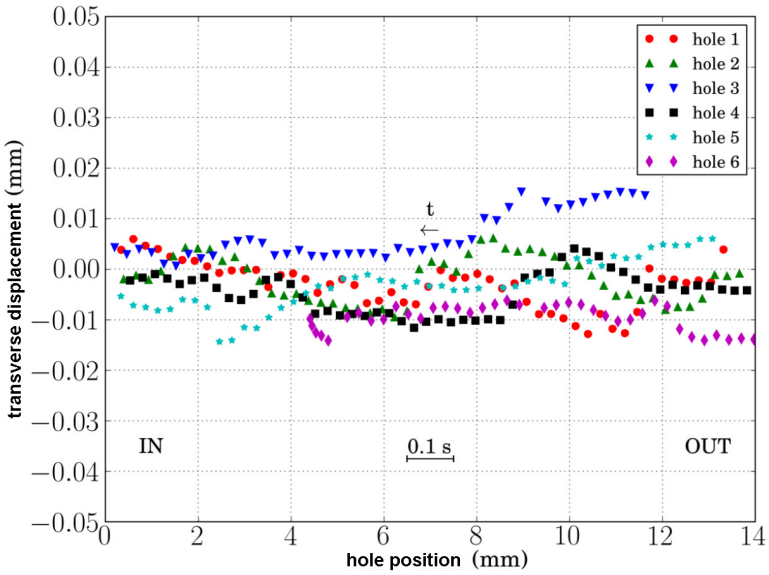

Figure 3.11: Tracking of the hole positions in the camera reference system at 10 mm/s. Image taken from [81].

The next test consisted of moving the blade in a small range (6 mm) in both directions with the hole centred in the camera image, with 1 second pause at each end for 15 cycles. The aim of the test was to assess the repeatability of the blade position during several scans at 5 and 10 mm/s. The results are presented in Figs. 3.13 and 3.14. The accuracy in the positioning of the scanning blade is of the order of 1 μm, which might as well be influenced at this level by the uncertainties introduced by other possible effects on the experimental set-up, such as vibrations of the camera support, resolution of the acquired images and level of detection of the optical recognition software.

Then the test was repeated, this time moving the blade in both directions starting with hole 1 centred on the camera up to hole 6, for a total stroke of 100 mm during 15 cycles. This is a repetitive measurement but with a longer stroke. The blade positioning in the direction of the movement changed less than 5 μm between the first and last cycle.

Another test consisted of moving the full stroke of the blade (138.7 mm) touching both limit switches, without resetting the home position for 10 consecutive cycles. This test was done to measure the accuracy in the position of the blade using the limit switches as reference. The blade speed was 10 mm/s. The repeatability in the position had a standard deviation of 3 counts for each limit switch. This translates into a standard deviation in distance of σ= 2 μm.

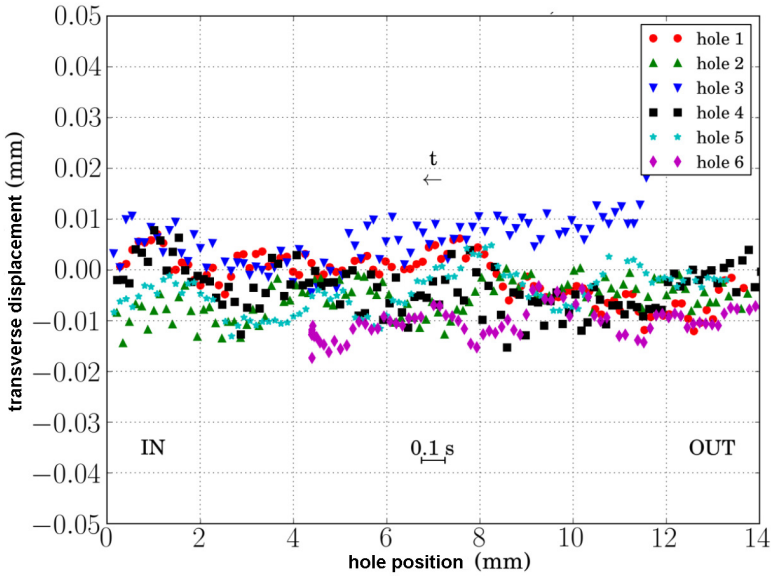

Figure 3.12: Tracking of the hole positions in the camera reference system at 5 mm/s. Image taken from [81].

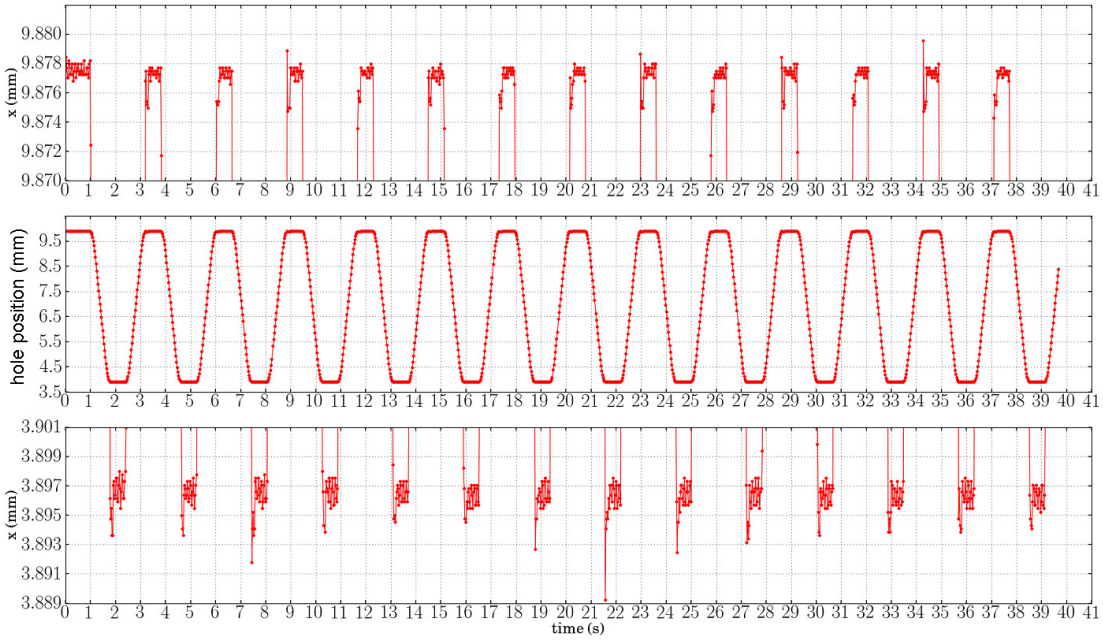

Figure 3.13: Tracking of hole 1 moving the slit 6 mm back and forth at 10 mm/s. Top & bottom are zooms of the central plot. Image taken from [81].

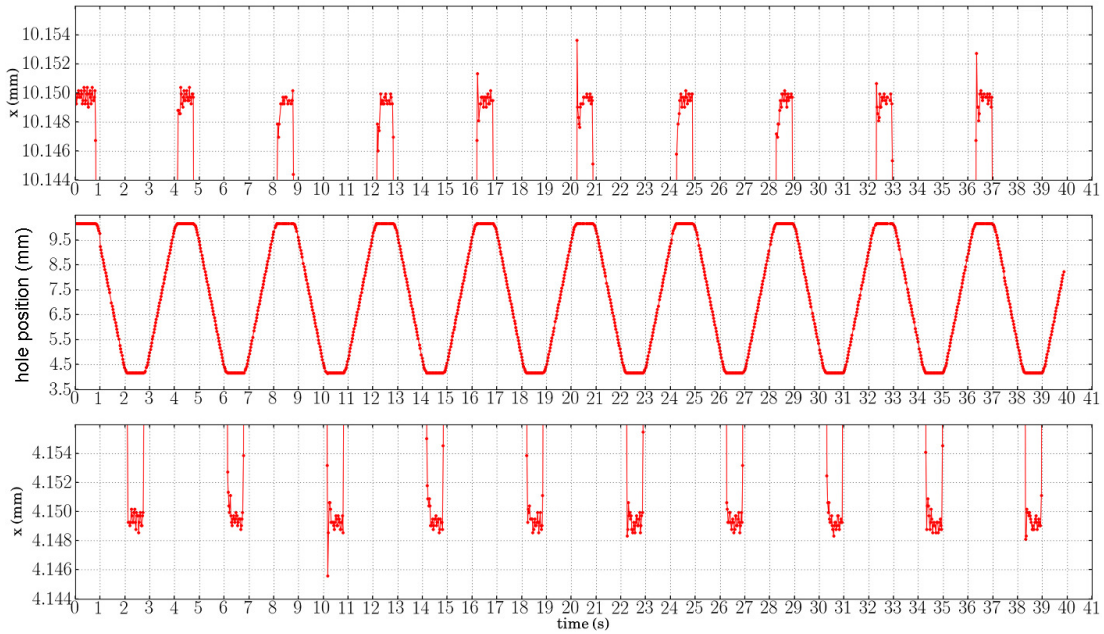

Figure 3.14: Tracking of hole 6 moving the slit 6 mm back and forth at 5 mm/s. Top & bottom are zooms of the central plot. Image taken from [81].

In order to check that the motor was not losing steps along its movement, a test was done starting from the OUT position and moving the blade fully IN in steps of 7 mm until the forward limit switch was reached, then moving back to the OUT position in a single movement. This sequence was done 10 times. The standard deviation on the number of counts during the 10 cycles was of a few counts (out of a total of 277,000 for the full stroke), which indicates that the loss of counts was not a concern.

A stress test of the slit scanner system was done moving the actuator at full stroke for 100 cycles, with 1 second pause between motions. The temperature of the stepper motor was monitored during the test and did not rise above 30 °C. A general inspection of the device was done in order to check for signs of wear or any issues related with the design and implementation of the mechanical system. No significant issues were found.

3.2.3 Conclusions

The proposed mechanical design for the slit scanner actuator of the HIE-ISOLDE short boxes is a solid solution that has been thoroughly tested using a HIE-DB prototype. The repeatability on the positioning of the blade is required to be better than 100 μm, according to specifications, in order not to worsen the resolution for the beam profile measurements. The repeatability in the position of the blade measured indirectly by tracking six holes drilled on it is better than 20 μm, a value that clearly fulfils the

specifications. The chosen stepper motor can provide the needed torque and move the slit at the reference speed of 10 mm/s without problems. The system is quoted to be Ultra-High Vacuum (UHV) compatible. A preliminary stress test of the system was performed, where 100 continuous cycles were done at full stroke without any issues observed.

The design of the system with two guiding rods and the moving force applied directly on the centre of the actuator is a reliable solution. The design with two parallel metal rods provides a smooth and accurate guiding of the blade throughout its full stroke. The use of a ball bearing and the endless screw to reduce the friction in the conversion from rotational to linear motion is a good solution, increasing the smoothness of the blade movement. The screw pitch of 1 mm is adequate and, together with the stepper motor, provides sufficient resolution when positioning the blade. Limit switches are placed correctly and allow a full stroke of 138.7 mm which covers the complete scanning range for both slits, i.e., the acquisition of vertical and horizontal profiles.

3.3 PIPS Detector

A PIPS detector will be used for longitudinal beam profile measurements. These include:

- Energy spread of the beam, with a resolution of $<1\%$ (2σ).
- Bunch length, with a resolution of <100 ps.

Absolute beam energy measurements are a requirement in the machine, and this could be achieved with a ToF detection system, should a chopper be introduced in HIE-ISOLDE.

Measuring the relative beam energy is also very important for the phase-up of the superconducting cavities. The synchronous phase of the RF cavities is set relative to the phase at which the average beam energy is maximized by tracking the beam energy sinusoidal modulation as a function of RF phase. At REX this was done using the dipole magnet at the end of the LINAC, proving to be a robust and reliable procedure but very time-consuming and difficult to automate. As the number of accelerating cavities used to post-accelerate ions at ISOLDE will increase from 5 to 34, an automatic application for tuning the cavity phases is required. Silicon detectors are likely the best solid-state-detector solution in terms of spectroscopy and timing performance for this particular application. More details are presented in chapter 5.

3.4 Collimators & Stripping Foils

A number of supplementary fixed position apertures are required in the machine in order to be able to reproducibly define the beam position in one or both planes when tuning the accelerator, to clean beam halo produced by off-axis or off-momentum particles, or to measure the energy spread in the dispersive section when a thin vertical slit is placed at the entrance of the dipole magnet. These apertures should be able to stay "in beam" together with the Faraday cup. The collimator blades can be 1 mm thick steel or another metal, depending on mechanical and vacuum constraints [75]. There are two types of collimator blades, each with 4 apertures:

⇒Type 1

- 2.5 mm diameter circular hole, for quick centring of the beam
- 5 mm diameter circular hole, for tight collimation of the beam
- 10 mm diameter circular hole, for tight collimation setting up of low energy beams
- 20 mm diameter circular hole, for loose collimation of low energy beams

⇒Type 2

- 2 mm vertical slit, for tight position definition for energy scans
- 5 mm vertical slit, for loose position definition for energy scans
- 10 mm vertical slit, for loose position definition for energy scans
- 15 mm vertical slit, for loose position definition for energy scans

A schematic of these collimators is shown in Fig. 3.15.

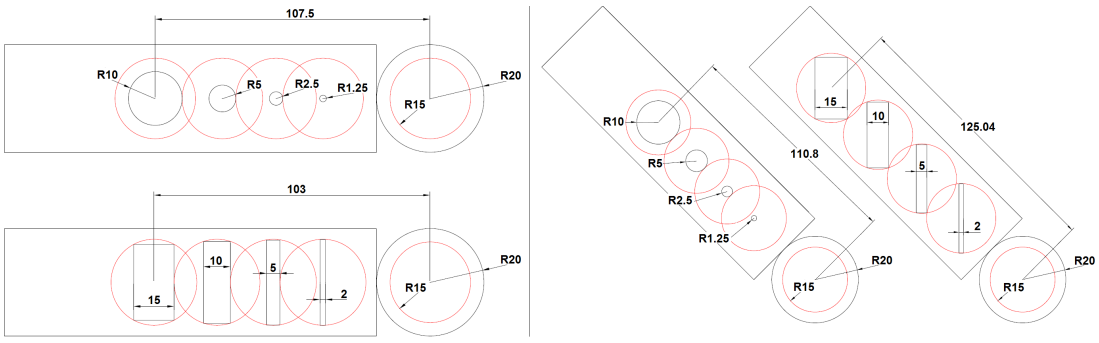

Figure 3.15: Schematics of the different collimator blades type 1 (Left) and type 2 (Right). Image taken from [75].

In addition, lightweight carbon stripping foils with varying thickness in the range of tens or hundreds of μg/cm^2 are needed for beam charge-state cleaning. These will be

installed upstream of the dipole magnets. Support frames with three 30 mm diameter circular aperture are foreseen [75]. The foils are required to be "in beam" together with the Faraday cup, so that the beam intensity transmitted through the foil can be measured immediately downstream.

3.5 Emittance Meter

The main emittance measurement device for HIE-REX will be the NTG emittance meter, see Fig. 2.10, which will be installed at the end of the baseline. Nevertheless, two of the short diagnostic boxes mentioned above could also be used as a complementary method. If installed in the centre of the long drift in the High-Energy Beam Transfer lines (HEBT) between doublets, there are sufficient quadrupoles upstream to match the beam to a range of parameters at this position. The future resolution of this device will be limited by the slit width chosen for the two slit scanners involved and the distance between them. This system also needs a minimum beam intensity in order to acquire enough signal, which is discussed in Chapter 4.

3.6 Chapter Summary

The Beam diagnostics system for the HIE-REX LINAC consists of reliable instruments with a robust design that have been thoroughly tested. The purpose-built diagnostics box fits in the longitudinal space available in the intercryomodule region, while housing all the different devices required for the operation of HIE-ISOLDE. The diagnostics box with its modular design allows an easy installation/removal of any device in the side ports. A Faraday cup was developed and tested as a suitable diagnostics device to measure the range of beam intensities of the HIE-ISOLDE LINAC. The Faraday cup will operate together with the slit scanner in order to measure transverse beam profiles in the challenging space available for diagnostics. With this scanning technique, horizontal and vertical beam profiles can be acquired with an accuracy of 10% on the beam size, and the position of the beam can be extracted from the mean of the distribution of the acquired profiles. PIPS detectors will be used for longitudinal beam profile measurements, which include energy spread and bunch length. They will be measured with a resolution of $<1\%$ (2σ) and <100 ps respectively, as specified from beam dynamics studies [75]. Additionally, other devices such as collimators and stripping foils will help setting up the accelerator, cleaning beam halo or changing the charge-state of the ion beam. In order to measure transverse emittance, the previous NTG emittance meter will be used by default, while the option of using two short diagnostic boxes with the two slit scanners and a Faraday cup is also feasible, as discussed in Chapter 4. The im-

plementation of this beam diagnostic system was made possible due to a comprehensive R&D program and collaboration with industry partners. Thanks to productive discussions with key people involved in the project, awareness of the importance of beam diagnostics was raised, resulting in more longitudinal space in the boxes downstream of the LINAC and more time allocated for beam tests.

Chapter 4

Faraday Cup

This chapter details the development of the HIE-ISOLDE FC and represents the bulk of the experimental work of this thesis. It introduces the Faraday cup as a general device for beam intensity measurements for later comparison between the different prototypes proposed. The design aspects section covers the specific requirements that the HIE-ISOLDE FC must satisfy. Experimental results with ion beams are presented in each prototype section, where the improvement in the FC readout of prototype 3 is shown. At the end of the chapter, a study of the collection efficiency of these FCs is detailed together with results from particle tracking and electrostatic simulations.

4.1 Motivation

A Faraday cup is very simple in concept. A metal cup is placed under vacuum conditions to intercept a charged-particle beam, and doing so the charge of each particle is stopped in the metal. It is important to note that when measuring electric currents, any charge escaping from the cup will induce measurement errors. These errors in the current measurement are reduced with the addition of a bias ring or repeller to the cup, as shown in Fig. 4.1. The ring reduces the probability of escape for secondary electrons that are released upon ion impact. Some Faraday cups may have a weak magnetic field perpendicular to the beam axis to prevent secondary electrons from leaving the Faraday cup [82], and they may operate with a slight positive bias on the metal cup to collect secondary electrons. The detection threshold of a Faraday cup depends on the sensitivity of the ammeter in the circuit that it is connected to and the level of noise present. The current passes through a resistor and the voltage difference is measured.

The cup is an element in a circuit; the current flow through the circuit can be very accurately measured and it is directly proportional to the number of particles that have been intercepted by the Faraday cup. For instance, a current of 1.6 nA in the circuit corresponds to the arrival of 10^9 single-charged ions per second at the Faraday cup. Because the detection is based solely on charge, Faraday cups exhibit no mass

discrimination, which could be an advantage in other experiments. In addition, ions of higher charge states produce a correspondingly larger signal.

Faraday cups have been in operation for decades [83]. Although they are beam destructive, these simple and reliable instruments provide absolute beam current measurements which are very valuable in linear accelerators. Optimising the design of a Faraday cup so that a specific beam type can be monitored efficiently is challenging. Faraday cups for low-intensity, low-energy beams have previously been studied [84, 85]. For this particular machine, i.e., the HIE-ISOLDE LINAC, the challenges in terms of the Faraday cup are mainly the compact longitudinal space available for the FC, only 16 mm long, the measurement of relatively low ion beam intensities of only 1 to 1,000 pA, and its integration when working with all other devices in the same box, i.e. the slit scanner, collimators, etc.

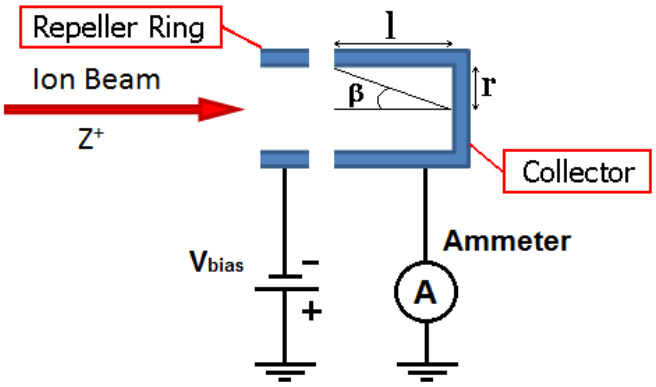

Figure 4.1: Operating principle of a Faraday cup.

In a simplified model, we can consider a collector of a Faraday cup of a given length l and diameter $d = 2r$. Let β be the angle defined by the edge of the cup and the axis perpendicular to the collector. With this geometry, we have

$$cos\beta = \frac{l}{\sqrt{l^2 + r^2}} = \frac{1}{\sqrt{1 + (r/l)^2}} \quad (0 < \beta < \pi/2). \tag{4.1}$$

In this simplified model, it is assumed that secondary electrons are emitted from the central axis of the collector and their trajectories are well approximated by straight lines. This is only valid for electrons without the presence of an electromagnetic field. If there is no electrostatic potential present, all secondary electrons emitted in an angle between 0 and β will escape the cup, while all those electrons emitted at an angle above β will hit some part of the the cup and will be collected. In this way we can define the

solid angle of captured electrons Ω_C as

$$\Omega_C = 2\pi(cos\beta) = \frac{2\pi}{\sqrt{1+(r/l)^2}} \quad (0 < \beta < \pi/2). \tag{4.2}$$

For a current of secondary electrons I_B that are emitted isotropically, we will observe a current of electrons I_C collected after hitting the walls of the cup,

$$\frac{I_C}{I_B} = \frac{\Omega_C}{2\pi} = \frac{1}{\sqrt{1+(r/l)^2}} = cos\beta \quad (0 < \beta < \pi/2) \tag{4.3}$$

and therefore the current of lost electrons I_L can be calculated by the following expression,

$$\frac{I_L}{I_B} = 1 - \frac{1}{\sqrt{1+(r/l)^2}} = 1 - cos\beta \quad (0 < \beta < \pi/2). \tag{4.4}$$

Thus, eqs. 4.3 and 4.4 lead to Fig. 4.2.

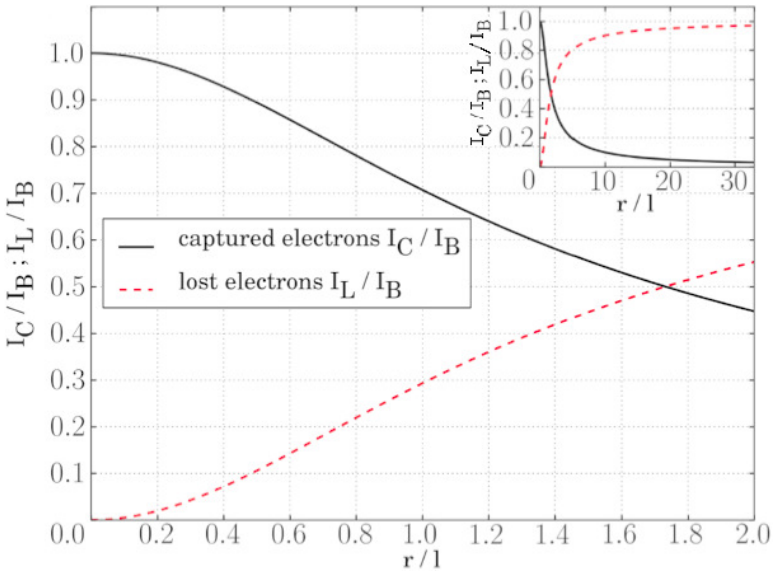

Figure 4.2: Fraction of captured and lost electrons as a function of r/l. Insert in the figure represents the same plot at a larger scale.

This implies that, just taking into account the geometry of a Faraday cup, the r/l ratio has a strong effect on the efficiency in capturing electric charges.

The objective of a Faraday cup is to stop all charged particles from the incoming particle beam and to fully contain the subsequent electromagnetic particle emission so that the charge absorbed directly corresponds to the charge in the incident beam. However, in practice this is not straightforward and there are a number of sources of current losses that can result in false measurements and need to be taken into account for the design of a FC. These include penetration losses, electron escape losses and

leakage current sources.

In order to estimate an adequate thickness of the collector electrode to avoid penetration losses, simulations were carried out using Stopping and Range of Ions in Matter (SRIM) [86]. The most critical beam conditions were simulated, these being alpha particles at 10 MeV/u, as helium ions are sometimes found in the rest gas of the EBIS. In the simulations performed, alpha particles impinged perpendicular to a stainless steel target, and the observed result is that ions are implanted up to a maximum of 255 μm with a longitudinal straggling of 10 μm. This value is much smaller than the 2.5 mm required by mechanical considerations.

In electron escape losses, two phenomena can be distinguished in the case of a FC for ions: Backscattered electron losses are related to electrons bound to the ion nuclei which are released with relatively high energy (5 keV) upon impact with the FC. These electrons require a very high voltage to be collected in the FC, therefore the backscattered electrons emitted inside the angle cone defined by the FC aperture are very likely to escape. Secondary Electron Emission is the second phenomenon to take into account in electron escape losses. Low-energy (<20 eV) secondary electrons are emitted in the surface of the FC collector, which could escape from the FC if no potential barrier is present. An important aspect must be taken into account when choosing a proper material for the collector of a Faraday cup. The secondary electron emission yield γ, defined as the average number of electrons released from a target surface per incident particle, changes with the target material. While the dependance of γ on the target material (Z_2) is difficult to determine quantitatively, γ is proportional to the atomic number of the projectile Z_1 [87] for the projectiles and energies present at REX-ISOLDE. It is important to note that this Faraday cup is designed for use with stable ion beams only. If used with a beam of radioactive ions, activation problems will appear, which would be another source of charged particle losses.

The energy spectra of secondary electrons emitted from a solid target being hit by charged particles are very complicated because many different collision processes are involved prior to low-energy secondary electron emission [88]. Regarding the angular distribution of secondary electrons, previous studies suggest that the electron emission angle depends on the energy of the incident particle, being this related to the interaction time between the incident particle and the target atoms [89].

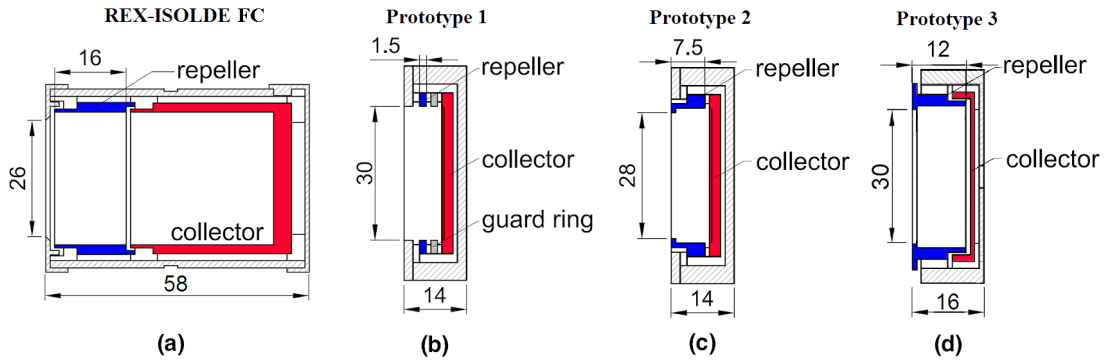

Figure 4.3: Schematics of the Faraday cups discussed in this paper. (a) REX-ISOLDE FC; (b) Prototype 1; (c) Prototype 2; (d) Prototype 3.

Table 4.1: Geometric parameters of REX and HIE collector plates

Faraday cup	r (mm)	l (mm)	r/l	1-cosβ	β (degrees)
REX-ISOLDE FC	14.8	32.0	0.46	0.907	24.7
Prototype 1	15.0	0.5	30	0.033	88.1
Prototype 2	14.0	0.5	28	0.036	87.9
Prototype 3	15.0	1.0	15	0.066	86.2

4.2 Design Aspects

Four different Faraday cups are discussed in this chapter. Their cross sections are presented in Fig. 4.3 and their geometric parameters are presented in Table 4.1.

The first is the standard FC used at REX-ISOLDE and the other three are compact FCs designed and developed in the form of this PhD thesis for the HIE-ISOLDE LINAC.

The short Faraday cup design posed a challenge due to the space restrictions in the intercryomodule region where it will operate. In the 58 mm long diagnostic box a maximum of 16 mm of longitudinal space is available for the Faraday cup, with a beam aperture of 30 mm. The Faraday cup for HIE-ISOLDE is required to operate with stable ion beams for energies between 0.3 - 10 MeV/u and intensities between 1-10^3 pA [77]. It will be used to:

1. Measure absolute beam intensity.
2. Measure transverse beam profiles using a slit scanner directly in front of the cup.
3. Extract the horizontal and vertical beam position from the beam profile.

There is no need for active cooling of this Faraday cup since the maximum beam power deposited in the cup, which is when the pilot beam is used, is negligible at <0.2 W in this LINAC.

4.3 Prototype 1

The first attempt to design a Faraday cup for the HIE-ISOLDE LINAC was motivated by the design of the FC used at REX-ISOLDE, but simply reducing every element to fit in the 14 mm long space available inside the compact diagnostics box. The mechanical design of Prototype 1 was done between the Beam Instrumentation group at CERN and Added Value Solutions, an external contractor, prior to the start of this PhD work.

The exterior of Prototype 1 was made of Aluminium 6082; The collector cup, guard ring and repeller ring were made of AISI 316L stainless steel, and the isolator parts were made of Vespel SP-1.

Numerical simulations were done for all prototypes in order to assess the design of the cups, analysing the electrostatic potential distribution and secondary electron emission. CST Particle Studio [90] was used to study the electrostatic fields and particle tracking in these cups. The electrostatic potential in the central axis of the FC varies according to the length and radius of the cup, so the electrostatic potential is maximum close to the repeller ring and has minimum effect in the centre which is the beam axis, provided that the cup is well centred on the beam.

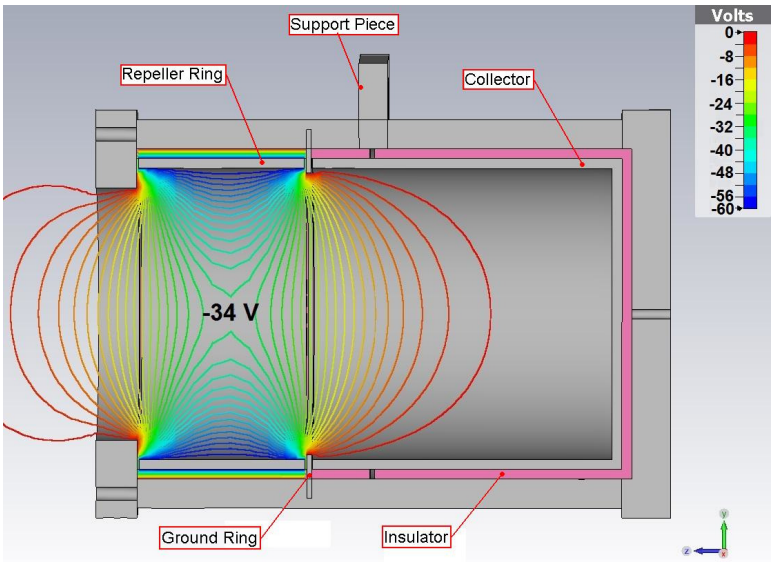

Figure 4.4: Electrostatic potential distribution in the REX-ISOLDE Faraday cup.

In Figs. 4.4 and 4.5 the electrostatic potential distribution along the cross section of the REX-ISOLDE and Prototype 1 Faraday cups is shown using a bias of -60 V for comparison. The minimum electrostatic barrier in the center of the REX-ISOLDE Faraday cup is -34 V, much higher than that of Prototype 1 which is just -5 V. In addition to a higher electrostatic barrier in the cup's centre, the geometric design of

the REX-ISOLDE Faraday cup, i.e., its deep collector relative to its aperture, allows for a much smaller solid angle for particles to escape, as discussed previously.

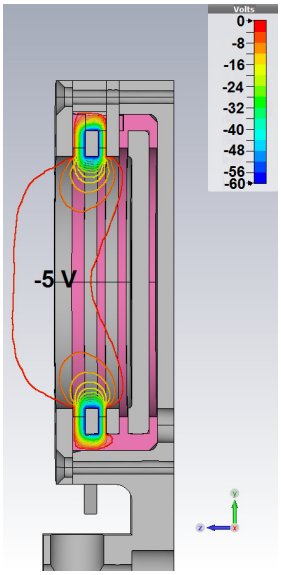

Figure 4.5: Electrostatic potential distribution in Prototype 1.

In the case of Prototype 1 its short length of only 14 mm and large escaping angle of 176° would require a further increase in bias voltage to maintain the same collection efficiency as the REX-ISOLDE Faraday cup. The results of the electrostatic simulations indicate that for a repeller voltage of -60 V, Prototype 1 shows an electrostatic potential in the centre of the cup almost seven times lower than that of the REX-ISOLDE Faraday cup. In order for Prototype 1 to show the same electrostatic potential in the centre as that of the REX-ISOLDE Faraday cup, its repeller needs to be biased at -400 V, as shown in Table 4.2. The potential in the centre of a Faraday cup increases proportionally to the bias voltage supplied to the repeller ring. Whether both Faraday cups can measure a similar beam intensity having the same electrostatic potential in the centre is the subject of the tests carried out in the next section. It is important to note that when using the slit scanner in front of this Faraday cup for profile measurements, the presence of this metal plane connected to ground reduces the electrostatic potential in the central axis by almost a factor of 2 and thus the collection efficiency of the cup could be negatively affected.

4.3.1 Experimental Setup and Results

Prototype 1 was installed downstream of a REX-ISOLDE Faraday cup inside diagnostics box DB6 in the L20 beamline of the REX-ISOLDE LINAC, see Fig. 2.1. The aim of this test was to compare the beam intensity measured by Prototype 1 taking the

Table 4.2: Electrostatic potential on the central axis of Prototype 1 as a function of repeller ring voltage.

Repeller ring voltage (V)	Electrostatic potential at centre (V)
-7	-0.6
-15	-1.2
-30	-2.5
-45	-3.7
-60	-4.0
-100	-8.3
-200	-16.5
-300	-24.8
-400	-33.0
-500	-41.4

REX-ISOLDE Faraday cup as a reference. A picture of the set-up is presented in Fig. 4.6.

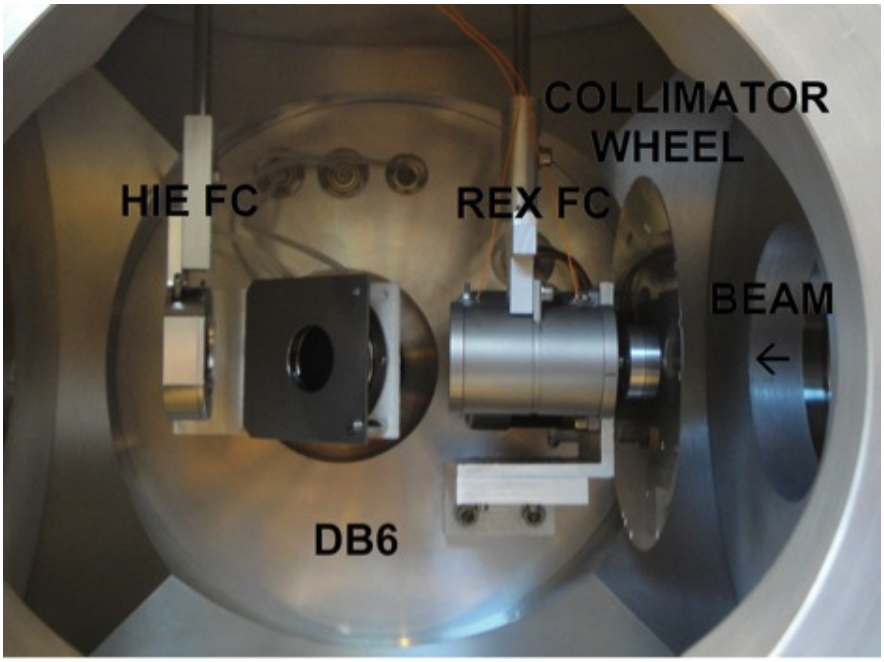

Figure 4.6: Prototype 1 (Left) and REX-ISOLDE FC (Right) FCs ready for experimental tests inside DB6.

The stable beam available at REX-ISOLDE is a mixture of ions with an A/q=4, from least to most abundant: He^{+},O^{4+},C^{3+},Ne^{5+}. The typical beam energies in this LINAC are shown in Table 4.3.

The beam energies used were E/A= 0.3, 1.2, 2.21 and 2.85 MeV/u. Tests were done with a centred beam using the maximum aperture available, i.e., a circular collimator

Table 4.3: Maximum output energies of the different cavities of the REX-ISOLDE LINAC.

Element:	RFQ	IHS	7GAP	9GAP
Energy (MeV/u)	0.3	1.2	2.2	2.85

of 15 mm diameter inside diagnostics box DB6. Using an HV power supply to bias the repeller ring through the feedthroughs on the box, and a picoammeter for signal readout, the beam intensity as a function of the negative repeller voltage was measured.

Once the measurements were completed with Prototype 1, all cabling was switched to the REX FC and the measurements repeated, therefore making sure that the data series were taken with the same electronics in order to avoid offset discrepancies between different picoammeters, that is, the different intensity value recorded by a given picoammeter when no beam is present).

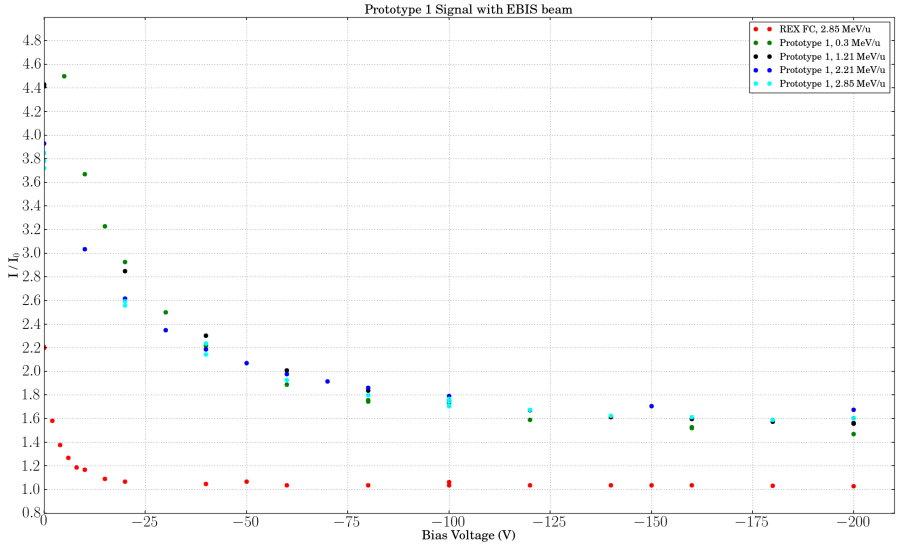

Figure 4.7: Prototype 1 normalised beam intensity as a function of bias voltage for different beam energies. Measurement of REX-ISOLDE Faraday cup at 2.85 MeV/u added for comparison.

In Fig. 4.7 the beam intensity measured by Prototype 1 is plotted as a function of the repeller voltage at the different energies measured. All curves are normalised to facilitate the comparison by a reference intensity value, which is the beam intensity measured by the REX FC at -60 V. At low negative voltages, on the left side of the plot, the FCs measure a beam intensity value much higher than the nominal beam current, due to the escape of secondary electrons generated on the surface of the Faraday cups.

As the picoammeter registers positive current, the escape of electrons, or negatively-charged particles is seen as an increase in the positive current registered. It can be seen that the beam intensity measured by the REX FC reaches a region of stable values, or plateau, fairly quickly at around -60 V, whereas Prototype 1 does not reach it even at -200 V. Furthermore, the value measured by Prototype 1 is between 50-75% higher than that of REX FC. This is due to electrons escaping the cup, in part because of the geometric design of Prototype 1, that is, its shallow collector electrode of 0.5 mm, its 1.5 mm thin repeller ring and its big aperture compared to the total length of the cup. No error bars were included in this analysis since the systematic error produced by the fluctuating nominal beam intensity of the LINAC is significantly larger than the statistical error produced by the picoammeter, our measurement instrument, which has a resolution of around 50 fA.

In an attempt to improve the signal readout from Prototype 1 compared to the REX FC, a set of tungsten wires 50 μm in diameter were soldered to the bias ring of Prototype 1 forming a square with 10 mm side through which the beam could go through. This 4-wire grid would increase the electrostatic potential across the aperture of the FC, especially around the centre of the cup. Unfortunately, beam tests with this bias ring were unsuccessful because of the fragility of the soldered joints during the processes of pumping and venting of the diagnostics box.

Once the results were analysed, the design was modified to improve the current measured by Prototype 1. This involved a complete modification of the inside parts of the cup, removing the guard ring, some insulators, changing the collector material to aluminium, reducing the aperture from 30 to 28 mm and also extending the repeller ring to 7.5 mm. This new prototype is Prototype 2, shown in Fig. 4.3(c).

4.4 Prototype 2

The potential distribution of this prototype biased at -60 V is shown in Fig. 4.8 using the electrostatic solver feature of CST. The extension of the repeller's length by 6 mm is very useful in order to increase the potential on the central axis by more than a factor 4. The guard ring has been removed in this prototype in order to allow more space for the repeller at the risk of introducing a possible leakage current from the repeller ring to the collector. The material of the collector was changed to Aluminium, which has a lower atomic number than steel and would therefore yield fewer secondary electron emission upon ion impact. The diameter has been reduced in this prototype to 28 mm, see Fig. 4.3, in order to avoid electron emission in the repeller ring upon the impact of grazing ions.

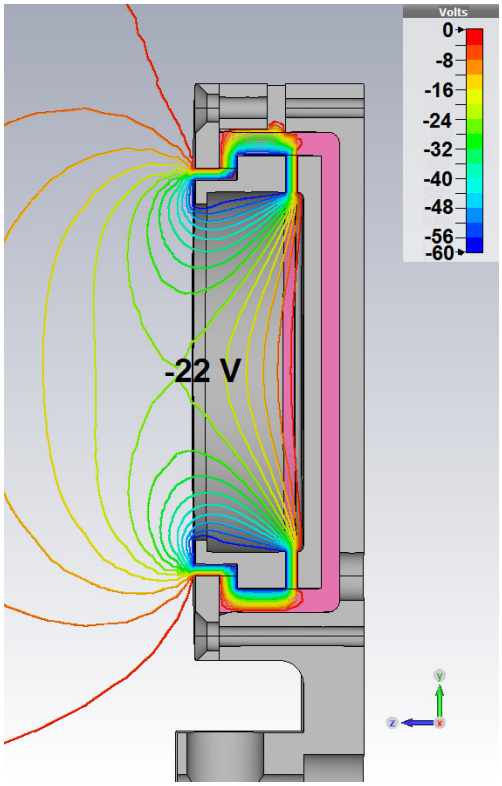

Figure 4.8: Electrostatic potential distribution in Prototype 2.

4.4.1 Experimental Setup and Results

Prototype 2 was installed in the REX-ISOLDE LINAC in the same manner as the former prototype. Tests were carried out at the same beam energies as above (0.3, 1.20 and 2.85 MeV/u) except 2.21 MeV/u, with the aim to compare the beam intensities measured by the Prototype 2 FC and that of the REX-ISOLDE Faraday cup.

As shown in Fig. 4.9, Prototype 2 measures similar beam intensities compared to the REX FC, with a maximum signal difference in the plateau region of 15% higher than that of REX. This represents a major improvement in performance compared to Prototype 1, which showed differences in beam intensity of 50 to 75% higher. Moreover, the signal of the REX FC reaches a plateau faster than Prototype 2 at all energies, and it maintains a stable beam intensity value between -50 and -500 V. In the case of Prototype 2 at 0.3 MeV/u, a downward trend in the signal beyond -200 V might indicate a full capture of the secondary electrons emitted in those conditions of beam energy, projectile, target material and design of FC. Going forward in the direction of making the repeller ring longer without significantly increasing the total cup length, Prototype 3 was built.

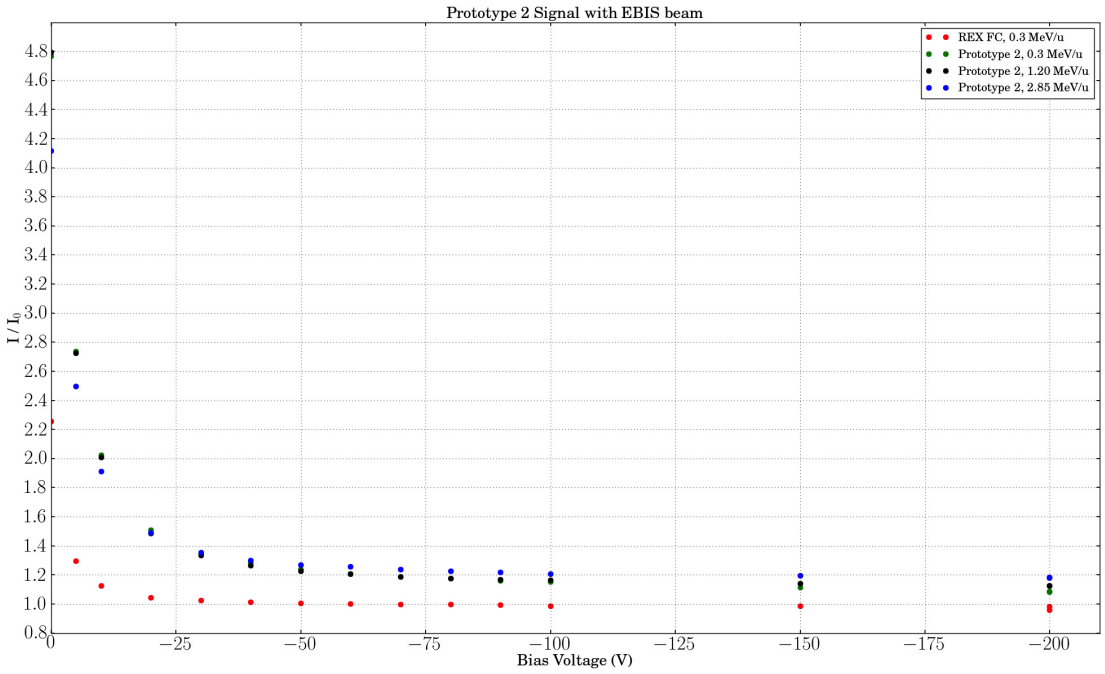

Figure 4.9: Normalized beam intensity measured by Prototype 2 as a function of bias voltage for different beam energies. Measurement of REX-ISOLDE Faraday cup at 2.85 MeV/u added for comparison.

4.4.2 Beam Profile Measurements with Prototype 2

Transverse beam profile measurements were done using the prototype of short diagnostic box installed in REX. Inside the box, the Faraday cup (Prototype 2) and the original slit scanner, with in-vacuum guiding, were set up for tests. The slit width of the scanning blade is 200 μm. After delivering a pilot beam from REX at 2.85 MeV/u up to the position of the diagnostic box, an acquisition routine started taking horizontal and vertical profile scans. The main aim of the test was to study whether the movement of the scanning blade produced any noise in the FC readings, changing the beam intensity and FC bias voltage. The blade speed was set to a minimum of 0.79 mm/s and a maximum of 1.00 mm/s. These scans had a 120 mm stroke in one continuous motion IN or OUT. The readout of the FC was done with a Keithley ammeter, adjusting the range manually to 2 pA, 200 pA or 2 nA according to the beam intensity measured. The results are presented in Figs. 4.10-4.15.

A series of scans was done without beam to measure the electronic noise level observed, which was $\leq$0.7 pA peak-to-peak. Moving the scanning blade in front of the FC did not affect the measured noise level. Another beam profile scan was measured at very low beam intensity, of only 17.8 pA, with steps of 0.5 mm and 1 second pause

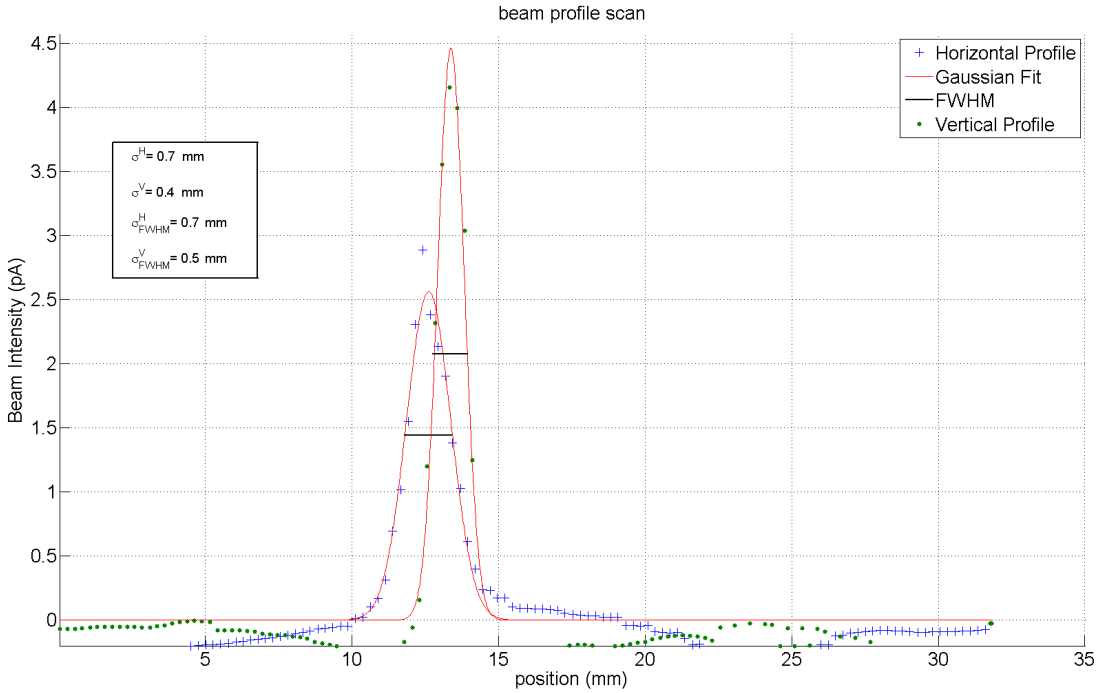

Figure 4.10: Horizontal and Vertical beam profiles of a REX pilot beam at 29.3 pA.

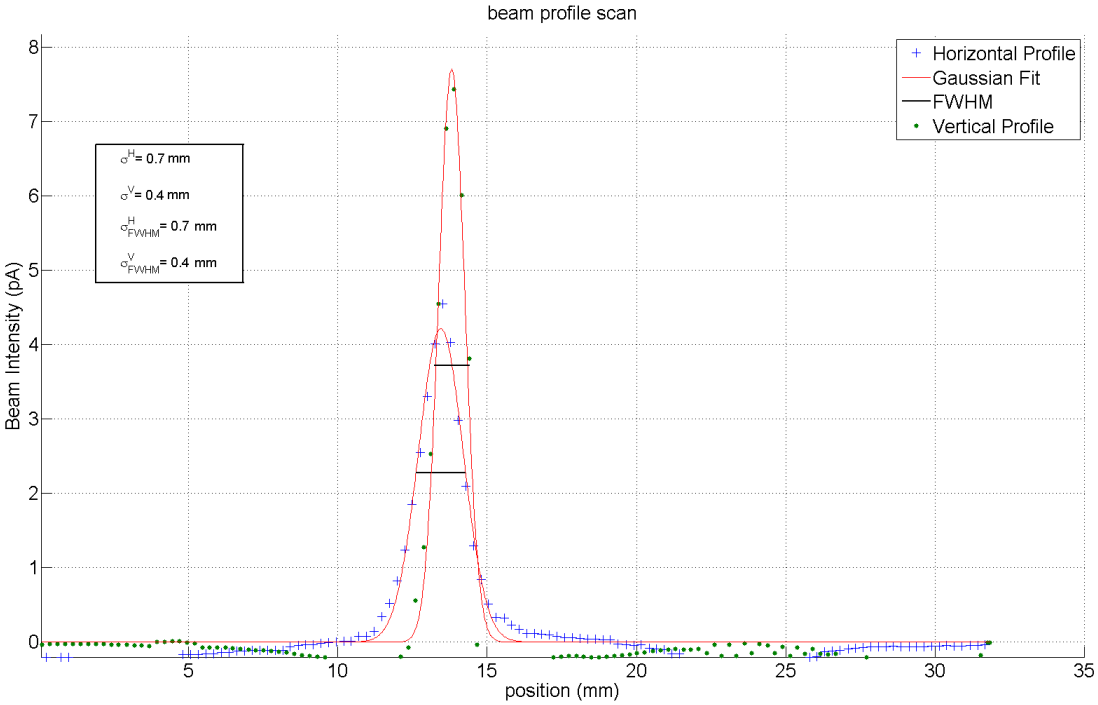

Figure 4.11: Horizontal and Vertical beam profiles of a REX pilot beam at 46.8 pA.

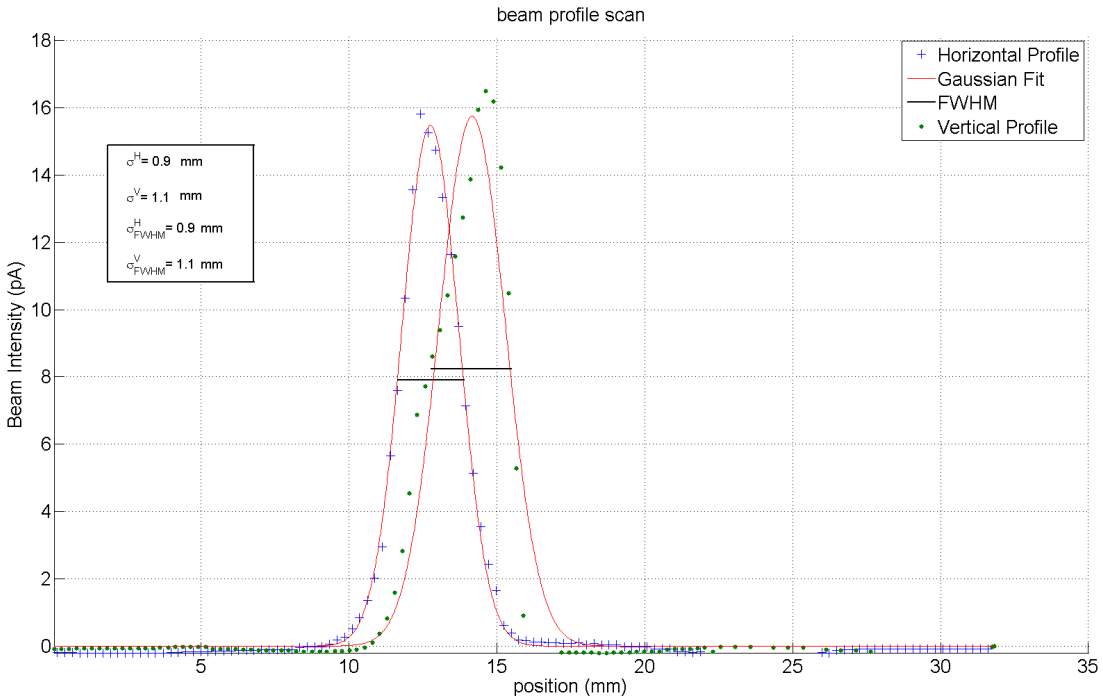

Figure 4.12: Horizontal and Vertical beam profiles of a REX pilot beam at 250 pA.

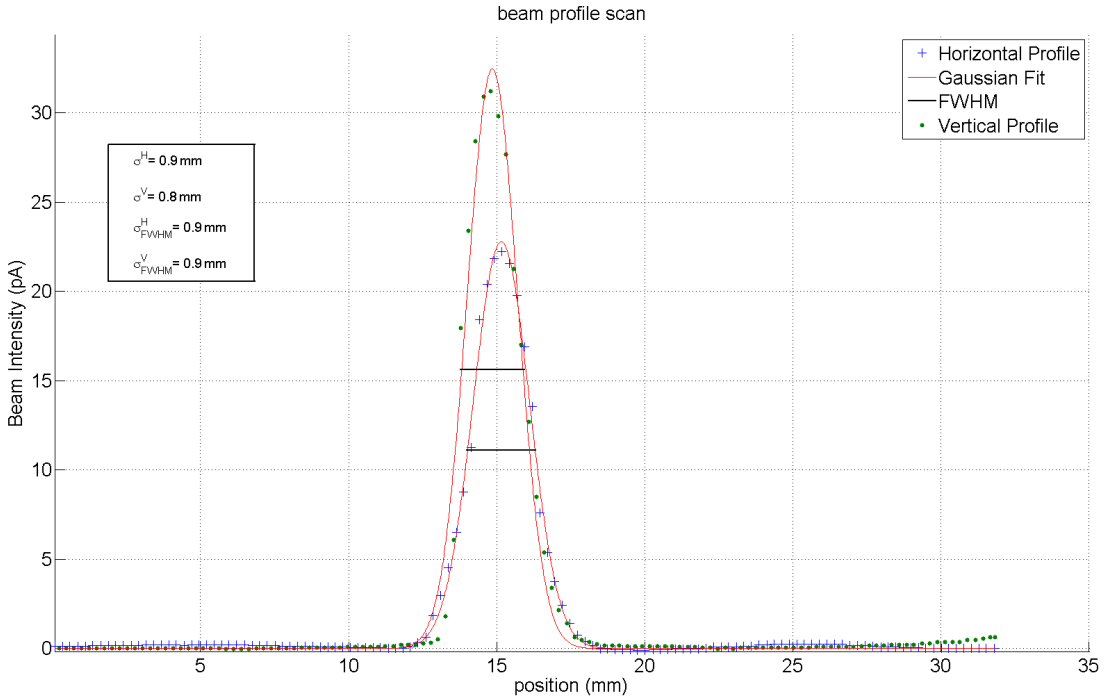

Figure 4.13: Horizontal and Vertical beam profiles of a REX pilot beam at 360 pA.

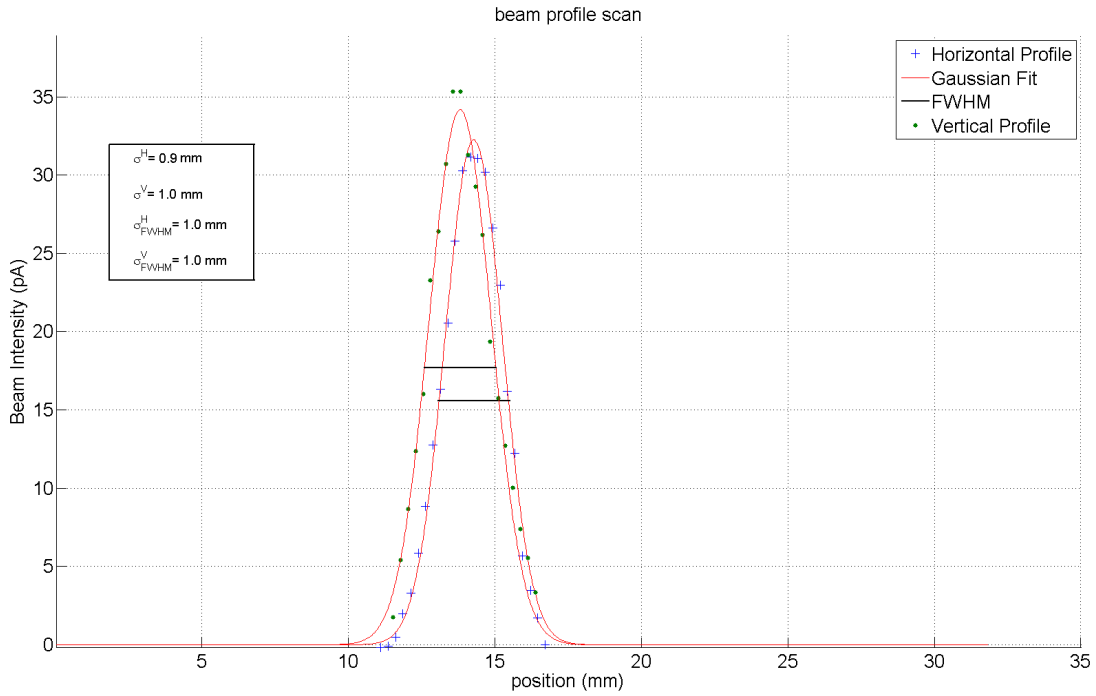

Figure 4.14: Horizontal and Vertical beam profiles of a REX pilot beam at 540 pA.

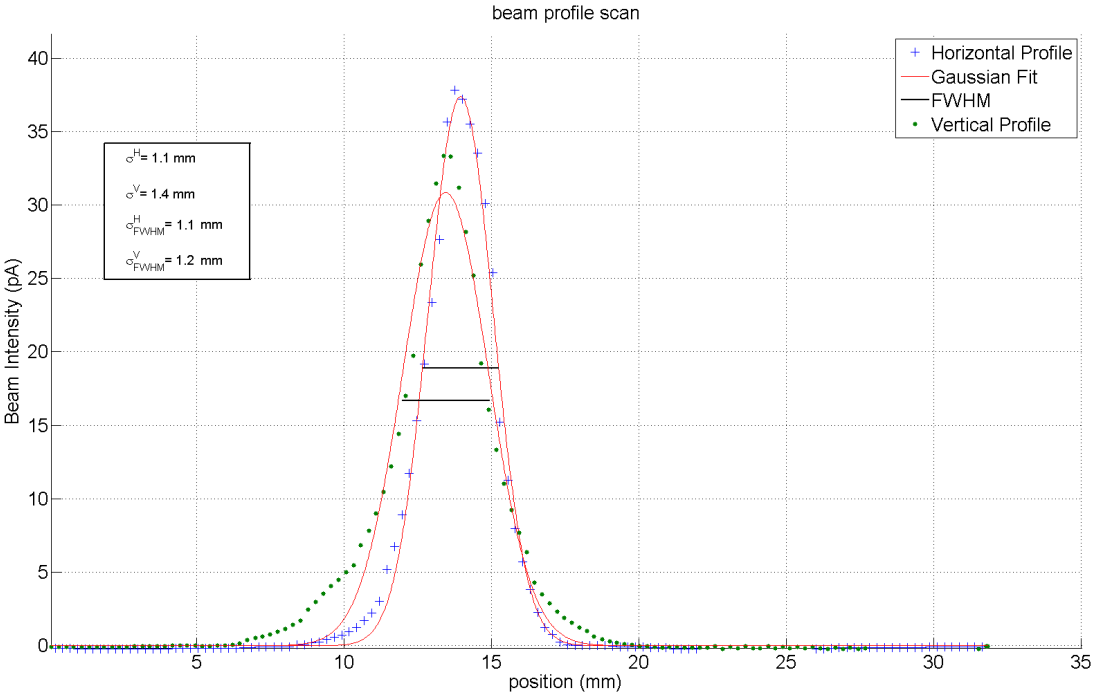

Figure 4.15: Horizontal and Vertical beam profiles of a REX pilot beam at 710 pA. Notice the stronger tails at this high current.

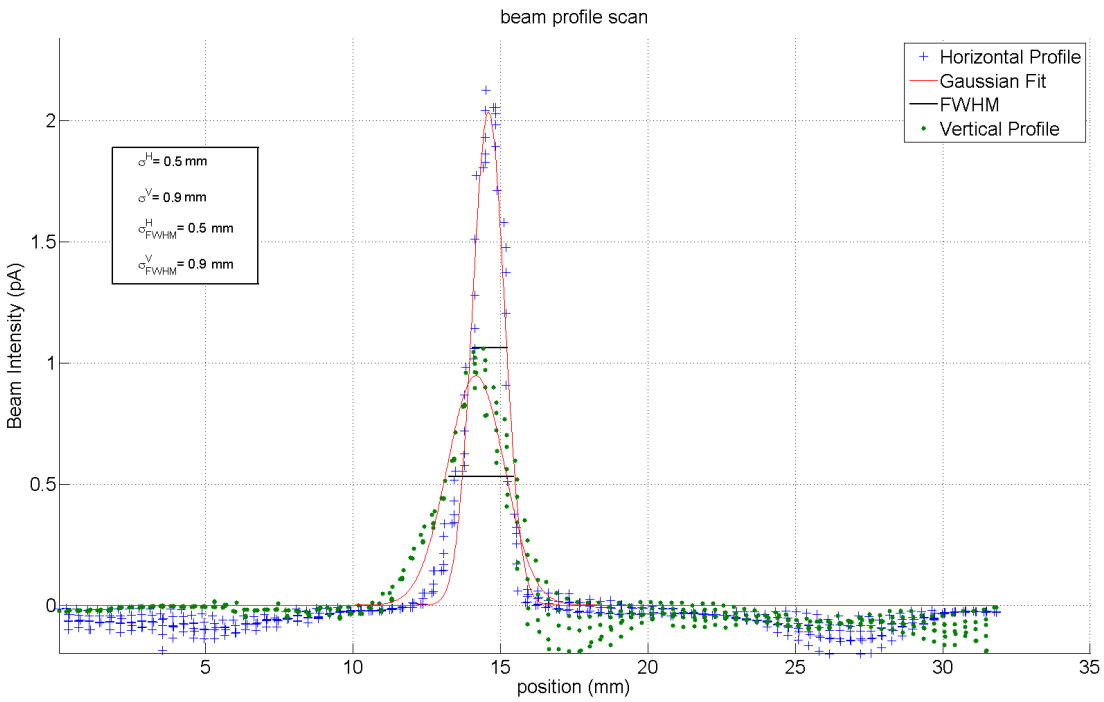

Figure 4.16: Horizontal and Vertical beam profiles of a REX pilot beam at 17.8 pA taken with 0.5 mm steps and 1 second pause in between.

between steps for a better current readout in each step. The range of the picoammeter was set to 20 pA. Fig. 4.16 shows that the signal-to-noise ratio was sufficient to measure transverse beam profiles even at this extremely low beam intensity.

4.5 Prototype 3

This prototype, as shown in Fig. 4.3, has a 1 mm flat aluminium collector electrode and a 12 mm long repeller ring spaced only 1 mm apart. Its aperture is 30 mm in diameter. According to results from the electrostatic simulations done in CST, Fig. 4.17 shows that this extended repeller ring allows for a minimum voltage in the beam axis of -37 V when biasing the ring at -60 V.

4.5.1 Experimental Setup and Results

Using ion beams from the ISAC-II facility at TRIUMF, as REX-ISOLDE was in a long shutdown period in 2013, the REX and Prototype 3 FCs were tested to compare and characterize their performance. The beam energies used were E/A= 1.5, 2.87 and 5.5 MeV/u, with beam intensities in the range of 100 - 4,000 pA. Different ion beams were successfully delivered from the Off-Line Ion Source (OLIS) [91] including $^{34}S^{7+}$, $^{4}He^{+}$ and $^{20}Ne^{5+}$. The beam species used in these tests along with their beam energies and

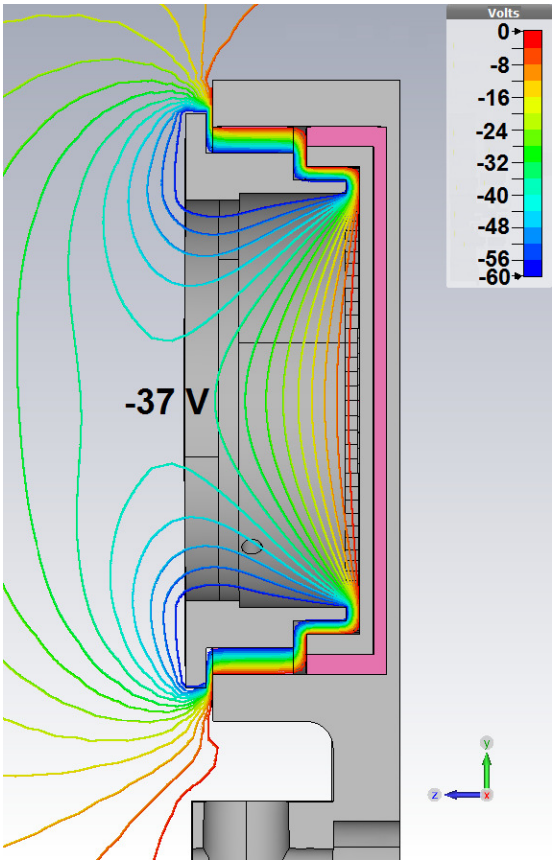

Figure 4.17: Electrostatic potential distribution in the third prototype of the HIE Short FC.

Table 4.4: Beam species with energies per nucleon and intensities delivered to the FCs at ISAC-II in TRIUMF for tests.

Species	E/A (MeV/u)	I_{beam}(pA)	Notes
$^{34}S^{+7}$	5.5	5, 230, 4000	Surface produced
$^{4}He^{+}$	1.5, 2.87, 5.45	117, 350, 400, 3000	
$^{20}Ne^{+5}$	1.5, 2.87, 5.5	210, 500, 700, 1100, 1200, 2500	

intensities are summarized in Table 4.4.

On 08/August/2013, the cups tested were the REX-ISOLDE Faraday cup and Prototype 3 using a beam of $^{34}S^{7+}$. Since this particular beam showed large fluctuations in intensity over a few minutes, and the hall probe of one of the dipole magnets was not working properly, causing difficulties delivering the beam to the diagnostics station, data acquired during this beam run were unsatisfactory and unreliable. However, familiarization with the ISAC-II machine, control displays and other troubleshooting was highly valuable for further tests. As there was a hardware limitation on the bias voltage that can be applied to the FCs between -60 and -350 V, a NIM HV power supply module was used to manually bias the FCs to voltages lower than -60 V.

On 23/August/2013, the REX and Prototype 3 FCs were tested using a beam of $^{4}He^{+}$. In order to determine possible systematic errors in the measurements coming either from the signal processing modules or from leakage currents flowing between the bias ring and the collector, the readout of the cups without beam, or $I_{\text{no beam}}$, was registered. No dependence on $I_{\text{no beam}}$ with voltages between 0 and -350 V was observed, therefore the influence of leakage currents was neglected. The beam intensity values measured without beam, the offset, were determined and subtracted from the data measured with beam. In all cases, the offset was lower than 0.5% of the measured beam intensity values.

In Fig. 4.18 the beam intensity measured by Prototype 3 is plotted as a function of the voltage in its bias ring, for different beam energies. it can be seen that the readout from Prototype 3 agrees very well with that of the REX FC, which is 42 mm longer in total. The same normalization as above was applied in these tests, so the current measured by the REX FC at -60 V is the reference value normalizing the plot. The signal from Prototype 3 reaches a plateau fairly quickly and between -60 and -350 V these FCs measure practically the same beam current for all energies.

On 14/September/2013, the REX and Prototype 3 FCs were tested with a $^{20}Ne^{5+}$ beam with energies of 1.5, 2.87 and 5.5 MeV/u. $^{20}Ne^{5+}$ is a very good isotope for tests since it is the main component of the pilot beam used at ISOLDE for beam tuning and

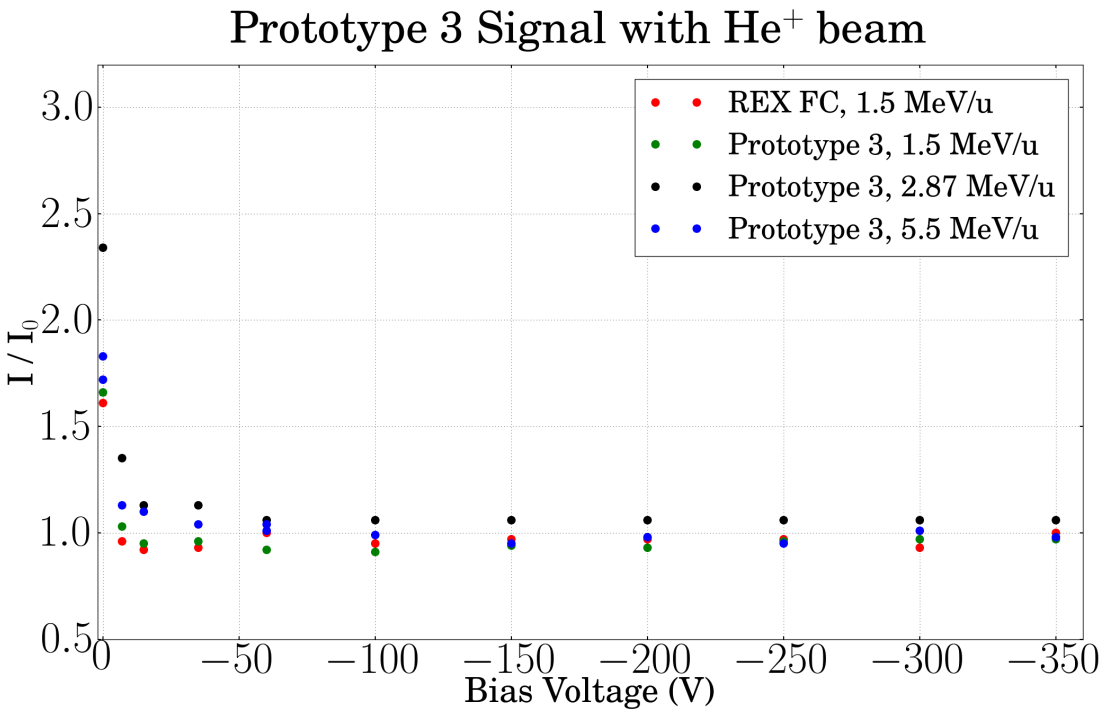

Figure 4.18: Prototype 3 normalized beam intensity as a function of bias voltage for different beam energies.

is therefore the most important test to validate Prototype 3. The same behaviour can be seen using the $^{20}Ne^{5+}$ beam at the same energies per nucleon, as shown in Fig. 4.19.

For bias ring voltages between -60 and -350 V, the beam intensity measured by the cups remains constant, indicating an efficient capture of the ions in the particle beam as well as secondary electrons. No evident performance differences were observed among the two FCs. This behaviour was observed for all beam energies and intensities.

Instability of beam current in these tests depended heavily on the isotope and type of beam delivered from OLIS and also the SC cavities of ISAC-II had an effect on current stability, maybe due to small RF phase variations in the cavities of the ISAC-II LINAC.

The beam intensity values measured by the REX and Prototype 3 FCs consistently agree with respect to one another with a ±10% deviation using $^{34}S^{7+}$, $^{4}He^{+}$ and $^{20}Ne^{+5}$ beams at energies ranging from 1.5 to 5.5 MeV/u. Although the geometric design of the Prototype 3 FC is different to what is used in standard cups, this difference did not influence the results significantly in these tests. In particular, the performance of Prototype 3 FC is consistent in all the tests mentioned above. These results are attributed to an extended repeller ring in Prototype 3 compared to Prototype 1, which greatly increases the electrostatic barrier in the central axis of the FC, thus containing effectively the secondary electrons.

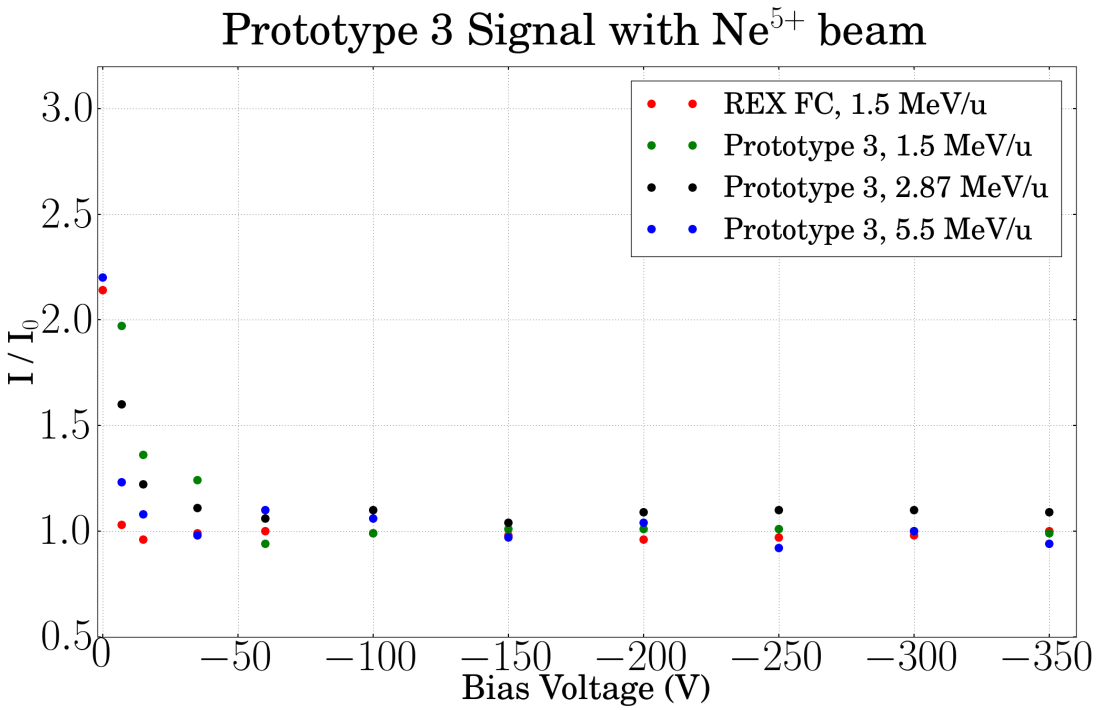

Figure 4.19: Prototype 3 normalized beam intensity vs bias voltage for different beam energies.

It would be interesting to characterize in future works the response of these FCs in an extended energy range (0.3 MeV/u < E/A < 10 MeV/u) in order to fully study the range of projectiles and energies that will be present at the ISOLDE facility once the HIE-ISOLDE upgrade is complete.

4.6 Particle Tracking Simulations

Particle tracking simulations using CST were run to study the probability of losing electrons on the different Faraday cup prototypes when electron emission occurs at different repeller voltages, electron energies and electron emission angles from a beam-sized surface centred on the collector electrode.

Electron loss probability was defined as the percentage of secondary electrons escaping the collector electrode over the total amount of secondary electrons emitted from the collector surface. In all simulations, 10^4 electrons were emitted simultaneously from a circular surface source of 3 mm in diameter facing the aperture of the Faraday cup and placed on the centre of the collector, which is precisely a critical area for the escape of electrons. In CST Particle Studio it is not possible to simulate ion-induced electron emission, hence the use of the electron source in the cup.

The electron collection probability ξ of a Faraday cup in these simulations can be written as

$$\xi = \frac{H - N - S}{N} \times 100, \tag{4.5}$$

with H the total number of electron hits in the cup's collector, N the number of electrons emitted from the source and S the number of secondary electrons produced in the simulation. From that, the electron loss probability η is simply

$$\eta = 1 - \xi. \tag{4.6}$$

the electron loss probability values for each Faraday cup prototype were obtained by counting the number of electrons that do not return to the collector electrode and dividing this by the total number of electrons emitted. This was performed for different configurations, sweeping the electron emission energy from 0 to 500 eV and the repeller ring voltage from 0 to -500 V for three electron emission angle cones of 0°, 45° and 90° with respect to the surface normal. Electrons are emitted in random angles within that cone in an isotropic fashion.

4.6.1 Prototype 1

In the case of Prototype 1, as shown in the top plot of Fig. 4.20, for secondary electrons with an emission angle cone of 0° and emission energies below 10 eV, secondary electrons are efficiently captured with bias voltages >-50 V. However, for emission energies above 60 eV, the loss probability is 100% regardless of bias voltage in the repeller ring, for the voltage range considered. This means that no electrons are captured in these conditions. The loss probability is very sensitive to bias voltage, decaying rapidly to 0% for emission energies below 60 eV. This is directly related to the ability of the secondary electrons to surpass the potential barrier in the centre of the cup for a given kinetic energy. For instance, the potential barrier in the centre of this cup biasing the repeller at -200 V reaches -16.5 V. This value represents an electrostatic barrier close to matching the kinetic energy of secondary electrons with an energy of 20 eV. Hence increasing the bias voltage a little over -200 V rapidly decreases the loss probability, as the electrostatic barrier is insurmountable for secondary electrons with a kinetic energy of 20 eV.

With an emission angle cone of 45°, secondary electrons are emitted anisotropically inside that emission cone. The central plot in Fig. 4.20 shows a similar behaviour than the plot on top, but with a more spread sensitivity to bias voltage.

On the bottom plot of Fig. 4.20, secondary electrons emitted in this prototype with an emission angle cone of 90° show the same pattern as above, but in this case the loss

probability decreases more gradually with bias voltage. For electrons with a kinetic energy of 20 eV, some 70% are lost with a bias voltage of -100 V, while only 10% are lost at a voltage of -200 V. The normal component of the electrons velocity is relevant for their escape. Therefore the larger their angle of emission with respect to the central axis, the lower the loss probability will be for that particular electron, as a result of a smaller normal component of the electron's velocity. Notice that the area of the three plots with 0% loss probability does not appear to be affected by the electron emission angle.

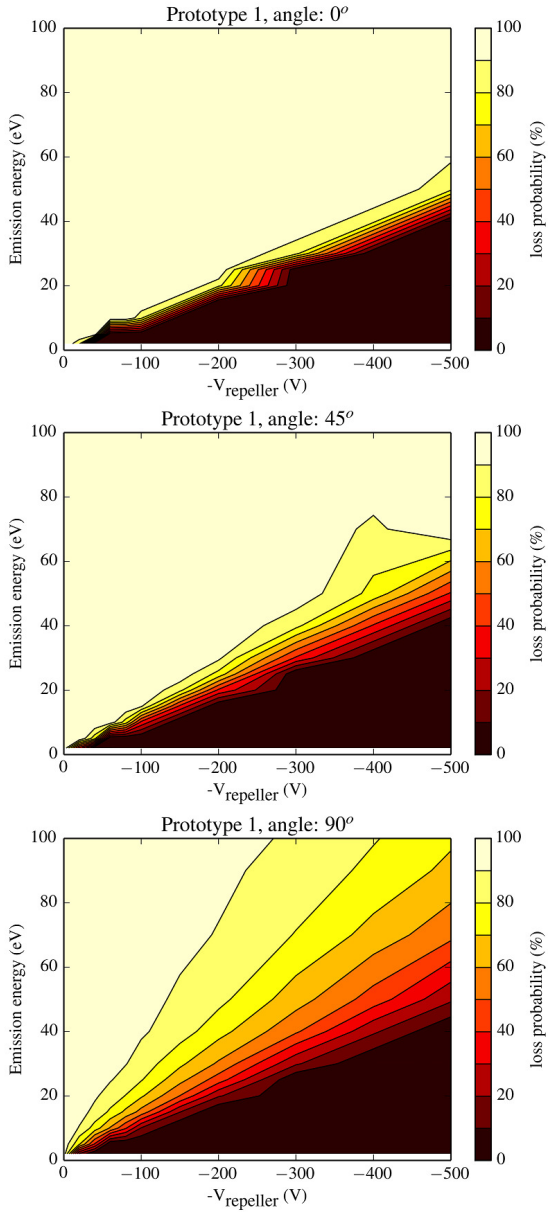

Figure 4.20: Electron loss probability of Prototype 1 at different emission energies, repeller ring voltages and maximum emission angle cones of 0°, 45° and 90°.

4.6.2 Prototype 2

The design of Prototype 2 represents a major improvement in the capture of secondary electrons in the collector. As shown in Fig. 4.21, all electrons emitted at 20 eV would be captured in the collector at voltages >-100 V for all emission angles. The vertical axis is now plotted from 0 to 500 eV to better appreciate the variations in loss probability for this Faraday cup.

For an emission angle cone of 0°, see top plot of Fig. 4.21, with this design of Faraday cup all electrons emitted with a kinetic energy ≥300 eV are lost regardless of bias voltage, in the voltage range considered. With this angle of emission, exactly as in the previous prototype, the electron loss probability appears to be very sensitive to bias voltage, changing from 100% or total loss of electrons to 0% or total capture within a variation of 100 V or less to the repeller ring voltage.

In the case of a 45° emission angle cone, the variation in electron loss probability from 100% to 0% becomes more gradual as the emission energy increases. The bumps that appear in the case of a 0% emission angle no longer appear in this plot. These bumps are attributed to secondary emission in other metal parts of the Faraday cup when the initial electrons are repelled towards the collector at a certain voltage threshold depending on emission energy. In this 45° emission angle the bumps are smoothed and hidden because not all secondary electrons are emitted perpendicular to the collector's surface.

In the case of a 90° emission angle, distortions in the general behaviour may be due to secondary electron emission in other metal parts of the FC such as the repeller ring. This increases the variable S in equation 4.5, which increases the electron collection probability ξ. As a result, the loss probability η is lowered.

4.6.3 Prototype 3

The simulation results for Prototype 3, shown in Fig. 4.22, indicate an improved electron collection probability at lower voltages compared to Prototype 2, for all emission angle cones. The design of Prototype 3 also shows 0% loss probability when biasing the repeller ring at -500 V in the case of electrons with an emission energy up to 300 eV.

In the case of an emission angle cone of 45°, see the central plot in Fig. 4.22, as occurs in previous prototypes, the variation of loss probability is more gradual than with a 0° angle cone, increasing with the emission energy of the electrons.

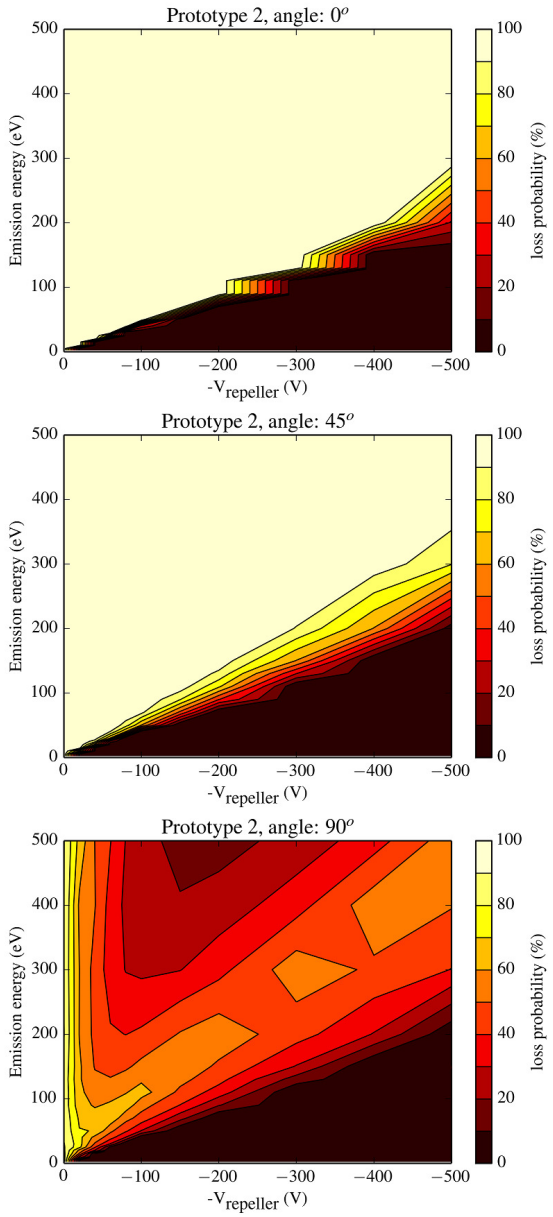

Figure 4.21: Electron loss probability of Prototype 2 at different emission energies, repeller ring voltages and maximum emission angles of 0°, 45° and 90°.

With an emission angle cone of 90°, Prototype 3 shows a very similar behaviour to Prototype 2, but with an increased area of 0% loss probability. Moreover, the area representing 100% loss probability for Prototypes 2 and 3 at this emission cone is severely reduced compared to other emission cones. The "valley" that appears in the plots of 90° emission cones for Prototypes 2 and 3 represent an area where electrons have roughly the same kinetic energy as the electrostatic barrier, and therefore approximately half of them escape and the other half return to the collector, depending on their initial angle of emission and point of origin in the collector.

Prototype 3 has a 12 mm long repeller ring and covers the full 30 mm beam aperture. The thickness of the collector electrode, insulator and back of the FC body is 1 mm. As shown in Fig. 4.17, biasing the repeller ring at -60 V results in a voltage in the cup's centre of -37 V, well beyond the typical energy peak of ion-induced secondary electron emission, which is <20 eV [92]. Of course, the energy of the secondary electrons emitted does not follow a uniform distribution, and the shape of this energy spectrum is the most important unknown in order to quantify exactly how many secondary electrons escape or are captured in the Faraday cup.

Having computed the values of η for those ranges of electron emission energy, repeller voltage and emission cones, one would like to translate those into intensity measured by the Faraday cup to compare with the experimental data.

Beam intensity can be expressed as

$$I_{beam} = \frac{dN_i}{dt} \cdot Z^+ \cdot e, \tag{4.7}$$

with N_i the number of ions that arrive at the Faraday cup during the time t, Z^+ the charge state of the ion and e the elementary electric charge. As γ is the electron yield per incident ion, the beam intensity measured by the Faraday cup is

$$I_{FC} = \frac{dN_i}{dt} \cdot Z^+ \cdot e - \frac{dN_i}{dt} \cdot \gamma \cdot e \cdot \xi, \tag{4.8}$$

therefore the ratio between the intensity measured by the FC and the real intensity is

$$\frac{I_{FC}}{I_{beam}} = 1 - \frac{\gamma}{Z^+} \cdot \xi. \tag{4.9}$$

However, knowing precisely the total ion-induced electron emission for this particular target-projectile combination at the beam energies available in REX is not straightforward. Very few studies exist about ion-induced electron emission for this particular projectile-target combination and energy range. A previous study suggests that ion-induced electrons are emitted inside an escape cone with a maximum angle

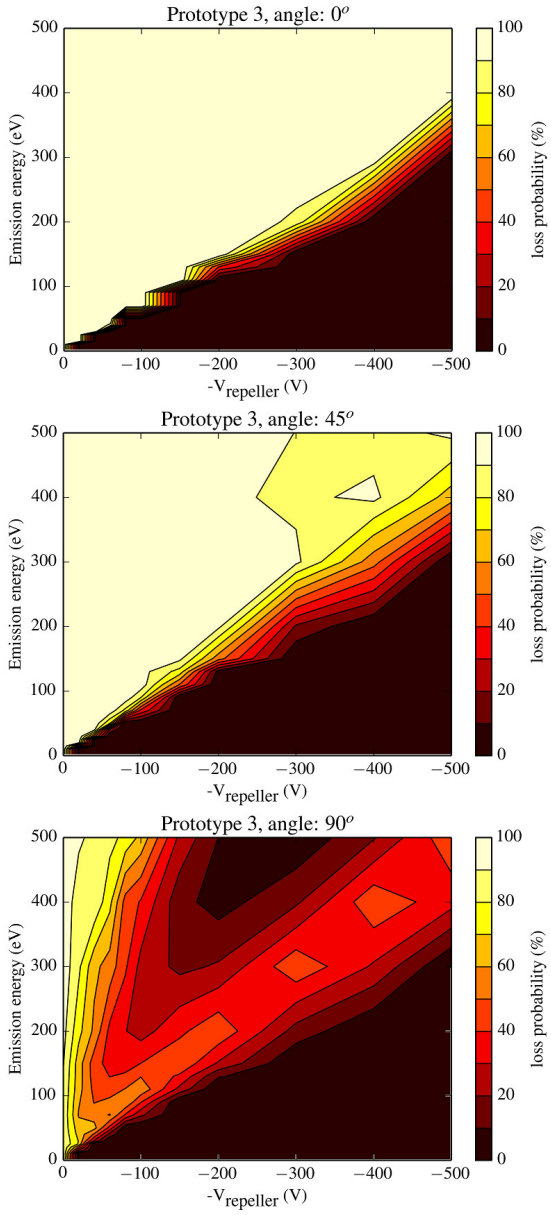

Figure 4.22: Loss probability of Prototype 3 at different emission energies, repeller ring voltages and maximum emission angles of 0°, 45° and 90°.

$\theta^{\max}$ with respect to the surface normal [93]

$$\cos\theta^{\max} = \sqrt{\frac{W}{E_i}} \quad (E_i \geq W), \tag{4.10}$$

with E_i the electron energy and W the energy barrier height which can be written for metal conductors as

$$W = E_F + e_0\phi, \tag{4.11}$$

with E_F the Fermi energy and $e_0\phi$ the metal's work function and the surface potential ϕ [93].

About the shape of the energy emission spectra, it is common to find a broad peak at very low energies, of a few eV, and then the yield falls off towards higher electron energies. For illustration, Fig. 4.23 shows the case of an aluminium target bombarded with ions at 0.5 MeV [94].

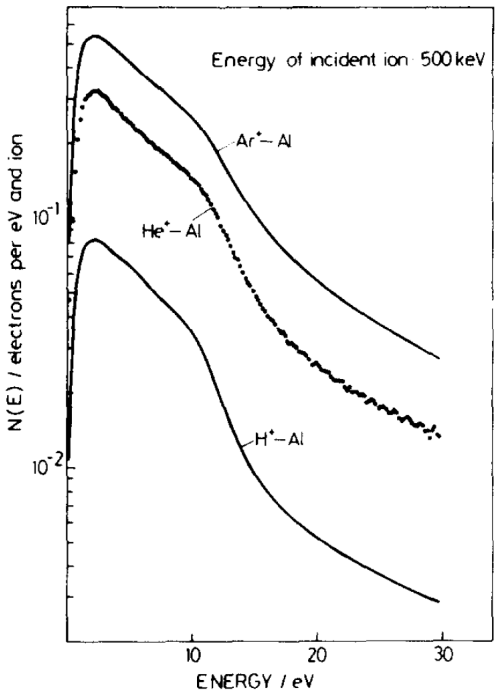

Figure 4.23: The energy distribution curves for impact of H^+, He^+ and Ar^+ at 0.5 MeV. The original data points are displayed for He^+ impact. Image taken from [94].

Taking all of this into account, it is difficult to quantify how many electrons are escaping the Faraday cups, and what their emission energies are exactly. A complete theoretical model that explains how ion-induced electrons are emitted for this particular projectile-target combination and energy range is missing in order to fully explain the differences in beam intensity measured by the prototype cups and the REX cup observed at a voltage between -60 and -500 V in the experimental plots of normalized

intensity of Figs. 4.7 and 4.9.

4.7 Chapter Summary

A compact Faraday cup has been developed at CERN to measure low-energy, low-intensity ion beams and, when used together with the slit scanner, it is able to measure transverse beam profile and beam position. This is the main beam instrumentation system for the HIE-ISOLDE project. An extension of the repeller ring in the longitudinal direction from 1.5 to 12 mm has shown to eliminate the loss of secondary electrons from the Faraday cup even for relatively low bias voltages of around -60 V. All prototypes discussed in this chapter have been built and tested using ion beams with a mass-to-charge ratio $A/q \leq 4.5$. The minimum beam intensity measured by a FC is related to the sensitivity of the ammeter it is connected to, which in our case it was around 50 fA, while the level of electronic noise observed was $\leq$0.7 pA peak-to-peak. Error bars were not included in the data analysis since the systematic error produced by the fluctuating nominal beam intensity of the LINACs was significantly larger than the statistical error produced by the picoammeter, the measurement instrument.

The outcome of the research effort on the short Faraday cup prototype for HIE-ISOLDE can be summarized as an improvement in the beam current readout matching the readout of other standard FCs used regularly at ion facilities within 10% on average at different beam intensities and energy ranges of the LINACs. The development of the Prototype 3 Faraday cup involved several experimental tests with ion beams as well as numerical simulations in order to satisfy the challenging space requirements of the HIE-ISOLDE superconducting LINAC and its wide variety of ion beams. The Faraday cup is the keystone of the beam diagnostics system of HIE-ISOLDE in order for operators and users to monitor the beam.

Chapter 5

PIPS Detector

In this chapter the working principle of PIPS detectors is detailed along with a summary of the main parameters that limit their performance. The different types of silicon detectors used in this work and their technical specifications are described, as well as a description of the data acquisition electronics for energy and timing measurements. Experimental tests with two PIPS detectors were performed with the aim to acquire an absolute time of flight measurement in REX-ISOLDE. Energy spectroscopy and timing measurements for the stable beams of REX-ISOLDE obtained with Si detectors are presented in this chapter. By using an alpha source as a calibration reference, the absolute beam energy of the ions in the pilot beam with a mass-to-charge ratio of $A/q = 4$ was measured in the energy range 1 MeV $< E <$ 8 MeV. The ToF of the particles in the beam at an energy range of 2.18 MeV/u $< E/A <$ 2.27 MeV/u was determined by time stamping the arrival time in identical Si detectors in two diagnostic boxes separated by 7.7 m. The results obtained with these two techniques are compared with the values obtained using a spectrometer magnet .

5.1 Motivation

The longitudinal beam profiles, i.e. the energy spread and bunch length are essential parameters to be measured at REX in order for the operators to accelerate the beam efficiently through the different accelerating structures and deliver beam to the experiments. The beam energy in HIE-REX ranges from 0.3 to 10 MeV/u. An absolute energy measurement would allow operators to efficiently deliver beam to the users. In a LINAC, acceleration of the beam in the MeV range is done with RF resonant cavities. The phase of the RF power fed to each cavity is set to make sure the beam is efficiently accelerated in a stable way. The standard procedure of tuning the RF phase relies on relative measurements of the average beam energy downstream of the cavity. The synchronous RF phase is set relative to the RF phase at which the average beam energy is maximized by tracking its sinusoidal modulation as a function of RF phase

[72]. Measuring the relative beam energy is therefore important for the HIE-REX superconducting LINAC.

At REX, absolute beam energy was measured using the XBEN.MD120 bending magnet at the end of the LINAC as a spectrometer, see Fig. 2.1. This was done using two vertical slits, one upstream and one downstream of the dipole, and a Faraday cup at the exit of the dipole. With this technique, the average beam energy is measured using the dispersion developed in the spectrometer magnet, which is calibrated taking the nominal output beam energy from the RFQ, which is 0.3 MeV/u$\pm$1.5 % FWHM. The beam intensity measured by the Faraday cup is recorded as a function of the magnetic field in the spectrometer magnet. The change in dipole field is approximately proportional to the change in beam energy. Such a procedure is robust and reliable but it is time consuming, as it takes more than 5 minutes to do a magnetic field scan because the intensity must be changed gradually. The number of cavities used to post-accelerate ions at ISOLDE will increase from 5 to 34 with the HIE-ISOLDE upgrade, motivating the development of a faster, and eventually automated, solution for tuning the phases of the superconducting cavities. Absolute energy measurements can also be achieved with a ToF detection system. For this purpose, solid-state detectors, namely PIPS detectors were tested. They were installed in diagnostic boxes downstream of the LINAC.

Usage of PIPS detectors for beam diagnostics purposes has already been studied in view of using them after the last HIE-ISOLDE superconducting cryomodule. The experimental set-up, data acquisition and analysis of the present work is based on [71, 72]. There are however two main new contributions with respect to the previous work:

- The channels to energy conversion scale used for energy spectroscopy was obtained using a calibration source as a reference which emitted alpha particles at four different energies. Hence the absolute energy of the projectiles could be measured and compared to the results from the spectrometer magnet.

- The time of arrival of the particles with respect to the master-clock of the cavities RF system was measured at two different locations (DB4 and DB5) with the aim of obtaining an absolute ToF measurement.

Timing measurements are also important, as ToF can be used to derive the absolute beam energy, provided the distance between detectors is known with the required accuracy. In addition, the knowledge of the time structure of the beam during transmission and delivery is important for the operation of the machine. The timing resolution of

the ToF system is <200 ps, corresponding to an energy resolution better than 1%, according to previous tests [71, 72].

5.2 Principle of Operation

When a particle impinges in the detector medium, it deposits energy until it is stopped and electron-hole pairs are created in this process. The average energy necessary in order to create an electron-hole pair in silicon is around 3.6 eV [95], therefore assuming a $^{20}Ne^{5+}$ ion at 2 MeV/u, this would create around 1.1×10^7 electron-hole pairs per ion. These charges can then be collected and measured by means of an electric field applied between two electrodes on the opposite faces of the material layer.

At the PN junction of the silicon, due to the electron-hole diffusion on each side of the semiconductor material, a depletion layer free of carriers is created. By biasing the detector with a reverse bias this depleted region is widened, and this forms the sensitive volume of the detector [96]. Free electrons in the detector created by charged particles traversing the material are collected by one of the electrodes. As a consequence, integrating the charged collected by the electrodes generates an electric pulse in the circuit connected to the detector. Fabrication details of PIPS detectors are shown in Fig. 5.1.

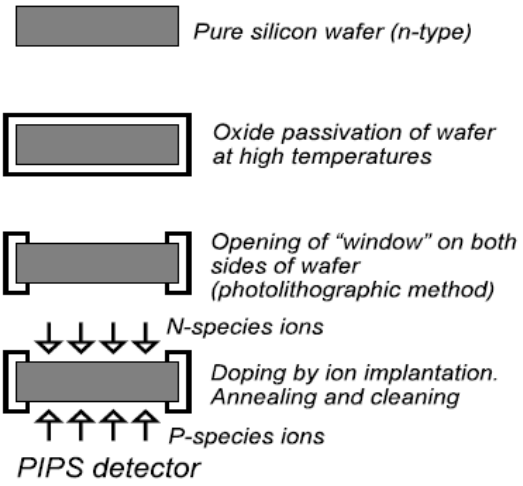

Figure 5.1: Fabrication process of a PIPS detector. Modified image taken from [96].

Electrical contacts to the electrodes are done via standard co-axial connectors, generally BNC or Microdot [97]. The main parameters affecting the performance of this detector are the thickness of the depletion region, the amount of leakage current, its surface area, energy resolution and breakdown voltage [96].

The thickness of the depletion layer free of carriers is dependent on the bias voltage applied and the resistivity of the detector material, which in turn depends on the concentration of dopants. The need for a thick depletion layer or large sensitive volume, in our case, is not due to the range of the ions in the detector. A thick depletion layer is needed because the two electrodes create a parasitic capacitance over the layer. Therefore the thicker the sensitive volume, the smaller the capacitance value and the less electronic noise will be produced by the detector. The quoted capacitance for this detector is 29 pF [97].

Silicon detectors have small leakage currents, typically between 1 and 10 nA/cm^2 for PIPS detectors [96]. Leakage currents are a source of electronic noise, and should be minimized in a high-performance detector.

The surface area of the sensitive volume of the PIPS that is exposed to the particle beam affects performance in a positive and a negative aspect. A large surface area allows for a higher counting efficiency. However, a large area also means a large parasitic capacitance value, which reduces the resolution. PIPS detectors with surface areas of 25 mm^2, or 5.6 mm diameter, and 50 mm^2, or 8 mm diameter were tested in REX-ISOLDE.

Energy resolution in a PIPS is determined mainly by the active area, capacitance and leakage current of the detector, by the statistical nature of the conversion of radiation energy into electrical charge, by the charge collection process itself and by the noise in the electronic components. The energy resolution for the partially depleted detectors used in REX-ISOLDE is 11 keV in Full Width at Half Maximum (FWHM) [97].

The breakdown voltage refers to the maximum reverse bias that can be applied to the PIPS detector. A high bias voltage is preferred as it maximizes the thickness of the depletion layer and ensures an optimal collection of charge carriers. Nevertheless, reaching the breakdown voltage value incurs in the risk of destroying the detector. If resolution is not of high concern, the PIPS detector should be operated at the recommended bias voltage or below. Typical operating voltages are 40 V for 100 μm, 60 V for 300 μm, 100 V for 500 μm and 350 V for 1000 μm thick detectors.

5.3 Technical Considerations

Two types of PIPS detectors have been tested in this PhD thesis. The first one is the Partially Depleted (PD) PIPS, which is widely used in α-spectroscopy. The second

detector is a modified PD detector dubbed Timing (TM) PIPS, with better timing performance thanks to an increased (20 nm) aluminium front electrode layer. This increased conductive layer has a negative impact on energy resolution of about 4 keV in FWHM [97] as more beam energy is deposited in this dead layer. Time resolutions of the order of 140 ps (FWHM) can be achieved by this detector [97]. The energy resolutions of different PIPS detector types are presented in Table 5.1.

Table 5.1: Performance of Partially Depleted PIPS detectors according to area and thickness.

Thickness	100 μm		300 μm		500 μm	
Resolution keV (FWHM)	Active Area: 25 mm^2	50 mm^2	25 mm^2	50 mm^2	25 mm^2	50 mm^2
α	12	12	11	11	10	11
β	6	6	5	5	4	5

Since single particles produce measurable electrical pulses, this kind of detector can be used for particle counting. Every event can be recorded and in this way very low currents (a few pps) can be measured. The count rate needs to be sufficiently low (kHz level) to avoid detector damage and the occurrence of multiple events (pile-up).

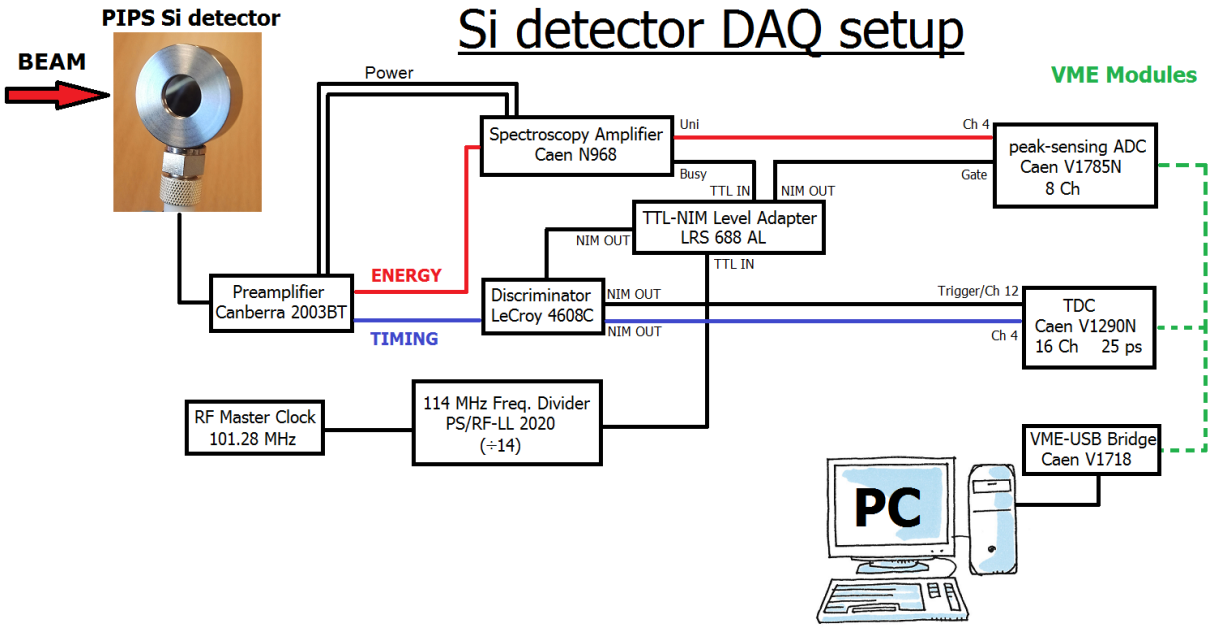

Figure 5.2: Silicon detector data acquisition set-up.

5.4 Data Acquisition Electronics

The data acquisition electronics for the silicon detector used in this experiment is depicted in Fig. 5.2. The voltage bias for both detectors was supplied by a Mesytec MHV-4 power supply. The silicon detector is connected to the preamplifier through a vacuum compatible, 30 cm, 93 Ωm BNC to Microdot Male-Male coaxial cable (Ref. CA 30 - BNC-M / M-M).

In a first step, the electric charge generated by an impinging particle is integrated by a charge-sensitive preamplifier, model Canberra 2003BT with a charge-sensitivity of 0.45 V/pC and converted into an output potential. This translates to a scale of 20 mV/MeV for silicon detectors at room temperature. The noise contribution of the preamplifier is 2 keV FWHM. Any capacitance added to the input of the preamplifier will further increase the electronic noise and degrade the energy resolution of the detection system. The capacitance is best reduced by using a cable as short as possible between the detector and preamplifier. The circuit schematic of the preamplifier is shown in Fig. 5.3. The first stage acts as an operational integrator which produces an output potential proportional to the integrated charge on the capacitor C. The timing output is derived from the integrator error signal through a pulse shaping network.

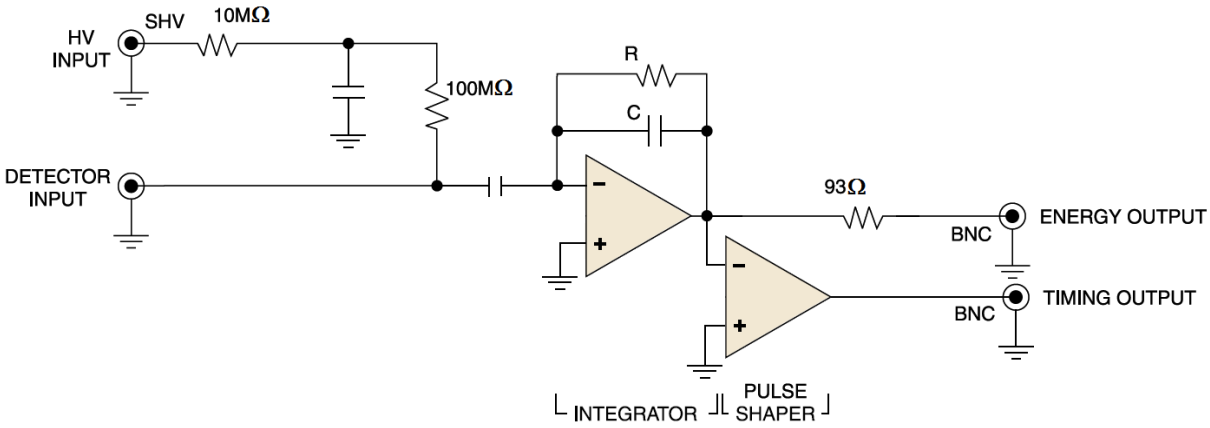

Figure 5.3: Circuit of the 2003BT charge-sensitive preamplifier. Modified image taken from [97]

The energy output signal is a positive exponential pulse with a fast rise time (t_r <12 ns at C_{det}= 0 pF) and a 250 μs exponential decay constant [72]. The Caen N968 spectroscopy amplifier acts as a shaper for the energy signal, reducing its long decay tail in order to avoid pile-up detection, see Fig. 5.4. The pulse is converted from an exponential to a Gaussian of 0.5 to 10 μs width suitable for single-particle counting. The time constant of the pulse-shaping filter in the amplifier, which is the shaping time, can be selected from 0.5, 1, 2, 3, 6 and 10 μs. Then the amplifier output is processed

by a Caen V1785N peak-sensing ADC for pulse-height analysis and acquisition of the energy spectra.

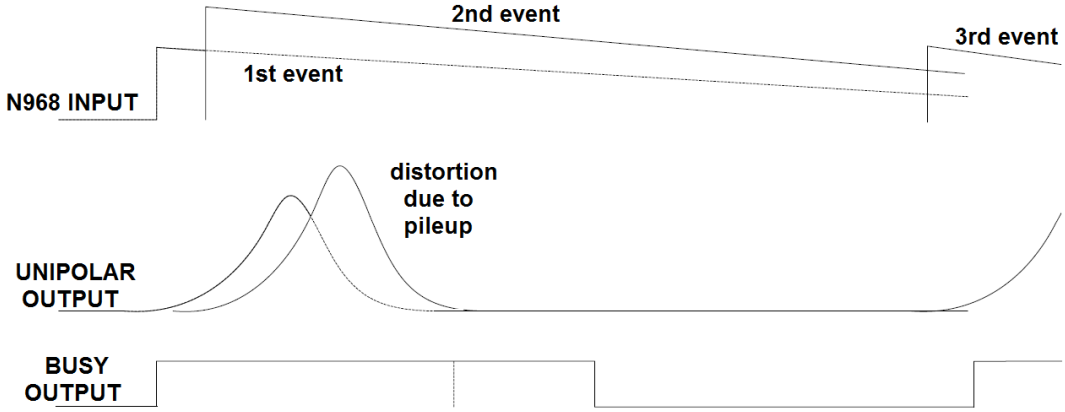

Figure 5.4: From top to bottom: Energy output of the 2003BT preamplifier, output of the N968 Spectroscopy Amplifier and busy output. Modified image taken from [98].

The timing output is a negative rectangular pulse of constant amplitude ∼150 mV, and width proportional to the rise time of the energy output with a very short fall time of less than 3 ns [72].

The distribution of the particles' arrival time is measured versus a reference signal obtained from the RF system. The Caen V1290N Time-to-Digital Converter (TDC) was selected for this purpose, as it allows recording the "time stamp" of multiple events. This Versa Module Eurocard bus (VME) board has a time resolution, or Least Significant Bit (LSB) of 25 ps, while the full range is 52 μs. In order to get a timing spectrum of the beam, two channels are active during the time measurements: the particle timing signal and the RF reference signal, see Fig. 5.2. The time stamps of detection events for both channels are acquired and hence the time interval between the particle arrival and the RF reference signal is calculated through a LabVIEW routine [99]. The maximum rate of a periodic signal that can be accepted by one channel without losing hits has been previously estimated around 7 MHz [72]. Therefore the RF frequency of 101.28 MHz is divided by a factor 14 using the frequency divider, characterized by a 114 MHz maximum input frequency. This 7.23 MHz signal synchronized with the RF can be used as a reference in the TDC. In addition to this, the reference signal and the particle signal need to be converted into the NIM standard because of the technical requirements of the TDC input. The timing pulse was adapted using a LeCroy 4608C discriminator, which comprises an adjustable amplitude threshold of -5 mV to 1 V, an adjustable output width from 4.5 ns to >100 ns, rise times and fall times better than 2 ns, and a maximum rate of 150 MHz [100].

In the TDC V1290N, the data acquisition mode can be set to Continuous Storage Mode or to Trigger Matching Mode [72]. In Continuous Storage Mode the data are loaded into the output buffer of the module. When working in Trigger Matching Mode, the TDC organizes the data in "events" with respect to an arbitrary external trigger signal. A time acquisition window is defined with respect to the trigger signal, therefore only the events that are inside this acquisition window are forwarded to the output buffer in a First In First Out (FIFO) readout scheme. The Trigger Matching Mode is suitable in this context because of the pulsed beam at HIE-ISOLDE and the very low average count rate of beam particles necessary for the PIPS, of less than 1 kHz [72].

The structure of the macro pulse of the beam in HIE-ISOLDE is dominated by the low duty cycle of the LINAC, i.e., the ratio of the RF pulse duration to the EBIS period), which has a maximum value of only 10%. Therefore, the continuous storage mode would predominantly acquire the RF reference signal with respect to the measured particle signals, recording empty acquisition windows at times. The most efficient TDC acquisition mode in this particular set-up consists of triggering on the particle signal itself in the so-called Trigger Matching Mode, such that a short acquisition window is set around the detection event to include the divided RF reference signal at the same time. The final timing measurement is obtained off-line in a Matlab or Python routine calculating the time interval between the trailing edges of the detection event and the closest RF reference signal detected before it [72].

It is worthwhile to mention that all the connections related with this time acquisition system have been done with cables of similar length and type for both detectors, in order to avoid the introduction of a differential delay in the arrival time of the signals to the TDC.

5.5 Range of Projectiles in the Detector

Using Stopping and Range of Ions in Matter (SRIM) [86], the range in silicon for different ions available in REX and HIE-REX were compared. The results are summarized in Table 5.2. For ions lighter than ^{12}C above 5.5 MeV/u, the range in silicon exceeds 300 μm therefore a thicker detector would be necessary in that case.

Radial straggling of the ions inside the detector with respect to the point of impact is less than 5 μm in all cases, so this effect is irrelevant in measurements.

Table 5.2: Range of ion species in silicon at characteristic HIE-REX energies as calculated with SRIM.

	Output Energy (MeV/u)					
Ion Species	0.3	1.21	2.21	2.85	5.5	10
^{4}He	4.18 μm	23.13 μm	57.22 μm	86.03 μm	255.31 μm	712.21 μm
^{12}C	3.80 μm	13.98 μm	27.61 μm	37.88 μm	94.63 μm	245.35 μm
^{16}O	3.94 μm	13.25 μm	25.06 μm	33.67 μm	79.29 μm	195.20 μm
^{20}Ne	4.31 μm	13.15 μm	23.52 μm	30.92 μm	69.01 μm	162.89 μm
^{40}Ar	5.30 μm	14.06 μm	23.46 μm	29.88 μm	60.86 μm	130.10 μm
^{238}U	10.69 μm	24.78 μm	35.23 μm	41.20 μm	64.30 μm	103.84 μm

5.6 Radiation Damage

Radiation damage from beam exposure needs to be considered in order to maximize the lifetime of the silicon detector. The radiation damage of the detector is directly related to the integrated dose, which depends on the beam intensity impinging in the detector and the total exposure time. Typical symptoms of radiation damage in a detector are higher leakage current/noise, peak broadening and sometimes double peaks. Estimates of radiation damage in Si detectors quote threshold values for noise increase of 10^{10} protons/cm^2 and 10^9 α-particles/cm^2 [101]. Therefore for a 50 mm^2 PIPS detector bombarded with α-particles at 1 kHz counting rate, we can expect to see damage effects after 555.5 hours of use.

Beam intensity should be reduced as much as possible in order to reduce radiation damage, but the acquisition rate should be high enough in order to acquire data reasonably fast. A common approach used to reduce the beam intensity is to scatter the beam off a tilted gold foil into the the detector located away from the beam axis [102, 103, 104]. Such systems are typically used either where the average beam current is high (mA level) or when the integrated radiation dose gives serious cause for concern for the longevity of the silicon detector. However, such systems result in poor energy resolution caused by the scattering processes. In these tests with the PIPS detectors the ion beam was attenuated with copper foils and directly intercepted. Radiation damage issues are not a high concern at REX and HIE-REX because of the low average beam current of less than 1 nA, due in part to the fact that the maximum duty cycle of the LINAC is only 10%. However, regardless of whether the beam is directly or indirectly detected, or whether the beam is continuous or pulsed, the peak beam intensity must be in the kHz level such that single-particle detection is possible [71].

5.7 Experiments with Ions

5.7.1 Experimental Setup and Results

In January 2013, a beam run for machine development concerning the silicon detector monitor was scheduled at REX-ISOLDE. The aim was to replicate previous measurements [71], but this time with two PIPS detectors in order to obtain an absolute ToF measurement. Both detectors were PIPS of the timing series TMPD50-16-300RM. The detectors were installed in the pneumatic actuators of the beam profiler in diagnostic boxes DB4 inside the LINAC vault and in DB5, upstream of the bending magnet and downstream of the last accelerating cavity of REX in the long drift section of the REX LINAC, see Fig. 2.1. The detectors were separated by a distance of 7,666.8 ±0.5 mm [105]. Canberra 2003BT preamplifiers were directly connected to the feedthrough of each diagnostic box in order to be connected as close as possible to the silicon detectors. From the preamplifiers, basically the same electronics as in previous measurements [71] were kept.

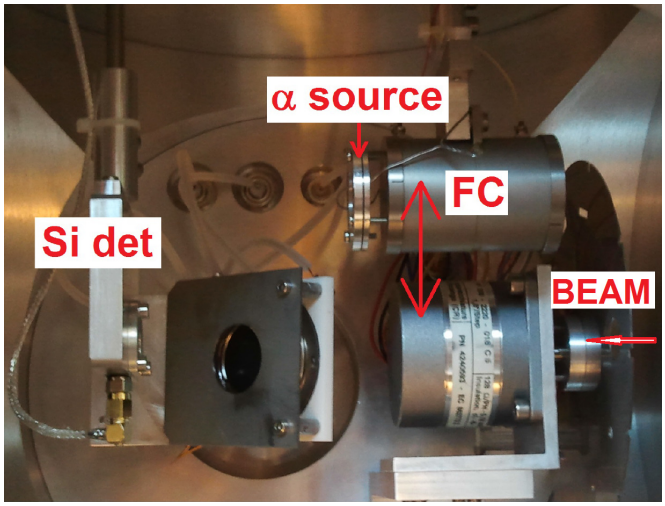

Figure 5.5: Installation of the silicon detector and the α-source in DB5. Using the pneumatic actuator of the FC, the source could be positioned facing the detector.

Energy Spectroscopy

Energy spectroscopy measurements of the REX beam were performed using the energy signal of the 2003BT preamplifier. A radioactive α-source was attached to the back of the Faraday cup in DB5, as shown in Fig. 5.5, such that it was directly facing the silicon detector as long as both devices are IN or OUT of the beam path. The source contains ^{148}Gd, ^{239}Pu, ^{241}Am and ^{244}Cm. The last calibrated activity was 4× 1 kBq. According to [106], these elements emit alpha particles at the energies summarized in Table 5.4. The most intense alpha peaks of these isotopes were used for the calibration

of the channel/energy relation of the ADC Multichannel Analyser (MCA). The channel corresponding to the maximum of each peak was calculated, and the points for the channels/energy relationship enumerated in table 5.3 were obtained. From the data, the following linear relationship between energy and channels for the calibration of the MCA can be obtained:

$$E(keV) = 2.0360 \times \text{Channel} - 74.8 \tag{5.1}$$

Table 5.3: Channels vs Energy for the peaks of the alpha source, obtained from the spectrum of Fig. 5.6.

Channel	$\langle E_\alpha \rangle$ (keV)
1600	3182.7
2569	5156.6
2731	5485.6
2888	5804.8

The calibration of the energy scale of the MCA was done using as reference alpha particles with energies between 3 and 6 MeV. To have a good peak resolution and also to restrict the analysis to the well calibrated region of the MCA scale of 12 bits, or 4096 channels, only projectiles with energies not higher than 8 MeV were considered. Using the stable beam of REX-ISOLDE with a mass-to-charge ratio of A/q = 4, and beam energies of E/A = 0.3 MeV/u and E/A = 1.87 MeV/u, beam was delivered for energy spectroscopy measurements. The energy of the beam was also measured using the bending magnet as a spectrometer, placing two vertical slits 3 mm wide in DB5 and DB7. For the energy measurement using the dipole bending magnet and the Faraday cup in DB7, the stable beam intensity was $\simeq$10 pA.

An initial measurement was done without beam to check the visibility of alphas in the detector and to calibrate the energy scale. The results are shown in Fig. 5.6. The uncertainty in the determination of the channel corresponding to the maximum yield, i.e. the position of the peak in channels, introduced by the fitting procedure depending on the selected function and the achieved convergence is less than one channel. In terms of absolute energy, that value corresponds to roughly 1 keV and therefore is negligible as compared to other possible sources of error measuring the energy of the particles. The energy resolution of the calibration α-source coming from the broadening of the energy peaks due to the energy lost by the alpha nuclei in their path while leaving the source has not been taken into account in this experimental set-up as this is not a high precision energy calibration, nevertheless this value was assumed to be very small in this type of intensity-calibrated α-sources with very well defined energy peaks.

From the Gaussian fitting of the alpha peaks, the obtained energy resolution is

Table 5.4: Alpha particle energies and relative intensities [106] for the isotopes present in the alpha source used.

Source	E_α (keV)	I_α (% branch)
^{148}Gd	3182.68	100
^{239}Pu	5156.59	73.3
	5144.3	15.1
	5105.8	11.5
^{241}Am	5544.5	0.36
	5485.56	85.1
	5442.8	13.3
^{244}Cm	5804.77	76.4
	5762.16	23.6

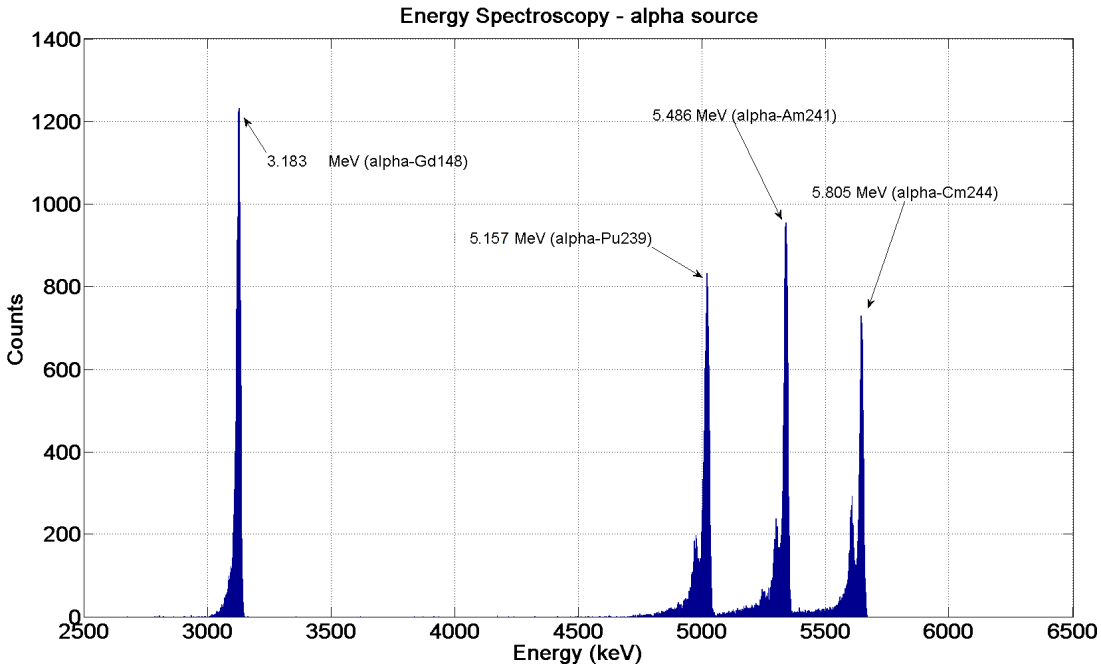

Figure 5.6: Energy spectrum of the α source.

worse than the value quoted by Canberra, of 16 keV FWHM [97], mainly due to a higher electronic noise contribution measured in the system. In addition, the quality of the alpha source and its position with respect to the detector may also influence the final resolution, as related to the energy losses of the alpha particles in the source itself and to angular effects in the detector's entrance window. Although not directly in front of the PIPS, the α-source was present inside the box while doing measurements, so this could have influenced the measured energy spectrum of the beam somehow in the energy range close to that of the alphas.

In order to operate the Si detectors for energy spectroscopy and ToF measurements, the detection of individual particles is required and therefore the beam intensity needed to be reduced to levels of a few hundred particles per second. Moreover, as in this set-up the beam hits the detector directly, the particle rate into the detector had to be kept under control in order to prevent their damage or destruction by excessive radiation. During this work, the beam intensity was reduced by placing attenuator foils upstream of the LINAC in DB2 and DB3, see Fig. 2.1, with transmission factors of 1% and 0.01%, respectively. Although the attenuation system with foils allowed the scheduled measurements to be performed, the attenuation factors obtained during consecutive measurements showed a low reproducibility, and most of the times the adjustment of the faint beam intensities was done by a trial and error approach. The main limitation of the beam attenuation system with foils lies in its non-systematic attenuation nature. This could be related to damage of the foils due to beam exposure, or to the slightly different relative positions of the two foils whenever they are placed on the beam path.

The energy scan measured with the dipole bending magnet is presented in Fig. 5.7 and the full energy spectrum obtained of the REX-ISOLDE beam and the α-source is presented in Fig. 5.8. The predominant ion species in the beam is $^{12}C^{3+}$, followed by $^{20}Ne^{5+}$, $^{4}He^{+}$ and $^{16}O^{4+}$. The main parameters obtained from these measurements are summarized in Table 5.5.

Table 5.5: Energy spectrum of the REX-ISOLDE beam (A/q=4, E/A=0.3 MeV/u) using two different methods.

Method	Particle	$\langle$E$\rangle$(MeV)	$\langle$E/A$\rangle$(MeV/u)	FWHM (%)
PIPS Si detector	$^{20}Ne^{5+}$	5.716	0.286	3.7
	$^{16}O^{4+}$	4.602	0.288	3.3
	$^{12}C^{3+}$	3.480	0.290	3.7
	$^{4}He^{+}$	1.168	0.292	9.3
Spectrometer magnet	REX pilot beam		0.300	1.5

For all the peaks obtained using the PIPS detector, the mean energy per nucleon is

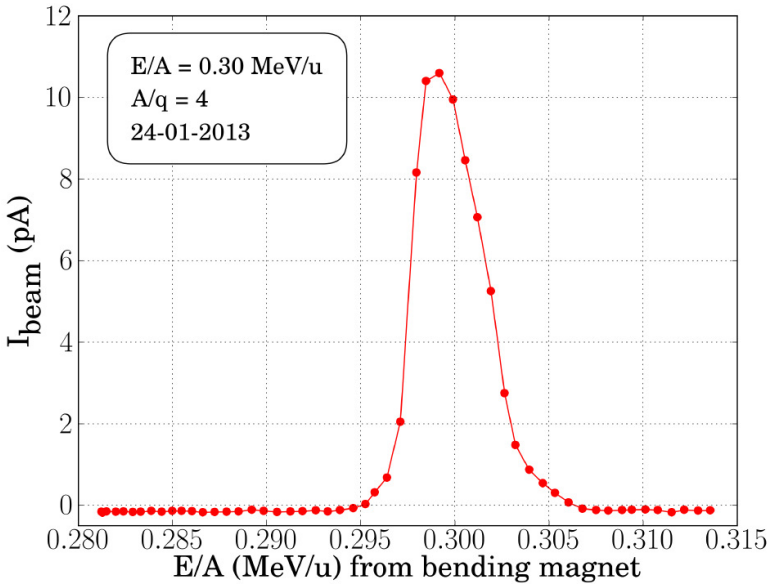

Figure 5.7: Energy scan of the REX-ISOLDE beam measured using the bending dipole magnet (A/q=4, E/A= 0.3 MeV/u).

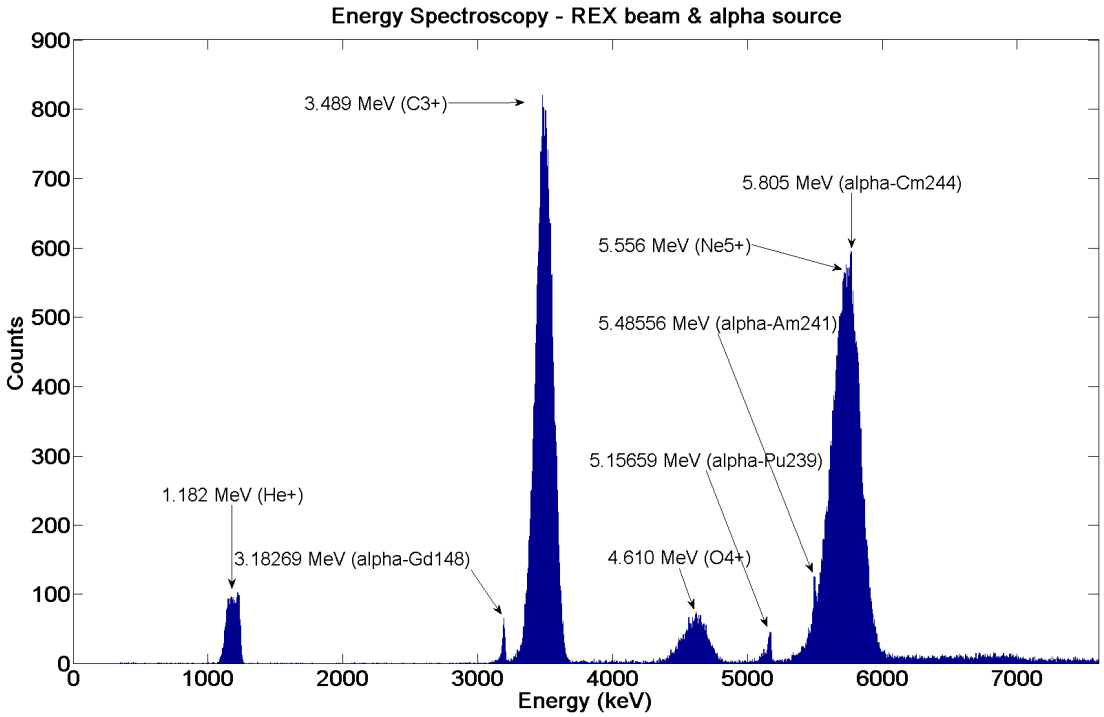

Figure 5.8: Energy spectrum of the REX-ISOLDE beam measured with the Si detector and calibrated with an α source. A/q=4, E/A=0.3 MeV/u.

lower than the value obtained from the spectrometer magnet method. The reasons for these discrepancies could be due to:

- An incorrect estimation of the calibration constant value for the bending magnet. The calibration constant is determined experimentally every year using as a reference the output beam energy of the RFQ beam as E/A = 0.3 MeV/u with a beam of A/q = 4. This value is measured within 1.5 % FWHM, according to the information registered in the REX-ISOLDE logbook [107].

- Energy loss of the projectiles in the entrance window (dead layer) of the Si detector. An estimation of the full energy loss problem in the entrance window has been performed for the beam particles at different energies and is presented in Appendix A. The effect of the energy loss of the particles in the entrance window is not negligible, in particular for the lowest energies considered in this work. However, it should be taken into account that as the energy calibration of the scale has been performed using as reference the energy deposited by alpha particles in the active zone of the detector, the overall effect in the determination of the projectile energy is much smaller.

- A dependence of the detector efficiency with the projectiles' charge. The conversion efficiency of the energy deposited in the detector to electron-holes pairs (directly related with the charge pulse that is sent to the preamplifier) is not similar for all ions, and this might introduce a systematic deviation in the determination of the absolute energy for projectiles of different masses. More information about this effect, called "pulse height defect", can be found in [108, 109].

The width of the $^4He^+$ peak acquired with the silicon detector appears to be much larger, as shown in Fig. 5.9, and in all cases the width is larger than that obtained with the bending magnet. It is interesting to point out that the relative energy resolution of the Si detectors appears to increase with the absolute energy of the detected particle.

Time of Flight

After the energy measurements, arrival time data were taken with the two detectors, first in DB4 and then the same process was repeated in DB5. The beam intensity was measured at 1.6 pA in DB5 before attenuation. Then beam attenuators were placed in DB2 and DB3 with transmission factors of 1% and 0.01%, respectively. The repetition rate in the LINAC was slowed to 20 Hz. With such settings, the acquisition rate measured with the scope for the silicon detector was around 3 Hz. The beam energy in these measurements was varied gradually between 2.18 and 2.27 MeV/u, by changing the amplitude of the RF in the last 7-gap resonator, 7GAP3. This small change in

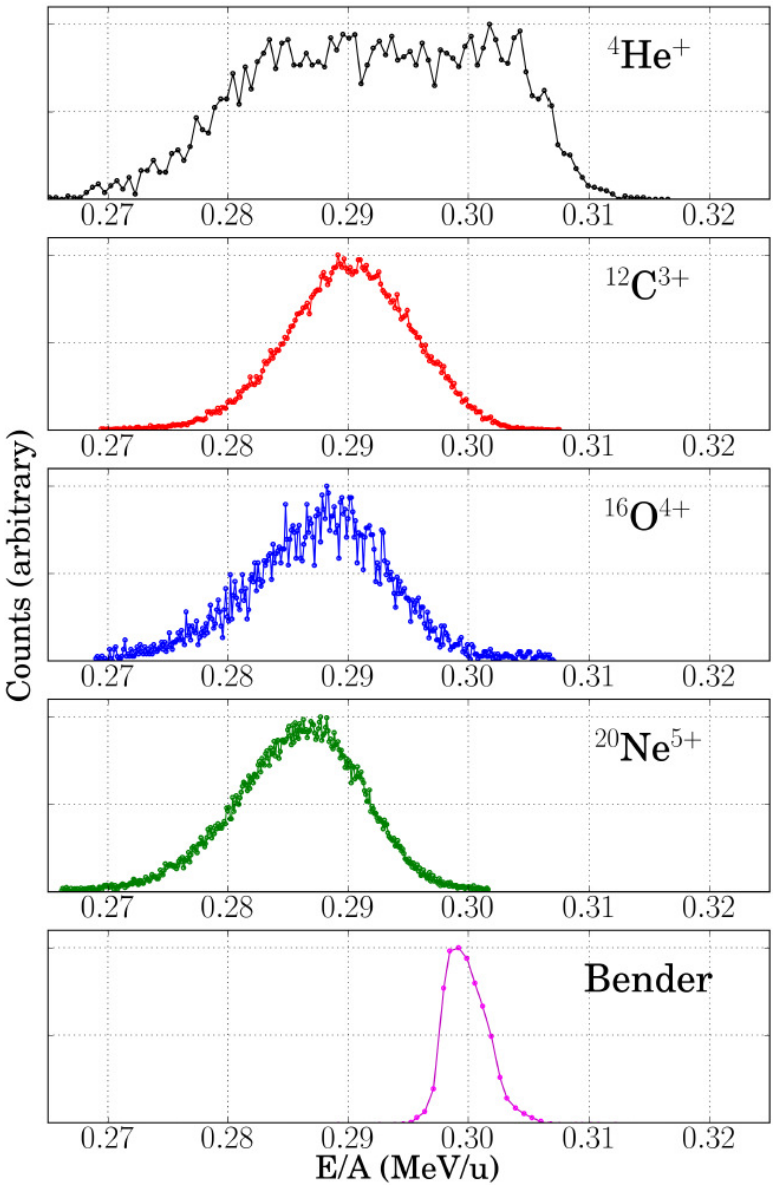

Figure 5.9: Energy per nucleon for the different components of the REX beam (E/A = 0.3 MeV/u) acquired using the Energy signal of the Si detector. Bottom plot: magnetic field scan of the REX beam (A/q = 4) using the dipole bending magnet.

beam energy was done to make sure the arrival time of the particles is measured with respect to the same bunch.

The time of flight measurements involved the use of two Si detectors, installed in DB4 and DB5. The detector placed in DB4, inside the concrete vault, together with its preamplifier were highly sensitive to electromagnetic background, probably X rays, when the 9-gap cavity was on. This background could not be shielded, and as a consequence the maximum energy that could be used with the ToF technique was the output beam energy of all the REX-ISOLDE cavities except the 9-gap, i.e. 2.2 MeV/u. On the other hand, the use of very low energy beams is restricted due to the de-bunching of the beam that destroys its time structure, making it impossible to work in that range. A series of measurements was done at beam energies around E/A = 2.2 MeV/u, and a test was done to decrease the ToF as the accelerating voltage applied to the last 7-gap cavity was increased. Unfortunately, for that set of energies the results of the energy scan with the dipole magnet were affected by a failure present in the collimator wheel of DB7, downstream of the bender. As a consequence, the final comparison of the energies obtained with the bending magnet and the Si detectors was not done in optimum conditions. On the last day, a measurement of the time of flight for particles with E/A = 2.26 MeV/u could be performed, and the comparison with the results of the energy scan with the bender was possible as the problem in the collimator of DB7 had been solved.

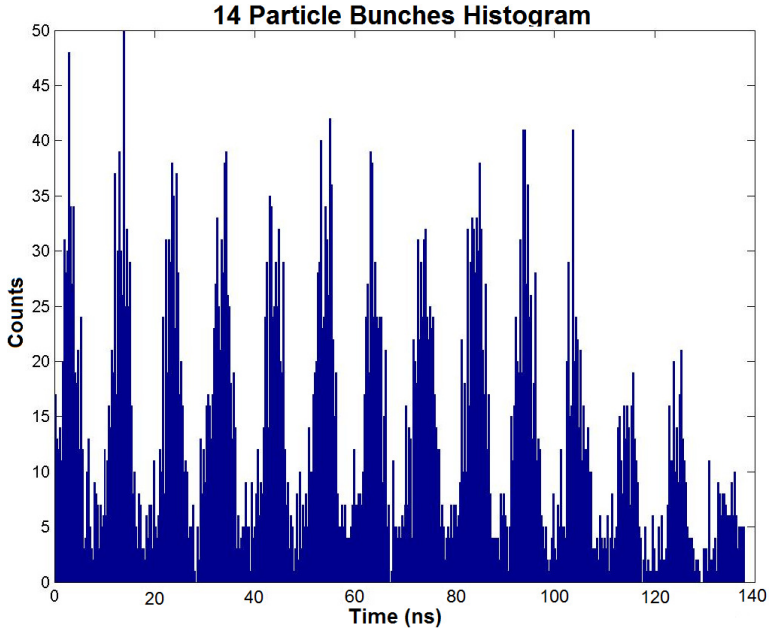

Figure 5.10: Timing spectrum of the REX beam. A/q = 4, E/A = 2.18 MeV/u beam. Detector installed in DB5.

The TDC receives hits in two channels: one took the adapted pulse coming from the arrival time of particles into the detector, and the other from the master clock of the RF system. The time of arrival of the hits was recorded using a digital counter with a resolution or Least Significant Bit (LSB) = 24.41 ps and processed off-line to produce histograms of the time difference between the particle arrival time to the detector and the RF clock divided by 14, i.e., $T_{RFdivided}$= 14×9.87 ns = 138.18 ns. One example of such a time spectrum is shown in Fig. 5.10. 14 bunches can be identified corresponding to the particle arrival time with respect to the divided RF pulse, which is the reference signal given by the master-oscillator of the LINAC [72]. It is worth making a brief comment about the bin size of the CAEN TDC V1290N. When data from the timing measurements was first analysed, a systematic deviation was found between the time measured by the TDC and the time produced with a pulse generator. This had been attributed to a possible error in the scale of the TDC. The results presented in the following tables for the ToF analysis were corrected for this issue, therefore times were computed as $t_{TDC}^{corrected}$= $K_{correction}$×t_{TDC}. The LSB of the TDC is actually 24.41 ps and not the value stated in the CAEN manual, which is LSB 25 ps. The correct way to calculate the LSB is to consider that the clock frequency is 40 MHz, and that each clock period of 25 ns corresponds to the digitized value of 2^{10}LSB = 1024 LSB, therefore 1 LSB = 25 ns / 1024 bits = 24.41 ps. Taking that relation into account, the correction factor is $K_{correction}$=$\frac{1000}{1024}$=0.977.

In Fig. 5.11 the data of Fig. 5.10 is shown, but in this case the time values have been overlapped to the first two periods to account for the periodicity on the arrival time of the particles, that is T_{RF}= 9.87 ns. Note that the width of the bins in this histogram is smaller than in the one displayed in Fig. 5.10. A fit was performed on the two bunches histograms similar to the displayed in Fig. 5.11 for all the acquired spectra. The fitting function chosen was the sum of five Gaussian distributions, all of them with the same height and width, and with a time separation between them equal to the RF period of 9.87 ns. The central Gaussian distribution was fitted to the first particles bunch, i.e., the one with the peak present between t=0 and t=10 ns. An example of the result of this fit is shown in Fig. 5.11. The position of the Gaussian peak, $\Delta t_{ParticletoRF}$, was taken as the reference for the time of arrival of the particle with respect to the RF pulse. The standard deviation of the fitted peak, Δt, represents a convolution of the time resolution of the system and the dispersion on the arrival time of the particles to the detector, which is the bunch length. The numerical values included in the legend of the figure should be read as $\Delta t_{ParticletoRF} - \Delta t$. More examples of the two bunches histogram are shown in Fig. 5.12. Note that the spectrum of particles arriving to diagnostics box DB4, located just upstream of the LINAC, exhibits double peaks. This might be an indication of a certain time structure of the

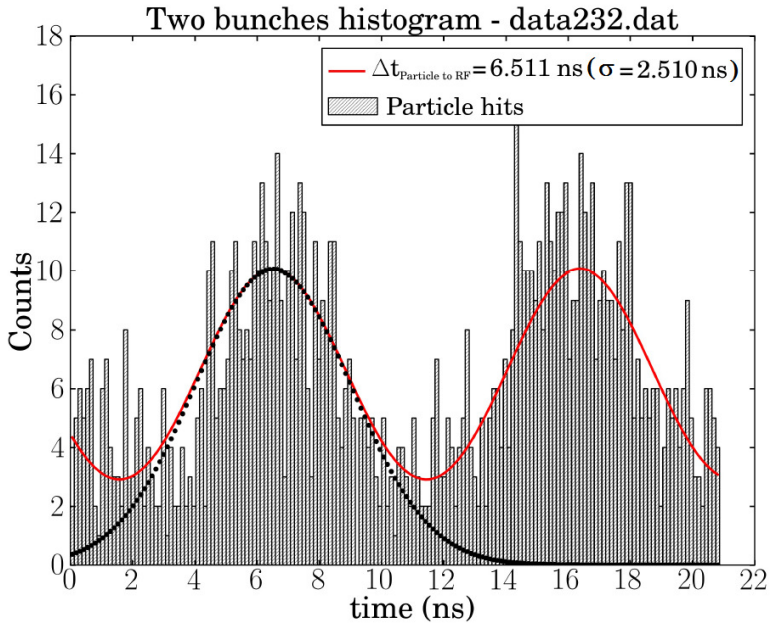

Figure 5.11: Timing spectrum overlapped in two RF periods. A/q = 4, E/A = 2.18 MeV/u beam. Detector installed in DB5. Solid line: fit to the data with five Gaussian distribution (see text for details). Dotted line: Gaussian distribution corresponding to the first peak. The time difference between the particle hit and the RF pulse was 6.51 ns. The bunch length (1 σ) of the distribution was 2.51 ns.

particles inside the bunches, also called bunch filamentation. In addition, the shape of the spectra is influenced by how finely the data are binned and by the settings in the electronics set-up, such as discriminator thresholds, etc. The bunch length is also considerably lower in DB4 than in DB5, as expected due to the increased de-bunching of the beam for projectiles travelling longer distances drifting from the RF cavities.

Performing the data analysis described above on the acquired spectra, the values for the ToF presented in table 5.6 were calculated. In all cases, at least two spectra were acquired with the same beam conditions, in order to determine the time resolution of the system, which is of the order of 0.15 ns.

Absolute ToF Between Detectors

Using the average ToF values from table 5.6, the difference in time of arrival of the particles to the two detectors can be calculated as:

$$(\Delta t_{Part}^{DB5-DB4}) mod T_{RF} = (\Delta t_{Part-RF}^{DB5} - \Delta t_{Part-RF}^{DB4}) mod T_{RF} \tag{5.2}$$

Note that $\Delta t_{Part}^{DB5-DB4}$ does not depend on the reference start time given by the RF master-clock signal, as the terms including the RF clock cancel out. For the determi-

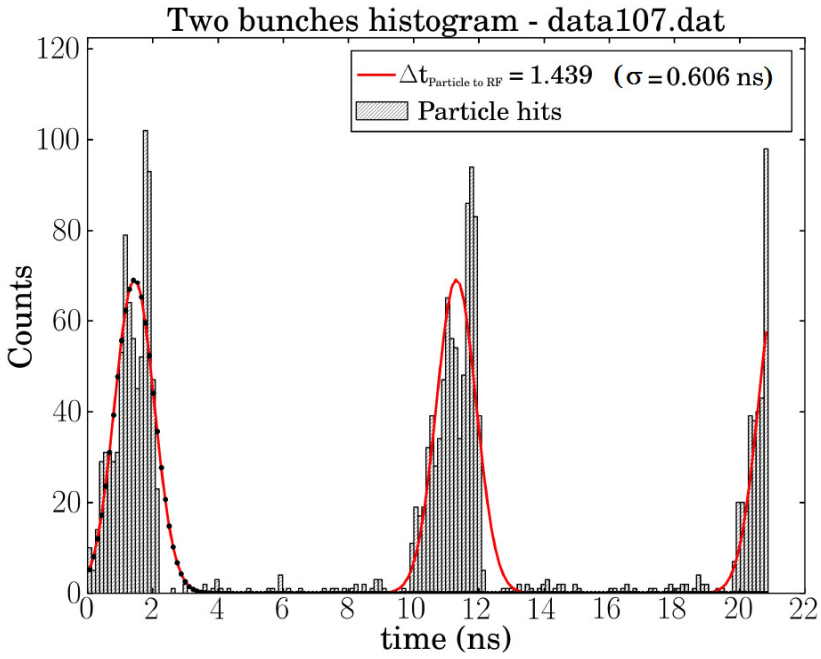

Figure 5.12: Timing spectrum of the REX beam (E/A= 2.18 MeV/u, A/q=4).

Table 5.6: Results of the ToF spectra analysis.

7GAP3 pickup voltage (mV)	Beam Energy (MeV/u)	Diagnostics box location	$\bar{\Delta t}_{Part-RF}$ (ns)	$\sigma_{\Delta t}$ (ns)
1334	2.18±0.05	DB4	4.15	0.20
		DB5	6.67	0.16
1467	2.21±0.05	DB4	3.06	0.10
		DB5	3.38	0.06
1601	2.24±0.05	DB4	2.3	0.02
		DB5	9.31	0.05
1735	2.27±0.05	DB4	1.43	0.01
		DB5	6.32	0.10

nation of the particles ToF there is one unknown parameter, which is the number of complete RF periods that have passed during the flight of the particles (N). Thus,

$$(\Delta t_{Part}^{DB5-DB4}) = (\Delta t_{Part-RF}^{DB5} - \Delta t_{Part-RF}^{DB4}) mod T_{RF} + N \cdot T_{RF} \tag{5.3}$$

Table 5.7: Final results from the ToF spectra analysis.

7GAP3 pickup voltage (mV)	E/A$_{magnet}$ (MeV/u)	(Δt$_{Part}^{DB5-DB4}$)mod T$_{RF}$ (ns)	Number of periods N	Δt$_{Part}^{DB5-DB4}$ (ns)	E/A$_{ToF}$ (MeV/u)
1334	2.18±0.05	2.5	38	377.7	2.16±0.07
1467	2.21±0.05	0.3	38	375.5	2.18±0.07
1601	2.24±0.05	7.0	37	372.3	2.22±0.07
1735	2.27±0.05	4.9	37	370.2	2.25±0.07

Due to the periodic structure of the beam, N cannot be deduced experimentally with these conditions. However, it can be estimated using the energy of the particles obtained with the spectrometer magnet method as a reference. The final results of the absolute ToF measurements with the Si detectors as a function of the 7GAP3 pick-up voltage are summarized in table 5.7. Due to the wrong collimating set-up when taking the energy measurement using the bending magnets, the results of E/A_{bender} can only be taken as a rough estimate, and a quantitative comparison with the ToF values cannot be done. However, the results presented in table 5.7 for the E/A measurements measured with the dipole magnet and with the ToF system show a qualitative agreement. Regarding the width of the fitted Gaussian distributions to the timing spectra, the bunch length (1 σ) in DB4 changes from $\sim$0.6 ns at E/A = 2.27 MeV/u, to $\sim$1.2 ns at E/A = 2.21 MeV/u. These values include also the experimental dispersion introduced in the detection and processing of the signal for both the RF and particle hits. For the detector placed in DB5, we have a bunch length of $\sim$1.7 ns at E/A = 2.27 MeV/u, and $\sim$2.5 ns at E/A = 2.21 MeV/u. It might be useful to compare these values with the expected bunch length calculated with beam optics methods.

5.8 Cavity Phase-up

An RF cavity phase-up on the last 7-gap resonator of REX-ISOLDE to demonstrate the ToF principle was already achieved [71]. At 101.28 MHz, the bunch spacing is only 9.87 ns, making it challenging to differentiate between bunches arriving at the PIPS detector. This measurement was possible by slowly varying the RF phase such that the bunch being tracked never moved more than half of 9.87 ns in arrival time and could always be identified. Such a measurement is time-consuming because small steps in

RF phase are required, however, the ToF principle was validated and is a viable option for phasing the cavities should a beam chopper be incorporated into the HIE-REX machine which would enable differentiation between bunches arriving at the monitor. The independent measurements made in the time and energy domains can be used to validate one another. From measurements of the change in beam energy as a function of RF phase it is possible to calculate the change in time of flight as a function of RF phase with the drift distance between the last accelerating cavity and the detector as a known parameter.

The aforementioned bunch spacing of roughly 10 ns is too short to allow experiments making use of ToF techniques. For this purpose a pre-buncher/chopper system has been proposed for the HIE-ISOLDE project in order to allow 100 ns bunch spacing while maintaining high transmission and full background suppression between bunches. This implies the installation of a pre-buncher operating at one tenth of the base frequency upstream of the RFQ and a beam chopper line. The extra space necessary for this system is obtained by shifting the superconducting LINAC by one cryomodule length as shown in Figure 5.13. A Multi-Harmonic Buncher (MHB) could be placed before the RFQ at REX to increase the bunch spacing of post-accelerated beams in HIE-ISOLDE, as shown in Fig. 5.14.

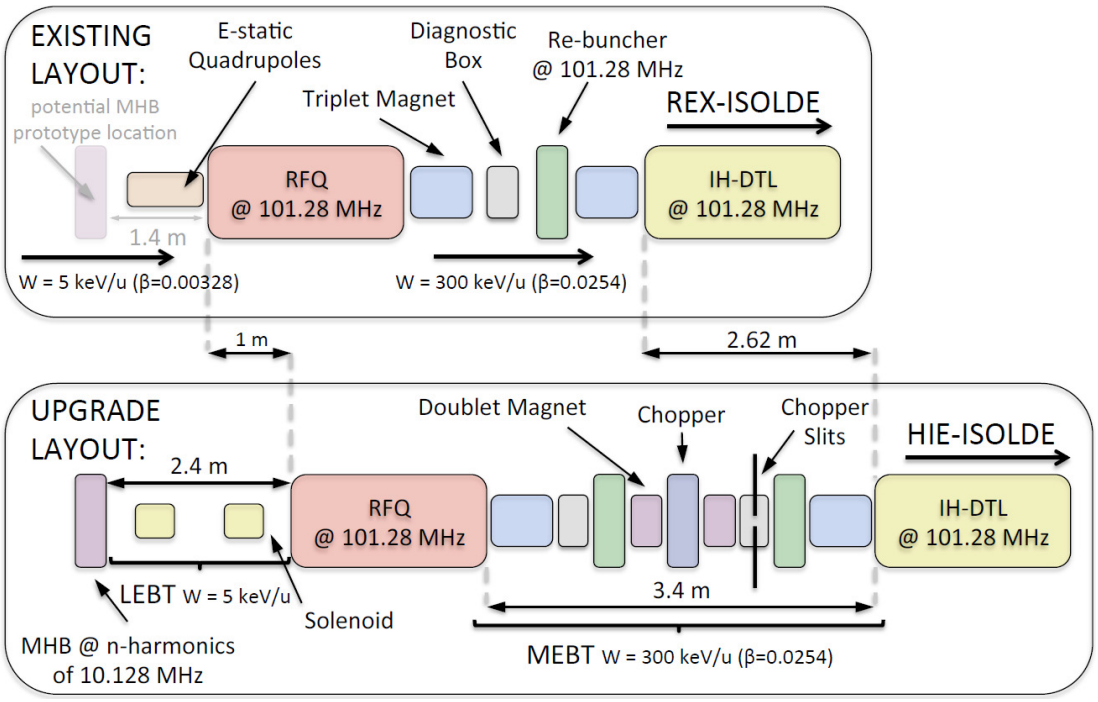

Figure 5.13: Schematic of the existing (top) and upgrade layout (bottom) with 10 MHz bunching system. Image taken from [110].

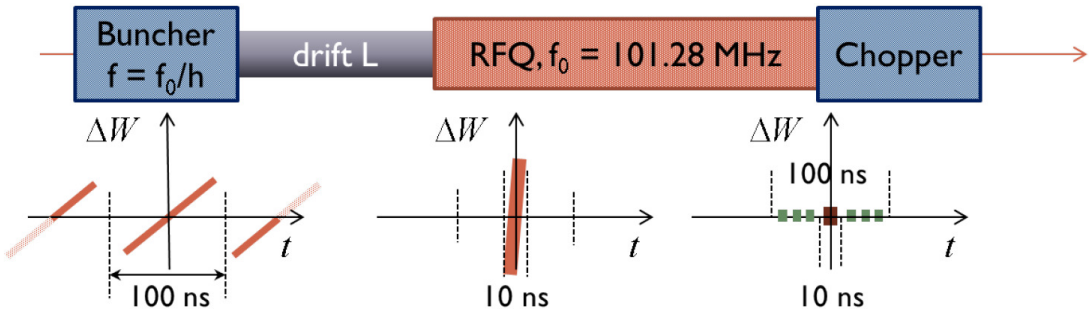

Figure 5.14: Schematic of the pre-buncher concept in longitudinal phase space along with the RFQ and beam chopper for HIE-ISOLDE. Image taken from [111].

Operating at a sub-harmonic frequency of 10.128 MHz, i.e., one tenth of the fundamental frequency of the RFQ, transmissions as high as 80% can be achieved in the main bunches separated by 98.7 ns [111]. It would be desirable for some REX-ISOLDE users to make particle identification employing ToF techniques, and in order to allow this, less than 1% of the beam should be populating the satellite bunches outside of the main pulses spaced at 98.7 ns. The optimal effective voltage for a drift length of 1.4 m between the pre-buncher and the RFQ was calculated to be $V_{eff} = 0.8$ kV, without any deterioration in the simulated nominal rms longitudinal emittance of $\varepsilon_{rms} = 0.28$ ns keV/u [112].

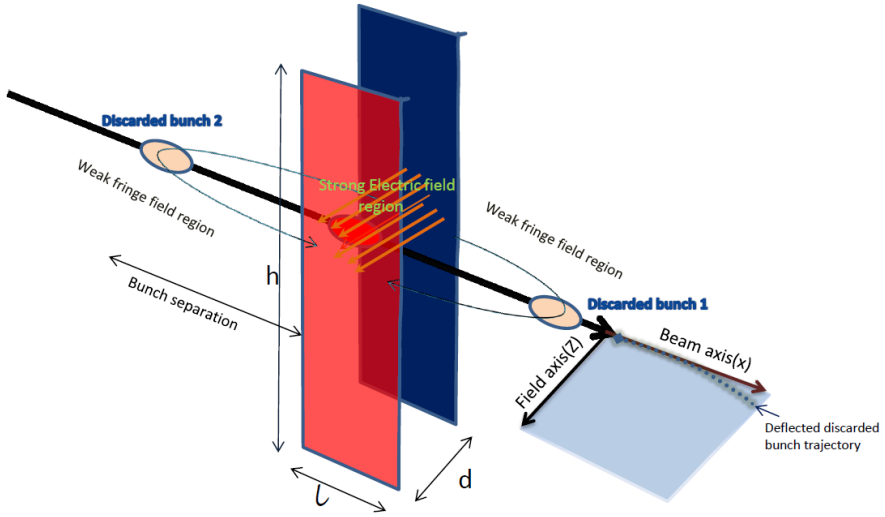

Figure 5.15: Working principle of the beam chopper system for the HIE-ISOLDE LINAC. Image taken from [110].

A beam chopper is needed in order to remove the ∼15% of beam populating the 101.28 MHz satellite bunches. The principle of the beam chopper is shown in Fig. 5.15. The feasibility of cleanly separating the main 10.128 MHz bunches from the 101.28 MHz satellite bunches with a travelling-wave type chopper at HIE-ISOLDE has

been investigated in [110] using a simple model comprising a chain of 20 synchronised capacitors pulsed at a voltage of 1.2 kV. Even with a relatively large transverse aperture of 30 mm it appears feasible to remove the satellite bunches spaced at 75 mm without significantly perturbing the main bunch. A required deflection of 4 mrad for beams with $A/q = 4.5$ and the mechanical length of the system can be kept under 0.5 m. The deflection imparted on the main pulse is estimated to be 1% of that received by the discarded satellite bunches and the transverse emittance growth of the beam is small if the rise/fall times are kept below 5 ns [110].

5.9 Chapter Summary

Absolute particle energy and time of flight measurements were done using Si detectors at REX-ISOLDE, using the stable beam with a mass-to-charge ratio of $A/q = 4$. Si detectors are not considered to be radiation hard, therefore irradiation with a non-attenuated beam with an intensity $I \geq 0.1$ pA should be avoided as this could result in destruction of the detector. For single particle counting/identification as required by these methods, the suggested particle rate is ≤ 10 kHz. A series of attenuating foils with a total transmission factor of $\sim 10^4$ are required in order to obtain this value at REX.

By measuring the energy spectrum, the peaks corresponding to the different components of the particle beam can be clearly identified. Measurements of the relative beam mass composition can be achieved with this method. The channels to energy scale is calibrated using α-sources. The relationship between the ADC channels and the deposited energy follows a linear behaviour. Standard α-sources emit particles in the energy range of 3 to 6 MeV. Using light ions as projectiles, an independent method for determining the energy per nucleon of REX-ISOLDE beams can be performed with the PIPS detectors, as shown in this chapter. That method can be applied for cross-checking the calibration accuracy of the dipole magnet method that is normally used to determine the beam energy. The mean energy per nucleon obtained with the Si detector is about 3% to 5% lower than the result from the dipole magnet method for a beam with $E/A = 0.3$ MeV/u, $A/q = 4$. The peak corresponding to $^4He^+$ ions from a beam with $E/A = 1.87$ MeV/u was also acquired, and its mean E/A value was measured to be 1% lower compared to the result of the spectrometer magnet.

Using two PIPS detectors installed at different positions on the REX beam line, the ToF of the beam particles was determined. As a consequence of the periodic time structure of the beam bunches with an RF period of $T_{\mathrm{RF}} = 9.87$ ns, the total integer number N of RF periods during the particles' flight between the two detectors cannot

be determined. However, N can be estimated if the energy per nucleon is known with an accuracy of the order of ∼1%. That value can be obtained for example with the spectrometer magnet method. The data analysis involves the acquisition of at least two time histograms using a TDC, and a fitting routine to those histograms. The detection chain of both detectors should be as similar as possible to prevent the introduction of time delays that will affect directly the time of flight calculation. From the fitting of the time histograms, one can extract the mean time of flight of the particles and information about the bunch length. The achieved resolution for each time of flight measurement with the present set-up is of the order of 0.15 ns, which is the difference between spectra acquired with the same beam conditions. The ToF results for a beam with $E/A = 2.26$ MeV/u gave an E/A value 2.3% lower than that obtained with the energy scan performed with the bending magnet. The applicability of the ToF technique at different E/A values is heavily dependent on the distance between the two detectors. For very low energies, overlapping of different bunches by de-bunching the beam can be critical if the distance between detectors is large. On the other hand, the resolution of the system increases for longer times of flight, and therefore longer distances between the detectors. The determination of N, the total integer number of RF periods during the flight, is critical for the implementation of this technique when no beam chopper or a particular time structure of the beam pulses is present. The requirements concerning the estimation of N with an independent technique increase with N, and therefore with the distance of separation between the two detectors. The detector of DB4 inside the LINAC's concrete vault was severely affected by background, probably originated by X-rays impinging on the detector itself or its preamplifier, when the 9-gap cavity was on. A noise-rejection system must be implemented should any installation of this kind of detectors be foreseen in a high-radiation environment.

The ToF procedure is time-consuming and not suitable for a quick and automated procedure, however it is required for absolute beam energy measurements since the dipole method is not calibrated. Nonetheless, it is considered a viable option for phasing the RF cavities should the bunch spacing be increased with the addition of a beam chopper in the HIE-ISOLDE upgrade.

Chapter 6

Beam Instrumentation for Low-energy Antiprotons

Beam diagnostics for antiproton beams at low energies are required for essentially all experiments at the AD, but they will be particularly important for the future ELENA ring and its 100 keV beam lines to the different experiments, in order to provide the experiments with antiproton beams of the desired characteristics [113]. The biggest challenge for the beam instrumentation system of ELENA is to measure all the parameters of a very low intensity antiproton beam of less than $4{\cdot}10^7$ antiprotons/s. Many monitors have been successfully developed and operated at the AD, but beam profile monitoring remains a challenge. A dedicated beam instrumentation and detector test stand has been recently set up at the AE$\bar{g}$IS experiment in the AD. Located downstream of AE$\bar{g}$IS, it allows for parasitic use of the antiproton beam at different energies for testing and calibration of different detectors.

With the aim to explore and validate different candidate technologies for future low-energy beam lines, as well as for the downstream antihydrogen detector in the AE$\bar{g}$IS experiment, measurements were carried out by different research groups within the AE$\bar{g}$IS collaboration using silicon detectors, nuclear emulsions and the purpose-built Secondary Emission Monitor (SEM) provided as part of this thesis. The SEM is a beam-destructive device developed to suit the needs of the future Ultralow-energy Storage Ring (USR), and its use to monitor 200 keV protons has already been tested at INFN-LNS [114].

The main reasons behind the test of this SEM were first to try measuring a beam profile of the $\bar{p}$ beam if possible; second, compare different configurations of the device. Another important aim was to examine the sensitivity of the device to pions or other secondary products of the $p - \bar{p}$ annihilation.

In this chapter, the results of a series of tests taken with the SEM at the AE$\bar{g}$IS

experiment in December 2012 before the first Long Shutdown (LS-1) at CERN are presented, exposing the monitor for the proton tests in [114] to a 300 keV beam of antiprotons. A summary of the different detector types involved in the beam run is given with regard to a possible future permanent use at the low-energy beam line of AE$\bar{g}$IS, summarizing their main achievements and comparing advantages and disadvantages of each detector. An option configuration is given, recommending a whole set of diagnostics to fully characterize low-energy $\bar{p}$ beams.

For the purpose of testing the different detectors discussed in this chapter with the

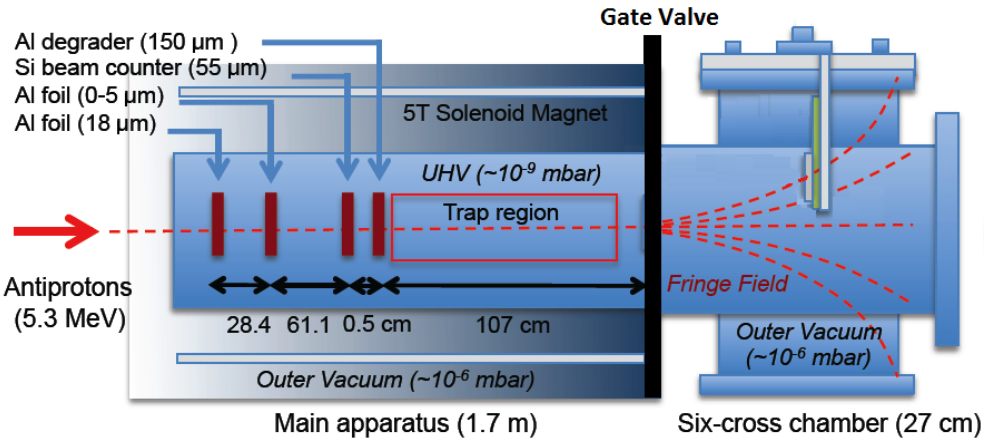

Figure 6.1: Schematic of the detector chamber installed at the end of the AE$\bar{g}$IS apparatus. Modified image taken from [59].

antiproton beam at AE$\bar{g}$IS, a six-way cross was installed at the very end of the AE$\bar{g}$IS main apparatus, as shown in Fig. 6.1. The chamber was connected to AE$\bar{g}$IS with a gate valve. The vacuum level in the chamber was $\sim 10^{-6}$ mbar. While passing through the AE$\bar{g}$IS apparatus, the antiprotons lose energy from 5.3 MeV to 100 keV first through two aluminium degraders, one fixed and one mobile, then a silicon beam counter and another fixed aluminum degrader, as shown in Fig. 6.1. What follows is a description and summary of the measurements obtained from the different detectors in the AE$\bar{g}$IS collaboration obtained while using this detector chamber.

6.1 Secondary Emission Monitor

6.1.1 Working Principle

The SEM consists of a metallic foil biased to a negative potential, a grounded metallic mesh, a two-stage MCP stacked in chevron configuration with a phosphor screen, and a CCD camera.

In a first configuration, the primary particle beam goes through the mesh at an

angle of 45° and produces secondary electrons in the 10 eV range from the surface of the foil. These secondary electrons are accelerated by the negative potential on the foil and fly through the mesh towards the beam imaging system. When the electrons reach the MCPs, an electron cascade occurs, resulting in an increased electron output, with typical gains of 10^6, which will eventually hit the phosphor screen, producing visible light that is finally registered by the CCD camera. The monitoring of antiproton beams with electron multiplier MCPs has already been demonstrated [115, 116].

This 45° orientation preserves the beam aspect ratio as seen by the camera. A

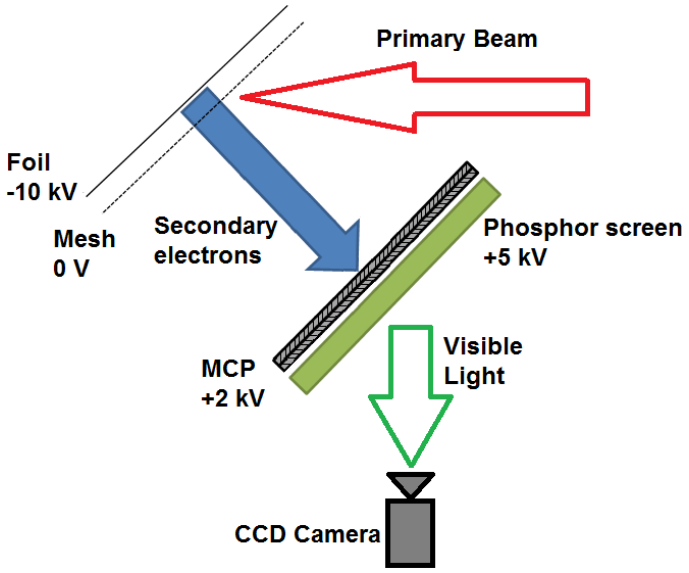

Figure 6.2: Working principle of a foil-based secondary emission monitor.

schematic showing the working principle of the SEM in this configuration is presented in Fig. 6.2. Here, only the negatively charged particles generated at the foil reach the surface of the MCP placed at a certain distance, because the direction of the $2{\cdot}10^5$V/m electric field present between the foil and the mesh will only accelerate the negatively charged particles towards the MCPs. The limitations of the device are that such a high electric field could severely distort the response of the monitor for keV energy beams, as the electrostatic kick of this field on a keV particle could displace the image seen in the monitor away from the reference trajectory. These distortions can reach 0.6 mm in the case of a 300 keV antiproton beam, and as much as 8 mm for a 20 keV beam [114]. However, this is not a concern for high-energy or heavy-ion applications [114]. The range of antiprotons in aluminium is 4.5 μm at 300 keV and approximately 0.8 μm at 20 keV [117], therefore by using a 200 μm aluminium foil this is a destructive beam monitor.

A different configuration of the monitor is possible removing the foil and mesh part, allowing the primary beam to hit the MCP directly. In that case, the monitor

consists of the two-stage MCP together with the phosphor screen all in one stack. The MCP-phosphor device is placed at 45° with respect to the beam, and then a CCD camera monitors the light coming from the back of the phosphor screen. A schematic showing the working principle of the SEM in this configuration is presented in Fig. 6.3. Extensive numerical studies into the effect of the voltage settings were previously carried out in the work of [114].

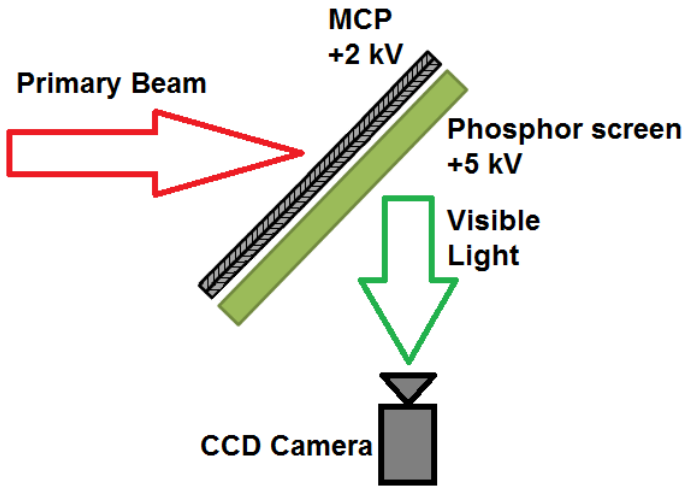

Figure 6.3: Working principle of a MCP-based secondary emission monitor.

6.1.2 Experimental Setup

The aim of testing this monitor at the AE$\bar{g}$IS experiment was to test its capability as a beam profile monitor with a 300 keV $\bar{p}$ beam, compare the two configurations of the device and examine its sensitivity to pions or other secondary products of the $p - \bar{p}$ annihilation.

The experimental detector chamber was installed downstream of the 1 T magnet, at the end of the AE$\bar{g}$IS line in the AD Hall at CERN. The monitor is mounted inside a ConFlat (CF) 6-way cross vacuum vessel, which was a shared detector chamber for different detector groups such as MIMOTERA and the 3D Pixel sensor during the December 2012 antiproton beam run. Inside this vacuum vessel, the monitor can be installed either in the foil-based or in the direct MCP configuration and it can be moved in and out of the beam path with a pneumatic actuator. A comparison of both settings is shown in Fig 6.4.

The equipment used in this experimental test is the following:

- Vacuum vessel CF 6-way cross spherical body 2xDN160 4xDN100
- 200 μm thick UHV clean aluminium foil

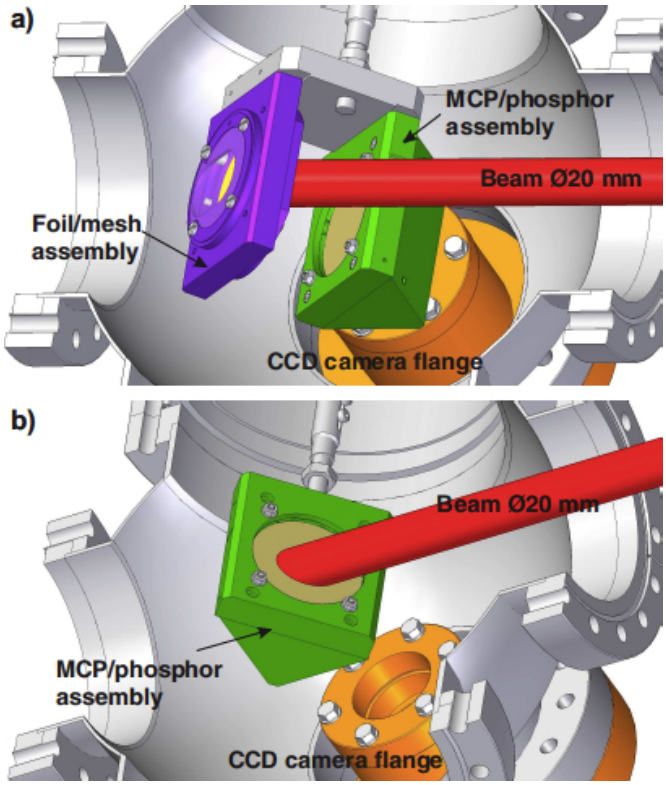

Figure 6.4: View of the two configurations of the monitor: (a) With foil and mesh. (b) MCPs placed directly in the beam path. Image taken from [118].

- Nickel mesh with 80 lines per inch, or 3 wires per mm approx., each wire being 25 μm thick. This accounts for a transmission factor of 85%.
- 2x MCP 50-15 from TOPAG [119], with a channel bias angle of 8° and a gain at 1100 V of 10^4.
- P-43 phosphor screen from Proxivision, with an active diameter of 42 mm and a phosphor layer thickness of 4μm.
- CCD Camera DCU223C with C-mount lens MVL5WA and USB 2.0 IN/OUT Trigger cable from Thorlabs [120].

A 3-channel HV power supply (19" THQ from ISEG [121]) is used to supply voltages to the MCP, phosphor and foil. Two D Power Source (DPS) series modules with an exchangeable polarity and 5 kV SHV output connectors can supply up to 3 kV/4 mA and 5 kV/2mA to the MCP and the phosphor screen, respectively. Peak-to-peak ripple and noise for DPS modules are typically less than 2 mV and 7 mV maximum. A single C Power Source (CPS) module with a fixed polarity and 16 kV LEMO output connector can supply up to -10 kV/1mA to the foil, as the mesh is connected to ground. Peak-to-peak ripple and noise for the CPS modules is typically less than 200 mV and 500 mV maximum. The chevron type MCP can be supplied with a maximum

of 2 kV and no more than 1 kV should be applied to a single microchannel plate. In order to apply the correct voltages with a single HV power supply and to vary them for both MCPs at the same time, a custom-made voltage divider was used. It incorporates two micro-ammeters in series with the power supply to monitor current flow across the MCPs, two digital voltmeters to read the voltage divided between the microchannel plates and two current limiting resistors to help prevent damage to the MCPs in the event of a HV breakdown within the internal detector assembly. More technical details of the voltage divider can be found in [114].

For the interface between air and vacuum, four 5 kV SHV feedthroughs and one 10 kV SHV feedthrough were welded to the actuator flange. The first three feedthroughs supply voltage to the front, middle and rear of the MCP assembly, the fourth 5 kV SHV is used for the phosphor screen, whereas the 10 kV SHV is used for the foil. The two-stage MCP and phosphor assembly is stacked in a sandwich with metal rings placed between the components as shown in Fig. 6.5.

Kapton insulated wires rated up to 5 kV were soldered to the contact rings. For the

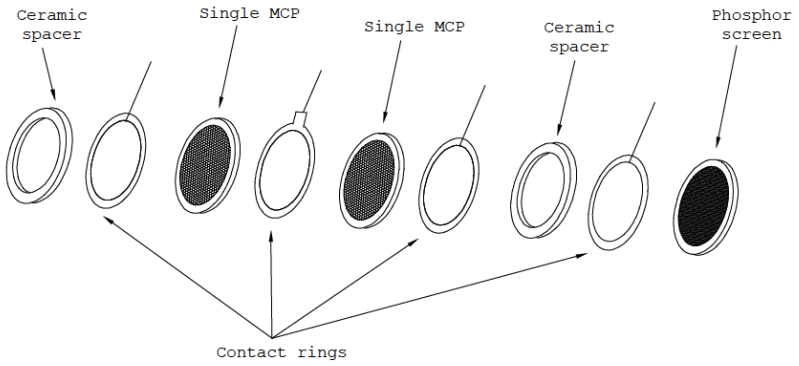

Figure 6.5: schematic of the MCP-phosphor screen assembly. Image taken from [122].

foil, a stiffer Kapton insulated wire rated up to 10 kV was used.

Prior to the run, leakage current measurements of each MCP were taken ramping up the voltage, to check their resistance. Then the trigger of the camera was adjusted to take shots synchronously with the $\bar{p}$ beam, which delivered one shot every 110 s. Once the device was in place the background of the camera was checked and an alpha source was installed inside the chamber facing directly the MCPs, to check the sensitivity of the monitor. When the vacuum reached the working level of 10^{-7} mbar alpha particles were clearly identified in the SEM, and finally some calibration adjustments were done before antiproton measurements. Once the alpha source was removed, vacuum pumping resumed to begin the measurements with the first configuration.

6.1.3 Results

Once the nuclear emulsion tests were complete (see section 6.2), the detector chamber was vented to remove the nuclear emulsions detector and replace it by one of the silicon detector prototypes. Once the detector chamber was sealed again, pumping resumed and SEM measurements continued. Later on, the results from the emulsion tests confirmed that indeed very few antiprotons reached the end of the line, approximately only 0.4 $\bar{p}$ /mm^2/shot. The duration of the $\bar{p}$ pulse from the AD is 200 ns at extraction. Note that the AD intensity of $3{\cdot}10^7$ $\bar{p}$/pulse gives a flux after the beam degrader foil of about 10^7 [123].

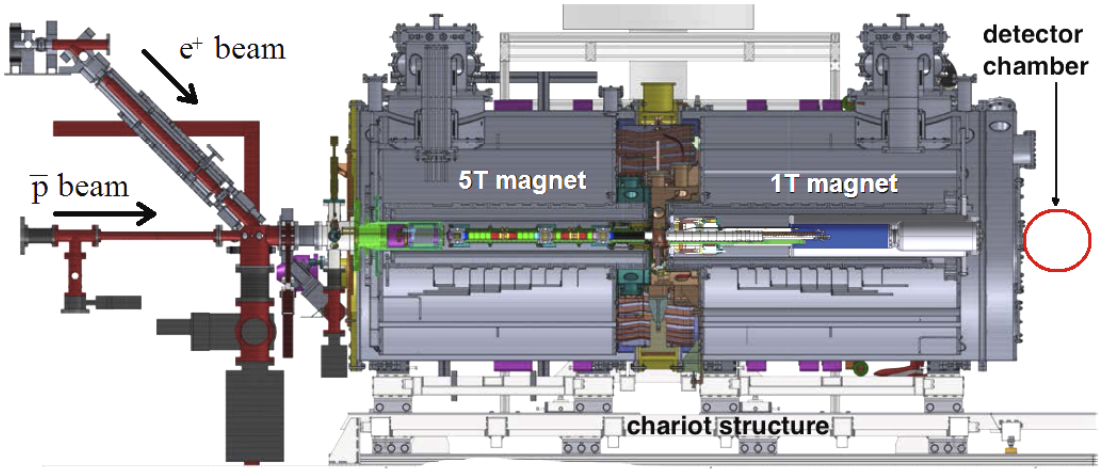

Figure 6.6: Layout of the AE$\bar{g}$IS experiment. Modified image taken from [59].

This particle beam consisted mostly of the higher energy $\bar{p}$ and because the beam focus at the degrader is at the entrance of the 5 T magnet, this beam will continue in a slightly divergent manner through the 5 T magnet and the 1 T magnet downstream. For reference, the AE$\bar{g}$IS set-up is shown in Fig. 6.6.

During the first $\bar{p}$ shots, biasing was optimized for the MCPs (gain) and phosphor screen (luminescence), and the exposure time of the camera was tuned reaching the following nominal settings:

- MCP stack biased at +1.95 kV
- Phosphor screen biased at +4.75 kV
- Camera exposure time between 2 and 10 ms

MCP Stand-alone Configuration

In this configuration, the two-stage MCP is tilted at 45° with respect to the beam, together with the phosphor screen stacked right behind it, and this stack is also at 45° with respect to the camera, as shown in Fig. 6.7. This 45° orientation preserves the beam aspect ratio as seen from the camera.

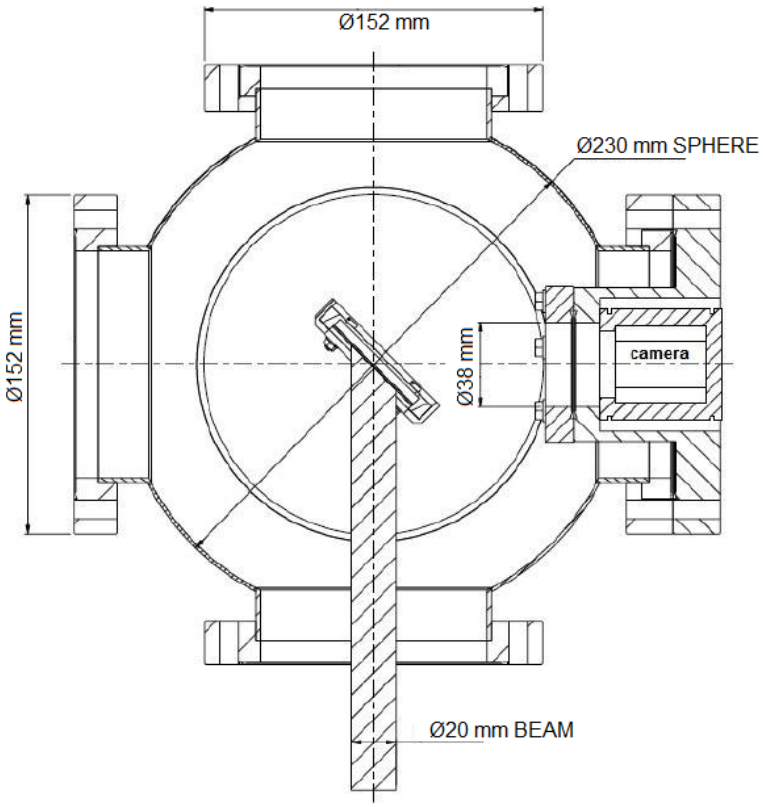

Figure 6.7: Drawing of the detector chamber with the SEM monitor in MCP stand-alone configuration. The camera is installed outside vacuum, facing the phosphor screen of the monitor through a view port.

In this initial part of the test, traces of antiproton annihilations were observed, as well as evidence of other particles. It was possible to switch between measuring only the annihilation products or measuring all the beam by opening/closing the gate vacuum valve immediately upstream of the detector chamber. Antiprotons were annihilated in the closed gate valve, whereas some annihilation products such as pions can make it through to the detector. Some example images are shown in Figs 6.8 and 6.9.

In these pictures, the magnets' B-field was off, the beam degrader foil was in and the Faraday cup was out of the beam path. All these devices are located upstream of the detector chamber. In all these images a dark spot is always appearing. This corresponds to damage in the MCPs due to vacuum discharges. The red circle in the

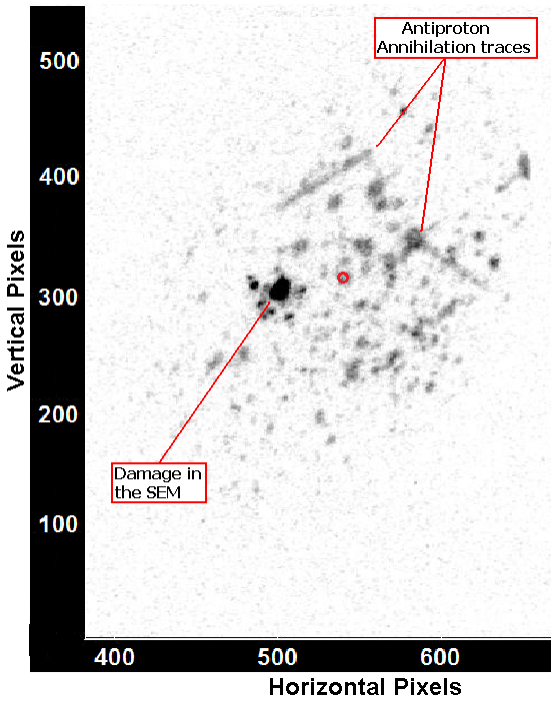

Figure 6.8: Antiproton annihilation traces in the SEM when the antiproton beam hits the MCPs directly. The red circle represents the "centre of mass" of the beam captured in the image.

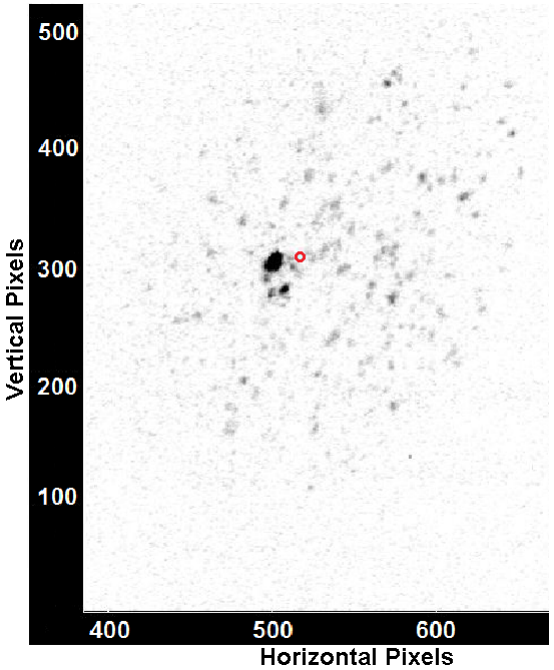

Figure 6.9: Secondary particle traces hitting the MCPs with the gate valve closed (No antiprotons). The red circle represents the "centre of mass" of the beam captured in the image.

images represents the calculated "centre of mass" of the beam image.

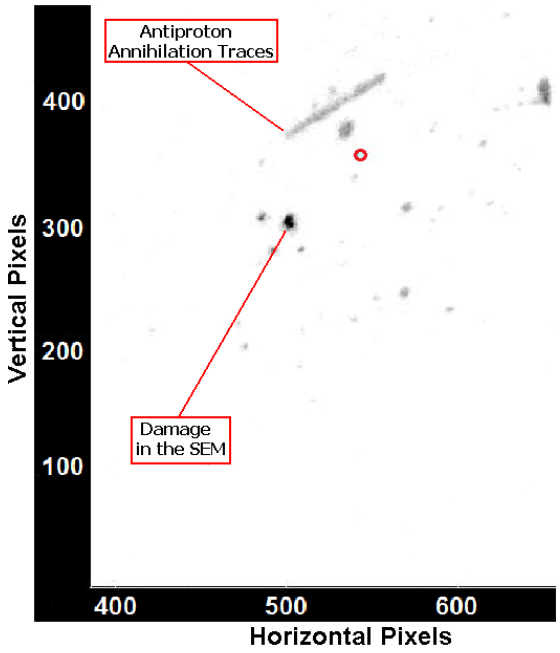

Figure 6.10: Antiproton annihilation trace obtained with the SEM in the MCP stand-alone configuration.

More examples of $\bar{p}$ annihilations in this configuration of the SEM can be seen in Figs. 6.10 and 6.11.

From the experimental data, after background substraction and superimposition of 20 consecutive images for statistics, annihilation events can be clearly seen when the MCP/Phosphor is exposed directly to the antiproton beam of the AD, as shown in Fig. 6.12. The 1 T and 5 T magnets were not ready to work back then, therefore the antiproton beam was severely defocused in this beam run and perhaps was larger than the 42 mm of the active diameter in the phosphor screen. It was unclear if the antiproton beam being monitored by the SEM was the core of the beam or the tail of it.

Foil-based SEM Configuration

In this second configuration, the foil+mesh assembly is put in front of the MCP/phosphor stack, at a distance of 52 mm. This distance is a compromise between the spatial resolution and the maximum beam diameter that can be observed. With this assembly, it is ensured that a beam as large as 20 mm in diameter can be monitored. The thin foil of the assembly was connected to channel 3 of the power supply and biased to -9 kV to allow all electrons produced in the foil to accelerate past the mesh towards the

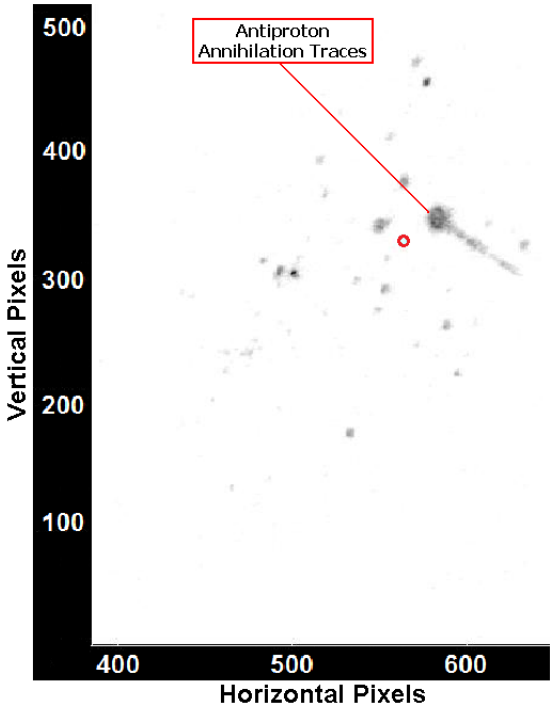

Figure 6.11: Antiproton annihilation trace obtained with the SEM in the MCP stand-alone configuration.

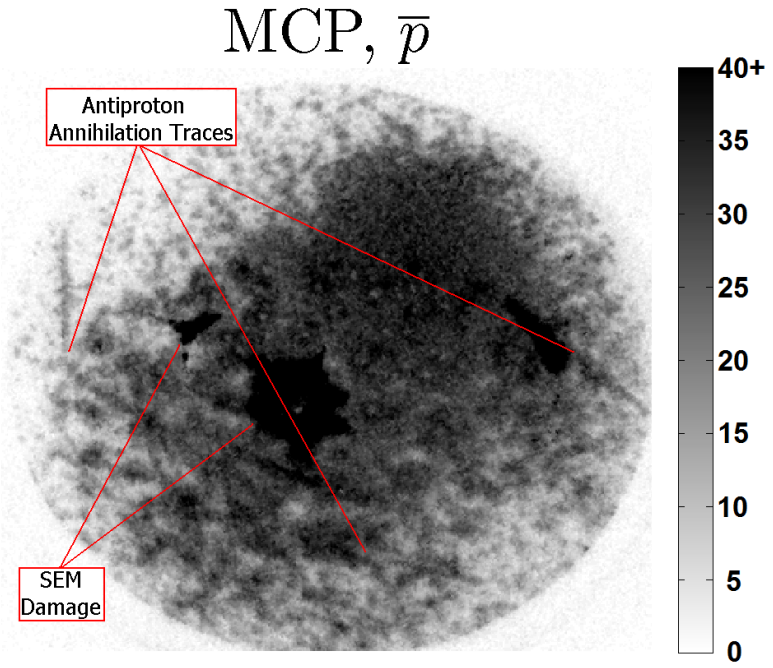

Figure 6.12: Antiproton beam detected by the SEM in the MCP stand-alone configuration. Scale in 8-bit grayscale palette.

MCPs. According to previous simulation studies, the spatial resolution of the monitor when the foil is biased to -9 kV is around 2 mm FWHM [114]. The concept of this configuration can be seen in Fig. 6.13.

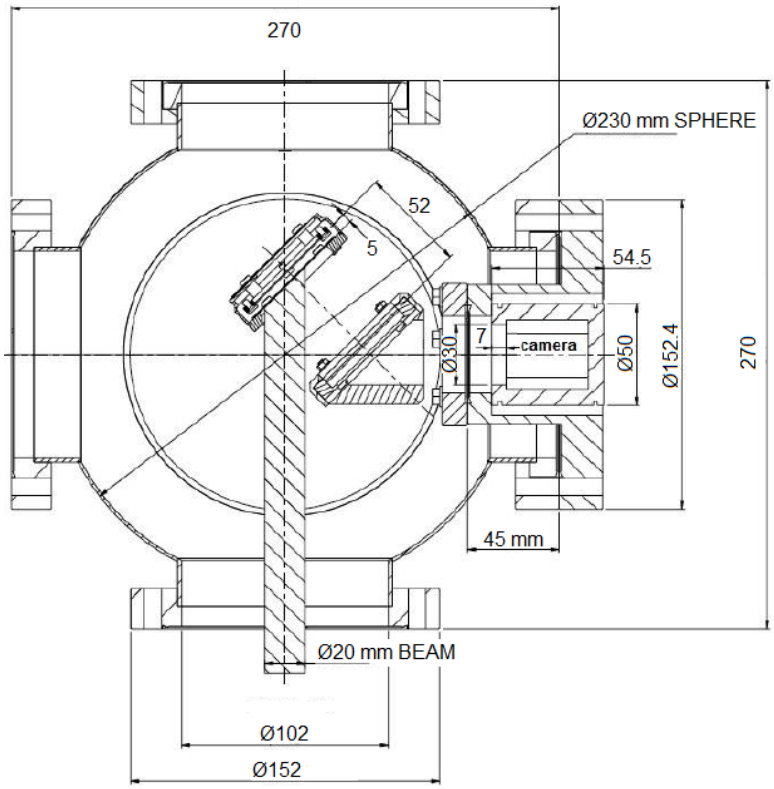

Figure 6.13: Drawing of the detector chamber with the SEM monitor in the foil-based configuration. The camera is installed outside vacuum, facing the phosphor screen of the monitor through a view port.

In Fig. 6.14, an image of the $\bar{p}$ beam with the foil-mesh assembly is presented. Damage in the SEM is visible as in the previous configuration. In this foil-based configuration, the average intensity of the recorded images is lower than in the previous configuration, as expected due to a more indirect measurement method using the secondary electrons generated in the foil. From the experimental data, after superimposition of consecutive images for statistics, secondary particles can be seen when the foil-based SEM is exposed to the antiproton beam of AE$\bar{g}$IS, as shown in Fig. 6.15. The maximum pixel intensity recorded by the SEM in this configuration is approximately half of the intensity recorded in the previous MCP stand-alone configuration.

Although the antiproton beam from the AD was successfully monitored with both configurations of the SEM, the beam conditions were insufficient in order to measure beam profiles. The $\bar{p}$ beam was blown-up after the 1 T magnet, likely covering all the

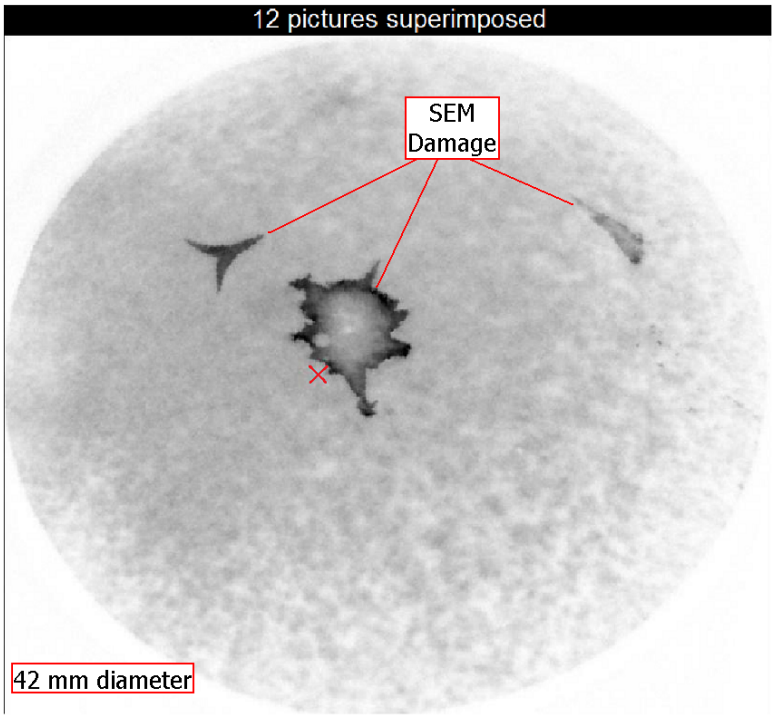

Figure 6.14: Image superimposition of 12 pictures showing secondary particles detected with the foil-mesh assembly. Foil voltage= -9 kV. The red cross represents the "centre of mass" of the beam captured in the image.

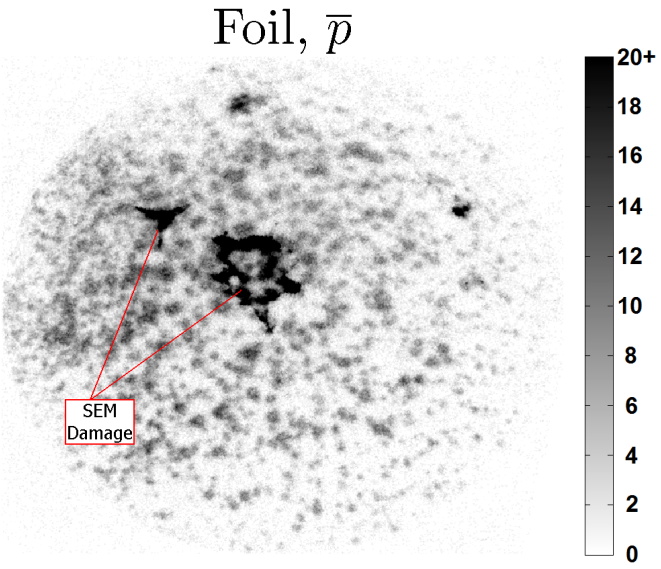

Figure 6.15: Antiproton beam detected by the SEM in the foil-based configuration. Scale in 8-bit grayscale palette.

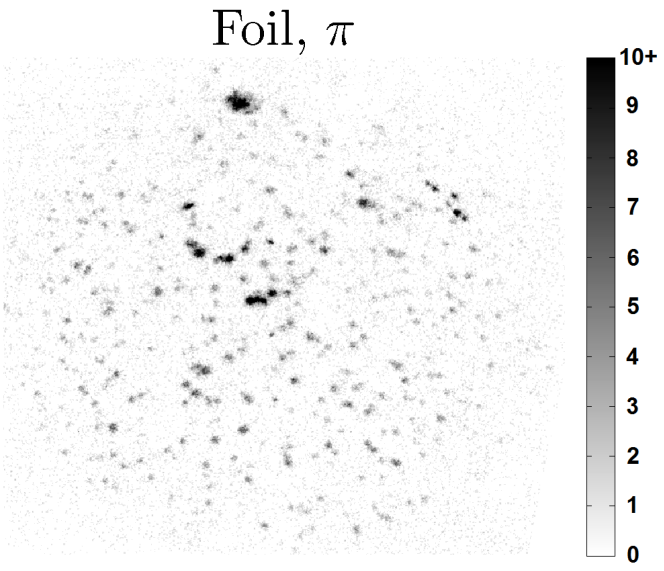

Figure 6.16: Antiproton annihilation products detected by the SEM in the foil-based configuration with the gate valve closed. Scale in 8-bit grayscale palette.

active area of the detector and the beam was particularly difficult to steer on axis. In future measurements, it would be interesting to measure in the same location of AE$\bar{g}$IS but with the 1 T and 5 T magnets switched on to prevent the antiproton beam from blowing up. Another possibility would be to install the SEM in a waist location of the AD lattice according to its beam optics to have a smaller beam size that would allow easier detection with the SEM.

The advantage of the SEM is that it can easily be inserted in the beam path to measure transverse beam profile, and the intensity of the image can be easily tuned by biasing the MCPs or the phosphor screen. Its main limitations are its relatively large volume, its increased complexity compared to other detectors and a cost two orders of magnitude higher than the nuclear emulsion detector. With these features, the SEM seems an ideal detector for beam steering into experimental stations in low-energy antiproton facilities such as the ELENA ring.

6.2 Nuclear Emulsions

A schematic showing a vertex detector proposed for the AE$\bar{g}$IS experiment is shown in Fig. 6.17. The vertex detector is made of nuclear emulsions. This detector will be used to measure the vertical deflection of the antihydrogen atoms on the gravitational field of the Earth at AE$\bar{g}$IS. A time of flight detector is needed downstream to measure the velocities of the antihydrogen atoms, and to record the approximate position of the

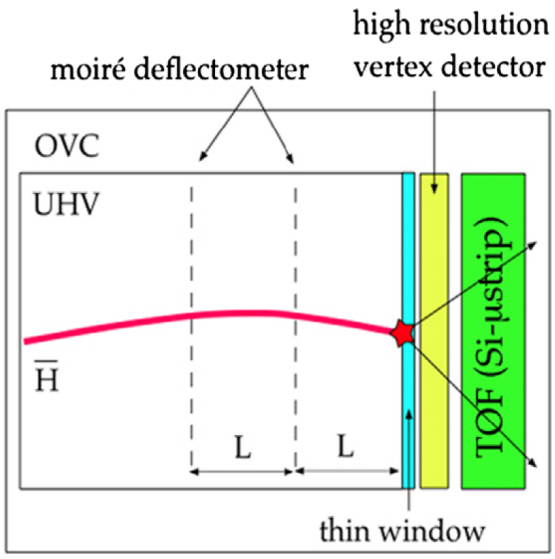

Figure 6.17: Schematics of the vertex detector (Nuclear emulsions) and the ToF detector. Image taken from [124].

annihilation vertex. The thin window in the detector chamber, a 2 μm titanium foil, limits the position resolution due to multiple scattering, but is needed to separate the ultra-high vacuum part, at a level of 10^{-9} mbar, from the outer vacuum region, at 10^{-6} mbar, containing the emulsion films. This is a novel application of emulsion films [125] and the first time that nuclear emulsions are used in a vacuum environment.

The emulsion detector is composed of two sensitive emulsion layers coated with a substrate on the inner side, as presented in Fig. 6.18. A protective gelatin layer 1 μm thick covers the outer surfaces. The detection units are silver bromide crystals 0.2 μm in diameter homogeneously distributed in the gel, which upon excitation by a charged particle, show filaments of Ag atoms. These images are then digitized with an optical microscope. Using a PC, a tracking algorithm searches the digitized images for aligned sequences of grain clusters. A linear fit is then performed to define the position and angle of the microtrack which crosses the emulsion layer. Due to distortions along the particle trajectory, the microtrack cannot be used directly. Instead, a search is made for a matching microtrack in the opposite layer and the annihilation track is defined by the straight line joining points A and B, see Fig. 6.18.

The average energy of the antiprotons reaching the nuclear emulsions detector at the end of AE$\bar{g}$IS was around 100 keV, which corresponds to a range of $\sim$1 μm in the emulsion detector. Therefore, the antiprotons were annihilated at the surface of the emulsion detector. The annihilation detector was installed in a small vacuum chamber shown on the left of Fig. 6.19. The chamber had an inner diameter of 100 mm and the distance from the gate valve to the detector was 114 mm. The emulsion films

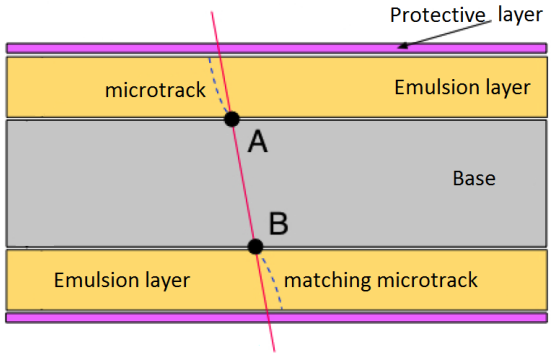

Figure 6.18: Schematic of the nuclear emulsions detector. Modified image taken from [62].

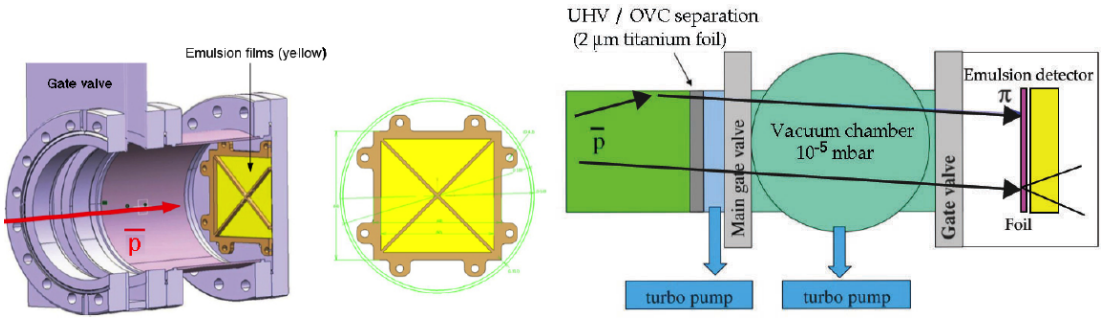

Figure 6.19: Left: vacuum chamber containing the nuclear emulsions detector. Right: beam line set-up. Secondary particles, mainly pions, are generated by antiprotons annihilating in the upstream part of AE$\bar{g}$IS or directly in the emulsion detector. Modified image taken from [62].

were held by a stainless steel frame known to be chemically compatible with emulsions. The detector chamber was closed with a gate valve located upstream for mounting and dismounting without breaking the AE$\bar{g}$IS vacuum, and to protect the films from light exposure.

Emulsion detectors can measure the vertical precision on the measured annihilation vertex of antihydrogen atoms in the AE$\bar{g}$IS experiment with a precision around 1 μm, which is an order of magnitude better than the position sensitive detector originally proposed in the AE$\bar{g}$IS design study [53, 54]. Vertex resolutions in the range of 1 μm have been obtained which, when combined with the time of flight measurements, lead to an order of magnitude reduction of the data taking time originally foreseen to reach the goal of 1% uncertainty in $\frac{\Delta g}{g}$ [62].

Among the advantages of nuclear emulsions as position sensitive detectors are their high position resolution, relatively low cost of a few hundred pounds, possibility to make large size detectors if required, no need for in-vacuum connections for voltage or readout and their 3D directional measurements. The two main disadvantages of nuclear emulsions are their lack of timing information on the events detected and their offline nature. The nuclear emulsions need to be removed from the detector chamber and readout of the events must be done with a microscope connected to a PC, which is time consuming, as this process may take up to 48 hours.

6.3 Silicon Detectors

According to the AE$\bar{g}$IS design report, the position sensitive detector that will be used to measure the gravitational acceleration for antihydrogen at AE$\bar{g}$IS is composed of an active silicon detector, where annihilations take place, followed by an emulsion detector. The silicon detector is required to provide online measurements of the antiproton annihilations, as well as the time of flight information needed to calculate the effect of gravity on antihydrogen. This kind of antiproton annihilations on a silicon detector has been observed only once, in an experiment which has made use of antiprotons with a momentum of 608 MeV/c in a non-segmented detector [126].

In AE$\bar{g}$IS, the silicon detector will act as the annihilation surface. As the kinetic energy of antihydrogen atoms in AE$\bar{g}$IS, of the order of 100 mK, will be insufficient to detect their signal, antihydrogen will be indirectly detected through the detection of its annihilation products. The silicon detector will also act as a separation membrane between the ultra-high vacuum region of the antihydrogen trap and the high vacuum region where the emulsion detector will be located, exactly as the Ti foil in these tests shown in Fig. 6.19. The maximum active thickness of the silicon detector must be

50 μm in order to minimize the scattering of the annihilation products to be detected downstream in the emulsion detector. In addition, in order to avoid the black body radiation from the silicon detector increasing the thermal velocity of the incoming antihydrogen, the whole detector assembly will be kept at cryogenic conditions, with a $T \leq$77 K.

Several different silicon detector technologies have been tested in the antiproton beam run of December 2012, before the first long shutdown at CERN. Among them, a 3D pixel sensor and the Minimum Ionizing MOnolithic active pixel sensor for the TERA foundation (MIMOTERA) detector, a type of ultra-thin pixel sensor [127]. These detectors allow for the first ever study of annihilation of low-energy antiprotons on silicon. Antiproton annihilations were identified using the 3D pixel detector. Extensive amounts of data were acquired and compared with simulation results [59].

6.3.1 MIMOTERA

The MIMOTERA is characterized by its large area, of 17x17 mm^2, low granularity with each square pixel being 153 μm in size, and a dynamic range of over 3 orders of magnitude. The MIMOTERA has been designed to be virtually unaffected by cross-talk, due to the presence of multiple readout diodes for each pixel of the detector [59].

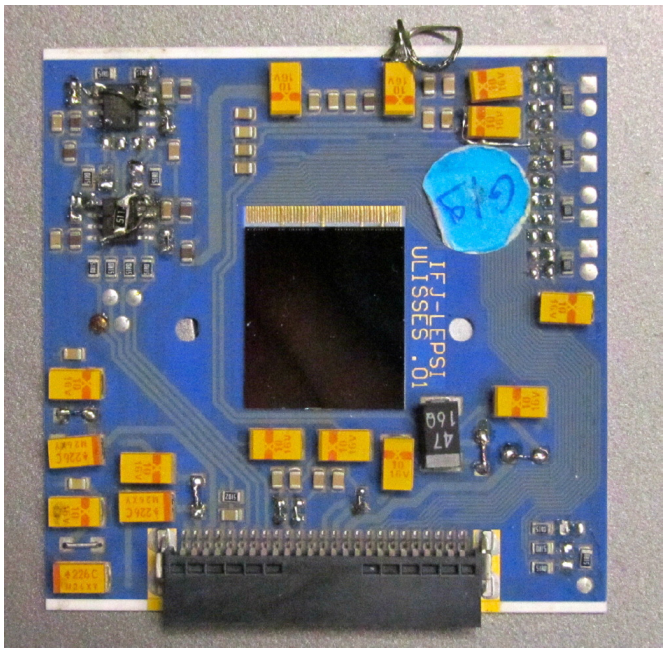

Figure 6.20: The MIMOTERA mounted on its PCB. The active area of the detector is 17.136×17.136 mm^2. Image taken from [59].

The MIMOTERA mounted on its PCB board is shown in Fig. 6.20. The epitaxial layer is only 14 μm thick and has an entrance window of about 100 nm [127]. This is possible by using a thin Si wafer and back-thinning it. The sensor consists of 112×112 = 12,544 pixels, each with a size of 153×153 μm^2. This leads to an active area of 17×17 mm^2, which is divided into four sub-arrays of 28×112 pixels that are read out in parallel. The clock rate for the readout for a single pixel can be set in LabView as 2.5, 5, 10, and 20 MHz [127]. At the maximum setting the readout of one sub-array therefore takes 50 ns×(112+2)×(28+2)= 170 μs. As the four sub-arrays are read out in parallel, this is identical to the readout time for one frame of the whole detector. In the following measurements a clock rate of 2.5 MHz per pixel has been chosen, which leads to an integration time of 1.4 ms [127].

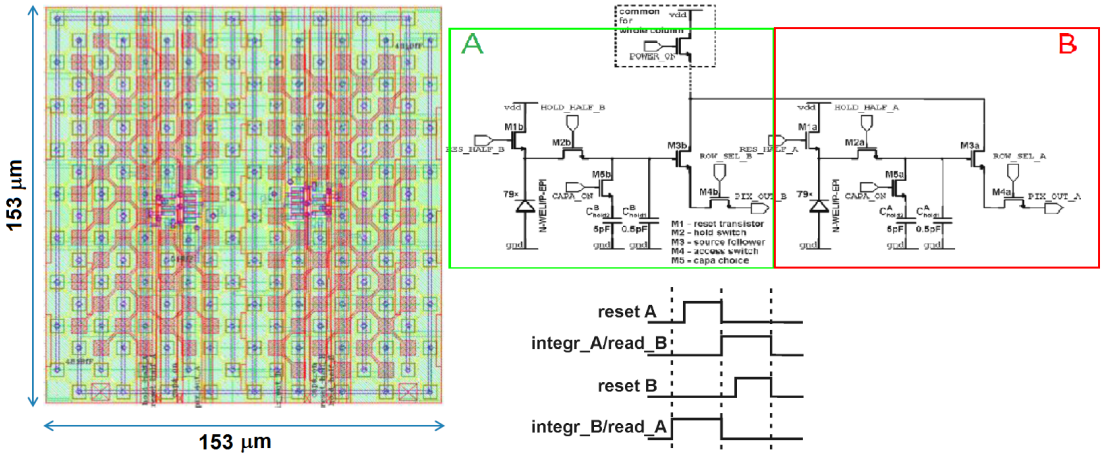

Figure 6.21: Layout of a MIMOTERA pixel and charge collection scheme. Image courtesy of N. Pacifico.

The design of a single pixel of the MIMOTERA detector makes it a unique device. Each of the pixels consists of 2×81 diodes, 5×5 μm^2 each, building two independent readout matrices. This architecture makes MIMOTERA a detector with no dead time: while matrix A is collecting the generated charge carriers, the charges stored in the diodes of matrix B are read out, the diodes are reset, afterwards the process is inverted. Hence, no signal charges get lost during the readout and the detector is free of dead time [127]. A layout of a single pixel of the MIMOTERA and the readout schematic are shown in Fig. 6.21.

The small thickness of the active region of the MIMOTERA detector allows to collect more than 98% of the generated charge carriers. The single pixel noise level was measured by the MIMOTERA group to be 30.3 keV [59].

A sample raw frame of experimental data taken with the MIMOTERA is shown

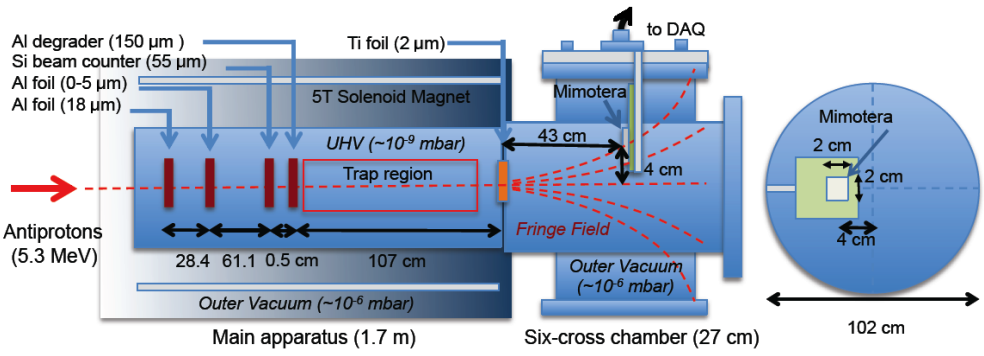

Figure 6.22: Schematic of the experimental set-up. The centre of the Si detector is mounted 40 mm off axis and 430 mm from the AE$\bar{g}$IS device. Modified image taken from [59].

in Fig. 6.23. Antiprotons impinging or annihilating in the detector were identified by clusters of neighbouring pixels. Only signals exceeding 150 keV, or 5 standard deviations of the noise level, were considered. The aluminium foils covering the detector were used to study the energy loss of antiprotons in silicon. Some in-plane tracks were also observed with the MIMOTERA detector, i.e., antiproton annihilation tracks developing in the plane of the active region of the detector. Annihilation products were identified calculating the range and $\frac{dE}{dx}$ for the most important species produced in antiproton annihilations.

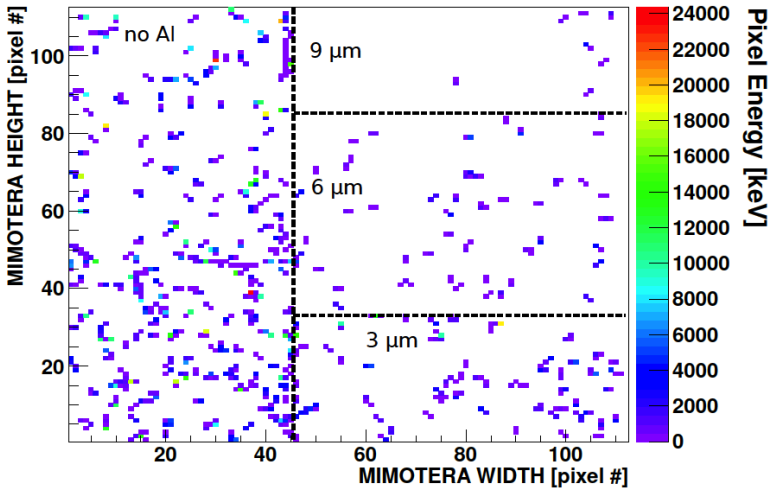

Figure 6.23: Sample of a raw triggered frame after applying a noise cut of 150 keV and excluding one-pixel clusters. Around 60% of the detector was covered with aluminium foils with a thickness of 3, 6 and 9 μm. Image taken from [59].

The MIMOTERA detector was used to measure annihilations of low-energy antiproton beams for the first time. This is an important milestone and the first step on the way to designing a position sensitive detector for measuring the gravitational

acceleration for antihydrogen. These results allow the identification of methods to determine the position of the annihilation vertex, both by position extrapolation from antiproton tracks and centre of mass methods. It also serves as the basis for simulations and design of the first prototype antihydrogen silicon detector for AE$\bar{g}$IS. More detailed results from this antiproton beam run in AE$\bar{g}$IS by the MIMOTERA group were published in [59].

The main advantages of the MIMOTERA as a particle detector include its large active area and pixel resolution, and its lack of dead time which makes it an ideal detector to acquire timing information of particle events. The MIMOTERA detector is not suitable for absolute beam energy measurements when working alone due to its thin active layer of only 14 μm, but it is well suited as a time-of-flight detector which could be used in pairs to measure absolute beam energy in many particle accelerators, not just antiproton machines, if the drift distance to each detector is known accurately.

The main limit of the MIMOTERA detector is its position resolution. When used with low-energy antiproton beams, the position resolution of the MIMOTERA detector is approximately 20 pixels, which corresponds to $\pm$3 mm [127].

6.3.2 3D Pixel Sensor (CNM 55)

While the small thickness and the relatively low granularity of the MIMOTERA detector, only 153 μm of pixel pitch, was important to determine the typical energy range of the clusters and thus the needed dynamic range of the final detector, it is highly desirable to study the particle tracks in more detail to better understand the achievable resolution of the annihilation point. For this reason, a thicker pixelated detector was tested by the AE$\bar{g}$IS collaboration.

Pixel detectors with cylindrical electrodes that penetrate the silicon substrate, so-called 3D detectors, offer advantages over standard planar sensors in terms of radiation hardness, since the electrode distance is decoupled from the thickness of the active volume of the detector. The 3D pixel sensor (CNM 55)[129], shown in Fig. 6.24, was installed in the chamber after the MIMOTERA measurements. The installation was done in the same way as for the MIMOTERA detector, providing similar beam conditions as in the MIMOTERA beam run. This 3D pixel sensor and the readout ASIC [130] were originally designed for the B Layer [131] currently being installed at the ATLAS [132] experiment at CERN, optimised for looking at high energy particles from events occurring every 25 ns. This technology offered interesting features relevant for this application. The sensor consists of 80 columns x 336 rows = 26,880 cells [133]. The

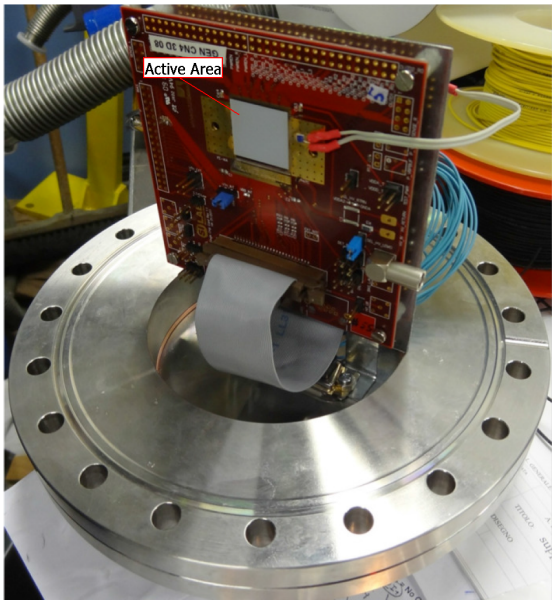

Figure 6.24: CNM 55 3D Pixel sensor mounted on a single chip card. The whole system is mounted on a flange before being installed in the six-way-cross CF vacuum chamber. Image taken from [128].

pixel size is 250×50 μm^2 and the electrodes have a diameter of 10 μm. The thickness of the active volume is 230 μm and its passivation layer is ∼3 μm thick and composed of three layers of material: 1.5 μm Al, 0.8 μm doped polysilicon and 1.150 μm thermally oxidized silicon, one on top of the other.

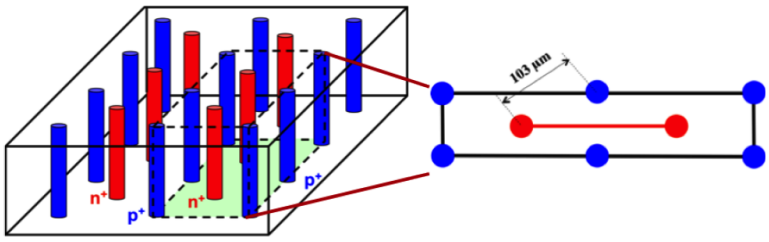

Figure 6.25: Schematic view of the 3D pixels illustrating the electrodes in the CNM 55 sensor. Each pixel consists of two readout electrodes, shown in red, and six ohmic electrodes, shown in blue. Image taken from [128].

A schematic view of the architecture of the pixels is given in Fig. 6.25. The volume within the dashed lines represents a single 3D pixel consisting of two readout n-columns surrounded by six ohmic p-columns. The 3D design of the electrodes results in a higher average electric field between the electrodes and a shorter collection path, which is the reason for a larger signal to noise ratio than the one for the planar pixel technology. The USBpix hardware, used for the readout, is based on a multi-purpose IO-board, called S3MultiIO, with a USB 2.0 interface to a PC and an adapter card which connects

the S3MultiIO to the Single Chip Adapter Card (SCC), where the FE and the sensor are mounted [134]. The S3MultiIO system contains a programmable Xilinx XC3S1000 FG320 4C FPGA, which provides and handles all signals going to the FE chip. More details about the architecture of the pixels can be found in [128].

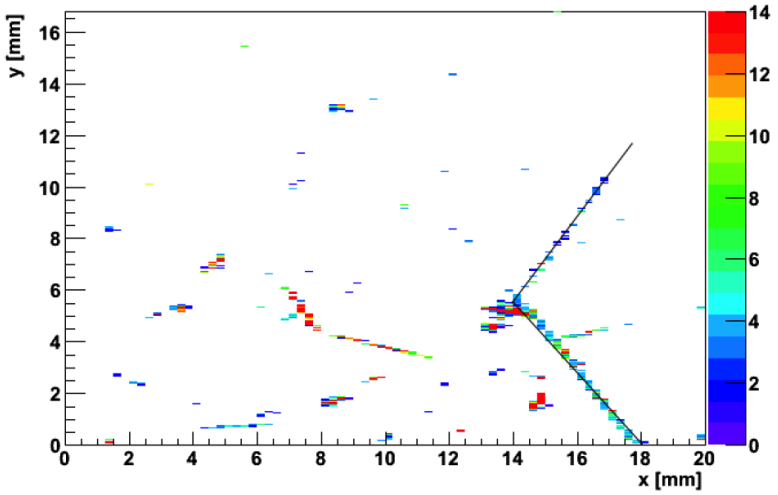

Figure 6.26: Sample frame of the 3D sensor with two fitted proton tracks coming from an antiproton annihilation. Annihilation tracks as these shown here are used to reconstruct the annihilation point. Image taken from [128].

Tests of the 3D pixel sensor provided valuable material for further analysis of antiproton annihilations in silicon, in particular of the annihilation prongs. As the two detectors were installed in the same position in the vacuum chamber, the energy distributions for the incoming antiprotons were very similar. A raw frame showing the acquisiton of antiprotons is shown in Fig. 6.26. When compared to a typical acquisition frame of the MIMOTERA detector tested, more and longer tracks can be observed, as a result of the thicker active volume. Antiproton annihilation tracks are more likely to be observed due to the higher geometrical acceptance for annihilation products travelling at angles different from that of normal incidence.

Cluster energy is lower than what was observed with the MIMOTERA detector. This is due to a thicker passivation region, which is more likely to stop heavy fragments that would produce high energy deposits, and also due to saturation of the single channel amplifiers. The measured charge is thus expected to be lower than the charge effectively deposited in the bulk of the detector in some cases.

When travelling through the 3D pixel sensor, antiproton annihilation prongs produce tracks from a few mm up to 1.5 cm long. The annihilation point can therefore be reconstructed by fitting the tracks and the error on the annihilation point calculated.

The position resolution achieved with the CNM 55 sensor is 56.5 μm on the X axis, with a pixel size of 250 μm, and 24.3 μm on the Y axis, with a pixel size of 50 μm [128]. The resolution on the position could be further improved by using weighted fitting algorithms accounting for the charge of the pixels composing the tracks. However, a sensible application of such algorithm would require no saturated pixels composing the annihilation tracks. Future work with this detector includes a better tracking algorithm for antiproton annihilations and improved cluster analysis.

6.4 Optimizing Instrumentation for Low-energy Antiproton Beams

ELENA and the future beamlines at other facilities like FLAIR will require a full set of beam instrumentation devices. The measurements presented in this section allow comparing and defining a full set of instruments to diagnose low-energy antiprotons. This section will discuss which of the previously discussed diagnostics devices and which locations are best suited for a permanent installation on the LNE02 low-energy beam line and the subsequent AE$\bar{g}$IS experiment in order to fulfil its goals. The ELENA ring will provide 100 keV antiproton beams to several different experimental beam lines, as shown in Fig. 6.27.

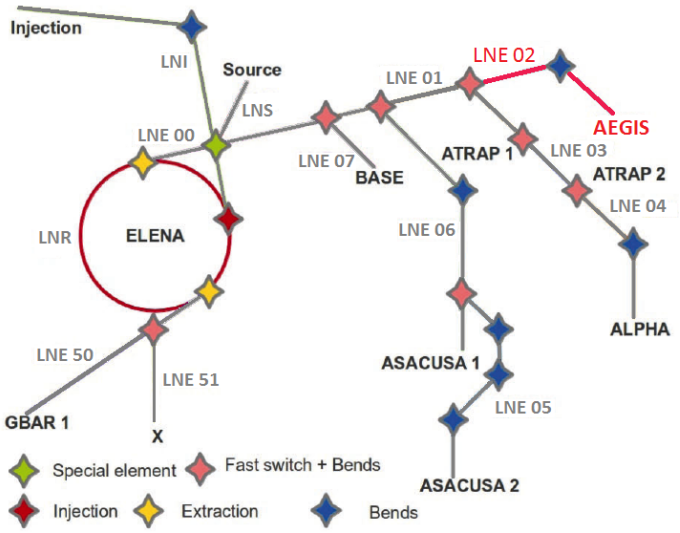

Figure 6.27: A sketch showing the layout of the different beamlines at the ELENA ring. Modified image taken from [50].

Beam line LNE02 will be 6.9 m long and comprise the following electrostatic elements: 1 bending dipole, 7 matching quadrupoles, 3 FODO quadrupoles and 4 dual-plane correctors [50]. Figure 6.28 shows the optics for the LNE02 line. After the strong

bend, two doublets and a triplet will be installed for beam matching into the experiment. A drift space of around 1 m before the AE$\bar{g}$IS experiment is foreseen.

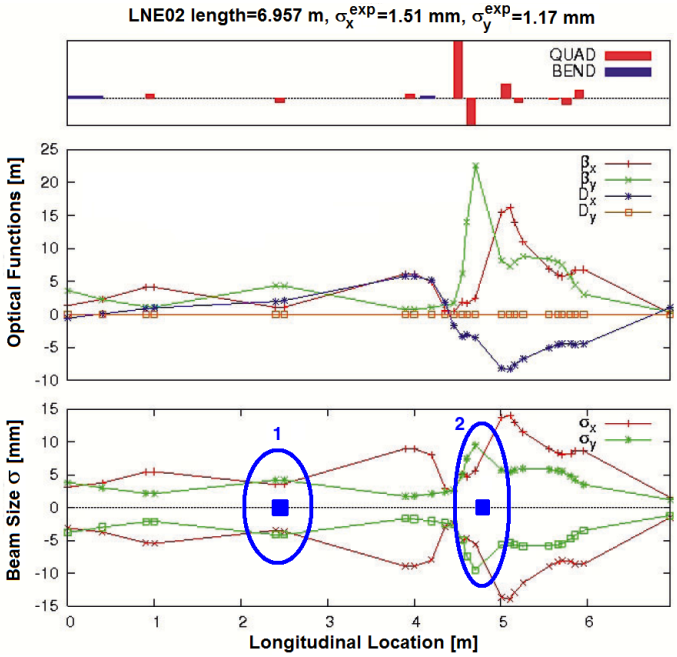

Figure 6.28: The optics and beam sizes of the LNE02 beam line. Proposed locations for beam profile monitors are circled in blue. Image taken from [50].

In order to adequately measure transverse beam profile and beam size, beam profile monitors could be installed in beam line LNE02. Suggested locations for beam profile monitors in this beam line are presented in Fig. 6.28. A first monitor could ideally be located before the bending element, in the area between metres 2 and 3 of the LNE02 beam line where the beam size in the horizontal plane matches that of the vertical plane. A suitable location for a second beam profile monitor could be just after the two dual-plane correctors towards the end of the line, where the beam size in both planes is relatively large, with σ_x±10 mm and σ_y±5 mm. This would ensure a proper beam monitoring before final steering into the AE$\bar{g}$IS experiment. The SEM could accomplish this task. With its 42 mm active area, it can easily be inserted in and out of the beam path to monitor the beam. If enough space is available for the SEM, it could be used in the foil based configuration, which would extend the lifetime of the MCPs and phosphor screen, as these would not be directly exposed to the beam. The SEM is an on-line beam profile monitor capable of monitoring the antiproton beam delivered from the AD facility into the AE$\bar{g}$IS experiment, with a beam energy ranging from 100 keV to 5.3 MeV and intensities of around $3{\cdot}10^7$ antiprotons in single bunches 120 ns long and delivered every 100 s. As antiprotons will be extracted at 100 keV from the ELENA ring [50], the SEM is a good candidate to monitor the low-energy antiproton

beam delivered by the ELENA ring.

Ideally, a permanent antihydrogen detector for the AE$\bar{g}$IS experiment should detect the annihilation points with high position resolution and also give timing information of the events. A nuclear emulsions detector such as the one discussed earlier in the chapter could fulfil this mission with the highest position resolution of all the detectors mentioned, i.e., 1μm. Instead of the 2 μm titanium foil required to separate the ultra-high vacuum part from the outer vacuum region, a thin Si detector such as the MIMOTERA could be used as an entrance window for the nuclear emulsions detector. This would keep the nuclear emulsions in place and at the same time provide timing information of the arriving antihydrogen atoms. This would be at the cost of limiting the position resolution on the annihilation point to some extent due to scattering.

6.5 Chapter Summary

Several antiproton detector technologies were successfully tested by different research groups in a dedicated detector chamber in AE$\bar{g}$IS during the antiproton beam run of December 2012. In the work leading to this thesis, the low-energy antiproton beam as well as single annihilation events were detected using two different configurations of the SEM. For the first time, the stand-alone MCP configuration was successfully tested, showing clearer beam images, but introducing background from antiproton annihilation products, mostly pions. The SEM offers charge differentiation when used in the foil based configuration and it is expected to exhibit a longer lifetime compared to the MCP stand-alone configuration, as the MCP and phosphor screen are not exposed to the beam directly. Among its main disadvantages, the SEM is relatively larger than the other diagnostic devices and it also has an increased electric and mechanical complexity with its multi-channel power supply. The electric field in the detector can influence the particle beam, creating distortions in the beam position anywhere from 0.6 mm to 8 mm for a 300 keV and 20 keV antiproton beam, respectively.

The SEM was the only on-line beam imaging monitor in the latest AE$\bar{g}$IS run and the only one sensitive enough for the initial low-intensity beam steering necessary to commission the detectors from the other groups. These measurements were destructive for all detector technologies and configurations. The SEM is therefore an important beam imaging monitor for antiproton facilities, providing support to the delivery of beam to the experiments.

The AE$\bar{g}$IS collaboration measured promising results with the nuclear emulsions detector for its use as a future annihilation detector. Data of antiproton annihilations

are taken off-line and the antiproton annihilation vertex can be measured with a precision of 1 μm, much better than the 56.5 μm obtained with the 3D silicon detector tested. It was the first time that this nuclear emulsion technology was used in a vacuum application. The main advantages of nuclear emulsions as position sensitive detectors are their high position resolution, relatively low cost of a few hundred pounds, possibility to make large size detectors if required, no need for in-vacuum connections for voltage or readout and their 3D directional measurements. Its main drawback is the lack of timing information of the events and its slow readout speed, requiring up to 48 hours to complete the data readout. Overall, the nuclear emulsions detector is a suitable candidate for the future position sensitive antihydrogen detector in AE$\bar{g}$IS.

Two types of silicon pixel detectors with different electrode geometries were tested by the AE$\bar{g}$IS collaboration to study antiproton annihilations in silicon and to characterize their performance as future permanent detectors in the AE$\bar{g}$IS experiment. The singular architecture of the MIMOTERA detector makes it a detector with essentially no dead time. This makes it an ideal detector to gather the necessary time of flight information to calculate the gravitational acceleration of antihydrogen in the AE$\bar{g}$IS experiment. Due to its small thickness and low granularity, the MIMOTERA detector is suitable for analyses on the deposited energy in the form of energy clusters. The main disadvantage of the MIMOTERA detector is its very thin active layer, which limits the detector's capability to measure absolute beam energy, and the fact that its single-channel amplifiers tend to saturate easily.

Data taken by the 3D silicon detector group showed a good position resolution on the annihilation point of 56.5 μm on the X axis and 24.3 μm on the Y axis, and a detailed study of the various tracks produced by the annihilation prongs. Identification of tracks from annihilation prongs is possible up to 2.9 mm in the case of MIMOTERA and up to 15 mm long in the case of the 3D pixel sensor. Their main results were published in [59] for the MIMOTERA and in [128] for the 3D pixel sensor.

Taking advantage of the experimental results from all detector groups, I have combined my findings from the analysis of all detector performances to instrument the LNE02 low-energy beamline leading to the AE$\bar{g}$IS experiment as an example of permanent installation of beam instrumentation devices for this part of the facility.

Chapter 7

Conclusions

In the framework of this PhD thesis, a series of beam instrumentation devices have been studied and characterized for their permanent use in different accelerator facilities. At the ISOLDE facility, a series of purpose-built diagnostic boxes will house all the devices required to successfully monitor the beams to be delivered in the future HIE-ISOLDE superconducting LINAC.

In Chapter 1, an overview of the different accelerator facilities related to this research work is given. Regarding ion facilities, a brief history of the ISOLDE facility and its achievements is presented, in addition to a description of the REX-ISOLDE post-accelerator and a detailed summary of the main elements of the upgrade of ISOLDE, the HIE-ISOLDE project. In order to introduce the reader to the series of tests carried out with instruments monitoring antiproton beams, a description of the AD facility and the AE$\bar{g}$IS experiment is given, including the AD beam cycle, antihydrogen production scheme of AE$\bar{g}$IS and the future addition of the ELENA ring. Table 1.2 summarizes the main beam parameters at the ELENA ring.

Chapter 2 presents the status of the beam diagnostics system at REX-ISOLDE along with its performance limits. The system comprises a set of collimator wheels, the REX-ISOLDE Faraday cup, the REX-ISOLDE beam profile monitor and the NTG emittance meter. In addition, tests carried out with the PIPS Si detector to be used at the HIE-ISOLDE Linac and a study of a PIN photodiode as a possible diagnostics tool for the time structure of the beam are presented.

preliminary measurements indicate that the PIN photodiode is responsive to the time structure of the EBIS pulse under the given conditions in the machine. The signal-to-noise ratio appeared to be sufficient to identify the changes in beam pulse distribution even for relatively low-intensity beams. Further tests are needed in order to characterize the performance of the photodiode accurately, but these preliminary

tests indicate that the PIN photodiode could be used as a possible tool in operations to monitor the EBIS pulse.

In Chapter 3, the beam diagnostics system for HIE-ISOLDE is presented. The instrumentation requirements of the HIE-ISOLDE superconducting Linac are presented, and the space constraint between cryomodules is shown as a challenge to be overcome by the diagnostics box and its devices. The working principle of the beam profile monitor using a Faraday cup and the slitscanner is shown in Fig. 3.4.

Section 3.2.1 studies the effect of the slit width of the slitscanner on the beam profiles. Table 3.1 summarizes the effect of slit width on ΔFWHM and on beam transmission. According to the calculations shown, the most favourable slit width for the HIE-ISOLDE slitscanners would be 1 mm. This value is a compromise between measuring a beam profile with little distortion with respect to the original beam and it also allows enough beam intensity to be transmitted to the Faraday cup.

Stress tests on the slitscanner were performed to assess the robustness and precision of the slitscanner. It was made clear that the initial design of the system, guiding the blade on rails with DICRONITE coating, was not satisfactory as it led to jamming of the system under high vacuum conditions. Subsequent tests with the alternative solution, guiding the scanning blade from the outside using a high-precision actuator from AVS proved to be successful. The tests done with the optical test bench used to assess the motion of this new motion actuator showed a maximum excursion for each hole in the direction perpendicular to the blade movement of less than 20 μm. This result was obtained with the scanning blade moving at 5 and 10 mm/s.

A stress test of the slit scanner system was performed moving the actuator at full stroke for 100 cycles, with 1 second pause between each full stroke. The temperature of the stepper motor was monitored during the test and did not rise above 30 °C. A general inspection of the device was done in order to check for signs of wear or any issues related with the design and implementation of the mechanical system. No significant issues were found.

Chapter 4 represents the major priority for the HIE-ISOLDE beam instrumentation system, the development of a short Faraday cup to monitor stable ion beams. A new design of short Faraday cup was required because of the limited longitudinal space available between cryomodules. Starting from a brief geometric model that highlights the importance of an adequate radius-to-aperture ratio, the three prototypes of Faraday cup developed and tested for this project are compared with the standard Faraday

cup from REX-ISOLDE. In the final prototype, Prototype 3, the repeller ring was designed 12 mm thick, increasing the collection efficiency of the cup and measuring beam intensity values that match within 10%, on average, those measured by a longer Faraday cup such as the REX-ISOLDE Faraday cup at different beam intensities and energy ranges. The Prototype 3 Faraday cup is the result of an intensive R&D program involving several experimental tests and numerical simulations in order to satisfy the challenging space requirements of the HIE-ISOLDE superconducting LINAC.

Profile scans done with the slitscanner without beam were performed and the electronic noise observed in the Faraday cup, of $\leq$0.7 pA peak-to-peak, does not appear to be related to the motion of the scanning blade. A transverse beam profile was measured successfully at the very low beam intensity of 17.8 pA.

Numerical simulations to analyse the collection efficiency of the different prototype Faraday cups showed that Prototype 3 reaches full collection efficiency of electrons at much lower bias voltages compared to the previous prototypes despite its compact design. This was a major achievement to ensure an adequate monitoring of the beam intensity in HIE-ISOLDE.

Chapter 5 describes the experimental tests done using two PIPS Si detectors with the aim to acquire an absolute time of flight measurement downstream of the REX-ISOLDE Linac. The absolute beam energy of the ions in the pilot beam with a mass-to-charge ratio of $A/q = 4$ was measured in the energy range 1 MeV $<$ E $<$ 8 MeV. The ToF of the particles in the beam at an energy range of 2.18 MeV/u $<$ E/A $<$ 2.27 MeV/u was determined by time stamping the arrival time in identical Si detectors installed in two separate diagnostic boxes.

The energy spectrum of the REX-ISOLDE pilot beam achieved with the PIPS silicon detector and calibrated with a triple-α source is shown in Fig. 5.8. The suggested rate of particle arrivals to the detector is $\leq$10 kHz. A series of attenuating foils (transmission factor $\sim 10^4$) is required in order to obtain this value at REX. The resolution achieved for the beam energy determination using the Si detector was worse than 3% FWHM in the ion species studied. This energy resolution is lower than the one typically obtained with the bending magnet for particle beams with E/A = 0.3 MeV/u, of 1.5% FWHM.

An absolute ToF measurement was done measuring the relative ToF at two different PIPS detectors in separate boxes located 7.7 m from each other. The final results of the absolute ToF measurements with the Si detectors as a function of the 7GAP3

pick-up voltage are summarized in Table 5.7. The measurement of beam energy with the ToF technique is heavily dependent on the distance between detectors. At very low energies, overlapping of particle bunches can be critical if the distance between detectors is large. This procedure is considered a viable option for phasing the RF cavities should the bunch spacing be increased with the addition of a beam chopper in the HIE-ISOLDE upgrade.

As discussed in Chapter 5, the PIPS silicon detector presents a satisfactory performance and is a suitable detector for energy and timing measurements in HIE-ISOLDE, but it lacks radiation-hardness. In this aspect, other technologies have previously been studied at REX-ISOLDE, like Chemical Vapour Deposition (CVD) diamond for energy and intensity measurements [135]. The main advantages of CVD diamond are its high radiation tolerance, low detector capacitance and high charge mobility. Nevertheless, previous results with single and polycrystalline CVD diamond detectors at REX-ISOLDE showed decreased counting efficiency in the range of 10^2-10^7 pps ($^{12}C^{4+}$ ions) over a relatively short period of time and unstable leakage current that changed from tens of pA to a few nA [135]. The energy resolution of this system (0.6%) is similar to that of the PIPS detector.

Another possible technology to be developed is inorganic scintillators due to their intrinsic radiation hardness. A commercially available inorganic scintillator crystal like YAP:Ce provides a high light yield (21000 photons/MeV), fast rising time (1 ns) and short decay time (30 ns) which, coupled to a photomultiplier tube or to an avalanche photodiode [136, 137] could result in a reliable monitor for counting RIBs in a heavy ion facility like HIE-ISOLDE. The use of a YAP:Ce inorganic scintillator as an ion detector has been successfully tested for α spectroscopy [138]. These low-intensity diagnostic tools are very compact devices that can easily fit in the tight space available in typically crowded diagnostic boxes of a superconducting LINAC.

Several VME modules have been investigated in order to improve the energy and timing data acquisition chains for the PIPS silicon detector. It would be desirable to avoid all NIM modules in order to control all the acquisition parameters directly from a PC. In this sense, a Caen 724 Digitizer could provide high-resolution (14-bit, 100 MHz) energy spectra and can be programmed remotely through 16 LVDS inputs/outputs. It can be self-triggered, triggered with an external signal or by software command. The digitizer is provided with FPGAs that can run Digital Pulse Processing (DPP) and Pulse Height Analysis (PHA), continuously acquiring data in a circular memory buffer.

This digitizer would simplify the energy chain even further, as it would be directly connected to the Si detector preamplifier, getting rid of the N968 shaping amplifier and

the gating through the TTL-NIM level adapter, allowing at the same time to set all the acquisition parameters remotely.

Chapter 6 relates to the tests of different detector technologies using the antiproton beam available at AE$\bar{g}$IS. At the Antiproton Decelerator hall, the AE$\bar{g}$IS experiment offered new possibilities to test several candidate technologies to monitor low-energy antiproton beams and study detector resolutions and limitations with regards to a permanent installation of these devices. My main contribution focused on testing the SEM in its two possible configurations. Transverse beam profiles could not be measured due to the beam conditions present at that time. However, the MCP directly hit, tested for the first time with an antiproton beam, allowed identification of antiproton annihilation traces, while the foil-based SEM yielded images more difficult to analyse because this configuration monitors the antiproton beam in an indirect way. Images taken opening and closing a gate valve upstream of the SEM confirmed the presence of pions and other secondary particles from the antiproton annihilations in both configurations of the monitor. The SEM was the only on-line monitor in the latest AE$\bar{g}$IS beam run and it was key for the initial low-intensity beam steering. Within the AE$\bar{g}$IS collaboration, a nuclear emulsions detector, an ultra-thin pixel Si detector and a 3D pixel Si detector were tested. These measurements at the Antiproton Decelerator (AD) were beam destructive for all detectors and their configurations.

In addition, a summary of the experimental results from all detector groups in combination with my findings from the analysis of all detector performances is used to instrument the LNE02 low-energy beamline leading to the AE$\bar{g}$IS experiment as an example of permanent installation of beam instrumentation devices for this part of the facility.

As an alternative measurement instrument for antiprotons it would be desirable to install, for instance, a segmented, ultra-thin diamond detector for beam position, profile, intensity and timing measurements at the AD hall or a combination of different Si detector technologies to obtain full information about the antiproton beam. Further research and development efforts in testing these detector technologies are needed in this direction.

Appendices

Appendix A

Energy loss of ions at the entrance window of the Si detectors

The PIPS Si detectors used in this work were a special series adapted for timing measurements. The special feature for such adaptation is the addition of a 20 nm aluminium layer implanted at the entrance window. That extra thickness increases the energy loss of the ions in the entrance window (<50 nm) [97] of the detector given by the ion-implanted contacts. The energy deposited by the ions in the entrance window was considered as that produced in an equivalent layer of 70 nm of Si ($\rho_{Si} = 2.3\ \frac{g}{cm^3}$). This is a very good approximation and it will give a maximum value for the energy loss in the entrance window of the detector (ΔE_{window}). As this energy is deposited in a non-sensitive region of the detector, it introduces a systematic error for the energy spectroscopy studies (i.e. the detected energy is less than the projectile energy). In table A.1 the energy loss values calculated with SRIM 2012 [86] for a 70 nm Si thick entrance window are presented for the different projectile types and energies used in this work. The influence of these undetected energy losses on the projectiles energy measurement is of the order of 2% for the lowest energies and decreases with the projectile energy. It should be noted that the quoted values for the energy loss in the entrance window should not be added directly to the mean energy results from the energy spectrometry measurements, as the calibration for the energy scale was done with alpha particles that also lose energy in the entrance window.

Table A.1: Energy loss at the entrance window of the SRIM Si detector (TM series), calculated as an equivalent thickness of 70 nm, using SRIM 2012 stopping power tables [86].

Particle	Atomic mass	E/A_{IN} (MeV/u)	ΔE (keV/u)	E/A_{OUT} (MeV/u)	$\Delta E_{window}/E$ (%)
He	4	0.30	5.0	0.295	1.7
C	12	0.30	6.9	0.293	2.3
O	16	0.30	7.3	0.293	2.4
Ne	20	0.30	6.9	0.293	2.3
He	4	1.87	1.9	1.868	0.1
C	12	1.87	5.0	1.865	0.3
O	16	1.87	5.8	1.864	0.3
Ne	20	1.87	6.6	1.863	0.35
He	4	2.27	1.7	2.268	0.1
C	12	2.27	4.6	2.265	0.25
O	16	2.27	5.4	2.265	0.3
Ne	20	2.27	6.1	2.264	0.3

Appendix B

Table of ion beams delivered at REX-ISOLDE

Table B.1: List of ion beams delivered at REX-ISOLDE. (Didier Voulot, private communication).

Year	Ion species	A	Z	Charge state	Half life	E/A (MeV/u)	Breeding time (ms)	REX yield (p/s)
2001	Na	25	11	6	59.6 s	2.00	15	
2001	Na	26	11	7	1.07 s	2.00	15	
2002	Li	9	3	2	178.3 ms	2.35	8	
2002	Na	24	11	7	14.96 h	2.30	15	
2002	Na	25	11	6	59.6 s	2.30	15	
2002	Na	26	11	7	1.07 s	2.30	15	
2002	Na	27	11	7	304 ms	2.30	15	
2002	Na	28	11	9	30.5 ms	2.30	15	
2002	Na	29	11	8	44.9 ms	2.30	15	
2002	Mg	30	12	7	335 ms	2.30	14	
2002	Sm	153	63	30	46.27 h	0.30	30	
2003	Li	9	3	2	178.3 ms	2.20	8	
2003	Mg	30	12	7	335 ms	2.25	18	
2003	Mg	32	12	9	120 ms	2.25	18	
2003	Zn	74	30	18	96 s	2.25	38	
2003	Zn	76	30	18	5.6 s	2.25	38	
2003	Kr	88	36	21	2.84 h	2.25	18	
2003	Eu	156	62	30	15.2 d	0.30	38	
2004	Li	9	3	2	178.3 ms	2.60	6	1.9×10^{5}
2004	Li	11	3	3	8.5 ms	2.90	6	
2004	F	17	9	5	64.8 s	2.55	8	1.5×10^{2}
2004	Mg	28	12	9	20.9 h	2.15	16	2.8×10^{6}
2004	Mg	30	12	7	335 ms	2.70	16	8×10^{5}
2004	Mg	32	12	9	120 ms	2.85	16	1.1×10^{4}
2004	Zn	74	30	20	96 s	2.90	78	
2004	Zn	76	30	20	5.6 s	2.90	78	
2004	Zn	78	30	21	1.47 s	2.90	78	
2004	Se	70	34	17	41.1 min	2.85	6	
2004	Cd	122	48	30	5.5 s	2.85	148	
2004	Cd	124	48	30	1.29 s	2.85	148	
2004	Cd	126	48	31	510 ms	2.85	148	
2004	Sn	110	50	27	4.11 h	2.80	98	2×10^{7}
2004	Pm	148	87	30	5.37 d	0.30	38	
2005	Li	9	3	2	178.3 ms	2.76	3.5	7×10^{5}
2005	Be	11	4	3	13.8 s	2.24	10	1×10^{5}
2005	Be	11	4	3	13.8 s	2.24	18	
2005	Ni	68	28	19	29 s	2.83	98	1.1×10^{6}
2005	Cu	68	29	19	30 s	2.83	98	1.8×10^{6}
2005	Cu	69	29	20	3 min	2.83	98	1.9×10^{5}
2005	Cu	70	29	19	5 s	2.83	98	4.9×10^{5}
2005	Se	70	34	19	41.1 min	2.85	58	7×10^{3}
2005	Kr	88	36	21	2.84 h	2.19	70	5.7×10^{6}
2005	Kr	92	36	22	1.84 s	2.19	98	3.1×10^{6}
2005	In	108	49	30	58 min	2.83	198	5.6×10^{6}
2005	Sn	108	50	30	10.3 min	2.83	198	5.2×10^{6}
2005	Xe	138	54	34	14.1 min	2.84	198	4.9×10^{6}
2005	Xe	140	54	34	13.6 s	2.84	198	2.3×10^{6}
2005	Xe	142	54	34	1.24 s	2.84	198	1.9×10^{6}
2006	Li	8	3	3	840.3 ms	3.15	18	1.7×10^{5}
2006	Be	10	4	3	1.6×10^{6} years	2.93	15	8.8×10^{6}
2006	Be	11	4	4	13.8 s	2.92	25	1.8×10^{5}
2006	Mg	29	12	9	1.3 s	2.75	28	2.1×10^{5}
2006	Mg	31	12	9	230 ms	2.75	28	1.9×10^{4}
2006	Cu	67	29	19	61.9 h	2.99	68	3×10^{6}
2006	Cu	69	29	20	3 min	2.97	98	2.5×10^{6}
2006	Cu	71	29	20	19.5 s	2.95	98	1.7×10^{6}
2006	Cu	73	29	19	3.9 s	2.88	68	1.1×10^{6}
2006	Zn	80	30	21	537 ms	2.79	78	3×10^{3}
2006	Ga	73	31	19	4.86 h	2.88	68	
2006	Cd	124	48	30	1.29 s	2.86	248	
2006	Cd	126	48	31	510 ms	2.85	248	1.1×10^{4}
2006	Sn	106	50	26	2.1 min	2.85	67	1.5×10^{5}
2006	Sn	108	50	26	10.3 min	2.85	67	6.9×10^{6}
2006	Xe	138	54	34	14.1 min	2.85	330	7×10^{6}
2006	Xe	144	54	34	1.15 s	2.70	198	2.3×10^{4}
2007	F	17	9	5	64.8 s	2.60	18	7.8×10^{3}
2007	Mg	30	12	7	335 ms	2.86	14	
2007	Mg	30	12	7	335 ms	2.27	15	
2007	Mg	30	12	7	335 ms	1.91	15	
2007	Mg	30	12	7	335 ms	1.56	15	
2007	Mg	31	12	9	230 ms	2.99	28.5	9×10^{3}
2007	Sr	96	38	23	1 s	2.87	120	2×10^{4}
2007	Ba	140	56	33	12.75 d	2.84	171	9.9×10^{6}
2007	Ba	142	56	33	10.7 min	2.84	168	7.6×10^{5}
2007	Ba	148	56	35	610 ms	2.84	230	
2007	Hg	184	80	43	30.6 s	2.85	170	4×10^{3}
2007	Hg	186	80	43	1.4 min	2.85	170	4×10^{5}
2007	Hg	188	80	44	3.25 min	2.85	170	9.4×10^{5}
2008	C	9	6	3	126.5 ms	2.89	3.5	
2008	C	10	7	3	19.3 s	2.89	3.5	
2008	Mg	30	12	7	335 ms	2.85	8.0	4×10^{4}
2008	Mn/Fe	61	25	21	710 ms	2.90	298	4×10^{5}
2008	Mn/Fe	62	25	21	625 ms	2.90	298	

Year	Ion species	A	Z	Charge state	Half life	E/A (MeV/u)	Breeding time (ms)	REX yield (p/s)
2008	Cu	70	29	19		2.92	65	7×10^{6}
2008	Cd	100	48	24	49.1 s	2.88	59	
2008	Cd	102	48	25	5.5 min	2.88	69	1×10^{6}
2008	Cd	104	48	25	57.7 min	2.88	69	4×10^{6}
2008	Hg	182	80	44	10.8 s	2.85	200	2.6×10^{3}
2008	Hg	184	80	44	30.6 s	2.85	200	6.8×10^{4}
2008	Hg	186	80	44	1.4 min	2.85	200	2×10^{5}
2008	Hg	188	80	45	3.25 min	2.85	200	3.5×10^{5}
2008	Rn	202	86	47	9.85 s	2.80	200	3×10^{4}
2008	Rn	204	86	47	1.24 min	2.80	200	1×10^{5}
2009	Be	11	4	3	13.8 s	2.85	20	6×10^{4}
2009	Na	29	11	7	44.9 ms	2.85	13	4×10^{4}
2009	Na	30	11	7	48 ms	2.85	13	5×10^{3}
2009	Mn/Fe	62	25	21/15	625 ms	2.85	298/28.5	6.2×10^{4}
2009	Ni	66	28	16	54.6 h	2.90	28.5	5×10^{6}
2009	Ni	68	28	16	29 s	2.89	28.5	4×10^{4}
2009	Kr	72	36	22				
2009	Kr	94	36	22	200 ms	2.85	48.5	1.7×10^{5}
2009	Kr	96	36	22	80 ms	2.85	48.5	
2009	Sn	107	50	26	4.11 h	2.85	59	4×10^{5}
2009	Sn	109	50	26	18.0 min	2.85	59	8.4×10^{6}
2009	Xe	138	54	33	14.4 min	2.87	160	6×10^{6}
2009	Po	200	84	48	12.5 h	2.85	250	2×10^{6}
2010	Be	11	4	3	13.8 s	2.83	17.3	3.5×10^{6}
2010	C	9	6	4	126.5 ms	2.87	8.0	
2010	Ar	44	18	13	11.87 min	2.16	59	1.9×10^{5}
2010	Zn	78	30	20	1.47 s	2.82	59	3×10^{5}
2010	Kr	72	36	17	17 s	2.82	24.4	
2010	Kr	92	36	22	1.84 s	2.84	63.8	1×10^{6}
2010	Kr	94	36	22	0.2 s	2.84	63.8	
2010	Kr	96	36	23	80 ms	2.84	63.8	3×10^{3}
2010	Rb	93	37	22	5.8 s	2.84	71	1.4×10^{6}
2010	Rb	95	37	23	377 ms	2.84	79	2×10^{6}
2010	Rb	97	37	23	170 ms	2.84	79	5×10^{5}
2010	Rb	99	37	23	50.3 ms	2.84	69	
2010	Pb	192	82	45	3.5 min	2.84	230	2.4×10^{6}
2010	Rn	202	86	47	9.85 s	2.84	129	1.4×10^{3}
2010	Ra	224	88	52	3.66 d	2.78	355	8.4×10^{4}
2011	Pb	186	82	44	4.8 s	2.84	248	
2011	Pb	188	82	44	25.5 s	2.84	248	2×10^{5}
2011	Pb	190	82	44	1.2 min	2.84	248	
2011	Pb	194	82	45	12 min	2.84	248	1.3×10^{6}
2011	Pb	196	82	46	36.4 min	2.84	248	6.8×10^{5}
2011	Pb	198	82	46	2.4 h	2.84	248	
2011	Nd	140	60	34	3.37 d	2.83	97	2.4×10^{5}
2011	Kr	96	36	23		2.82	58	
2011	Cd	128	48	30	0.30 s	2.82	118	3.1×10^{5}
2011	Cd	126	48	30	0.51 s	2.82	118	2.5×10^{5}
2011	Rn	220	86	52	55.6 s	2.82	398	3.1×10^{5}
2011	Rn	208	86	50	24.4 min	2.82	398	
2011	Na	26	11	6	1.07 s	2.82	12.0	5×10^{5}
2011	Na	30	11	7	48 ms	2.82	15.0	
2011	Kr	72	36	17	17 s	2.85	33.5	
2011	Ra	224	88	52	3.66 d	2.82	396	7.2×10^{5}
2011	Ni	66	28	17	54.6 h	2.60		3.7×10^{6}
2011	Sr	98	38	26	653 ms	2.82	158	
2011	Zn	72	30	20	46.5 h	2.70	68	
2011	Zn	72	30	20	46.5 h	2.94	88	6.9×10^{6}
2011	Zn	74	30	20	96 s	2.94	88	1.9×10^{6}
2011	Zn	76	30	20	5.6 s	2.94	88	2×10^{6}
2012	Cd	123	48	29	2.1 s	2.84	168	
2012	Kr	72	36	17	17 s	2.85	31	
2012	Sm	140	62	34	14.8 min	2.85	147	1.3×10^{5}
2012	Sm	142	62	34	72.4 min	2.85	147	2.8×10^{5}
2012	Be	12	4	4	23.6 ms	2.85		
2012	Li	8	3	3	840.3 ms			
2012	Na	21	11	8	22.48 s	3.05		6.3×10^{6}
2012	Mg	30	12	8	335 ms	2.89	18.7	7.8×10^{5}
2012	He	6	2	2	806.7 ms			
2012	Rn	210	86	51	2.4 h	2.85	396	2.2×10^{5}
2012	Rn	212	86	51	24 min	2.85		1.5×10^{5}
2012	Rn	221	86	53	25 min	2.85		4×10^{3}
2012	Po	196	84	48	5.8 s			8.7×10^{4}
2012	Po	198	84	48				
2012	Po	200	84	48				
2012	Po	202	84	49				
2012	K	48	19	11				
2012	Zn	72	30	20	46.5 h			
2012	Rb	98	37	23	114 ms	2.85	73.7	7.3×10^{4}
2012	Ar	35	18		1.78 s			
2012	Ti	44	22	13	60.4 years	2.10	40	1.4×10^{6}
2012	Ti	44	22	13	60.4 years	1.95	40	6.1×10^{5}

Acknowledgements

I would like to express my appreciation and gratitude to my PhD supervisor, Prof. Dr. Carsten P. Welsch and to my supervisor at CERN, Enrico Bravin, who have fully supported and secured not only my scientific work but also a healthy work-life balance. I would also like to acknowledge the generous support of the European Commission under the Marie Curie actions Contract No. GA-PITN-2010-264330.

I am very grateful to the operations team at ISOLDE, particularly Didier Voulot, Emiliano Piselli, Miguel Luis Lozano Benito and Davide Lanaia, for their endless effort over these years setting up the machine and making possible to run so many tests at REX. The reader of this thesis will easily notice the amount of work that has been done together with and thanks to this fantastic group of people.

I would like to thank the AE$\bar{g}$IS team at CERN, particularly Michael Doser, Olof Ahlen and Andreas Knecht, for their support and help during the December 2012 antiproton runs.

I appreciate the invaluable help of the staff at TRIUMF, especially Bob Laxdal, Victor Verzilov, Bill Rawnsley and Josef Holek who shared their broad knowledge and experience in beam diagnostics and electronics. Special thanks go to the ISAC operators, Tiffany Angus, Spencer Kiy and Edward Parton who delivered beam against all adversity for the here-described tests on the Faraday cups.

There are many other people who have supported and helped me over the years and I appreciate their good will and patience to answer my numerous questions. I would like to express my deep gratitude to Francesca Zocca, Matthew Alexander Fraser, Fredrik John Carl Wenander, Yacine Kadi and many, many others. Special thanks go to William Andreazza, Michel Duraffourg, Gerrit Jan Focker for their mechanical and technical support.

Thanks to all members of the QUASAR group at the University of Liverpool, the Cockcroft Institute and CERN, and to all CATHI fellows for sharing the jour-

ney through my PhD studies. Everyone has contributed to the joy of this time, but especial thanks go to my two office colleagues, Esteban Daniel Cantero, who always kept the focus of our research on the right direction, and Georges Trad, whom I hope to return the favour one day for the spare time he devoted debugging my Matlab routines.

Finally, I would like to thank my family, my parents, Jose Bernardo and Maria del Carmen, my brother Fernando, my mother in law, Amparo, and my beloved wife, Estefania. I am forever grateful for your endless support taking care of everyday life problems so that I could focus on my research work. To you all, a big thank you.

Bibliography

[1] D Neidherr, G Audi, D Beck, K Blaum, Ch Böhm, M Breitenfeldt, RB Cakirli, RF Casten, S George, F Herfurth, et al. Discovery of Rn 229 and the Structure of the Heaviest Rn and Ra Isotopes from Penning-Trap Mass Measurements. *Physical review letters*, 102(11):112501, 2009.

[2] D Beck, F Ames, G Audi, G Bollen, H-J Kluge, A Kohl, M König, D Lunney, I Martel, RB Moore, et al. Direct mass measurements of unstable rare earth isotopes with the ISOLTRAP mass spectrometer. *Nuclear Physics A*, 626(1):343–352, 1997.

[3] MD Lunney, G Audi, C Borcea, M Dedieu, H Doubre, M Duma, M Jacotin, J-F Képinski, G Le Scornet, M de Saint Simon, et al. MISTRAL: A new program for precise atomic mass determinations of nuclides far from stability. *Hyperfine interactions*, 99(1):105–114, 1996.

[4] Beams Department, ISOLDE Operation Website. `http://ab-dep-op-iso.web.cern.ch/ab-dep-op-iso/HTML/hall_overview.htm` <Accesssed: 31 July 2014>.

[5] M Lindroos, Peter A Butler, Marc Huyse, and Karsten Riisager. HIE-ISOLDE. *Nuclear Instruments and Methods in Physics Research Section B: Beam Interactions with Materials and Atoms*, 266(19):4687–4691, 2008.

[6] VN Fedoseyev, G Huber, U Köster, J Lettry, VI Mishin, H Ravn, and V Sebastian. The ISOLDE laser ion source for exotic nuclei. *Hyperfine Interactions*, 127(1-4):409–416, 2000.

[7] A Gustafsson, A Herlert, and F Wenander. Mass-selective operation with REX-TRAP. *Nuclear Instruments and Methods in Physics Research Section A: Accelerators, Spectrometers, Detectors and Associated Equipment*, 626:8–15, 2011.

[8] J Äystö and V Rubchenya. Neutron-rich nuclei and fission; recent developments and future aspects. *The European Physical Journal A-Hadrons and Nuclei*, 13(1-2):109–115, 2002.

[9] Erich Kugler. The ISOLDE facility. *Hyperfine Interactions*, 129(1-4):23–42, 2000.

[10] REX-ISOLDE Website. `http://rex-isolde.web.cern.ch` <Accesssed: 31 July 2014>.

[11] D Voulot, F Wenander, E Piselli, R Scrivens, M Lindroos, HB Jeppesen, LM Fraile, S Sturm, and P Delahaye. Radioactive beams at REX-ISOLDE: Present status and latest developments. *Nuclear Instruments and Methods in Physics Research Section B: Beam Interactions with Materials and Atoms*, 266(19):4103–4107, 2008.

[12] M Pasini, S Calatroni, N Delruelle, M Lindroos, V Parma, and P Trilhe. A SC upgrade for the REX-ISOLDE accelerator at CERN. *Energy (MeV/u)*, 8:10, 2008.

[13] Dietrich Habs, O Kester, T Sieber, H Bongers, S Emhofer, P Reiter, PG Thirolf, G Bollen, J Aystö, O Forstner, et al. The REX-ISOLDE project. *Hyperfine interactions*, 129(1-4):43–66, 2000.

[14] Fredrik Wenander. Charge breeding of radioactive ions with EBIS and EBIT. *Journal of Instrumentation*, 5(10):C10004, 2010.

[15] CP Welsch, K-U Kühnel, and A Schempp. Development of rebunching cavities at IAP. *arXiv preprint physics/0007088*, 2000.

[16] D Habs, O Kester, K Rudolph, P Thirolf, G Hinderer, E Nolte, G Bollen, H Raimbault-Hartmann, H Ravn, F Ames, et al. The REX-ISOLDE Project. *Nuclear Instruments and Methods in Physics Research Section B: Beam Interactions with Materials and Atoms*, 126(1):218–223, 1997.

[17] J Eberth, G Pascovici, HG Thomas, N Warr, D Weisshaar, D Habs, P Reiter, P Thirolf, D Schwalm, C Gund, et al. MINIBALL A Ge detector array for radioactive ion beam facilities. *Progress in Particle and Nuclear Physics*, 46(1):389–398, 2001.

[18] HIE-ISOLDE Website. `http://hie-isolde.web.cern.ch/hie-isolde/` <Accesssed: 31 July 2014>.

[19] K Hanke, A Lombardi, M Vretenar, C Rossi, C Carli, S Maury, F Gerigk, and R Garoby. Status of the Linac4 Project at CERN. Technical report, 2010.

[20] E Mané, J Billowes, K Blaum, P Campbell, B Cheal, P Delahaye, KT Flanagan, DH Forest, H Franberg, C Geppert, et al. An ion cooler-buncher for high-sensitivity collinear laser spectroscopy at ISOLDE. *The European Physical Journal A-Hadrons and Nuclei*, 42(3):503–507, 2009.

[21] Y Kadi, D Parchet, R Catherall, W Venturini Delsolaro, G Vandoni, E Siesling, MA Fraser, E Bravin, Y Blumenfeld, S Calatroni, et al. Status of the HIE-ISOLDE Project at CERN. 2012.

[22] TRIUMF Website. `http://www.triumf.ca/home/about-triumf/history` <Accesssed: 31 July 2014>.

[23] JB Warren. The TRIUMF Project. In *Proc. of 5th Int. Cyclotron Conf*, pages 73–84, 1969.

[24] I Bylinskii, RA Baartman, G Dutto, K Fong, A Hurst, M Laverty, C Mark, F Mammarella, M McDonald, AK Mitra, et al. TRIUMF 500 MeV cyclotron refurbishment. *Cyclotrons and Their Application, Giardini Naxos, ITALY*, page 143, 2007.

[25] P.G. Bricault, M. Dombsky, P.W. Schmor, and G. Stanford. Radioactive ion beams facility at TRIUMF. *Nuclear Instruments and Methods in Physics Research Section B: Beam Interactions with Materials and Atoms*, 126(14"):231 – 235, 1997. International Conference on Electromagnetic Isotope Separators and Techniques Related to Their Applications.

[26] RE Laxdal et al. ISAC-I and ISAC-II at TRIUMF: Achieved performance and new construction. In *Proceedings of LINAC*, page 296, 2002.

[27] K Abe, N Abgrall, H Aihara, Y Ajima, JB Albert, D Allan, P-A Amaudruz, C Andreopoulos, B Andrieu, MD Anerella, et al. The T2K experiment. *Nuclear Instruments and Methods in Physics Research Section A: Accelerators, Spectrometers, Detectors and Associated Equipment*, 659(1):106–135, 2011.

[28] R Keitel and JT Worden. The μSR facility at TRIUMF. *Hyperfine Interactions*, 32(1):901–906, 1986.

[29] JJ Burgerjon, AS Arrott, IM Thorson, TL Templeton, TA Hodges, RE Blaby, and RR Langstaff. The TRIUMF Thermal Neutron Facility. *Nuclear Science, IEEE Transactions on*, 26(3):3061–3064, 1979.

[30] Ewart W Blackmore. Operation of the TRIUMF (20-500 MeV) proton irradiation facility. *IEEE REDW*, pages 1–5, 2000.

[31] EW Blackmore, B Evans, and M Mouat. Operation of the TRIUMF proton therapy facility. In *Particle Accelerator Conference, 1997. Proceedings of the 1997*, volume 3, pages 3831–3833. IEEE, 1997.

[32] AR Berdoz, J Birchall, JB Bland, JD Bowman, JR Campbell, GH Coombes, CA Davis, AA Green, PW Green, AA Hamian, et al. Parity violation in proton-proton scattering at 221 MeV. *Physical Review C*, 68(3):034004, 2003.

[33] Pierre Bricault, Richard Baartman, Marik Dombsky, Andrew Hurst, Clive Mark, Guy Stanford, and Paul Schmor. TRIUMF-ISAC target station and mass separator commissioning. *Nuclear Physics A*, 701(1):49–53, 2002.

[34] Pierre Bricault, Friedhelm Ames, Tobias Achtzehn, Marik Dombsky, Francis Labrecque, Jens Lassen, Jean-Phillipe Lavoie, and Nathalie Lecesne. An overview on TRIUMFs developments on ion source for radioactive beams. *Review of Scientific Instruments*, 79(2):02A908–02A908, 2008.

[35] K Jayamanna, F Ames, G Cojocaru, R Baartman, P Bricault, R Dube, R Laxdal, M Marchetto, M MacDonald, P Schmor, et al. Off-line ion source terminal for ISAC at TRIUMF. *Review of Scientific Instruments*, 79(2):02C711, 2008.

[36] DA Hutcheon, S Bishop, L Buchmann, ML Chatterjee, AA Chen, JM D'Auria, S Engel, D Gigliotti, U Greife, D Hunter, et al. The DRAGON facility for nuclear astrophysics at TRIUMF-ISAC: design, construction and operation. *Nuclear Instruments and Methods in Physics Research Section A: Accelerators, Spectrometers, Detectors and Associated Equipment*, 498(1):190–210, 2003.

[37] AM Laird, L Buchmann, and T Davinson. Charged-particle reaction studies for nuclear astrophysics. *Hyperfine Interactions*, 225(1-3):207–214, 2014.

[38] Barry Davids and Cary N Davids. EMMA: A recoil mass spectrometer for ISAC-II at TRIUMF. *Nuclear Instruments and Methods in Physics Research Section A: Accelerators, Spectrometers, Detectors and Associated Equipment*, 544(3):565–576, 2005.

[39] CE Svensson, P Amaudruz, C Andreoiu, A Andreyev, RAE Austin, GC Ball, D Bandyopadhyay, AJ Boston, RS Chakrawarthy, AA Chen, et al. TIGRESS: TRIUMF-ISAC Gamma-Ray Escape-Suppressed Spectrometer. *Journal of Physics G: Nuclear and Particle Physics*, 31(10):S1663, 2005.

[40] Patrick St-Onge, Jérôme Gauthier, Barton Wallace, and René Roy. HERACLES: a multidetector for heavy-ion collisions at TRIUMF. *Hyperfine Interactions*, 225(1-3):229–234, 2014.

[41] RE Laxdal and M Marchetto. The ISAC post-accelerator. *Hyperfine Interactions*, 225(1-3):79–97, 2014.

[42] RE Laxdal, RJ Dawson, M Marchetto, AK Mitra, WR Rawnsley, T Ries, I Sekachev, V Zvyagintsev, et al. ISAC-II Superconducting Linac Upgrade-Design and Status. In *this conference*, 2008.

[43] S Baird, D Berlin, J Boillot, J Bosser, M Brouet, J Buttkus, F Caspers, V Chohan, D Dekkers, T Eriksson, et al. Status of the antiproton decelerator: AD. *Nuclear Physics B-Proceedings Supplements*, 56(1):349–357, 1997.

[44] L Bojtár. Antiproton decelerator status report. *proc. of COOL09, Lanzhou, China, MOM1MCIO02*, page 1, 2009.

[45] P Belochitskii. Status of the Antiproton Decelerator and of the ELENA Project at CERN. In *Proceedings of COOL*, pages 6–10, 2007.

[46] Antiproton Decelerator, The Antimatter Factory. `https://espace.cern.ch/AD-site/SitePages/Antimatter%20factory.aspx` <Accesssed: 31 July 2014>.

[47] ALPHA Experiment. `http://alpha-new.web.cern.ch` <Accesssed: 31 July 2014>.

[48] ATRAP Antihydrogen Experiment. `http://gabrielse.physics.harvard.edu/gabrielse/overviews/Antihydrogen/Antihydrogen.html` <Accesssed: 31 July 2014>.

[49] Yasunori Yamazaki. Production of ultra slow antiprotons, its application to atomic collisions and atomic spectroscopy-ASACUSA project. *Nuclear Instruments and Methods in Physics Research Section B: Beam Interactions with Materials and Atoms*, 154(1):174–184, 1999.

[50] D Kuchler, M Paoluzzi, M Hori, T Eriksson, F Pedersen, G Vanbavinckhove, B Puccio, S Maury, S Fedemann, J Harasimowicz, et al. Extra Low ENergy Antiproton (ELENA) ring and its Transfer Lines: Design Report. Technical report, CERN, 2014.

[51] G Tranquille, P Belochitskii, S Maury, W Oelert, and T Eriksson. ELENA: from the first ideas to the project. In *Conf. Proc.*, volume 1205201, page THPPP017, 2012.

[52] T Eriksson, ME Angoletta, L Arnaudon, P Belochitskii, L Bojtar, M Calviani, F Caspers, S Federmann, L Jørgensen, R Louwerse, et al. AD Status and Consolidation Plans.

[53] A Kellerbauer, M Amoretti, AS Belov, G Bonomi, I Boscolo, RS Brusa, Matthias Büchner, VM Byakov, L Cabaret, C Canali, et al. Proposed antimatter gravity measurement with an antihydrogen beam. *Nuclear Instruments and Methods in Physics Research Section B: Beam Interactions with Materials and Atoms*, 266(3):351–356, 2008.

[54] G Yu Drobychev, U Gendotti, I Boscolo, H Walters, M Büchner, André Rubbia, MK Oberthaler, P Nédélec, S Zavatarelli, C Carraro, et al. Proposal for the AEGIS experiment at the CERN antiproton decelerator (Antimatter Experiment: Gravity, Interferometry, Spectroscopy). Technical report, 2007.

[55] Sebastiano Mariazzi, Stefano Aghion, Claude Amsler, Akitaka Ariga, Tomoko Ariga, Alexandre S Belov, Germano Bonomi, Philippe Bräunig, Roberto S Brusa, Johan Bremer, et al. Aegis experiment: Towards antihydrogen beam production for antimatter gravity measurements. *The European Physical Journal D*, 68(3):1–6, 2014.

[56] AEGIS Experiment. `http://aegis.web.cern.ch/aegis/home.html` <Accesssed: 31 July 2014>.

[57] Lowell S Brown and Gerald Gabrielse. Geonium theory: Physics of a single electron or ion in a Penning trap. *Reviews of Modern Physics*, 58(1):233, 1986.

[58] Guy Savard, St Becker, G Bollen, H-J Kluge, RB Moore, Th Otto, L Schweikhard, H Stolzenberg, and U Wiess. A new cooling technique for heavy ions in a Penning trap. *Physics Letters A*, 158(5):247–252, 1991.

[59] S Aghion, O Ahlén, AS Belov, G Bonomi, P Bräunig, J Bremer, RS Brusa, G Burghart, L Cabaret, M Caccia, et al. Annihilation of low energy antiprotons in silicon. *arXiv preprint arXiv:1311.4982*, 2013.

[60] G Testera, AS Belov, G Bonomi, I Boscolo, N Brambilla, RS Brusa, VM Byakov, L Cabaret, C Canali, C Carraro, et al. Formation of a cold antihydrogen beam in AEGIS for gravity measurements. *arXiv preprint arXiv:0805.4727*, 2008.

[61] Michael Doser, Y Allkofer, C Amsler, AS Belov, G Bonomi, I Boscolo, RS Brusa, VM Byakov, L Cabaret, A Calloni, et al. Measuring the fall of antihydrogen: the AEGIS experiment at CERN. *Physics Procedia*, 17:49–56, 2011.

[62] S Aghion, O Ahlén, C Amsler, A Ariga, T Ariga, AS Belov, G Bonomi, P Bräunig, J Bremer, RS Brusa, et al. Prospects for measuring the gravitational free-fall of antihydrogen with emulsion detectors. *Journal of Instrumentation*, 8(08):P08013, 2013.

[63] P Van den Bergh, Marc Huyse, K Krouglov, Piet Van Duppen, and L Weissman. The REX-ISOLDE beam diagnostic system. In *The CAARI 2000: Sixteenth international conference on the application of accelerators in research and industry*, pages 235–238. American Institute of Physics, 2001.

[64] ACF Metals. `http://www.techexpo.com/WWW/acf-metals/` <Accesssed: 31 July 2014>.

[65] O Kester, T Sieber, S Emhofer, F Ames, K Reisinger, P Reiter, PG Thirolf, R Lutter, D Habs, BH Wolf, et al. Accelerated radioactive beams from REX-ISOLDE. *Nuclear Instruments and Methods in Physics Research Section B: Beam Interactions with Materials and Atoms*, 204:20–30, 2003.

[66] Vespel parts and shapes, DUPONT products. `http://www.dupont.com/products-and-services/plastics-polymers-resins/parts-shapes/brands/vespel-polyimide.html` <Accesssed: 31 July 2014>.

[67] Hamamatsu Image Intensifiers. `http://www.hamamatsu.com/resources/pdf/etd/II_TII0004E02.pdf` <Accesssed: 31 July 2014>.

[68] GJ Focker. CERN ISOLDE and REX Beam Instrumentation. *Proc. of DITANET Workshop on low current, low energy beam diagnostics, Hirschberg, Germany*, page 7, 2009.

[69] J Dietrich, I Mohos, J Häuser, G Riehl, and F Wenander. High sensitive beam emittance analyzer. In *Proc. of EPAC*, volume 2, pages 1864–1866, 2002.

[70] NTG Highly Sensitive Emittance Analyzer. `http://www.ntg.de/uploads/media/P-BEA_CERN-FZJ.pdf` <Accesssed: 31 July 2014>.

[71] F Zocca, MA Fraser, E Bravin, Matteo Pasini, D Voulot, and F Wenander. Development of a silicon detector monitor for the HIE-ISOLDE superconducting upgrade of the REX-ISOLDE heavy-ion Linac. *Nuclear Instruments and Methods in Physics Research Section A: Accelerators, Spectrometers, Detectors and Associated Equipment*, 672:21–28, 2012.

[72] F Zocca, E Bravin, MA Fraser, M Pasini, D Voulot, and F Wenander. HIE-ISOLDE-PROJECT-Note-0008: "Development of a Silicon Detector Monitor for the HIE-ISOLDE Superconducting Upgrade of the REX-ISOLDE Linac". Technical report, 2011.

[73] HAMAMATSU Si PIN Photodiode S3590-08. `http://www.hamamatsu.com/us/en/product/category/3100/4001/4103/S3590-08/index.html`. Accessed: 31 July 2014.

[74] CAEN Charge-sensitive Preamplifier A1422. `http://www.caen.it/csite/CaenProd.jsp?idmod=604&parent=13` <Accesssed: 31 July 2014>.

[75] EDMS Doc. 1213401, "Beam Diagnostic Boxes for HIE-ISOLDE". `https://edms.cern.ch/document/1213401/2.3` <Accesssed: 31 July 2014>.

[76] American Iron and Steel Institute. `http://www.steel.org/` <Accesssed: 31 July 2014>.

[77] A Sosa, MA Fraser, Y Kadi, CP Welsch, J Galipienzo, E Bravin, F Wenander, F Zocca, D Voulot, and A Larman. Beam Instrumentation for the HIE-ISOLDE Linac at CERN. In *Conf. Proc.*, volume 1205201, page MOPPR048, 2012.

[78] Added Value Solutions. `http://www.a-v-s.es/` <Accesssed: 31 July 2014>.

[79] MDC Vacuum. `http://www.mdcvacuum.com/Index.aspx` <Accesssed: 31 July 2014>.

[80] DICRONITE Website. `http://www.dicronite.com/index.php/en/` <Accesssed: 31 July 2014>.

[81] E. D. Cantero. EDMS Doc. 1370583, "Acceptance test for the linear motion actuator for the scanning slit of the HIE-ISOLDE short diagnostic boxes". `https://edms.cern.ch/document/1370583/1.1` <Accesssed: 31 July 2014>.

[82] Mark Gordon Inghram and Richard J Hayden. *A Handbook on Mass Spectroscopy*. National Academy of Sciences-National Research Council, 1954.

[83] KL Brown and GW Tautfest. Faraday-Cup Monitors for High-Energy Electron Beams. *Review of Scientific Instruments*, 27(9):696–702, 2004.

[84] J Harasimowicz and CP Welsch. Faraday cup for low-energy, low-intensity beam measurements at the USR. *Proc. BIW, Santa Fe, NM, USA*, 2010.

[85] CE Sosolik, AC Lavery, EB Dahl, and BH Cooper. A technique for accurate measurements of ion beam current density using a Faraday cup. *Review of Scientific Instruments*, 71(9):3326–3330, 2000.

[86] JF Ziegler, JP Biersack, and MD Ziegler. SRIM 2008-The Stopping and Range of Ions in Matter, SRIM Co., Chester, 2012.

[87] ER Cawthron. Secondary electron emission from solid surfaces bombarded by medium energy ions. *Australian Journal of Physics*, 24(4):859–870, 1971.

[88] Maurizio Dapor. *Electron-beam interactions with solids*, volume 10. Springer, 2003.

[89] K. Kiyohara, Y. Koba, H. Iwamoto, T. Nagasaki, and Y. Uozumi. Study of angular and energy distribution of secondary electrons emitted by high energy heavy ion impact. 2011.

[90] CST Particle Studio. `http://www.cst.com/Content/Products/PS/Overview.aspx` <Accesssed: 31 July 2014>.

[91] K Jayamanna, G Wight, D Gallop, R Dube, V Jovicic, C Laforge, M Marchetto, M Leross, D Louie, R Laplante, et al. A multicharge ion source (Supernanogan) for the OLIS facility at ISAC/TRIUMF. *Review of Scientific Instruments*, 81(2):02A331, 2010.

[92] D Hasselkamp, S Hippler, and A Scharmann. Ion-induced secondary electron spectra from clean metal surfaces. *Nuclear Instruments and Methods in Physics Research Section B: Beam Interactions with Materials and Atoms*, 18(1):561–565, 1986.

[93] D Hasselkamp. Kinetic electron emission from solid surfaces under ion bombardment. In *Particle Induced Electron Emission II*, pages 1–95. Springer, 1992.

[94] D Hasselkamp and A Scharmann. The ion-induced low energy electron spectrum from aluminium. *Surface Science Letters*, 119(2):L389–L392, 1982.

[95] KG McKay and KB McAfee. Electron multiplication in silicon and germanium. *Physical Review*, 91(5):1079, 1953.

[96] CNSTN, Nuclear Analytical Techniques. `http://www.cnstn.rnrt.tn/afra-ict/NAT/alpha/html/solidetecto.htm` <Accesssed: 31 July 2014>.

[97] Canberra PIPS detectors. `http://www.canberra.com/products/detectors/pips-detectors-standard.asp` <Accesssed: 31 July 2014>.

[98] CAEN. Spectroscopy Amplifier Mod. N968: Technical Information Manual. `http://www.caen.it/servlet/checkCaenManualFile?Id=5300` <Accesssed: 31 July 2014>.

[99] National Instruments, LabView System Design Software. `http://www.ni.com/labview/` <Accesssed: 31 July 2014>.

[100] CAEN. LeCroy 8-Channel NIM Discriminator Model 4608C: Operator's Manual. `http://cdn.teledynelecroy.com/files/manuals/4608cman.pdf` <Accesssed: 31 July 2014>.

[101] ORTEC - Introduction to Charged-Particle Detectors. `http://www.ortec-online.com/download/Introduction-Charged-Particle-Detectors.pdf` <Accesssed: 26 October 2014>.

[102] VA Verzilov, RE Laxdal, M Marchetto, and WR Rawnsley. Time Domain Diagnostics for the ISAC-II Superconducting Heavy Ion Linac. *DIPAC, Venice, Italy*, 2007.

[103] A Pisent, G Bisoffi, D Carlucci, M Cavenago, M Comunian, A Facco, E Fagotti, A Galatá, A Palmieri, M Poggi, et al. Results on the Beam Commissioning of the Superconducting-RFQ of the New LNL Injector. In *Proceedings of LINAC*, volume 6, 2006.

[104] L Weissman, D Berkovits, Y Eisen, S Halfon, I Mardor, A Perry, J Rodnizki, K Dunkel, C Piel, D Trompetter, et al. First experience at SARAF with proton beams using the Rutherford scattering monitor. *probe*, 2:45, 2009.

[105] M. K. Boruchowski. EDMS Doc. 1250497 "ISOLDE-REX: Silicon Detectors DB4 and DB5 Distance - Measurement of October 25th, 26th 2012". `https://edms.cern.ch/document/1250497/2` <Accesssed: 31 July 2014>.

[106] LBNL Nuclear Science Division, Alpha-particle Energy and Intensity Standards. `http://ie.lbl.gov/toipdf/alpha2.pdf` <Accesssed: 31 July 2014>.

[107] REX-ISOLDE logbook. `http://ab-dep-op-elogbook.web.cern.ch/ab-dep-op-elogbook/elogbook/eLogbook.php?lgbk=112&date=20140503&shift=1` <Accesssed: 31 July 2014>.

[108] David Comedi and John Davies. Pulse height response of Si surface barrier detectors to 5-70 MeV heavy ions. *Nuclear Instruments and Methods in Physics Research Section B: Beam Interactions with Materials and Atoms*, 67(1):93–97, 1992.

[109] M. Seidl, H. Voit, S. Bouneau, A. Brunelle, S. Della-Negra, J. Depauw, D. Jacquet, Y. Le Beyec, and M. Pautrat. MeV carbon cluster-induced pulse height defect in a surface barrier detector. *Nuclear Instruments and Methods in Physics Research Section B: Beam Interactions with Materials and Atoms*, 183(34):502 – 508, 2001.

[110] Abhisek Mukhopadhyay and MA Fraser. Investigating the Feasibility of a Travelling-wave Chopper for the Clean Separation of 10 MHz Bunches at HIE-ISOLDE. *Students International Research Projects Technical Report 2012-2013 Volume 5*, 2013.

[111] IB Magdau and M Fraser. Beam Dynamics Feasibility Study for an RFQ Subharmonic Pre-buncher at REX-ISOLDE. Technical report, 2013.

[112] MA Fraser, R Calaga, and IB Magdau. Design Study for 10MHz Beam Frequency of Post-Accelerated RIBs at HIE-ISOLDE. Technical report, 2013.

[113] Gérard Tranquille. The ELENA Beam Diagnostics Systems. Technical report, 2013.

[114] J Harasimowicz, CP Welsch, L Cosentino, A Pappalardo, and P Finocchiaro. Beam diagnostics for low energy beams. *Physical Review Special Topics-Accelerators and Beams*, 15(12):122801, 2012.

[115] GB Andresen, W Bertsche, Paul David Bowe, CC Bray, E Butler, CL Cesar, S Chapman, M Charlton, S Seif El Nasr, J Fajans, et al. Antiproton, positron, and electron imaging with a microchannel plate/phosphor detector. *Review of Scientific Instruments*, 80(12):123701, 2009.

[116] H Imao, HA Torii, Y Nagata, H Toyoda, T Shimoyama, Y Enomoto, H Higaki, Y Kanai, A Mohri, and Y Yamazaki. Observation of Ultra-Slow Antiprotons using Micro-channel Plate. In *PROCEEDINGS OF THE WORKSHOP ON COLD ANTIMATTER PLASMAS AND APPLICATION TO FUNDAMENTAL PHYSICS*, pages 311–317. American Institute of Physics, 2008.

[117] SP Møller, E Uggerhøj, H Bluhme, H Knudsen, U Mikkelsen, K Paludan, and E Morenzoni. Direct measurements of the stopping power for antiprotons of light and heavy targets. *Physical Review A*, 56(4):2930, 1997.

[118] J Harasimowicz, CP Welsch, JL Fernandez-Hernando, L Cosentino, P Finocchiaro, and A Pappalardo. Thin foil-based secondary emission monitor for low intensity, low energy beam profile measurements. *Proc. of IPAC11, San Sebastian, Spain*, pages 1413–1415, 2011.

[119] TOPAG Lasertechnik GmbH. `http://www.topag.de/en/` <Accesssed: 31 July 2014>.

[120] THORLABS. `http://www.thorlabs.de/index.cfm` <Accesssed: 31 July 2014>.

[121] ISEG. `http://www.iseg-hv.com/` <Accesssed: 31 July 2014>.

[122] Janusz Harasimowicz. *Development of Instrumentation for Low Energy Beams*. PhD thesis, University of Liverpool, 2013.

[123] Max Zolotorev, A Sessler, G Penn, JS Wurtele, and AE Charman. Enhancing trappable antiproton populations through deceleration and frictional cooling. *Physical Review Special Topics-Accelerators and Beams*, 15(3):033502, 2012.

[124] M Kimura, S Aghion, O Ahlén, C Amsler, A Ariga, T Ariga, AS Belov, G Bonomi, P Bräunig, J Bremer, et al. Development of nuclear emulsions with spatial resolution for the AEgIS experiment. *Nuclear Instruments and Methods in Physics Research Section A: Accelerators, Spectrometers, Detectors and Associated Equipment*, 732:325–329, 2013.

[125] C Amsler, A Ariga, T Ariga, S Braccini, C Canali, A Ereditato, J Kawada, M Kimura, I Kreslo, C Pistillo, et al. A new application of emulsions to measure the gravitational force on antihydrogen. *Journal of Instrumentation*, 8(02):P02015, 2013.

[126] PL McGaughey, NJ DiGiacomo, WE Sondheim, JW Sunier, and Y Yariv. Low energy antiproton-nucleus annihilation radius selection using an active silicon detector/target. *Nuclear Instruments and Methods in Physics Research Section A: Accelerators, Spectrometers, Detectors and Associated Equipment*, 249(2):361–365, 1986.

[127] R. Boll, M. Caccia, C.P. Welsch, and M.H. Holzscheiter. Using monolithic active pixel sensors for fast monitoring of therapeutic hadron beams. *Radiation Measurements*, 46(12):1971 – 1973, 2011. Proceedings of the 16th Solid State Dosimetry Conference , September 19-24 , Sydney , Australia.

[128] A Gligorova, S Aghion, O Ahlen, AS Belov, G Bonomi, P Braunig, J Bremer, RS Brusa, G Burghart, L Cabaret, et al. Annihilation of low energy antiprotons in silicon sensors. In *Nuclear Science Symposium and Medical Imaging Conference (NSS/MIC), 2013 IEEE*, pages 1–7. IEEE, 2013.

[129] S Grinstein, M Baselga, M Boscardin, M Christophersen, C Da Via, G-F Dalla Betta, G Darbo, V Fadeyev, C Fleta, C Gemme, et al. Beam test studies of 3D pixel sensors irradiated non-uniformly for the ATLAS forward physics detector. *Nuclear Instruments and Methods in Physics Research Section A: Accelerators, Spectrometers, Detectors and Associated Equipment*, 730:28–32, 2013.

[130] V Zivkovic, JD Schipper, M Garcia-Sciveres, A Mekkaoui, M Barbero, G Darbo, D Gnani, T Hemperek, M Menouni, D Fougeron, et al. The FE-I4 pixel readout system-on-chip resubmission for the insertable B-Layer project. *Journal of Instrumentation*, 7(02):C02050, 2012.

[131] Cinzia Da Via, Maurizio Boscardin, Gian-Franco Dalla Betta, Giovanni Darbo, Celeste Fleta, Claudia Gemme, Philippe Grenier, Sebastian Grinstein, Thor-Erik Hansen, Jasmine Hasi, et al. 3D silicon sensors: Design, large area production and quality assurance for the ATLAS IBL pixel detector upgrade. *Nuclear Instruments and Methods in Physics Research Section A: Accelerators, Spectrometers, Detectors and Associated Equipment*, 694:321–330, 2012.

[132] CERN ATLAS Collaboration. *The performance of the ATLAS detector*. Springer, 2011.

[133] ATLAS IBL collaboration et al. Prototype ATLAS IBL modules using the FE-I4A front-end readout chip. *Journal of Instrumentation*, 7(11):P11010, 2012.

[134] Malte Backhaus, M Barbero, L Gonella, J Große-Knetter, F Hügging, H Krüger, J Weingarten, and N Wermes. Development of a versatile and modular test system for ATLAS hybrid pixel detectors. *Nuclear Instruments and Methods in Physics Research Section A: Accelerators, Spectrometers, Detectors and Associated Equipment*, 650(1):37–40, 2011.

[135] Erich Griesmayer, H Frais-Kölbl, H Pernegger, T Aumeyr, J Leinweber, J Bergoz, D Dobos, F Wenander, and H Bayle. High-resolution energy and intensity measurements with CVD diamond at REX-ISOLDE. Technical report, 2009.

[136] VA Verzilov, Wesbrook Mall, et al. Progress with Low Intensity Diagnostics at ISAC. *IPAC10*, page 885, 2010.

[137] Carel WE Van Eijk. Inorganic-scintillator development. *Nuclear Instruments and Methods in Physics Research Section A: Accelerators, Spectrometers, Detectors and Associated Equipment*, 460(1):1–14, 2001.

[138] L Thinova, C Karasinski, J Tous, and T Trojek. Investigation of thin YAP and YAG scintillator characteristics for alpha radiation spectrometry. In *Journal of Physics: Conference Series*, volume 41, page 573. IOP Publishing, 2006.

List of Figures

1.1 Layout of the ISOLDE facility. Image taken from [4]. 2
1.2 Layout of the REX-ISOLDE LINAC. Image taken from [4]. 4
1.3 Layout of the HIE-ISOLDE Linac. Image taken from [4]. 6
1.4 Layout of the beam lines coming out of the cyclotron at TRIUMF. Image taken from [22]. 8
1.5 Layout of the ISAC I and II halls. Image taken from [42]. 9
1.6 AD deceleration cycle. Image taken from [46]. 10
1.7 Layout of AD, ELENA and experimental areas. Image taken from [52]. 12
1.8 3D Schematic of the AE$\bar{g}$IS experiment shows antihydrogen formation and post-acceleration regions towards the Moiré deflectometer and detector. Image taken from [56]. 13
1.9 Layout of the AE$\bar{g}$IS experiment. Image taken from [59]. 14
1.10 Principle of antihydrogen production at AE$\bar{g}$IS. Image taken from [56]. . 14

2.1 Schematic of the REX-ISOLDE post-accelerator showing the location of the different Diagnostic Boxes (DBs). Dotted lines mark the different sections in the machine indicated by sector valves. 17
2.2 Carbon stripping foils installed in a wheel of a REX-ISOLDE diagnostic box. 17
2.3 Picture of a collimator wheel and Faraday cup inside DB5. 18
2.4 From left to right: Perforated copper foils of different transmission factors (0.1 and 0.01%) and two horizontal slits (3 and 1 mm), manually operated in DB2, upstream of the RFQ. 19
2.5 Up to 6 perforated copper foils can be installed in this wheel, along with circular collimators of 1, 3, 5 and 15 mm diameter, being remotely operated in DB3, downstream of the RFQ. 19
2.6 Left: Cross section of the REX-ISOLDE Faraday cup. Right: Picture of the REX-ISOLDE Faraday cup. 20
2.7 Working principle of the SEE beam profiler at REX. Image taken from [68]. 21
2.8 Screenshot of the application monitoring the beam profiler at REX. . . 22
2.9 Working principle of a slit-grid emittance meter. 22

2.10 REX-ISOLDE NTG Emittance meter. 23
2.11 Emittance measurement with a 2.8 nA beam of Ar^{+2} at ISOLDE. The $\varepsilon^{95\%}$=2.77 π·mm·mrad, while the ε_{RMS}=1.93 π·mm·mrad. The integration time is one second. Image taken from [69]. 24
2.12 PIPS detector installed in REX DB5. Image taken from [71]. 25
2.13 PIN photodiode installed in REX DB7. 25
2.14 Time structure of the pulses from ISOLDE, the Penning trap, EBIS and REX. Image taken from [13]. 26
2.15 Photodiode signal as a function of beam current. 27
2.16 Photodiode signal as a function of beam energy. 28

3.1 Layout of the intercryomodule region in HIE-ISOLDE. Image by E. Urrutia (personal communication, May 22, 2014. 30
3.2 Left: layout of the HIE-ISOLDE diagnostic box showing the linear-motion actuators. Right: Detail of the DB as seen from the back. (a) Vertical collimator slits; (b) slit scanner; (c) Vacuum port; (d) Blade of stripping foils; (e) Faraday cup; (f) PIPS Si detector. Image by W. Andreazza (personal communication, June 2, 2013). 31
3.3 Original 3D design of the HIE-ISOLDE Faraday cup. Image by P. Noguera (personal communication, Feb 24, 2012). 32
3.4 Illustration of the Beam Profile Monitor principle. Modified image taken from [75]. 33
3.5 Normalized intensity of a σ=1 mm beam as a function of slit position with different values of slit width as parameters. The coloured lines represent the different slit widths. 34
3.6 Effect of the slit width on the beamlet intensity measured from a 50 pA σ=1 mm gaussian beam. The coloured lines at the bottom represent the different slit widths. 34
3.7 Left: AVS out of vacuum guiding system for the slit scanner. Top right: Thermocouple attached to stepper motor for temperature monitoring. Bottom right: Limit switches. Image taken from [81]. 37
3.8 Experimental setup at AVS for the acceptance test of the slit scanner system. Image taken from [81]. 38
3.9 Picture of the scanning blade. Notice the almost imperceptible holes on the blade. Image taken from [81]. 38
3.10 Left: Camera frame showing the light passing through a slit and a hole. Right: Horizontal and vertical profiles of the light passing through the hole. Image taken from [81]. 39
3.11 Tracking of the hole positions in the camera reference system at 10 mm/s. Image taken from [81]. 40

3.12 Tracking of the hole positions in the camera reference system at 5 mm/s. Image taken from [81]. 41
3.13 Tracking of hole 1 moving the slit 6 mm back and forth at 10 mm/s. Top & bottom are zooms of the central plot. Image taken from [81]. . . 41
3.14 Tracking of hole 6 moving the slit 6 mm back and forth at 5 mm/s. Top & bottom are zooms of the central plot. Image taken from [81]. 42
3.15 Schematics of the different collimator blades type 1 (Left) and type 2 (Right). Image taken from [75]. 44

4.1 Operating principle of a Faraday cup. 48
4.2 Fraction of captured and lost electrons as a function of r/l. Insert in the figure represents the same plot at a larger scale. 49
4.3 Schematics of the Faraday cups discussed in this paper. (a) REX-ISOLDE FC; (b) Prototype 1; (c) Prototype 2; (d) Prototype 3. 51
4.4 Electrostatic potential distribution in the REX-ISOLDE Faraday cup. . 52
4.5 Electrostatic potential distribution in Prototype 1. 53
4.6 Prototype 1 (Left) and REX-ISOLDE FC (Right) FCs ready for experimental tests inside DB6. 54
4.7 Prototype 1 normalised beam intensity as a function of bias voltage for different beam energies. Measurement of REX-ISOLDE Faraday cup at 2.85 MeV/u added for comparison. 55
4.8 Electrostatic potential distribution in Prototype 2. 57
4.9 Normalized beam intensity measured by Prototype 2 as a function of bias voltage for different beam energies. Measurement of REX-ISOLDE Faraday cup at 2.85 MeV/u added for comparison. 58
4.10 Horizontal and Vertical beam profiles of a REX pilot beam at 29.3 pA. . 59
4.11 Horizontal and Vertical beam profiles of a REX pilot beam at 46.8 pA. . 59
4.12 Horizontal and Vertical beam profiles of a REX pilot beam at 250 pA. . 60
4.13 Horizontal and Vertical beam profiles of a REX pilot beam at 360 pA. . 60
4.14 Horizontal and Vertical beam profiles of a REX pilot beam at 540 pA. . 61
4.15 Horizontal and Vertical beam profiles of a REX pilot beam at 710 pA. Notice the stronger tails at this high current. 61
4.16 Horizontal and Vertical beam profiles of a REX pilot beam at 17.8 pA taken with 0.5 mm steps and 1 second pause in between. 62
4.17 Electrostatic potential distribution in the third prototype of the HIE Short FC. 63
4.18 Prototype 3 normalized beam intensity as a function of bias voltage for different beam energies. 65
4.19 Prototype 3 normalized beam intensity vs bias voltage for different beam energies. 66

4.20 Electron loss probability of Prototype 1 at different emission energies, repeller ring voltages and maximum emission angle cones of 0°, 45° and 90°. 68
4.21 Electron loss probability of Prototype 2 at different emission energies, repeller ring voltages and maximum emission angles of 0°, 45° and 90°. 70
4.22 Loss probability of Prototype 3 at different emission energies, repeller ring voltages and maximum emission angles of 0°, 45° and 90°. 72
4.23 The energy distribution curves for impact of H^+, He^+ and Ar^+ at 0.5 MeV. The original data points are displayed for He^+ impact. Image taken from [94]. 73

5.1 Fabrication process of a PIPS detector. Modified image taken from [96]. 77
5.2 Silicon detector data acquisition set-up. 79
5.3 Circuit of the 2003BT charge-sensitive preamplifier. Modified image taken from [97] 80
5.4 From top to bottom: Energy output of the 2003BT preamplifier, output of the N968 Spectroscopy Amplifier and busy output. Modified image taken from [98]. 81
5.5 Installation of the silicon detector and the α-source in DB5. Using the pneumatic actuator of the FC, the source could be positioned facing the detector. 84
5.6 Energy spectrum of the α source. 86
5.7 Energy scan of the REX-ISOLDE beam measured using the bending dipole magnet (A/q=4, E/A= 0.3 MeV/u). 88
5.8 Energy spectrum of the REX-ISOLDE beam measured with the Si detector and calibrated with an α source. A/q=4, E/A=0.3 MeV/u. . . . 88
5.9 Energy per nucleon for the different components of the REX beam (E/A = 0.3 MeV/u) acquired using the Energy signal of the Si detector. Bottom plot: magnetic field scan of the REX beam (A/q = 4) using the dipole bending magnet. 90
5.10 Timing spectrum of the REX beam. A/q = 4, E/A = 2.18 MeV/u beam. Detector installed in DB5. 91
5.11 Timing spectrum overlapped in two RF periods. A/q = 4, E/A = 2.18 MeV/u beam. Detector installed in DB5. Solid line: fit to the data with five Gaussian distribution (see text for details). Dotted line: Gaussian distribution corresponding to the first peak. The time difference between the particle hit and the RF pulse was 6.51 ns. The bunch length (1 σ) of the distribution was 2.51 ns. 93
5.12 Timing spectrum of the REX beam (E/A= 2.18 MeV/u, A/q=4). . . . 94

5.13 Schematic of the existing (top) and upgrade layout (bottom) with 10 MHz bunching system. Image taken from [110]. 96
5.14 Schematic of the pre-buncher concept in longitudinal phase space along with the RFQ and beam chopper for HIE-ISOLDE. Image taken from [111]. 97
5.15 Working principle of the beam chopper system for the HIE-ISOLDE LINAC. Image taken from [110]. 97

6.1 Schematic of the detector chamber installed at the end of the AE$\bar{g}$IS apparatus. Modified image taken from [59]. 101
6.2 Working principle of a foil-based secondary emission monitor. 102
6.3 Working principle of a MCP-based secondary emission monitor. 103
6.4 View of the two configurations of the monitor: (a) With foil and mesh. (b) MCPs placed directly in the beam path. Image taken from [118]. . . 104
6.5 schematic of the MCP-phosphor screen assembly. Image taken from [122].105
6.6 Layout of the AE$\bar{g}$IS experiment. Modified image taken from [59]. . . . 106
6.7 Drawing of the detector chamber with the SEM monitor in MCP stand-alone configuration. The camera is installed outside vacuum, facing the phosphor screen of the monitor through a view port. 107
6.8 Antiproton annihilation traces in the SEM when the antiproton beam hits the MCPs directly. The red circle represents the "centre of mass" of the beam captured in the image. 108
6.9 Secondary particle traces hitting the MCPs with the gate valve closed (No antiprotons). The red circle represents the "centre of mass" of the beam captured in the image. 108
6.10 Antiproton annihilation trace obtained with the SEM in the MCP stand-alone configuration. 109
6.11 Antiproton annihilation trace obtained with the SEM in the MCP stand-alone configuration. 110
6.12 Antiproton beam detected by the SEM in the MCP stand-alone configuration. Scale in 8-bit grayscale palette. 110
6.13 Drawing of the detector chamber with the SEM monitor in the foil-based configuration. The camera is installed outside vacuum, facing the phosphor screen of the monitor through a view port. 111
6.14 Image superimposition of 12 pictures showing secondary particles detected with the foil-mesh assembly. Foil voltage= -9 kV. The red cross represents the "centre of mass" of the beam captured in the image. . . . 112
6.15 Antiproton beam detected by the SEM in the foil-based configuration. Scale in 8-bit grayscale palette. 112

6.16 Antiproton annihilation products detected by the SEM in the foil-based configuration with the gate valve closed. Scale in 8-bit grayscale palette. 113
6.17 Schematics of the vertex detector (Nuclear emulsions) and the ToF detector. Image taken from [124]. 114
6.18 Schematic of the nuclear emulsions detector. Modified image taken from [62]. 115
6.19 Left: vacuum chamber containing the nuclear emulsions detector. Right: beam line set-up. Secondary particles, mainly pions, are generated by antiprotons annihilating in the upstream part of AE$\bar{g}$IS or directly in the emulsion detector. Modified image taken from [62]. 115
6.20 The MIMOTERA mounted on its PCB. The active area of the detector is 17.136×17.136 mm^2. Image taken from [59]. 117
6.21 Layout of a MIMOTERA pixel and charge collection scheme. Image courtesy of N. Pacifico. 118
6.22 Schematic of the experimental set-up. The centre of the Si detector is mounted 40 mm off axis and 430 mm from the AE$\bar{g}$IS device. Modified image taken from [59]. 119
6.23 Sample of a raw triggered frame after applying a noise cut of 150 keV and excluding one-pixel clusters. Around 60% of the detector was covered with aluminium foils with a thickness of 3, 6 and 9 μm. Image taken from [59]. 119
6.24 CNM 55 3D Pixel sensor mounted on a single chip card. The whole system is mounted on a flange before being installed in the six-way-cross CF vacuum chamber. Image taken from [128]. 121
6.25 Schematic view of the 3D pixels illustrating the electrodes in the CNM 55 sensor. Each pixel consists of two readout electrodes, shown in red, and six ohmic electrodes, shown in blue. Image taken from [128]. 121
6.26 Sample frame of the 3D sensor with two fitted proton tracks coming from an antiproton annihilation. Annihilation tracks as these shown here are used to reconstruct the annihilation point. Image taken from [128]. . . . 122
6.27 A sketch showing the layout of the different beamlines at the ELENA ring. Modified image taken from [50]. 123
6.28 The optics and beam sizes of the LNE02 beam line. Proposed locations for beam profile monitors are circled in blue. Image taken from [50]. . . 124

List of Tables

1.1 Parameters of the HIE-ISOLDE LINAC. 6
1.2 Main beam parameters at the ELENA ring. 11

3.1 Effect of the slit width of the slit scanner on the measured beam transmission and beam size. 35

4.1 Geometric parameters of REX and HIE collector plates 51
4.2 Electrostatic potential on the central axis of Prototype 1 as a function of repeller ring voltage. 54
4.3 Maximum output energies of the different cavities of the REX-ISOLDE LINAC. 55
4.4 Beam species with energies per nucleon and intensities delivered to the FCs at ISAC-II in TRIUMF for tests. 64

5.1 Performance of Partially Depleted PIPS detectors according to area and thickness. 79
5.2 Range of ion species in silicon at characteristic HIE-REX energies as calculated with SRIM. 83
5.3 Channels vs Energy for the peaks of the alpha source, obtained from the spectrum of Fig. 5.6. 85
5.4 Alpha particle energies and relative intensities [106] for the isotopes present in the alpha source used. 86
5.5 Energy spectrum of the REX-ISOLDE beam (A/q=4, E/A=0.3 MeV/u) using two different methods. 87
5.6 Results of the ToF spectra analysis. 94
5.7 Final results from the ToF spectra analysis. 95

A.1 Energy loss at the entrance window of the SRIM Si detector (TM series), calculated as an equivalent thickness of 70 nm, using SRIM 2012 stopping power tables [86]. 134

B.1 List of ion beams delivered at REX-ISOLDE. (Didier Voulot, private communication). 136